Numerical Modelling of the Compression-After-Impact Behaviour of Composite Sandwich Panels

By

Christopher T. James
MEng (Hons) CEng MIMechE

A Doctoral Thesis in Partial Fulfilment of the
Requirements for the Award of Doctor of Philosophy
of Loughborough University

June 2015

Department of Aeronautical and Automotive Engineering
Loughborough University
Leicestershire
United Kingdom

Abstract

Sandwich panels using fibre-reinforced composite skins and low-density cores are being increasingly used in the aerospace industry due to their superior specific strength and stiffness, and increased design flexibility over traditional metallic and composite structures. However, it is well-known that sandwich panels are highly vulnerable to the effects of impact damage, with even low-energy impacts potentially causing very severe reductions in the in-plane compressive strength of these structures. The objective of this project was to produce a faithful and reliable numerical model for the simulation of the compression-after-impact strength of composite sandwich panels. An in-depth literature review revealed that delamination within the skins of a sandwich panel is a damage mechanism that has gone almost entirely neglected in previous efforts at modelling this problem, despite the proven significance of this mechanism in the failure of impact damaged sandwich panels in compression. Consequently, the use of the cohesive zone model for delamination initiation and propagation is the key unique feature of this model, with Hashin's criteria being used for intra-laminar damage formation, and a simple plasticity response capturing core crushing. An experimental study is performed to produce a thorough dataset for model validation, featuring differing levels of damage induced via quasi-static indentation, and novel asymmetric panels with skins of unequal thickness (the thinner skin being on the unimpacted side).

The experimental study revealed that the use of a thinner distal (undamaged) skin could improve the strength of mildly damaged sandwich panels over undamaged sandwich panels using the same asymmetric configuration. It is believed that this effect is due to the movement of the neutral plane of the sandwich panel caused by the reduction in the stability of the damaged skin through stiffness reduction and geometric imperfections. This removes the eccentricity of the compressive loading that exists in the undamaged asymmetric panels, which has mismatched axial stiffness between the indented skin and the thinner distal skin, and thus a noticeably lower ultimate strength than the undamaged symmetric panels.

The sandwich model is developed using pre-existing experimental and material data, and trialled for a variety of different skin lay-ups, core thicknesses and indenter sizes. The numerical model generally agreed well with the ultimate stress found in the experiments for these different configurations, but is quite poor at estimating the magnitude of the damage induced by the indentation. When used to model the experimental study, the model gave generally good, conservative estimates for the residual compressive strength of both the symmetric and asymmetric panels. The tendency of the asymmetric panels to become stronger with mild damage was not captured by the model per se, with the numerical results instead showing an insensitivity to damage in the asymmetric panels, which was not shared by the symmetric panels. However, the numerical model did exhibit erroneous strain-stress responses for both panel configurations, particularly for the undamaged and mildly damaged cases. Investigations revealed that this erroneous behaviour was caused by inconsistency in the material data, which had been collected partially via experimentation and partly from literature sources. Overall, the model developed here represents a promising advancement over previous efforts, but further development is required to provide accurate damage states.

Contents

Acknowledgements **5**

Publications **6**

Nomenclature and Keywords **7**

1: Literature Review **9 - 31**
1.1 Introduction 10 – 12
1.1.1 Objectives and Work Structure *12*
1.2 Reviews 13 - 14
1.3 Experimental Work 14 - 19
1.4 Impact and Residual Strength Modelling 19 - 25
1.5 Improving the Impact-Resistance of Composite Structures 25 - 27
1.6 Review Tables 28 - 31

2: Modelling of Damage in Composite and Sandwich Structures **32 - 62**
2.1 Composite Failure Theories 33 - 35
2.1.1 Hashin-Rotem Criterion *36 - 38*
2.1.2 Damage Initiation and Evolution for Fibre-Reinforced Materials in Abaqus *38 - 43*
2.2 Delamination Modelling 43 - 46
2.2.1 Implementation of the Cohesive Zone Model *46 - 51*
2.3 Behaviour of Core Materials 51 - 52
2.4 Finite Element Modelling with Abaqus 52 - 53
2.4.1 Selection of an Appropriate Solver *53 - 56*
2.4.2 Finite Element Selection *56 - 59*
2.4.3 Material Data Requirements *60 - 61*
2.4.4 Contact *61 - 62*

3: Experimental Work **63- 89**
3.1 Sample Preparation 64 - 67
3.2 Impact and Indentation Tests 67- 76
3.3 Compression-after-Impact (CAI) Tests 77 - 89

4. Skin Model Development: Quasi-Static Indentation of a Composite Plate **90 - 115**
4.1 Problem Description 91 - 93
4.2 Elastic Response 93 - 105
4.2.1 Load Application *93 - 100*
4.2.2 Element Comparison *100 - 103*
4.2.3 Solver Comparison *104 - 105*
4.3 Inelastic Response 105- 78
4.3.1 Solution of the Non-Linear Problem *105 - 107*
4.3.2 Initial Load Drop – Delamination *108 - 111*
4.3.3 Damage Evolution – Intralaminar Damage *111 - 115*

5. Sandwich Model Development 116 - 148
5.1 Czabaj, Singh et al Experimental Studies 117 - 118
5.2 Model Description 118 - 124
5.3 Preliminary Model Results 124 - 127
5.4 Residual Strength Prediction 127 - 134
5.5 Damage Extent Prediction 134 - 138
5.6 Parametric Study – Effect of Inaccuracies in Material Data Input 139 - 147
5.7 Summary 147 - 148

6: Numerical Modelling of Experimental Work 149 - 173
6.1 Model Description 150 - 152
6.2 Numerical Modelling Results 152 - 158
6.3 Damage and Failure Progression 159 - 166
6.4 Investigation of the Unexpected Stress-Strain Response 167 - 173

7: Numerical Modelling of Combined Loadings in Sandwich Panels 174 - 179
7.1 Model Description 175 - 179
7.2 Results 179 – 191

8: Summary and Conclusions 192 - 195

Appendices & References 196 – 220
Appendices 197 - 190
- *A: Results from Material Property Tests 197*
- *B: Impact Jig Pendulum Setting 198 - 199*
- *C: Instrument Calibration 200 - 202*
- *D: Raw Compression-after-Impact Data – Symmetric Panels 203*
- *E: Raw Compression-after-Impact Data – Asymmetric Panels 204*
- *F: Damage Magnitude Results from Development Sandwich Model 205*
- *G: Complete Results for the Parametric Study 206*
- *H: Damage Magnitude Results from the Parametric Study 207*

References 208 - 220

Acknowledgements

First of all, it is appropriate for me to acknowledge my funding sources, primarily the Department of Automotive and Aeronautical Engineering at Loughborough University, which has kindly provided me financial means without which this whole endeavour simply would not have been possible. This has been supplemented by a generous grant from the Bank of Mum & Dad, which has provided additional support. I am deeply grateful to both benefactors.

I would like to thank my supervisors, Dr. Andrew Watson and Dr. Paul Cunningham for the tremendous amount of support, encouragement and expertise they have offered me throughout this project, as well as no small amount of patience! Additionally, I would like to thank Dr. Gang Zhou for his invaluable input in the early stages of this project, and Dr. Christopher Harvey, for taking the time to review this work at various stages, and for the feedback offered.

I extend my thanks to the technical staff in the mechanical workshop at AAE, whose help allowed my experimental work to go as smoothly as it did. I offer special thanks to Dave Roche for producing my jigs and fixtures, and also to Mike Smeeton in Civil Engineering for his support in using the machinery in that department for some of my testing. I would also like to thank Gill Youngs for handling the administrative side of the research so admirably.

I want to thank my fellow researchers for their assistance at various points in my work, and also providing an enjoyable working environment. My colleagues Pete Nash and Shuo Dai especially were very helpful, particularly during my experimental work, and I am grateful for their assistance.

Special thanks are due to Clint Davies-Taylor of Simulia, UK. He has provided indispensable technical assistance in using *Abaqus*, and his knowledge has helped me over a number of significant hurdles. Without his help, this project would not have been as successful as it has been.

A final thanks to my friends and family in Nottingham, Northamptonshire and elsewhere. The names are far too numerous to mention them all, but you should know who you are! You all provided emotional support without which I would’ve surely gone peculiar, and simply made life that much more fun. Thanks to one and all!

Publications

- [1] James, C.T.; Watson, A.; Cunningham, P.R. Numerical Modelling of the Compression-after-Impact Performance of a Composite Sandwich Panel. Journal of Sandwich Structures and Materials 2015; 17(4): 376-398

- [2] James, C.T.; Cunningham, P.R.; Watson, A. Experimental and Numerical Investigation of the Effect of Asymmetry on the Residual Strength of a Composite Sandwich Panel. Journal of Sandwich Structures and Materials 2015; 17(4): 417-445

Nomenclature

CAI	Compression-After-Impact
BVID	Barely-Visible Impact Damage
ASTM	American Society for Testing and Materials
FE	Finite Element
FML	Fibre Metal Laminate
WWFE	World-Wide Failure Exercise
FEM	Finite Element Methods
CDM	Continuum Damage Mechanics
HFGMC	High-Fidelity General Method of Cells
VCCT	Virtual Crack Closure Technique
ALE	Adaptive Lagrangian-Eulerian
XFEM	Extended Finite Element Method
QSI	Quasi-Static Indentation
IKE	Initial Kinetic Energy
CFRP	Carbon Fibre Reinforced Plastic
CPU	Central Processing Unit

Keywords

Composite sandwich panels

Compression-After-Impact

Numerical modelling

Delamination

“Engineering is the art of modelling materials we do not wholly understand, into shapes we cannot precisely analyse, so as to withstand forces we cannot properly assess, in such a way that the public has no reason to suspect the extent of our ignorance.”

Dr A.R. Dykes

British Institution of Structural Engineers, 1976.

Chapter 1

Literature Review

1: Literature Review

This report begins with an introduction of sandwich panels, their construction, benefits and drawbacks. This leads onto a detailed review of the relevant literature, including surveys and other reviews. The focus is on the compression-after-impact behaviour of composite and sandwich structures, and methods used to simulate this behaviour. A thorough consideration of past research facilitates the rest of the work done in this project.

1.1: Introduction

Sandwich panels, as implied by the name, are layered structures, typically featuring two thin sheets of stiff, (relatively) high-density material bonded to a thick inner core of softer, low-density material. The skins are required to transmit the in-plane normal and shear loading, while the core provides the required separation and stability for the skins, and transmits the transverse normal and shear loads [3]. By increasing the thickness of the panel, the core also increases the flexural rigidity of the panel for a small weight penalty [4]. Originally, metal sheets would form the skins (or facesheets) though contemporary sandwich panels usually use composite skins, due to the accepted advantages composites have over traditional structural materials in terms of specific strength, stiffness and design flexibility. Carbon and glass fibres - and on occasion, combinations of the two – are very common skin materials in the aerospace and marine industries respectively. Core materials are usually in the form of foams and honeycomb structures, with a modern development being the origami-style foldcore material, which offers some non-mechanical benefits, such as moisture drainage, over honeycombs in exchange for generally reduced mechanical properties [5]. Honeycombs will be the main core material of interest in this work, with honeycombs made from aluminium foil and aramid paper being typical choices in the aerospace industry.

Image hidden due to copyright restrictions.
Please refer to [11], Figure 1

Figure 1: Typical sandwich construction using honeycomb core [11]

Image hidden due to copyright restrictions.
Please refer to [5], Figure 1

Figure 2: Foldcore specimen [5]

In recent years, composite sandwich panels have seen increasing use in industrial applications due to their improved strength, weight, stiffness and damage resistance over traditional composite materials. The first industrial-scale use of sandwich materials was the De Havilland Mosquito aircraft built during the Second World War, which was made primarily of various species of wood sandwiched together [3]. Since then, they especially find routine usage in aerospace where the inherent efficiency of these structures over traditional stiffened skin constructions is highly desirable. This is particularly the case where weight reduction is and will remain of paramount concern. That such panels are seeing use in high-profile and large-scale aeronautical and marine applications, such as the Visby-class corvette of the Swedish Navy [6], is testament to their potential. As a specific example of the potential improvements offered, Abrate, in his extensive review of the impact on sandwich structures [7], mentions the Boeing 360 helicopter where *"compared to skin-stringer aluminium construction, the use of sandwich structures lead to an 85% reduction in the number of parts, a 90% reduction in tooling costs, and a 50% reduction in the number of man-hours needed to fabricate a helicopter."*

However, despite this promise, sandwich structures remain vulnerable to impact damage from a whole manner of sources, including damage resulting from maintenance activities such as dropped tools. This damage may be difficult to detect, and yet have severe implications for the performance of the panels, which may in turn have safety implications. Abrate [7] cites a very large number of studies that show significant degradation of tensile, compressive, shear and flexural properties in sandwich panels after low-velocity impact, with a panel retaining perhaps as little as 50% of its undamaged strength. As the effects of impact damage on residual in-plane compression performance are very complex, due to the dynamic nature of impact events and the myriad damage and failure mechanisms that exist in these structures, impact damage tolerant structural design requires this behaviour to be fully understood. 'Damage tolerance' refers to the ability of a structure to continue supporting the required loads after a damaging impact event, in contrast to 'damage resistance', which refers to the ability of a structure to remain undamaged by an impact event. Damage tolerance of aerospace structures must be demonstrated for an aircraft design to be officially declared airworthy [8].

Abrate [7] notes in his review that the majority of work performed in understanding impact damage behaviour is experimental, and often, conclusions made by one investigator may be in contradiction to the findings of another. This suggests a paucity of understanding of the impact behaviour of sandwich panels, a view shared by Tomblin et al [8] in their 1999 review of the field. The sheer variety of sandwich configurations, sensitivity to imperfections, and the interactions between damage and failure modes also contributes to this problem. Additionally, in commercial practice, extensive experimentation is something to be avoided, if not eliminated, due to the considerable financial and time cost that is entailed. As a result, it is imperative that reliable computer-based finite element numerical models are developed to study these performance characteristics, and thus make informed design decisions. Computer simulation using the finite element method is an indispensable tool in the designer's repertoire, reducing if not eliminating the considerable costs involved in the production and testing of prototypes.

1.1.1 Objectives and Work Structure

The aim of this project is to develop a reliable, faithful and fully validated numerical model for the Compression-after-Impact (CAI) behaviour of composite sandwich panels, using the commercial finite element software package *Abaqus*. This work fits into the wider area of damage and residual strength modelling for composite structures, which is a very active field of research. However, the modelling of sandwich structures appears to have been somewhat neglected of late, with only a few authors looking at the specific case of compression-after-impact for these structures.

The project first focuses on the understanding and development of numerical techniques in damage propagation during loading. The following literature review investigates experimental and numerical studies on impact damage and residual strength of sandwich panels, discussing aspects and issues pertinent to the development of a computer-based numerical simulation of impact damage and residual strength measurement for a composite sandwich panel and work performed to date in the development of such a model. Chapter 2 looks in more depth at damage modelling and aspects of numerical modelling relevant to this project, with a particular focus on composite failure theories, delamination modelling and some specific aspects of the finite element method required for this work.

An experimental study is presented in Chapter 3, which provides a good-quality set of results that can be used for further validation of the model, and investigates the use of different skin thicknesses on either side of the core in improving damage tolerance. A model for damage initiation and propagation in a composite plate is presented in Chapter 4, producing a damage state consistent with that for a low-velocity impact; modelling the more extreme penetrative damage often caused by high-speed impact events is beyond the scope of this work. This provides the basis for the skin model of the sandwich panel model. The sandwich panel model is presented in Chapter 5, and compared with existing experimental data. The model starts with an undamaged panel, and simulates both the impact damage and the subsequent compressive loading in a single analysis. This chapter also features a parametric study to explore some of the sensitive parameters in the numerical model input data. The experimental work from Chapter 3 is simulated and discussed in Chapter 6. A continuation study, looking at using the now-validated model to investigate the effect of combined biaxial compressive and pressure loads on the residual strength is then presented in Chapter 7.

1.2: Reviews

This literature review aims to facilitate further research in this vitally important research area. The reviews of Abrate [7] and Tomblin et al [8] provide valuable summaries of the work done in the years leading up to the late 1990s, with the latter proposing a damage tolerant design methodology that includes analytical models. Such an approach would be consistent with (American) Federal airworthiness regulations as they existed at the time. However, in practice, the problem of impact damage in sandwich panels is not open to analytical solution except for specific geometries and boundary conditions, and has the additional weakness of being unable to describe damage progression, which is critical to thorough understanding of the mechanics involved [9]. As a result, the current focus by most investigators has been on numerical solutions. The reviews of Abrate [7] and Tomblin et al [8] have been invaluable and frequently cited guides to more recent research efforts.

Tomblin et al [8] also included as part of their report a detailed discussion of the experimental work performed as part of the Boeing Advanced Composite Aircraft Structures Program, funded by NASA’s Advanced Composites Technology Program. This extensive study, which included a section on impact damage resistance, looked at two composite design concepts for the aft fuselage section of a wide body airliner, one of these concepts being a sandwich construction. Some of their key observations from the impact study included reduced indentation and damage area as core density and skin thickness was increased, a minor influence on damage resistance from the support type, with a greater dent depth noted when the structure was rigidly supported, and a reduction in indentation, but an increase in damage area as the impact tip size increased. Tomblin et al also published an extensive experimental study on the damage tolerance of impacted sandwich panels [10], the results of which have been used by other authors such as Lacy & Hwang [11,12] to calibrate and verify their numerical models.

One more recent review by Hayman [13] discusses the challenge of damage assessment and tolerance for sandwich panels from the perspective of the marine industry, where these structures are finding frequent use in high-performance vessels. Hayman makes the important observation that damage and defects are considered through designers applying high factors of safety, which while guaranteeing structural integrity, also results in inefficient (i.e. overly heavy) structures. The author reviews several means of detecting damage, and presents an approach to damage assessment for marine applications, considering the strength reduction and determining the required actions depending on the criticality of the damage location and damage extent. He also reviews models for damage aspects such as face-core debonds, contact damage (i.e. highly localised damage), face sheet wrinkle defects and dry zones. Note that some of these defects may be the product of manufacturing flaws, and as such are beyond the scope of the present investigation. Hayman also cautions that the accuracy of these models is not fully established for some cases.

Finally, McQuigg, in his 2011 thesis studying thin-gauge fabric-skinned sandwich panels via experimentation and numerical simulation, provides a helpful review of all aspects of impact and residual strength investigation for sandwich panels [14]. This includes discussions on damage characterisation, experimental work, and past and present numerical analysis efforts. Many of his sources are discussed in detail in the current review. He draws particular attention to the issue of progressive damage modelling in the composite skin; this aspect remains fairly poorly understood and is an area of some interest to researchers all of its own. It is highly relevant to sandwich panel modelling, since the skins carry the in-plane loads. Progressive damage and failure of composite materials will be discussed in depth in Chapter 2.

1.3 Experimental Work

Experimental work in this field broadly splits in damage characterisation studies and residual strength studies. Damage characterisation exercises determine how various geometric, loading and boundary conditions affect the development of damage mechanisms in sandwich panels. Impact damage can be manifest via core crushing, skin damage (in the form of matrix cracking and fibre fracture or buckling), interply delamination and skin-core debonding. Failure of the fibre-matrix interface may also be observed (e.g. fibre pull-out). A permanent indentation will usually be observed, though in the important case of BVID (Barely Visible Impact Damage) this may be very small. All of these can propagate with additional loading, as can local fibre buckling in damaged regions of the skin. In more extreme impacts, fibre shear-out may be observed. Figure 3 shows all of the important damage mechanisms for a quasi-statically loaded panel. Figure 4 shows an impact damaged panel.

Images hidden due to copyright restrictions.
Please refer to [15], figures 11 &16

Figure 3: Aluminium honeycomb sandwich panel under quasi-static load sectioned at ultimate failure. a) Hemi-spherical indenter (top) and b) flat-headed indenter (bottom) [15]

Image hidden due to copyright restrictions.
Please refer to [17], figure 5

Figure 4: Honeycomb sandwich panel impacted 25J [17]

A body of work investigating these problems has been produced at Loughborough University, and this research effort is on-going by the present author and others. Of particular interest are the studies of Zhou et al [15-17], which have sought to characterise the damage mechanisms, investigate the parameters governing said damage and to study the residual compressive strength of damaged sandwich panels. The damage mechanisms were found in [15] to be core crush, top-skin delamination and fibre fracture and/or shear-out, with the precise nature and evolution of the damage being dependant on the type of indenter (hemispherical or flat) used. In all cases, the bottom skin of the panel was undamaged, resulting in a loss of through-the-thickness symmetry that would be the subject of later investigations.

This work was built upon in a parametric study [16], where the authors varied skin thickness, core density and type (aluminium or Nomex), indenter nose shape and the boundary conditions and observed the effects of these changes on the damage and energy-absorbing characteristics of sandwich panels. They found that increasing the skin thickness increased the threshold load (where damage is first evident) and ultimate load (defined as when the top skin fractures). The threshold load is also heavily influenced by core density – a denser core will usually be stiffer, and thus provide additional support to the skins. The observed damage mechanisms will be affected by the shape of the indenter tip, as also observed in [15] and seen in Figure 3. Typically, a panel damaged with a flat-headed indenter will experience more extensive delamination remote from the loaded region, and is liable to suffer fibre shear-out. Finally, they observed that cores of similar density have similar damage and energy-absorption characteristics, and the material has little influence on the studied mechanical properties, though it was observed that the Nomex core exhibited ‘spring-back’ behaviour when unloaded.

It should be noted that these two studies used transverse quasi-static loads to damage the panels, not impact. This is a generally accepted model for low-velocity impacts, as explained in Chapter 3 of Reid & Zhou [18]: at impact velocities of less than 50ms^{-1} (Cartié & Irving suggest a lower threshold of 20ms^{-1} as the transition point between high-velocity and low-velocity impact behaviour [19]), multiple reflections of stress waves at the material boundaries result in a quasi-static equilibrium state. As a result, the mechanical properties of composite materials are relatively insensitive to strain rates between 10^{-3} – 10^{3} s^{-1}, with the behaviour changing to varying degrees depending on material, fibre configuration etc. These rates correspond with low-velocity impacts. This can be contrasted with Othman & Barton’s [20] experimental study on the influence of geometric effects on the damage evolution in both bare and stabilised (i.e. sandwich panels) honeycombs under three-point bending and low-velocity impact. Here it was noted that there was an increase in strength under dynamic loads over the quasi-static case. This suggests that even at low-velocities (Othman & Barton used an impact velocity of $9.85ms^{-1}$) strain rate effects may need to be included. The similarity in damage mechanisms for quasi-static and low-velocity events can be seen in Figure 3a and Figure 4, with the shape of the damage and the damage mechanisms observed being broadly the same for both cases. A comparison between static indentation and low-velocity impact on sandwich panels was also presented by Herup & Palazotto [21], concluding that the damage produced by the two methods was similar, but again with a higher load at damage initiation for the dynamic loading. They further state that the difference between the static and dynamic loadings increase as the skin thickness increased – the authors used skins with between 4 to 48 plies, which is clearly a very significant range of thicknesses. Typical sandwich panels will have skins at the thinner end of this range.

Zhou & Hill performed further investigations on the compression-after-impact strength of sandwich panels [17]. The authors noted that even significantly energetic impacts did not cause a significant reduction in compressive strength for some panels, particularly with denser core materials. However, at the threshold energy for BVID, the reduction of compressive strength became substantial, thus further illustrating the very real practical concerns for impacts on sandwich panels. This particular investigation used impact energies of up to 28J (for panels with Nomex cores – 26J for aluminium cores) and established reductions of compressive strength for both panels in the region of 50%. For example, the nomex core sandwich panel showed this degree of strength reduction at its threshold energy for BVID of 25J. The BVID threshold for the aluminium core sandwiches was considerably lower, at 3J, though the residual strength at this energy level was higher, with 71% of the virgin strength being retained. Reductions in strength of this order were notes by the sources in Abrate, along with the observation of there being no strength reduction below a certain threshold energy [7].

More recently, Zhou et al have performed further investigations into the behaviour of impact-damaged sandwich panels, with the role-sharing by the major damage mechanisms for energy absorption - whereby delamination, ply fracture and core crushing all play roles in the impact energy absorption - and the behaviour of unsymmetric sandwiches being of particular interest [22-25]. The work performed in [23] supports an observation made by Zhou & Hill [17] that the stabilising and supporting effect of the core could work to mitigate the effect of impact damage in the skins when the panel is loaded in compression, particularly in cases of small-scale damage and cores with relatively high shear and compressive strengths. As a consequence, characteristics established for monolithic composite panels by other researchers may not necessarily be valid for sandwich panels. Additionally, as also noted in [15], the impact damage creates an asymmetry in the panels since the damaged top skin will obviously not be as stiff as the undamaged bottom skin. This results in a bending moment in the compressively loaded panel that contributes the observed reduction in compressive strength.

The final work of interest from this group performed studies on the CAI strength of unsymmetric panels [24,25]. Various panels with thin and thick skins were tested where the ratio of thickness between the thicker, impacted top skin and the thinner undamaged bottom skin was constant at 1.25. The authors found that when the thicker skin was impact damaged, the reduction in compressive stiffness in that skin caused the effective compression resistance of the whole panel to ‘even up’ by moving the neutral bending plane of the panel closer to the geometric centreline, removing the eccentricity of the loading and thus the bending moment caused by the asymmetry, resulting in improved damage tolerance compared to the damaged symmetrical panels.

Asymmetric monolithic composite plates, while not under consideration in the current project, have interesting properties of their own, particularly that they have multiple equilibrium states and so can be used to make geometrically bistable structures that can undergo a large change in shape with only a small energy input. Schultz [26] and Diaconu et al [27] present conceptual studies in using these structures to produce morphing, variable-geometry aerospace structures, driven by piezoelectric actuators. The use of these unusual lay-ups in sandwich panels could prove an interesting area for further research.

Schubel et al [28] also experimentally investigated impact and CAI strength on sandwich panels. In their method, they applied the compression load via shear loading rather than end loading, to prevent the specimens failing at the ends – this behaviour was also observed by Zhou & Hill [17] in significant minority of their tests. The test samples were prepared in such a way that the damaged region accounted for approximately a third of the total specimen area, with the damage being through-the-width. The authors conclude that delamination in the skins is of paramount importance, since this damage mechanism reduced the compressive strength by more than 50% in their tests. As in [17], they also note that there was no significant damage produced until the impacts became relatively highly energetic.

The compressive loading may also be applied as a dynamic load. Ordinarily, the compressive load is applied as a static or quasi-static load, but Bailey et al [29] apply the compression load to damaged and undamaged sandwich panels at high speed using a modified Split Hopkinson pressure bar set-up. These dynamically-loaded panels are compared with those loaded by conventional static testing, for various amounts of damage applied via quasi-static indentation. The dynamically loaded panels show higher compressive strengths than the statically loaded panels at all levels of damage – the undamaged panels exhibit 26% greater strength under dynamic loading. However, the percentage residual strength noticeably decreases for the mildly damaged panels under dynamic loads.

Impact damage can propagate with sufficient compressive load. Ratcliffe et al have studied two specific damage propagation mechanisms for damaged sandwich panels: indentation growth (studied using finite element modelling) [30] and kink-bend propagation [31]. The former occurs when a residual dent buckles inwards and grows under compressive loading. This causes additional core crushing and eventually causes buckling across the width of the panel, resulting in failure. The latter failure mode occurs when damage acts as a stress concentration, which causes fibres in the loading direction to buckle normal to the skin, creating a band of broken fibres that grows perpendicular to the loading direction under compression. Failure occurs when a critical length of kink-band is reached, causing the band to suddenly propagate across the width of the panel. These failure modes are shown in Figure 5. In McQuigg et al’s experimental study [32], indentation propagation was observed in their thin-skinned specimens, with failure via crack propagation seen in the thicker-skinned specimens. The same behaviour is also observed by Czabaj et al [33].

Image hidden due to copyright restrictions.
Please refer to [30], figure 2.

Figure 5: Shadow Moiré images showing (left) kink-band propagation and (right) indentation growth [30]

Cartié & Irving [19] investigated the effect of material properties on the impact and CAI response of various grades of carbon-fibre composites. They note that the size of delamination generated by the impact event, and also the peak impact force, is primarily controlled by the mode 2 (shear-opening) fracture energy of the resin. The CAI strength is also intimately linked with this parameter, due to the influence of delamination on the compressive strength of composite plates. Thus, the strength and stiffness of the fibres is of lesser importance. The stacking sequence of the composite lay-up was also found to have a significant influence on the development of delamination via impact, in a study by Hitchen & Kemp [34]. They found that as the number of interfaces between plies of different orientation decreases (i.e. when there are a greater number of plies of the same orientation clustered together), so does the residual strength of the laminate, assuming a constant overall thickness. This is due to the delaminations, when they occur, being larger than when there are more interfaces between dissimilar orientations, increasing their destabilising effects. A numerical modelling-based study into the effect of clusters of plies with the same fibre orientation which was performed by Gonzalez et al came to a similar conclusion [35]. Hitchen & Kemp also find, however, that the total delamination area (i.e. the sum of all delaminations present in the laminate) does not necessarily harm the CAI strength, suggesting that only the largest of all the delaminations controls the residual strength. They refer to earlier work by Hong & Liu [36] showing that the delamination area increases as the change in orientation angle between adjacent plies increases.

Hwang & Liu [37] also performed a detailed investigation on the effects of multiple delaminations on the buckling behaviour of compressively loaded composite plates. They observe that when considering buckling stress under uniaxial compression, the key delamination in a plate is the one closest to the ‘impacted’ surface. Provided that the deeper delaminations are not of greater size than the near-surface delamination, the buckling stress between the two cases is virtually unchanged. This conclusion agrees with that made by Hitchen & Kemp [34]. The authors note that there is an effect if there are shorter delaminations closer to the impacted surface than the longest one, but that these cases are not representative of realistic impact damage.

Although it is desirable to use experimental data to validate numerical models, there is a problem of spread in the recorded results. This tendency can be seen in the limited repeat tests performed by Zhou & Hill [17]. Lacy & Hwang [11] note the great spread of data in the studies of Tomblin et al [10], and recommend caution when using only numerical modelling for residual strength studies. Gonzalez et al [35] note that the repeatability of their drop-tests (and thus the consistency of their data for the impact event) is extremely good, but that the repeatability of the CAI tests is rather poorer. Czabaj et al [33] suggest that scatter in the data for CAI tests may be inevitable due to the instability-dominated failure modes, and their inherent sensitivity to imperfections. This situation is not helped by the absence of a test standard for the compression-after-impact testing of sandwich panels – for example, McQuigg et al [32] made reference to the ASTM standards for CAI testing of monolithic composite plates [38] and the edge compression of undamaged sandwich panels [39] to develop their experimental program. Additionally, there is a general paucity of repeat tests. Zhou & Hill [17] made an attempt in this regard, as did Czabaj in the experimental work on the compression-after-impact strength of sandwich panels presented in his 2010 thesis [40], but generally, most experimental results produce (or at least present) just a single data point for each test condition, making it impossible to get a statistically rigorous view of the quality of the data. In defence of the experimenters, this is a particularly difficult problem to resolve, due to the already considerable expense and effort involved in production and instrumentation of test samples, but nevertheless, this issue must be addressed in order to provide good-quality results for the validation of numerical models; it is not particularly helpful to have a model that agrees with a given set of experimental data if the same data cannot itself be conclusively declared representative of reality.

1.4 Impact and Residual Strength Modelling

It is of tremendous practical importance to develop reliable models for damage formation, damage propagation and residual strength of sandwich panels. However, the complex interactions between failure and damage mechanisms, themselves dependant on a host of configuration related parameters, make this a very challenging proposition. Indeed, in their 1994 paper, Davies et al recommend that the numerical modelling of impact damage should be avoided if at all possible due to the complexity of the problem [41]. Although computing power has improved vastly in the two decades since, the challenge posed in creating a faithful, accurate and flexible model for residual strength simulation for composite and sandwich structures remains. There is no agreed standard method for this endeavour [12], so there are a host of different ways to do perform these simulations. Some authors will simulate the impact event itself. This necessitates an explicit dynamic model, especially for high-velocity events. Low-velocity impacts may be adequately modelled via quasi-static loading, which may or may not be applied through a simulated indenter. Another, semi-empirical approach requires impact experiments to be performed to calibrate the compression-after-impact model. The damage state from experimental impact studies would be determined via non-destructive imaging and/or sectioning of the panel, and this information entered into a numerical model for residual strength estimation. Examples of both of these approaches are given in the coming review. Compression-after-impact cannot be modelled without the use of one of these approaches to generate a damage state in the panel. Impact event simulations, whether dynamic or quasi-static approximations, may be performed in isolation, without necessarily having to perform a residual strength analysis. Indeed, much work has been performed on impact simulation, with rather less research effort being spent on compression-after-impact simulation [42].

High-speed impact events (impact velocity exceeding 50ms^{-1} [18]) are a very serious concern for designers of sandwich structures, and modern modelling techniques are quite capable of modelling these highly complex dynamic events, producing representative results for impacts by, for example, runway debris [43] and bird-strikes [44]. Studies by Meo et al [45] and Hoo Fatt & Park [46,47] compared experimental numerical and analytical results for damage development during a low-velocity impact event with reasonable accuracy. Olsson [48] presents an analytical solution for predicting the impact behaviour of sandwich panels, accounting for delamination and core crushing without requiring empirical data. Analytical solutions are valuable particularly for initial design studies as finite element analyses can prove extremely time-consuming, but are limited only to specific, simple structural configurations and load cases.

Hufenback et al [49] develop in their work analytical methods for simulating the effect of stress concentrations in composites. Since these are caused by holes and notches, they are clearly an area of concern for the structural designer. The above authors pay special attention to composites with elastic inclusions, which can be used to model stress concentrations. They present both analytical and experimental results, showing a good correlation between the two. Impact damage creates stress concentrations in a laminate and indeed, some authors have modelled impact-damaged regions of composite laminates using elastic inclusions, including Lacy & Hwang [11] and Xiong et al [50], the former researchers using a numerical analysis for sandwich panels (discussed in depth later) and the latter using an analytical solution for monolithic composite plates.

Kärger et al [9] used an in-house finite element code in conjunction with a special three-layer FE element (one layer each for the two skins and the core of a sandwich panel) to produce an efficient simulation of a low-velocity impact on a sandwich panel, and compared this with experimental results. The model does not extend to crack propagation. The indenter is modelled as a point mass, with a parabolic load distribution, and the results produced were satisfactory, despite the sacrifices in accuracy made necessary by the investigators' primary requirement for fast solutions. Key omissions in the model were delamination, matrix damage and crack growth in a fractured skin. Riks & Rankin [51] present a similar simplified finite-element sandwich model, using a pair of shell elements separated by an elastic medium that represents the core. This model is demonstrated for a panel with a skin-core debond.

Foo et al [52] developed a numerical model and analytical models for the impact of sandwich panels. The core was modelled as a geometric honeycomb meshed with shell elements in the FE model, with the skins modelled with solid elements. The analytical model used the principles developed by Aminanda et al [53] to model the core failure, in conjunction with a modified energy-balance to capture the load and deflection history for the panel during the impact event. The FE model showed a generally good agreement with the experimental model, despite being unable to capture some the subtleties of the panel response, including neglect of the unloading behaviour. It did however show the occurrence of core crushing, top skin delamination and fibre fracture, the same damage modes identified by Zhou et al [15]. Particularly, modelling the core geometry directly with shell elements, rather than using a homogenous core model, was able to provide an accurate prediction of failure initiation. The analytical model, using only a few empirical parameters, was able to provide fairly accurate results for elastic and damaged stiffnesses and critical loads. Residual strength was not considered in this work.

There are numerous further examples in the literature of work investigating the impact response (at various impact velocities) of monolithic composite plates via numerical methods, including contributions by Hou et al [54], Chan et al [55] and Tita et al [56]. These analyses show a trend towards greater complexity of material failure models, often using custom-developed subroutines. Particularly, delamination is recognised as a particularly important damage mechanism, and so the modelling of this is also receiving greater consideration. Impact on monolithic composite plates thus remains an active area of research.

Davies et al [57] produced a numerical model for the impact event and residual strength of a sandwich panel, solved using a dynamic explicit solver, and compared with experimental results. This work was a continuation of a previous work by the same authors [58]. The model produced good results, despite not attempting to model delamination - which has been stated in previously mentioned works to be of some significance [28] - or face-core debonding. They do however consider fibre failure, which was often neglected in earlier numerical models – the Chang-Chang criteria is used for this purpose, with fibre properties degraded to 5% of the undamaged properties. An interesting point to consider is that the thick-skinned panels failure via indentation propagation, which was later contradicted by the results of McQuigg et al [32]. Additionally, the authors noted the danger of using an overly thin skin in the design of sandwich panels – using a thin skin-thick core configuration, the energy absorbed (for a 80J impact) was 93%, but with a loss of compressive strength of 68%, whereas the thick skin-thin core configuration absorbed 76% of a 120J impact, with the loss of 34% of the compressive strength.

This apparent dichotomy between energy absorption and residual strength was studied by Prevorsek et al [59], where a comparison was made between the differing mechanisms and requirements for damage tolerance of composite laminates when the designer is concerned with retaining structural integrity or wishing to resist penetration, such as in armour. They note early on that the two requirements are irreconcilable, since in the case of penetration, the breakage of fibres is inevitable, with obvious consequences for structural integrity. The results of [57] seem to reinforce this conclusion.

Lacy & Hwang [11,12] used a semi-empirical approach, using the observations produced Tomblin et al via non-destructive imaging and sectioning of impacted panels [10] to prepare the numerical models, in their work to predict the CAI strength of damaged sandwich panels. In the former [11], the damage profile is implemented in a shell (skins) and solid (core) model. The damaged region of the top skin is modelled as an elastic inclusion, the stiffness of which varied between 0 – 100% of the undamaged properties. The honeycomb core is modelled as a homogenous orthotropic solid, akin to a foam material, with a non-linear material behaviour applied depending on whether the core was damaged or not. The authors note that this particular model shows some promise, with generally reasonable, conservative agreement with experimental results from Tomblin et al [10]. This model neglected progressive damage formation in the skins, with global panel failure assumed to be triggered at the first local failure. The model was improved by the same authors in [12] by adding a progressive damage model for the skins via established ply failure criteria. Generally, the CAI estimates produced by this model were within approximately 10% of experimental values, with a mean difference of 3.6% However, in this model, the skins were assumed to be undamaged by the impact event, a questionable assumption considering various damage characterisation studies. Both models are considered valid for small-scale, non-penetrating damage, and they both completely neglect delamination formation and propagation. Xie et al [60] also used a very similar approach in their model.

Hawyes et al [61] take the approach of modelling the damaged region of an impacted laminate as an open hole, the diameter of which corresponding to the extent of the delaminations in the impacted skin, determined using non-destructive methods. This assumption was used in conjunction with the cohesive zone model to model fibre microbuckling in the damaged region as an equivalent crack. This work used earlier studies by Soutis et al [62,63] as a basis. The resulting model produces a good agreement with experimental results for the CAI strength, but does not allow for interlaminar and through-the-thickness effects. It should be noted that these studies deals only with monolithic composite laminates, not sandwich panels, though the method could be used as part of a study into the behaviour for the latter; Zenkert et al [6] used the equivalent hole model of Soutis & Curtis [63] to predict the residual strength of marine sandwich panels under impact at varying locations and energies with both blunt and sharp indenters.

The recent work of Gonzalez et al [42] study the impact and CAI strength of monolithic composite panels using a continuum damage model by Maimi et al [64-66] and a three-dimensional, mixed-mode cohesive model by Gonzalez et al [67], utilising the Benzeggagh-Kenane criteria [68] for damage initiation. The continuum damage model is based on the work of Davila et al [69] and Pinho et al [70] and may be considered a development of the LaRC03 criteria [71]. The cohesive model is applied using the experimental insights provided by Gonzalez et al regarding the effects of ply clustering [35] and the numerical results support the experimental observations. The resultant model is particularly complex, with each ply and interface being modelled discretely with one element through-the-thickness for each. Additionally, the entire test fixture is modelled also, using rigid elements and a general contact law. The impact event itself is a dynamic event. The predicted force histories, residual strengths and displacements generally agree very well with experimental results, with better results found when fewer plies and interfaces were modelled. However, their method used considerable computing resources, requiring as long as two weeks to complete a simulation using six desktop computers working in parallel. Rivallant et al [72] and Dang & Hallett [73] also present recent models for the compression-after-impact performance of monolithic composite structures, both making extensive use of cohesive interfaces to capture delamination and matrix cracking. The latter work is particularly interesting as it studies a new kind of composite material using variable tow laminates, which feature curved fibres to further enhance design flexibility.

Lapczyk & Hurtado [74] present a progressive damage model for Fibre Metal Laminates (FMLs) using the widely-used Hashin criteria, a fracture mechanics approach based on the work of Camanho & Dávila [75] used in concert with a crack band model [76] to model the fracture growth associated with delaminations. As with Gonzalez et al, each laminate is modelled as its own discrete layer, with layers of adhesive between them. Such an approach may prove useful for capturing the development of delaminations, which, as has been remarked on previously, is of great importance for CAI strength.

Shipsha et al [77,78] performed experimental and finite element studies on the performance of foam-core sandwich panels under various loading conditions, including edge compression. The results from the experimental investigation [77] were used to provide parameters and comparative results for the numerical investigation [78]. The model incorporates the effect of core crushing and shear-bridging effects at the periphery of the damaged region, but significantly over-estimates the failure load in the compressive tests. Shipsha & Zenkert [79] further studied the influence of core failure in the residual strength of impact-damaged sandwich panels, investigating the effect of the residual dent often seen following an impact event. They hypothesised that core failure starts from a tensile failure of the core as the outer edge of the dent bulges away from the panel mid-plane under compressive load. This was tested experimentally and numerically, with the model showing a reasonable correlation with the experimental findings. Both models neglect skin damage, an omission that the authors acknowledge as a source of error and a potential improvement to the models.

Castanié et al [80] present a method to modelling the crushing of the core in sandwich materials, for use in CAI investigations. The work is based on previous studies on sandwiches with isotropic skins by Aminanda et al [53], and is extended here to include composite skins. The core is modelled as a grid of nonlinear springs in a finite element model, the location of the springs coinciding with the vertical edges of the core cells, which had been previously found to take the entire compressive load due to a postbuckling mode in low-density honeycombs [53]. The panel is found to fail shortly after the first failure of a spring adjacent to the periphery of the damaged region. This new model was then used in conjunction with the previously discussed model of Lacy & Hwang [11] and found that the model slightly underestimated the failure loads, as the authors expected. Ratcliffe & Jackson [30] used a similar model, using springs to model a core with an existing residual dent for their study to develop a simple analysis for sandwich panels failing via indentation growth, with favourable results when compared to an earlier study by Minguet [81]. Castanié et al [80] note that their approach doesn’t seem to work for low energy impacts leaving small dents, possibly due to the neglect of geometrical imperfections. As demonstrated by Zhou & Hill [17], it is precisely this kind of barely visible damage that is of most concern to practical users of these structures. Additionally, these authors state their belief that the reduction in stiffness of damaged skins is not of primary concern for thin skins - though a close reading of their sensitivity analysis seems to suggest that by neglecting this nonlinear behaviour, the error in the analysis may actually be significantly increased - and suggest that using the improved model of Hwang & Lacy [12] in conjunction with their model may produce improved results.

Additional recent contributions to the field are also made by Czabaj et al [33,40], and Lee et al [82]. These efforts tend to lean more towards direct modelling of the impact event prior to performing the compression simulation; in these cases, using a quasi-static indentation to induce damage, rather than the semi-empirical approach of Lacy & Hwang [11,12] and Shipsha & Zenkert [79], as well as explicit modelling of the honeycomb geometry of the core, rather than using an equivalent homogeneous, orthotropic material assumption. Lee et al do not mention what failure criteria are used in the skins. Czabaj et al use the Hashin criteria, as built into *Abaqus*. The model produced by Czabaj et al overestimates the CAI strength by around 20% compared to their experimental study, perhaps due to the neglect of delamination, and also the overestimated post-damage tensile strength of the core. Lee et al do not provide any kind of comparative results for their model, only stating that the residual strength is approximately 65% of the virgin strength, with the virgin strength also being determined by their model. Czabaj suggests the inclusion of a delamination model as a potential improvement to the simulation [40].

Accurate modelling of damage evolution and failure is a key point of interest in the work of McQuigg et al [14,32,83,84], reflecting a growing trend in the academic community towards the accurate simulation of this vital aspect of sandwich panel behaviour. This is another semi-empirical model, with the impact damage modelled as a residual dent with regions (to a uniform depth) of degraded material, for very thin-skinned sandwich panels with only two plies per skin. Progressive damage in the skins is predicted using *Helius:MCT* software, which uses the multi-continuum theory of Mayes & Hansen [85]. The model over-estimates the residual strength of the panel.

Edge compression is by no means the only means to determine the residual strength of sandwich panels. Klaus et al [5,86] studied the behaviour of novel folded core sandwich panels under post-impact four-point bending, with the former paper presenting a method that may also be suitable for CAI simulation. Staal et al [87] present both numerical and analytical models for damaged panels under four-point bending and edge compression, with a particular interest in localised wrinkling and buckling. Since bending generates both tensile and compressive loads in a panel, this could be a useful method for residual strength determination. However, compression after impact is generally considered the critical loading case due to its particular vulnerability to impact [28]. Ivanez & Sanchez-Saez [88] also use a three-point bending arrangement for drop-test simulations on sandwich beams with fabric composite skins. Another interesting variation on the theme of compressive loading is to subject a pre-loaded panel to a damaging event. An example is that of Wang & Shukla [89], who performed transverse blast tests on sandwich panels with varying amounts of compressive pre-load. These tests essentially perform a compression-after-impact test in reverse, and showed that the panels exhibit increased blast damage as the pre-load increases.

Table 1 gives a review of the key experimental studies relevant to this project. Table 2 gives a review of the key numerical models studied.

1.5 Improving the Impact Resistance of Composite Structures

At this point in the review, a minor digression is made from the subject of experiments and modelling of the residual strength of composite and sandwich structures, so that an exploration can be made into methods for improving the performance of these structures when subjected to impact and compression-after-impact events. The primary techniques introduced here are through-the-thickness reinforcement of laminates, self-healing panels and the use of carbon nanotubes and nanowires.

Through-the-thickness reinforcement can be achieved via Z-pinning (reviewed in depth by Mouritz [90]) or stitching, such as studied by Aymerich et al [91] and Yoshimura et al [92]. Z-pins function almost like nails in the skin to lock the plies together. The pins are typically tenths-of-a-millimetre in diameter, and are introduced into a laminate with a volume fraction in single-digit percentages. Stitching introduces through-thickness reinforcement fibres in a manner akin to stitching textiles. In both cases, the reinforcement is introduced into the laminate prior to curing. Both of these methods increase the ability of a laminate to resist delamination propagation (if not necessarily the initiation of delamination) and impact damage, by increasing the interlaminar fracture toughness. Z-pins also improve the through-the-thickness elastic properties. The drawback is reduced in-plane stiffness and strength, as the volume fraction of the fibres is reduced by the presence of the through-thickness reinforcements. In the case of Z-pins, resin-rich regions are also produced around the pins that reduce the fatigue resistance of the laminate. On the whole, given the significance of delamination to impact damage and compressive strength, these forms of through-the-thickness reinforcement could provide dramatic improvements in sandwich panel performance that would be well-worth investigating further.

Self-healing deals with the problem of impact damage differently, by attempting to restore the strength of a composite structure after a damaging event has occurred. Two experimental studies are presented by H.R. Williams et al [93] and G.J. Williams et al [94]. Both methods use networks of resin storage vessels built into the laminate, which fracture when damage occurs, releasing resin into the laminate to, in theory at least, seal cracks in the matrix. The former study uses a two-part resin system, and also tests driving repair resin into the laminate under pressure. The latter study trials panels with various densities of hollow glass fibres built into the laminate. In both studies, the technique shows promise, with the mass penalty that results from embedding non-structural fibres into the laminate potentially being negated by improvements to the design allowables that the self-repair mechanisms can offer. It may be particularly useful in cases of barely-visible impact damage, where fibre damage will be limited, and delamination is a more likely damage mechanism. However, both studies also caution that the technique needs considerable refinement and optimisation. Particularly, problems involving incomplete infiltration of resin into the damaged region of the laminates, and incomplete curing of the liquid resin are of some concern.

Another recent development that is being explored is the use of carbon nanowires and nanotubes as a means to improve the performance of conventional composite materials. The state-of-the-art is reviewed in depth by Chou et al [95], discussing numerous different methods of producing these nanoscale structures and how they might be used. What is abundantly clear is that carbon nanotubes show superior specific strength, modulus and fracture toughness when compared with conventional fibres. Two particularly interesting possibilities, relevant to the present discussion, are the modification of conventional carbon fibres and interlaminar surfaces of fabric composites by growing ‘forests’ of carbon nanotubes on the surface of the fibre and fabric respectively. These methods provide considerable improvements to the interfacial strengths and fracture energies, without unduly harming the in-plane properties, via crack-bridging. Carbon nanotubes also have exceptional electrical and thermal properties. Thus far, research has been limited to the laboratory environment, and thus considerable work is required to scale-up production of this remarkable material for it to enter common usage.

One final method of improving the impact damage tolerance of composite laminates that does not fall into the categories mentioned involves the use of a layer of ultra-high molecular weight polyethylene (UHMWPE) on the outer surface of a carbon-epoxy composite, in an example of hybridisation. Nettles & Lance [96] use this method both on a monolithic composite and a sandwich panel. UHMWPE has high specific strength, modulus and energy absorption capabilities, so potentially making it useful for improving the impact resistance of a structure. Sandwich structures hybridised in this manner showed reduced delamination and fibre breakage for a given impact energy, due to the improved energy absorption of the hybrid structure. However, it was found that the compression-after-impact strength was not markedly improved in this instance.

To summarise, this review shows that delamination is a crucial damage parameter controlling impact and compression-after-impact performance of composite laminates, and thus also has a significant influence on the performance of sandwich structures under these conditions. However, the numerical simulation of delamination initiation and propagation has not featured in any meaningful way in sandwich panel models thus far, presenting a gap in the literature that the present work may now address, utilising the tremendous flexibility offered by numerical modelling techniques.

1.6 Review Tables

Table 1: Key Experimental Studies (3 pages)

Authors	Materials						Test conditions					Results						Notes
	Skin			Core			Planar dims (mm)	USup imp dims (mm)	Indenter	B.C		#	Initial impact energy (J)	Damage dims (mm)	Damage depth (mm)	CAI Strn' (MPa)	Failure Mode	
	Mat'l	Lay-up	T (mm)	Mat'l	ρ (kg/m^3)	T (mm)				Im	CAI							
Zhou & Hill - 2009	C/E (T700 / LTM45)	(0/90)2s	1.024	5052 Al HC (4.4-3/16-15)	70	12.7	200 x 150	100 dia	HS ø20mm 1.5kg	C	C (ld) SS (ul)	1	0	0 dl, 0 cc	0	270.6-322.0	-	Damage dims are longitudinal damage extents (delam' and core crushing). Approx 2/3 of damaged samples failed at midsection
												2	2.6 – 3.69	29-42 dl 31-33 cc	0.6 – 0.75	190.7-219.0	-	
												3	5.2 - 5.4	37-38 dl 38 cc	1.0 - 1.2	195.3-221.8	-	
												4	9.06 - 9.51	50-53 dl 54-62 cc	1.3 - 1.5	190.3-243.9	-	
												5	13.18 - 13.76	54-55 dl 67-70 cc	2	203.8-215.2	-	
												6	25.18 - 25.54	50-67 dl 85-100 cc	2.0 - 4.5	150.4-187.6	-	
				Nomex HC (HRH-3/16-4.0)	64							7	0	0 dl, 0 cc	0	283.9-293.1	-	
												8	5.13 – 5.28	35 dl, 34 cc	0	162.4	-	
												9	9.23 – 9.43	60 dl, 63 cc	0	205.6	-	
												10	16.29 – 16.37	63 dl, 93 cc	0	187	-	
												11	28.2	75 dl, 102 cc	2	134.1	-	
Hwang & Lacy (2007)	C/E plain weave fabric (NB321 / 3K70P)	(90/45)	0.406	Nomex HC (PN2-3/16-3.0)	48.1	19.05	254.0 x 203.2	203.2 x 203.2	HS ø25.4mm	C	C (ld) SS (ul)	1	6.7	10.2 i, 12.7 f, 15.2 c	2.3 f, 5.9 c	185.6	-	Variable mass indenter (constant velocity). Damage dims are face indent (i), face degradation (f) and core damage (c) i ≤ f ≤ c
									HS ø76.2mm			2	7.2	15.9 i, 15.9 f, 25.4 c	0.4 f, 6.2 c	165.5	-	
		(90/45)2	0.813						HS ø25.4mm			3	6.7	3.2 i, 3.2 f, 15.9 c	0.8 f, 3.8 c	356	-	
												4	20.3	12.7 i, 15.9 f, 21.7 c	3.2 f, 7.8 c	317.5	-	
									HS ø76.2mm			5	7.2	9.5 i, 9.5 f, 28.6 c	0.4 f, 4.5 c	354.5	-	
												6	28.2	34.4 i, 41.3 f, 48.7 c	4.2 f, 6.6 c	236.9	-	
		(90/45)3	1.052						HS ø25.4mm			7	6.7	9.5 i, 9.5 f, 19.1 c	0.6 f, 4.1 c	482.6	-	
									HS ø76.2mm			8	11.1	12.7 i, 12.7 f, 28.6 c	0.6 f, 4.8 c	429.6	-	
		(90/45)	0.406			9.525			HS ø25.4mm			9	15.4	28.6 i, 30.2 f, 31.8 c	4.3 f, 6.2 c	114.2	-	
		(90/45)$_2$	0.813									10	21	25.4 i, 30.2 f, 34.9 c	3.4 f, 5.2 c	213.7	-	
		(90/45)2	0.762			19.05	254.0 x 152.4	-	HS ø76.2mm			11	10.2	20.3 i, 20.3 f, 23.6 c	0.3 f, 5.7 c	300.9	-	
							254.0 x 203.2	-				12		12.7 i, 12.7 f, 23.7 c	0.3 f, 5.7 c	265	-	
							254.0 x 304.8	-				13		14.0 i, 14.0 f, 23.4 c	0.3 f, 5.7 c	281.4	-	
							254.0 x 406.4	-				14		20.3 i, 20.3 f, 24.6 c	0.2 f, 5.7 c	280.7	-	

Zenkert et al (2005)	CFRP non-crimp fabric (T700)	(0/90/±45)s	1.8	Divinycell foam H80	80	60	300 x 300	0 x 0	HS, ø25mm 15.29 kg	Rigid	C (ld) F (ul)	1	0	-	-	-0.75*	Compressive failure initiated at dent, propagating across panel perpendicular to loading direction	*Strain-at-failure (%) **Initial residual dent (mm). Blunt damage creates BVID with significant delaminations. Sharp impact produces a slit in the face sheet. No visible damage progression at the surface until catastrophic failure.
												2	30	15 dl	-	-0.49*		
												3	50	20 dl	-	-0.47*		
		(0/90/±45)3s	5.4	Divinycell foam H200	200	50						4	100	20 dl	-	-0.43*		
												5	250	30 dl	-	-0.41*		
		(0/90/±45)s	1.8	Divinycell foam H80	80	60			Pyramid			6	30	20 ck	-	-0.43*		
												7	50	25 ck	-	-0.43*		
		(0/90/±45)3s	5.4	Divinycell foam H200	200	50						8	100	15 ck	-	-0.42*		
												9	250	22 ck	-	-0.41*		
		(0/90/±45)s	1.8	Divinycell foam H80	80	60			HS, steel ø150mm			10	5.5**	60±1.2 d 60±1.0 c	0.85±0.03 d 7.0±1.0 c	-0.72*		
												11	7.0**	92±1.5 d 90±1.5 c	0.91±0.03 d 11±1.2 c	-0.69*		
												12	10.0**	121±1.4 d 120±2.0 c	1.54±0.04 d 16±1.9 c	-0.64*		
												13	15.0**	158±2.3 d 155±2.0 c	2.65±0.06 d 23±2.1 c	-0.58*		
Davies et al (2004)	C/E (Fiberite 7714D / XAS)	(+45/0/-45/90)s	2	5052T Al HC (CIBA 4.5-1 / 8-10)	72	10	490 x 496	-	Flat face, ø20mm, 5.45kg	C	C (ld) SS (ul)	1	0	-	-	770*	Classical buckling	*Failure load (kN), Local indentation and global deflection, longitudial and transverse extents
												2	80	135 (long) 115 (trans)	2.77 (front) 1.55 (global)	535*	Buckling via dent propagation	
												3	120	170 (long) 145 (trans)	3.43 (front) 2.06 (global)	505*		
		(0/90)s	1			25						4	0	-	-	600*	Skin micro-buckling	
												5	20	75 (long) 60 (trans)	1.93 (front) 0.27 (global)	495*	Buckling via dent propagation	
												6	80	-	-	190*	Front skin penetrated, back face debond (by impact)	
Czabaj (2010)	C/E (IM7/8552)	(45/0/-45/90)s	1.016	5052 Al HC (HexWeb CR-III, 3.2mm cell size)	49.7	25.4	178 x 152	-	HS ø72.2 mm (lg) or ø25.4mm (sm)	Rigid	C	1	0	-	-	400.1	-	Damage induced via QSI to stated load level, damage depth for dent only, DL extents given as areas (mm^2), all values averaged
												2	2800 (lg)	58.2 (dt)	1.04	322.7	-	
												3	1300 (sm)	40.5 (dt), 215 (dl)	0.56	293.6	-	
						16.5						4	0	-	-	348.3	-	
												5	2800 (lg)	54.9 (dt)	0.99	274.7	-	
												6	1300 (sm)	34.6 (dt), 400 (dl)	0.47	247.3	-	
		(45/-45/0/90)s				25.4						7	0	-	-	444.1	-	
												8	2800 (lg)	62.1 (dt)	1.22	299.1	-	
												9	1300 (sm)	38.7 (dt), 302 (dl)	0.53	312.4	-	

Shipsha et al (2003)	E-glass weave (19S3) vinylester matrix (Jotun 8550)	(0/90/±45)2s quasi-isotropic	2.4	PMI foam Rohacell WF51	52	50	270 x 47	0 x 0	Steel cyl ø25mm, 60mm long	R	C (ld) Fr (ul)	1	0	0	0	175.7 ± 12.52	-	2-D impact. Edgewise comp' test ASTM C364-94. Main impact damage was core crushing and cavity formation. Loss of face stiffness < 5%, assumed undamaged in post-impact studies. Bottom face undamaged.
												2	6.6	53-55 cc, 24-25 cav	1-2 cav 1-2 cc	111.35 ± 1.63	Abrupt bifurcation local buckling	
												3	13.3	76-80 cc, 34-40 cav	2-3 cav 3-4 cc	62.42 ± 2.82		
												4	20	82-85 cc, 41-42 cav	3-4 cav 3-4 cc	48.35 ± 2.89		
												5	26.5	92-100 cc, 47-60 cav	4-5 cav 4-5 cc	41.35 ± 5.94		
												6	40	98-100 cc, 58-60 cav	5-6 cav 5-7 cc	22.57 ± 6.32	Slowly progressing local buckling	
									No impact - Artificial crack below face-core interface	-		7	0	70 (crack)	-	67.3 ± 3.54	Local buckling	
												8		80 (crack)	-	42.45 ± 5.58		
												9		90 (crack)	-	43.15 ± 6.57		
												10		100 (crack)	-	34.1 ± 0.42		
									Impact + crack	R		11	13.3	66-67 cc, 37-38 cav	2-3 cav 3-4 cc	45.2 ± 6.36		
												12	26.5	93-94 cc, 53-54 cav	4-5 cav 4-5 cc	33.2 ± 0.98		
Hawyes et al (2001)	C/E (T800 / 924)	(±45/0/90)2s	16 ply	-	-	-	-	-	-	-	-	1	7	9	-	260	Fibre microbuckling	Tested in accordance with CRAG methodology
		(45/0/-45/90)4s	32 ply									3	28	50	-	192		
		(±45/0$_2$)2s	16 ply									4	3.5	4	-	397		
													7	7	-	293		
														6	-	344		
		(±45$_2$0$_4$)s	16 ply									5		7	-	318		
		(45/0/-45/0)2s	16 ply									6		13	-	298		
		(0$_2$/±45)2s	16 ply									7		10	-	312		

C/E	Carbon/Epoxy
HC	Honeycomb
HS	Hemispherical
C	Clamped
SS	Simply-supported
DL	Delamination
CC	Core crush
R	Rigid
Fr	Free
Cav	Cavity
Ck	Crack
QSI	Quasi-static indentation
Dt	Dent

Table 2: Key Numerical Studies

Authors	**Solution Method**	**Modelling Details**			**Damage State Modelling**		**Failure Criteria**	**CAI Strength (Mpa)**	**Notes**
		Skin	**Core**	**Interfaces**	**Skin**	**Core**			
Lacy & Hwang (2003)	Abaqus	8-node shell, [90/45]$_n$ fabric	20-node solid HC	No DL / DB	Elastic inclusion, based on fraction of UD properties	Exp damage geometry, idealised NL (different curves)	Max strain criteria	Test 6 - IKE 28.3J: 208.4 - 210.2 *(236.9 exp)*	No progressive damage / DL before final failure
Hwang & Lacy (2007)	Abaqus	8-node shell, [90/45]$_n$ fabric	20-node solid HC	No DL / DB	UD skin (impact only)	Exp damage geometry, idealised NL (different curves)	Max stress, Tsai-Wu, Max strain	Test 6 - IKE 28.3J: 229.4 - 236.4 *(237 exp)*	-
Besant et al (2001)	FE77	8-node shell, QI	20-node solid HC	-	Via point-impact	Elliptic yield criteria	Chang-Chang	-	No CAI
Czabaj et al (2010)	Abaqus / Explicit	8-node shell, various QI	4-node shell, explicit HC geometry (local) 8-node solid (global)	No DL	QSI	Plastic hardening	Hashin	Q1-C1: 323 *(393 exp)*	-
Davies et al (2004)	FE77	8-node shell, QI & [0/90]$_s$	20-node solid HC	No DL / DB	Dynamic impact event	See Besent et al [30]	Chang-Chang	IKE 120J: 464 kN *(505 kN exp)*	-
Shipsha et al (2003)	Abaqus	20-node solid, QI & foam		-	UD skin (impact)	Exp damage geometry w' cavity & cracks	Point-stress (core only)	IKE 20J: 68.4 *(exp 48.35 ± 2.89)*	No DL or skin damage
Klaus et al (2012)	LS-Dyna	4-node shell, QI, sub-laminates	4-node shell, folded core	Tie constraint w' CZM	Dynamic impact event via simulated drop-weight	Elastic-plastic	Chang-Chang (impact), Hashin (bending), DL criterion	IKE 40J: ≈14kN *(exp ≈12.5kN)*	4-point bending
Gonzalez et al (2012)	Abaqus / Explicit	Discrete plies, 8-node solid, QI	-	8-node solid w' cohesive law	Dynamic impact event via simulated drop-weight	-	See Maimi, Gonzalez et al [78-81]	L4 - IKE 28.6J: 92 *(103 exp)*	-
Kärger et al (2008)	CODAC (implicit, dynamic)	3-layered, 8-node shell sandwich, Cytec skins, HC		No DL	Point mass indenter, parabolic contact load	See Besent et al [30]	Max stress, Hashin, Chang-Chang	-	No CAI, No matrix damage / crack growth
Foo et al (2008)	Abaqus / Explicit	Solid	Shell, explicit HC geometry	No DB	QSI	Elastic-perfectly-plastic	3D Hashin, DL criterion	-	No CAI
Lee et al (2012)	Abaqus	8-node shell, QI	4-node shell, explicit HC geometry	-	QSI	Elastic-plastic	-	456.1 *(696.3 UD)*	-
Castanié et al (2008)	Samcef	[90/45]$_n$ fabric	NL springs, HC	-	Exp damage geometry	Novel core crush criterion	-	Test 6 - IKE 28.2J: 196 *(exp 236.9)*	-
McQuigg et al (2012)	Abaqus / Standard	8-node continuum shell, [0/45] fabric	8-node solid HC	-	Exp damage geometry, stiffness reduction	NL crushing	CDM via Helius:MCT software	Up to 20% error (compared to exp)	-
Ratcliffe & Jackson (2008)	Abaqus / Standard	4-node shell, fabric	NL springs, HC	-	Residual dent	NL crushing	-	-	Primarily parameric study for factors influencing indentation growth
Xie et al (2006)	ANSYS	8-node solid	8-node solid, HC	-	Exp damage geometry, stiffness reduction	NL crushing	-	-	-

DL	Delamination
DB	Debond
IKE	Initial kinetic energy
exp	Experimental
NL	Non-linear
UD	Undamaged
QI	Quasi-isotropic lay-up
HC	Honeycomb
QSI	Quasi-static Indentation
CZM	Cohesive zone model
CDM	Contiuum damage mechanics

Chapter 2

Numerical Modelling of Damage in Composite and Sandwich Structures

2: Numerical Modelling of Damage in Composite and Sandwich Structures

This section provides a thorough discussion of all aspects pertinent to the numerical modelling of damage in composite sandwich structures. This includes a thorough review of composite damage and failure criteria, which will be required to simulate the failure of the skins of a sandwich panel, a discussion on the modelling of delamination and a review of finite element modelling considerations.

2.1 Composite Material Failure Theories

When dealing with impact damaged sandwich panels, it is absolutely essential to consider the mechanisms for damage progression and eventual failure of the panel, particularly since this aspect of damage formation and propagation in sandwich panels is often neglected. The present section relates only to intralaminar material damage mechanisms, that is to say, the theories discussed refer only to damage in the matrix and fibres of the plies. Interlaminar damage, of which delamination is most significant mechanism for the current study, will be addressed in a later section. Throughout this project, damage is considered at the macroscopic scale in the laminate, effectively a binary ‘is it damage or not?’ state. The specific mechanisms behind this damage, such as cracking of the fibres and matrix, are observed at the microscopic scale, and lie outside the scope of the current work.

For the failure of composite laminates – the usual skin material for modern sandwich panels – reference is made to the World Wide Failure Exercise (WWFE), an extensive long-term study spearheaded by Hinton, Soden & Kaddour to evaluate and compare the key composite failure criteria in common usage today [97-102]. Over the course of the study, 19 failure criteria are rigorously compared with each other and experimental results, with the goal of addressing long-held doubts regarding the reliability of failure theories in general. In the background report [97], there is a quote from Prof. Hashin, originator of the very widely used failure criterion that bears his name [103,104], that succinctly describes the scale of the challenge: *‘I must say to you that I personally do not know how to predict the failure of a laminate, and furthermore, that I do not believe that anyone does’*. Hashin’s criteria merits special consideration, as this is the only failure theory available as a standard option for damage in fibre-reinforced materials in *Abaqus*, and will be discussed in more detail in the next section. At the conclusion of this study, Soden et al [102] are reluctant to make recommendations in some areas, particularly regarding the initial strength (for first-damage) of multidirectional laminates of the kind that is of most relevance to this project and industry in general. Additionally, the WWFE does not address delamination initiation and propagation, or the integration of these failure theories into finite element software, two aspects of critical importance to the current work. It is illuminating that no commercial software vendors entered their failure prediction routines into the study, but it is unwise to make any assumptions about the accuracy and reliability of these routines based on this omission alone.

Of the theories studied in this exercise, the phenomenological failure criteria developed by Puck & Schürmann [105] generally gave the most accurate predictions for the numerous loading cases studied, especially when used in conjunction with other methods (accuracy is taken by Soden et al to mean a prediction within ±10% of experimentally measured results). This theory placed special emphasis on matrix cracking and non-linear behaviours due to microdamage and changes and fibre angle with increasing strain, and residual stresses due to hydro-thermal effects. Their criterion is solved via a specialised in-house computer program in a layer-by-layer manner, so that it may be valid for laminates rather than just uni-directional composites, as is the case in the Hashin-Rotem criteria. Finally, the criterion allows for reduction of material properties for modelling progressive failure. The key weakness of the Puck criteria is its dependence on empirical parameters that have no physical basis. Thus, optimising the predictions made relies on extensive curve-fitting of parameters, which in turn requires a good deal of experimentation and experience with the material system of interest. Additionally, like the Hashin-Rotem criteria, delamination onset is not included, though in the Puck criteria, there is functionality in the software used to warn that delamination is likely for certain load cases and material systems. The influence of in-plane shear stress is also not fully considered. On the important matter of FEM implementation, Puck & Schürmann state that work has been done performed by other researchers to implement their criteria in the commercial software *ANSYS*, and also to allow post-processing of data from *Abaqus*. A later work by Puck & Mannigel [106] improve on this work by accounting for the effect of combined normal and shear stress on the non-linear behaviour of the stress-strain analysis, by including a measure of the risk of inter-fibre fracture.

Another theory of note is the micromechanics-based theory Mayes & Hansen [85]. This is a development and implementation of the multi-continuum theory of Garnich & Hansen [107], which sought to resolve difficulties in capturing the inelastic response of composites when using a single, homogenised continuum, and had finite-element usage very much in mind. In the WWFE, this work produced results of only middling accuracy, but nonetheless, it has since been integrated into the progressive failure analysis software *Helius:MCT* (Firehole Technologies, Inc.) [83]. Other approaches using continuum damage mechanics (CDM), usually in concert with other criteria for fibre damage, were presented by Feng et al [108], Chen et al [109] and Yoshimura et al [110] at ECCM 15 Venice 2012, a major European conference on composite materials with contributors from around the globe. ECCM 15 also saw proposals for some rather more unusual ways to model damage. These include the work of Bouvet et al [111], who used cohesive elements to model transverse matrix cracks as well as delaminations, building up the model in a manner analogous to a brick wall, with fibre failure governed by a criterion written into the brick elements. Ivancevic & Smojver [112] used a High-Fidelity General Method of Cells (HFGMC) micromechanical model, with the unit cell of material divided into subcells, which were then assigned either fibre or matrix properties. Soni et al [113] also used a micromechanics method in their work, whereby multiple layers and fibres are modelled in a representative volume element for studying matrix damage and the strength of the fibre-matrix interface, an often ignored aspect of damage in composites.

An important example of a new and refined failure theory is the LaRC03 criteria [71], based in part on the work of Puck & Schürmann [105] and Hashin & Rotem [103,104], and can be considered as a refinement to the latter theory. Six criteria are produced that are not reliant on empirical parameters, as is the case with Puck's theory. An important feature of these criteria is the consideration of the 'in-situ' strength of the plies. That is to say, the beneficial influence that being part of a laminate has on ply strength is calculated and used in the failure criteria. The LaRC04 criteria [70] are a development of the LaRC03 criteria and are rather more sophisticated when compared to its predecessor criteria. These theories may be applied as a 3-D damage model for use with solid finite elements; this was the approach followed by Foo et al [52] and Gonzalez et al [42]. Both the LaRC03 and LaRC04 criteria can be readily applied to numerical modelling, and are able to capture some of the more complex failure mechanisms and interactions, such as fibre kinking under compression, and the involvement of fracture energy in matrix failure, that the Hashin-Rotem criteria could not. Additionally, they have the very significant advantage over the Puck criteria in that they have no dependency on empirical parameters in producing strength estimates; all the required parameters have a physical basis. The predictions from these theories have good agreement with the experimental data offered for comparison – Pinho et al [70] make the claim that the LaRC04 criteria are possibly better than existing criteria at predicting laminate failure - and Lapczyk & Hurtado [74] note in their paper that the LaRC03 criteria could offer improvements over the Hashin criteria for laminate failure. It is worth mentioning again the use of in-situ strength values. This addition is highly useful for practical composite designs, and improves the validity of the theory for use with laminated structures. Pinho et al [114,115] present a further development in the field, with a special focus on compressive failure and fibre kinking. This work includes a detailed implementation of the new model into an explicit finite-element solution, which they note is vital to successfully modelling failure initiation and propagation in composite materials. The final model successfully captures the key aspects of failure, giving good agreement with experimental failure envelops, and using only parameters with clear physical meaning.

From these more recent works, it can be seen that there is an increasing trend towards more detailed models for composite damage simulation, with authors particularly tending to use 3-dimensional elements (despite the complexities involved in using these elements, which will be discussed later) with a view to capture influential but often neglected stresses, for example non-linear shear failure, as accounted for by Feng et al [108]. These theories are often greatly concerned with the correct prediction of failure in complex, combined stress cases, such as combined normal-shear loading. Predicting failure in composite materials is and likely will remain a highly active research area. Utilising these new theories in finite-element analyses often require specialist sub-routines to be written by the users, which is typically a highly-involved and demanding endeavour. The accurate prediction of skin failure is likely to be a major issue in this work, one that will take a great deal of effort to resolve in a satisfactory manner.

2.1.1 Hashin-Rotem Criterion

As mentioned previously, an implementation of the Hashin-Rotem Criterion [103,116] is the sole standard option for simulating damage initiation in *Abaqus*. The original 1973 formulation was developed for the prediction of fatigue failure in uni-directional composites and can be expressed thus (a schematic of a composite plate, showing the fibre direction, is given for clarity in Figure 6):

Fibre failure:

$$\sigma_{11} = X_T \quad (For\ \sigma_{11} > 0)$$

$$|\sigma_{11}| = X_C \quad (For\ \sigma_{11} < 0)$$

Matrix failure:

$$\left(\frac{\sigma_{22}}{Y_T}\right)^2 + \left(\frac{\sigma_{12}}{S}\right)^2 = 1 \quad (For\ \sigma_{22} > 0)$$

$$\left(\frac{\sigma_{22}}{Y_C}\right)^2 + \left(\frac{\sigma_{12}}{S}\right)^2 = 1 \quad (For\ \sigma_{22} < 0)$$

(1)

Where:

σ_{11} = nominal longitudinal (to the fibre direction) stress
σ_{22} = nominal transverse (to the fibre direction) stress
σ_{12} = nominal in-plane shear stress
X_T = longitudinal tensile strength
X_C = longitudinal compressive strength
Y_T = transverse tensile strength
Y_C = transverse compressive strength
S = shear strength

This criterion was later modified by Hashin in 1980 [104,116] to make it valid for the 3D case (omitted for brevity). This was then reduced to the plane-stress case thus:

Fibre failure:

$$\left(\frac{\sigma_{11}}{X_T}\right)^2 + \left(\frac{\sigma_{12}}{S}\right)^2 = 1 \quad (For\ \sigma_{11} > 0)$$

$$|\sigma_{11}| = X_C \quad (For\ \sigma_{11} < 0)$$

Matrix failure:

$$\left(\frac{\sigma_{22}}{Y_T}\right)^2 + \left(\frac{\sigma_{12}}{S}\right)^2 = 1 \quad (For\ \sigma_{22} > 0)$$

$$\left(\frac{\sigma_{22}}{2S_T}\right)^2 + \left[\left(\frac{\sigma_{12}}{2S_T}\right)^2 - 1\right]\frac{\sigma_{22}}{Y_C} + \left(\frac{\sigma_{12}}{S}\right)^2 = 1 \quad (For\ \sigma_{22} < 0)$$

(2)

Where, in addition to the previously defined terms:

S_T = out-of-plane shear strength.

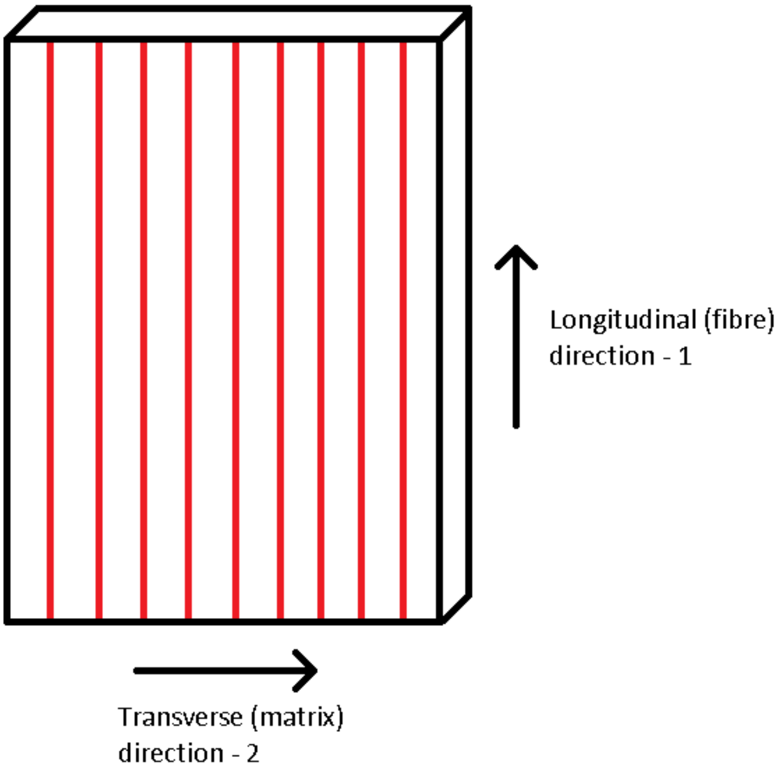

Figure 6: Composite plate schematic - the red lines indicate fibres

The 1980 criterion adds shear terms to the tensile fibre failure criteria and the compressive matrix failure criteria but leaves the 1973 Hashin-Rotem criteria otherwise unaltered. For all of the above, the criteria are met, indicating that damage has occurred for that particular mode, when the equality is satisfied. These two works were ground-breaking since they were the first to consider individual failure modes, and later became the basis of numerous other criteria. It has also been extensively utilised in commercial finite element software packages, and by the majority of researchers in the field.

However, there are some questions regarding the safety of the 1980 criterion's predictions especially. Lapczyk & Hurtado [74] note that the Hashin criteria has an important deficiency in accurate prediction of matrix and fibre compressive failure in particular, a weakness discussed in some detail in a review of failure criteria authored by Paris [116]. Of particular concern is the inclusion in the matrix compressive failure criterion of an out-of-plane shear strength term. This is contentious since out-of-plane shear stress doesn't feature in the 2D form of this criterion. This results in some significant inconsistencies in the failure predictions that are generated, must notably that increasing the value of the out-of-plane shear strength results in increasingly conservative predictions, with obvious potential for dangerously unsafe estimates of the strength of the composite as the allowable out-of-place shear stress decreases. Additionally, the influence of the shear stress term in fibre tensile failure has not been physically established, though Paris later proposes a means to establish this term's significance via micromechanical investigation. Dávila & Camanho [71] remark that the Hashin criteria fails to take into account the positive effect that moderate transverse compression has on shear strength, or the significant detrimental effect of shear stress on the longitudinal compressive strength.

2.1.2 Damage Initiation and Evolution for Fibre-Reinforced Materials in *Abaqus*

The implementation of Hashin's criteria for damage initiation in *Abaqus* uses a combination of both the 1973 and 1980 formulations, suggested by Matzenmiller et al [117,118], presented below. The work of Matzenmiller et al also provides the basis of the post-damage evolution material response.

Fibre failure:

$$F_f^t = \left(\frac{\sigma_{11}}{X_T}\right)^2 + \alpha\left(\frac{\sigma_{12}}{S_L}\right)^2 \quad (For\ \sigma_{11} > 0)$$

$$F_f^c = \left(\frac{\sigma_{11}}{X_C}\right)^2 \quad (For\ \sigma_{11} < 0)$$

Matrix failure:

$$F_m^t = \left(\frac{\sigma_{22}}{Y_T}\right)^2 + \left(\frac{\sigma_{12}}{S_L}\right)^2 \quad (For\ \sigma_{22} > 0)$$

$$F_m^c = \left(\frac{\sigma_{22}}{2S_T}\right)^2 + \left[\left(\frac{Y_C}{2S_T}\right)^2 - 1\right]\frac{\sigma_{22}}{Y_C} + \left(\frac{\sigma_{12}}{S_L}\right)^2 \quad (For\ \sigma_{22} < 0)$$

(3)

Where:

S_T = transverse shear strength
S_L = longitudinal shear strength.

α = formulation selection: this parameter takes a value between 1 or 0. If given a non-zero value, the software includes the shear term in fibre tension from the 1980 criterion, with the contribution of this term to the material behaviour determined by the value of this coefficient.

F_j^i = failure criteria status, with the superscript *i* and subscript *j* referring to loading direction (tensile or compressive) and material component (matrix or fibre) respectively. Damage is initiated when the value this parameter reaches unity.

It must be noted that the stresses in the damage initiation criteria, as it is referred to in the *Abaqus* documentation [118], are components of the effective stress tensor produced by the relationship: $\sigma = \mathbf{M}\sigma_t$, where σ_t is the true stress and **M** is the damage operator:

$$\boldsymbol{M} = \begin{bmatrix} \frac{1}{(1-d_f)} & 0 & 0 \\ 0 & \frac{1}{(1-d_m)} & 0 \\ 0 & 0 & \frac{1}{(1-d_s)} \end{bmatrix}$$

(4)

Where d_i are internal damage variables that reflect the current state of fibre *(f)*, matrix *(m)* and shear *(s)* damage. These are derived from the damage variables corresponding to each of the four failure modes, thus:

$$d_f = \begin{cases} d_f^t \; if \; \sigma_{11} \geq 0 \\ d_f^c \; if \; \sigma_{11} \leq 0 \end{cases}$$

$$d_m = \begin{cases} d_m^t \; if \; \sigma_{22} \geq 0 \\ d_m^c \; if \; \sigma_{22} \leq 0 \end{cases}$$

$$d_s = 1 - \left(1 - d_f^t\right)\left(1 - d_f^c\right)(1 - d_m^t)(1 - d_m^c)$$

(5)

Prior to the initiation of damage, **M** is equal to the identity matrix, so that the effective stress equals the true stress. The damage variables equal zero at the onset of damage, and increase up to unity as the material degrades, with a value of 1 indicating that a component has fully degraded. During the damage evolution phase of the material response, the damage operator becomes significant in the initiation of damage in the other material modes, as the effective stress is increased.

The internal damage variables are also used to modify the post-damage initiation material response. The material response is given by $\sigma = \boldsymbol{C_d}\varepsilon$, where ε is the strain and $\mathbf{C_d}$ is the stiffness matrix for the damaged material:

$$\boldsymbol{C_d} = \frac{1}{D}\begin{bmatrix} E_1\left(1-d_f\right) & E_1\nu_{21}\left(1-d_f\right)\left(1-d_m\right) & 0 \\ E_2\nu_{12}\left(1-d_f\right)\left(1-d_m\right) & E_2\left(1-d_m\right) & 0 \\ 0 & 0 & GD\left(1-d_s\right) \end{bmatrix}$$

(6)

Where:

$$D = 1 - \nu_{12}\nu_{21}\left(1-d_f\right)\left(1-d_m\right)$$

(7)

The value of the damage variables is calculated via a bilinear stress-displacement relationship using a characteristic length to eliminate mesh dependency during material softening. This principle is not dissimilar to the bilinear response of a typical cohesive zone model, such as that proposed by Camanho & Davila [75]. The use of a characteristic length results in an equivalent stress-displacement response, as shown in Figure 7. This length, L^c, is based on the element geometry and formulation, and is the length of a line across a typical first-order element, and half this length for a typical second-order element in a mesh.

Image hidden due to copyright restrictions.
Please refer to [118], figure 24.3.3-1

Figure 7: Equivalent stress-displacement response for damage evolution in a fibre-reinforced material [118]

The positive slope of this curve corresponds to the linear elastic material behaviour prior to damage initiation. The negative gradient region is produced by evolution of the respective damage variables for each mode, in accordance to the following equations. The equivalent displacement (which is not a crack, but actually analogous to strain) and stress is calculated separately for each damage mode as follows:

Fibre failure:

$$\delta_{eq}^{ft} = L^c\sqrt{\langle\varepsilon_{11}\rangle^2 + \alpha\varepsilon_{12}^2}$$

$$\sigma_{eq}^{ft} = \frac{\langle\sigma_{11}\rangle\langle\varepsilon_{11}\rangle + \alpha\tau_{12}\varepsilon_{12}}{\frac{\delta_{eq}^{ft}}{L^C}} \quad (For\ \sigma_{11} \geq 0)$$

$$\delta_{eq}^{fc} = L^c\langle-\varepsilon_{11}\rangle$$

$$\sigma_{eq}^{fc} = \frac{\langle-\sigma_{11}\rangle\langle-\varepsilon_{11}\rangle}{\frac{\delta_{eq}^{fc}}{L^C}} \quad (For\ \sigma_{11} < 0)$$

(8)

Matrix failure:

$$\delta_{eq}^{mt} = L^c\sqrt{\langle\varepsilon_{22}\rangle^2 + \varepsilon_{12}^2}$$

$$\sigma_{eq}^{mt} = \frac{\langle\sigma_{22}\rangle\langle\varepsilon_{22}\rangle + \tau_{12}\varepsilon_{12}}{\frac{\delta_{eq}^{mt}}{L^C}} \quad (For\ \sigma_{22} \geq 0)$$

$$\delta_{eq}^{mc} = L^c\sqrt{\langle-\varepsilon_{22}\rangle^2 + \varepsilon_{12}^2}$$

$$\sigma_{eq}^{mc} = \frac{\langle-\sigma_{22}\rangle\langle-\varepsilon_{22}\rangle + \tau_{12}\varepsilon_{12}}{\frac{\delta_{eq}^{mc}}{L^C}} \quad (For\ \sigma_{22} < 0)$$

(9)

The coefficient α in the terms for fibre tension is the same as defined previously for adjusting the contribution of shear to this failure mode. < > is the Macaulay bracket operator, defined as $\langle x\rangle = (x + |x|)/2$.

The evolution of the various damage parameters in the post-damage initiation regime ($\delta_{eq} \geq \delta_{eq}^{0}$) is given by:

$$d = \frac{\delta_{eq}^{f}\left(\delta_{eq} - \delta_{eq}^{0}\right)}{\delta_{eq}\left(\delta_{eq}^{f} - \delta_{eq}^{0}\right)}$$

(10)

Where δ_{eq}^{0} is the initial equivalent displacement at which the initiation criterion for a given failure mode is met, and δ_{eq}^{f} is the displacement at which the material is completely degraded for this failure mode. This relationship is presented in Figure 8. The value of the initial equivalent displacement is governed by the elastic properties and strength parameters for the various modes. The equivalent displacement at failure may be entered directly, but generally, this value is determined from the energy dissipated at failure for each mode, G^c, which corresponds the area beneath the complete stress-displacement curve in Figure 7. Each energy value represents the fracture toughness for each material component under transverse and longitudinal loading. The data from equation ***(10)*** for each damage mechanism links back into ***(4)*** and ***(6)*** as the load increases and damage propagates.

Image hidden due to copyright restrictions.
Please refer to [118], figure 24.3.3-2

Figure 8: Relationship between damage variable and equivalent displacement [118]

Maimi et al [64] discuss a number of methods of determining these energies, including the use of a standard double-cantilever beam test [119] to find the tranverse fracture toughness under tension G_{2+}, and the novel compact tension and compression techniques of Pinho et al [120] to find the fracture toughness of the fibres (longitudinal direction) under tension G_{1+} and compression G_{1-}. Maimi et al also propose an approximation for the transverse compressive fracture energy G_{2-}, based on the mode-2 transverse fracture energy G_6 (which itself may be found using an end-notched flexure test [121]). The strength and energy data is entered into *Abaqus* as required, and the above procedures are handled automatically as the solution progresses.

Abaqus also allows for damage stabilisation to overcome convergence difficulties in the implicit solver when using material models with softening and stiffness degradation. This technique applies a small, artificial viscosity to the damage variable, causing the stiffness matrix for the softening material to be positive. Provided this viscosity is small compared to the time increment, convergence is usually improved without compromising the accuracy of the results [118].

It is essential to note that damage for fibre-reinforced materials in *Abaqus* is only compatible with plane stress elements [118]. As a result, solid elements, which employ a 3-dimensional state of stress cannot be used with this option, and researchers wishing to simulate progressive damage and failure with solid elements are required to produce their own sub-routines in order to do so [42,52]. Use of a sub-routine is also necessary if the user wishes to use a different or more refined failure theory.

2.2 Delamination Modelling

In the study of delamination, the majority of authors use a cohesive model. Traditionally, delamination would be simulated using the Virtual Crack Closure Technique (VCCT), which operates on the assumption that the energy released during delamination propagation equals the energy required to reclose the crack [122]. Using this method, crack growth occurs when the energy release rate for the material, or a combination of release rates for mixed-mode cracks, equals a critical value. Fracture mechanics techniques such as this require a crack to be defined a priori, that is to say that it cannot be used to predict the emergence of a crack, only its propagation. Additionally, remeshing may be required in the region of the crack tip as the crack grows, which is a time-consuming task. Adaptive-Lagrangian-Eulerian meshing (ALE) is one method by which this remeshing can be achieved, which automatically optimises the mesh as the large deformations due to cracking start to develop [118] (this technique is useful in large-deformation problems in general, but is not considered further in this project).

The cohesive zone model – a crack propagation model originally developed for use with concrete or similar materials, the fundamental principles of which are described in some detail in a review by Elices et al [123] – has the key advantages of simplicity and the ability to model both crack initiation and propagation with a single model [124], as opposed to requiring a pre-defined crack and growth path in traditional fracture models. The model presumes that there exists a ‘process zone’ ahead of the crack tip where the damaged material undergoes irreversible deformation [125], but retains a degree of stiffness, for example via craze hackles [126]. Delamination usually occurs at interply interfaces where there are resin-rich regions, so the use of interface elements with a cohesive law provides a convenient and physically accurate means to simulate this form of damage [127].

The formulation of the cohesive zone model considers a crack as a discontinuity within a material domain, and then applying surface tractions to the boundary of this discontinuity [122,124]. The model relates the tractions to displacement jumps at this interface, where a crack may potentially occur. The initiation of damage in this interface is related to the interfacial strength, which is equal to the maximum traction on the traction-displacement jump (also referred to as traction-separation [118]) curve. The crack propagates when the area under the traction-separation curve equals the fracture toughness for a given mode, causing the traction to reduce to zero. The simplest traction-separation relationship is a bilinear form, such as that used by Camanho & Davila [75] and Turon et al [124], where the initial positive gradient up to the point of maximum traction, indicating the onset of damage, corresponds to the elastic response of the interface. The evolution of the cohesive zone after this point, where material softening occurs, also occurs in a linear manner. Polynomial relationships for the softening regime are also used, and may include allowances for interlaminar reinforcement [123,126,128,129]. *Abaqus* invariably uses a linear elastic pre-damage response. The user may then choose between a linear or exponential softening response depending on requirements [118]. Harper & Hallett [125] note that, while the bilinear softening response may not be entirely representative of the actual behaviour of the cohesive layer, it is perfectly adequate when the global structural response is all that is required. Additionally, they state that determining the true stress distribution associated with damage in this region are very difficult to measure experimentally, creating difficulties in calibrating more a complex material response. It should be noted the traction-separation law discussed here is applicable to cohesive layers of negligible thickness, such as exists between plies in a composite laminate. Thicker cohesive layers are simulated by other methods that will not be discussed here.

A number of different element formulations have been developed. Of foremost interest is the work of Camanho & Davila [75], who developed a mixed-mode cohesive model, taking into account the different crack opening modes shown in Figure 9 (shear mode 3 is generally considered as part of shear mode 2). The proposed element is an 8-node, zero-thickness element which has since been integrated into *Abaqus* [118] and has proven to be one of the more useful contributions in this area. A later contribution by Turon et al [124] develops a thermodynamically-consistent decohesion model under mixed-mode loading, and implements this with a user-defined element in *Abaqus/Standard,* with good agreement with experimental results for a skin-stiffener co-cured structured representative of realistic aerospace structures. Yang & Cox [126] present their own three-dimensional, mode-dependant cohesive element, after providing a survey of recent advances and trends in fracture mechanics for delamination, successfully reproducing experimental results that had not been modelled up to that point. They note an outstanding issue in developing standardised test procedures to calibrate the model parameters for a given material.

The cohesive zone model has been applied to the study of skin-core debonding in sandwich panels by Han et al [129]. The model provided a good agreement with an independent experiment, but required some preliminary experimental work to determine parameters for the cohesive zone model. Of these, the fracture energy is sensitive to error and has a significant effect on the load at which the debond propagates. Gopalakrishnan et al [130] also studied skin-core debond in sandwich beams, successfully using cohesive elements in a cantilever sandwich beam model and remarking on the considerable overestimate in failure load when these elements were not used. Two decohesion models (using bilinear and cubic polynomial interfacial material models respectively) were used by Chen [128] to model the failure of two kinds of composite structures under bending. Cohesive elements have also be used to model the failure of adhesively-bonded lap joints [131], and also in conjunction with composite failure criteria to simulate damage and failure of mechanically fastened joints in composite materials [132]. Note that the above works necessarily make extensive use of finite-element methods.

Some authors have recently started to consider coupling between matrix cracking and delamination. Delamination is governed by transverse shear stresses; however, matrix cracking may provide a location from which the delamination can initiate [71]. The proposed mechanism can be seen in Figure 10. Zubillaga et al [133] present an energy-based approach to model this coupling, with a view to avoid the severe computational demands typically found with the cohesive zone method and suggest their method could compliment other criteria, such as the Puck and LaRC criteria. Abisset et al [134] have also studied this phenomenon, using a damage mesomodel.

Image hidden due to copyright restrictions.
Please refer to [67], figure 2.

Figure 9: Crack formation modes. Mode 1 is opening, and Modes 2 and 3 are shear modes in the 1 and 2 directions respectively [67]

Image hidden due to copyright restrictions.
Please refer to [134], figure 1

Figure 10: Progressive damage due to matrix cracks: Either a new crack develops (left) or delamination is triggered (right) [134]

Another method for modelling of cracks such as those occuring in delamination is the Extended Finite Method (XFEM). This method is gaining increasing prominence as a complimentary or replacement approach to the cohesive zone method utilised by most researchers for the study of delaminations. This fracture mechanics technique models a crack as an enriched feature by adding degrees of freedom to elements with specialised displacement functions. This allows a crack to initiate and propagate along an arbitrary path (crack models using cohesive elements require the crack plane and path to be determined a priori), without requiring the mesh to match the geometry of the crack, or requiring remeshing as the solution progresses [118]. This makes it especially attractive for fracture in bulk materials such as concrete, but is perhaps not as necessary for modelling interply cracks. It may however be valuable for modelling intraply cracks, and examples of its use can be found in the work of Bouhala et al [135], who used this technique in conjunction with cohesive elements in simulating fibre-matrix debonding in a micromechanical study, and by Breitzman et al [136], who used XFEM along with continuum damage mechanics and the cohesive zone model to model matrix cracking, fibre failure and delamination respectively in a composite sample with a through hole loaded in tension. In the latter study, the CDM model was enhanced using the critical fibre volume method to better predict failure initiation, with very good agreement with experimental results. XFEM is not available in *Abaqus/Explicit,* which may potentially limit its utility for the time being [118].

2.2.1 Implementation of the Cohesive Zone Model in *Abaqus*

For a cohesive layer using a traction-separation law, *Abaqus* requires the following data: the elastic and shear stiffness of the layer, and the maximum interfacial stress and fracture energies for each of the crack opening modes. For mix-mode models, a mode-mixity ratio will also be specified, indicating which of the crack opening modes will dominate. The stiffness of the cohesive layer is typically referred to as a ‘penalty stiffness’ and exists to hold the top and bottom faces of a cohesive element together during the linear elastic phase of the material response [75]. This value needs to be sufficiently high to prevent spurious compliances during the linear elastic phase of the material response [75][127]. Camanho & Davila suggest that the penalty stiffnesses be defined as a function of the out-of-plane elastic moduli of the interface (i.e. E_3, G_{13} and G_{23}) and the thickness of the interface t_{coh}, giving:

$$K_{E3} = \frac{E_3}{t_{coh}}$$

$$K_{G1} = \frac{2G_{13}}{t_{coh}}$$

$$K_{G2} = \frac{2G_{23}}{t_{coh}}$$

(11)

Abaqus uses the same relationship for the penalty stiffness [118]. A typical interface thickness will be of the order of tens-of-microns, so the penalty stiffness will be a very large value. If it is overly large, numerical errors may arise due to limits of computer precision, but as stated previously, it must be high enough to ensure an accurate representation of the interface. Turon et al suggest an alternative method of calculate the penalty stiffness, with values within the same magnitude as those determined by other means [122]

The value to assign to the interfacial strength is a subject of some debate, as a number of works have suggested that the accuracy of the solution is insensitive to the precise value of this parameter once a crack has initiated and a cohesive zone exists in a structure [122,125,137]. These works suggest that lowering the value of the interfacial strength from its true value by a small degree may improve the efficiency of the simulation by increasing the length of the cohesive zone while still providing an accurate recreation of the material response. It is however necessary to ensure that an accurate value for the fracture energy is provided, since this is critical for crack propagation [125].

When using the maximum interfacial stress as the critical parameter for damage initiation, *Abaqus* provides two options for damage initiation in the interface [118]. The first is a maximum nominal stress criterion, given as:

$$max\left\{\frac{\langle t_1\rangle}{t_1^0},\frac{t_2}{t_2^0},\frac{t_3}{t_3^0}\right\}=F$$

(12)

Alternatively, one may choose the quadratic nominal stress criterion, which accounts for the interaction between the tractions in the interface, given by:

$$\left\{\frac{\langle t_1\rangle}{t_1^0}\right\}^2+\left\{\frac{t_2}{t_2^0}\right\}^2+\left\{\frac{t_3}{t_3^0}\right\}^2=F$$

(13)

In both of the above equations, t_1, t_2,and t_3 refer to the tractions in mode 1 (normal opening), 2 and 3 (first and second shear directions) respectively. The superscript *0* indicates the critical value for each traction. Both criteria are satisfied, thus indicating the initiation of damage, when *F* equals unity. *Abaqus* also provides the option to predict damage onset via critical strain values, using the same form as the above equations.

Damage evolution for cohesive models is slightly more complex than exists for intralaminar damage, due to the influence of mode mixity resulting from the interaction of the different crack opening modes. Mode mixity may be neglected altogether, especially if the analyst is only concerned with a single fracture mode, though reference is made here to the work of Grau et al [138], who demonstrate the importance of considering the relationship between different fracture modes in sandwich panels, via experiments and a numerical model. They find that if a constant fracture toughness is used, thus ignoring the influence of mode mixity, the maximum allowable pressure can be over-estimated by over 40%, with very serious implications to design safety.

As with intralaminar damage, a damage variable D is utilised, which is equal to 0 at damage onset, and increases up to unity, denoting a fully degraded interface element (and thus crack propagation). The traction components of the interface model are affected by this variable according to the following relationships [118]:

$$t_1 = \begin{cases} (1-D)t_1^t & (if\ t_1^t \geq 0) \\ t_1^t\ \ (no\ damage\ in\ compression) \end{cases}$$

$$t_2 = (1-D)t_2^t$$

$$t_3 = (1-D)t_3^t$$

(14)

Where the superscript t indicates the stress components predicted by the traction-separation law for the current strain without damage. As with intralaminar damage evolution, interfacial damage evolution utilises an effective displacement which takes into account the contribution of all three opening modes and is given by:

$$\delta_m = \sqrt{\langle\delta_1\rangle^2 + \delta_2^2 + \delta_3^2}$$

(15)

The subscripts 1, 2 and 3 denote normal opening, and the first and second shear opening modes respectively, as stated previously. The damage variable thus evolves according to the following bilinear softening law:

$$D = \frac{\delta_m^f(\delta_m^{max} - \delta_m^0)}{\delta_m^{max}\left(\delta_m^f - \delta_m^0\right)}$$

(16)

Where δ_m^{max} = maximum effective displacement attained during the load history,
δ_m^{0} = effective displacement at damage onset
δ_m^{f} = $2G_C / \tau_{eff}^0$, with τ_{eff}^0 as the effective traction at damage onset.

G_C is the area under the traction-separation curve, and represents the energy dissipated due to failure of the interface. The value of this parameter depends on the mode-mix – which is the influence of the different fracture modes on the overall behaviour of the crack - and the law used to define the interaction of these modes. The (energy-based) mode-mix definitions are as follows:

$$m_i = \frac{G_i}{G_T}$$

(17)

Where i equals 1, 2 or 3 and indicates the fracture mode (please refer to Figure 8), G_i is the work done by each traction and its related displacement in each mode, and G_T is the sum total of the work done by these tractions. It is useful to also define the work done by the shear tractions, G_s, separately by taking the sum of G_2 and G_3. The mixed-mode fracture energy may then be given be a power law:

$$G_C = \frac{1}{\left(\left\{\frac{m_1}{G_1^C}\right\}^{\alpha} + \left\{\frac{m_2}{G_2^C}\right\}^{\alpha} + \left\{\frac{m_3}{G_3^C}\right\}^{\alpha}\right)^{\frac{1}{\alpha}}}$$

(18)

Alternatively, if the first and second shear fracture energies are the same ($G_2^C = G_3^C = G_S^C$), the Benzeggagh-Kenane criterion [68] may be more appropriate. The fracture energy is thus given by:

$$G_C = G_1^C + (G_S^C - G_1^C)\left\{\frac{G_S}{G_T}\right\}^{\eta}$$

(19)

In the above equations, the superscript C indicates the critical fracture energy for the relevant mode. α and η are material parameters relating to the mode-mix ratio. As with intralaminar damage, damage stabilisation via viscous regularisation is available for interface material models, and behaves in much the same way as for intralaminar damage.

Another key consideration when implementing a cohesive zone model regards the mesh refinement, discussed in some depth by both Turon et al [122] and Harper & Hallett [125]. The length of the cohesive zone can be found using the following [122]:

$$l_{coh} = ME\frac{G_C}{(\tau^0)^2}$$

(20)

Where E is the elastic modulus of the material, G_C is the critical energy release rate and τ^0 is the interfacial strength. *M* is a parameter that is unique to a given cohesive zone model – Turon et al use a value equal to unity. Additionally, the material properties required change depending on the cracking mode, with mode I cohesive zones typically being a lot shorter than mode II cohesive zones for carbon-epoxy composites [125]. A fully-developed cohesive zone will thus have a length to the order of tenths-of-a-millimetre, and a number of cohesive elements must exist in this zone in order to capture the response of the interface correctly – too few elements and the distribution of tractions ahead of the crack tip may not be captured accurately [122]. Turon et al suggest five elements within the cohesive zone, whereas Harper & Hallett posit that three elements provide an acceptable degree of accuracy. In any event, the consequence of this is that the mesh for an accurate interface model must be highly refined for the whole region which may be expected to crack. This of course carries a considerable computational cost which, as stated before, may be mitigated to some degree by reducing the interface strength.

Figure 11 presents a schematic view of a cohesive element layer to show these concepts graphically, and shows the development of a cohesive zone under a mode-1 normal-opening type loading, relating this back to a typical bilinear traction-separation curve of the kind used within *Abaqus*. The orange elements are within the cohesive zone – note the scale and the typical number of elements that feature in this region. Note also that the displacement at failure (δ^f) is governed by the fracture energy of the cohesive layer, rather than input into the solver directly.

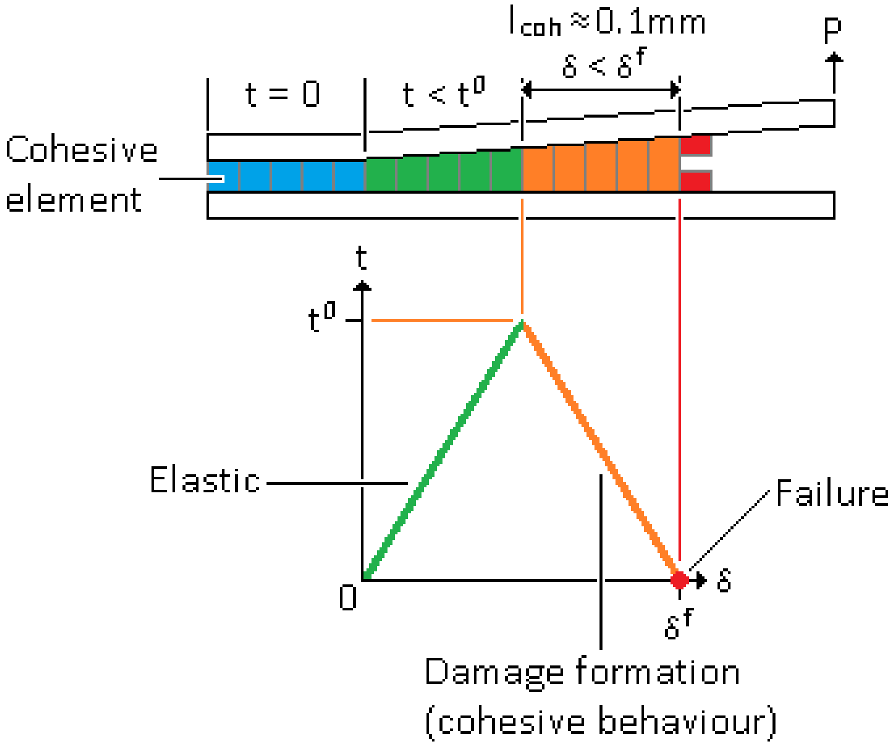

Figure 11: Schematic of a cohesive element layer, showing cohesive zone formation under loading

The cohesive zone model can be introduced into an *Abaqus* analysis in two main ways. The first method uses cohesive elements of the kind developed by Camanho & Davila [75]. These function as other numerical elements, being arrayed into a mesh which can be linked to the rest of structure via tie constraints, partitioning or other interactions. The two bonding faces acting effectively as shell elements, with the body of the element between these two faces forming the cohesive zone. The other approach is to use a cohesive surface interaction [118], particularly appropriate for very thin interfaces such as between composite plies. Here, there is no layer introduced between the two parts being bonded as such. Instead, the interaction is defined in a similar manner to tie constraints and similar interactions, with a mating face being defined on each of the parts being joined. The motion of nodes between these two surfaces will then be related to one another using the same cohesive layer properties that would be used in a cohesive element, so that the relationship between their displacements is governed by the cohesive response, rather than, say, the unbreakable link between nodes that would be typical for a tie constraint. In effect, the cohesive surface interaction behaves identically to a cohesive element, but without the need to introduce additional elements (and thus additional computational effort) into the problem.

2.3 Behaviour of Core Materials

The behaviour of core materials under loading must be properly considered in the modelling of sandwich panels. Of particular interest is the behaviour of honeycombs, which, as explained by Lacy & Hwang [11] and shown in Figure 12, exhibit after ultimate load progressive crushing at near-constant stress (region 2 in the stress-stress plot), followed by increasing stress with further deformation due to ‘densification’ (region 3 in the figure), where the crushed cell walls start to come into contact with one another and resist the applied load once more. This behaviour may be included in an orthotropic material model along with experimentally determined elastic properties – this is the approach followed by these authors. Additionally, materials such as nomex may exhibit springback upon unloading [17], requiring additional data for the unloading response. Core crushing cannot be neglected in a finite-element sandwich model, as inaccuracy will result [139]. It should be noted that the above assumes homogenous core behaviour. At the cellular level, honeycomb cores may exhibit any combination of elastic buckling (as they are simply thin-walled structures at this scale), plastic deformation and fracture; buckling may occur under both normal and shear loads [140].

The homogenised core approach to honeycomb modelling is investigated by Aktay et al [141], using a biphase material constitutive behaviour. This particular work uses semi-adaptive coupling to replace damaged and failed elements with discrete particle clusters to prevent numerical errors. Shi & Tong [142] present an analytical method for the homogenisation of honeycomb materials, calculating the equivalent in-plane normal and shear properties based on the material properties and geometry of the honeycomb. An alternative approach, for those authors using explicitly modelled honeycomb geometries, isotropic material behaviours may be used, typically applying elastic-perfectly-plastic or strain hardening behaviours as appropriate. The work of Chawla et al [143], studying bare honeycomb, is a good example of this approach, and it could be readily applied to a sandwich model, however, care must be taken if the honeycomb is produced from an anisotropic material, such as nomex paper, to ensure the material response is correctly captured [139]

Image hidden due to copyright restrictions.
Please refer to [11], figure 6

Figure 12: Loading behaviour of a typical honeycomb core [11]

2.4 Finite Element Modelling with *Abaqus*

At its most basic, the finite element method discretises a structure into a mesh of elements, with these elements joined together by nodes. When a load or other disturbance to the structure's equilibrium is introduced, stresses are developed in the elements which produce displacements in the nodes, which then propagate through the structure. The commercial finite element package *Abaqus* will be used in the development of the model. The majority of authors surveyed previously have used this software at some point in their work (please refer to Table 2, *'Key Numerical Studies'*), and it is the preferred choice for the current author, due to the comprehensive and intuitive modelling environment featured in the software, and the ability to readily perform both implicit and explicit analyses [144].

Abaqus features a number of means to model composite laminates, including 2-D shells and 3-D solids, with lamina properties applied, or by producing an assembly of discrete plies. The core can be modelled as a homogenous solid with orthotropic properties, or with explicit honeycomb geometry, the latter of which, though obviously complex and computationally expensive, can allow for improved model fidelity. There exist a number of techniques to model cohesive interfaces, which can be used to simulate delamination and debonds. The software allows the use of the Hashin criteria and progressive damage modelling via reduction of material properties and element removal as built-in tools.

Abaqus also offers highly generalised modelling capabilities via its user-defined subroutines and elements, allowing tremendous flexibly to perform advanced simulations that the in-built tools may be unable to provide. An example of this, often noted in the literature review, is the use of user-defined material behaviours, particularly for damage and failure. This capability also extends to the production of user-developed finite elements for highly specialised applications, often for cohesive zone models. Some of these techniques may be difficult to implement, either due to the computational demands of the techniques or the technical skill required by the user in developing the model.

2.4.1 Selection of an Appropriate Solver

There are three main procedures for solving general structural problems in *Abaqus*: static and dynamic implicit solutions, and explicit dynamic solution. Other procedures exist for frequency analysis, and thermal, fluid, electrical analyses, etc. One of these procedures may be selected for any given analysis step; a 'step' can defined as a part of a simulation history which controls analysis procedure, loading and output options [144]. An analysis may consist of a number of steps, which may require the use of different procedures; however, explicit procedures cannot be used with '*Standard*' (i.e. implicit) procedures within the same analysis [118]. A given solver may be more appropriate for certain problems than the others.

To aid the following discussion, two more definitions will be useful [144]: an 'increment' is taken to be a fraction of the total load to be applied within a step. The break-down of the total load in this manner is necessary when the structural response is non-linear. In *Abaqus/Explicit*, this increment is temporal, but has the same effect of splitting the applied load into fractions of the whole. An 'iteration' applies to implicit analyses only. This is where the solver attempts to converge on an equilibrium solution for a given increment, typically via Newton's Method. The solver will attempt a number of iterations in an effort to reach an equilibrium condition, and, depending on the severity of the non-linear response, may require a number of reductions in the size of the increment in order to do so.

The implicit solver uses an iterative approach to solve a stiffness matrix-based problem of the general form $[P] - [K][u] = 0$, where $[P]$ is the applied load vector, $[K]$ is the global stiffness matrix and $[u]$ is the nodal displacement vector, and the unknown that the implicit procedure will attempt to solve. The solution is dependent on the relationship between nodes, due to the matrix $[K]$. The implicit, dynamic solution differs in that it uses direct integration in order to better solve transient and non-linear problems, but the basis of solving a stiffness matrix-based problem via an iterative approach remains the same [144,145]. The explicit solver, on the other hand, directly integrates the kinematic behaviour of each individual node via solution of the nodal equations of motion, with the state of the node at each increment being based on the results from the previous increment [144,145]. Stated another way, an implicit procedure derives the state of the model at time $t + \Delta t$ based on information at time $t + \Delta t$, whereas an explicit solver derives the state of the model at time $t + \Delta t$ based on information at time t [146].

The explicit dynamic analysis procedure is implemented via integration of the equations of motion for a body (in this case, an individual element), used alongside a lumped element mass matrix. Thus, the equations been solved at each increment are as follows:

$$\dot{u}^N_{(i+\frac{1}{2})} = \dot{u}^N_{(i-\frac{1}{2})} + \frac{\Delta t_{(i+1)} + \Delta t_{(i)}}{2}\ddot{u}^N_{(i)}$$

$$u^N_{(i+1)} = u^N_{(i)} + \Delta t_{(i+1)}\dot{u}^N_{(i+\frac{1}{2})}$$

(21)

where u^N_i is a degree of freedom (i.e. a displacement or a rotation) component N, at an increment number i. The principle is very simple, finding the velocity and displacement of the body based on its previous state and the addition of an acceleration or velocity a half-step before the current increment. The remaining unknown in this system of equations is the acceleration of the body, defined as:

$$\ddot{u}^N_{(i)} = (M^{NJ})^{-1}(P^J_{(i)} - I^J_{(i)})$$

(22)

where M^{NJ} is the matrix mass, P^J is the applied load vector and I^J is the internal force vector. The internal force vector is assembled using the stiffness contributions of each individual element. This links the material and structural properties to the solution without needing a global stiffness matrix of the kind required by the implicit solution. The reader will immediately recognise the above equation as a rearrangement of Newton's Second Law, $F=ma$, thus underlining the computational simplicity of the explicit dynamic procedure.

The implicit solver, depending on the precise settings, can be used for both static and dynamic problems, provided the energy-dissipation in the latter is minimal [118]. The explicit solver, although a dynamic approach - indeed, its original purpose was to study high-speed transient events such as impact events – is also suitable for non-linear quasi-static problems [144], provided due precautions are taken to ensure that the structural response is indeed quasi-static. These validation steps will be discussed later. Examples abound in the literature where the explicit solver is used in this manner, typically in cases where there is complex contact and/or sliding non-linearity such as that found in metal-forming problems [147,148], or considerable material non-linearity, such as that caused by material softening and failure [146,148-151]. It is material non-linearity due to damage and failure that is of concern in the current problem. The use of *Abaqus/Explicit* for quasi-static transverse indentation of composite sandwich panels has been successfully demonstrated by Czabaj et al [33] and Foo et al [52].

The implicit solver is unconditionally stable with respect to the size of the time increment [144,147,152], making it the far more efficient choice for linear and mildly non-linear quasi-static problems, since there is no upper limit on the size of the increment. For example, where one is only concerned with the elastic behaviour of a simple structure, it is perfectly plausible for the implicit solver to solve the problem in a single increment. Additionally, the implicit solver can potentially provide more accurate results [152]. The key limitation of the implicit solver is a lack of robustness, which causes convergence problems in highly non-linear problems, particularly complex contact simulations, or where there is material softening due to damage. Indeed, this can cause, in the extreme, an analysis to abort as the solver fails to find a convergent solution. This weakness is noted in a number of papers, and it is well-known that the use of an explicit solver can overcome this difficulty [56,145-147,152,153]. To explain this deficiency in more depth, within the context of the current research, recall that the material properties in the damaged region are degraded during the damage evolution phase. Once this degradation reaches its maximum, the stiffness matrix becomes singular for the elements in that region, causing the implicit solver to abort the analysis when it attempts and inevitably fails to invert the matrix. Convergence failure can be delayed via the use of additional elements through the thickness of the plate, as it would allow the material to fail in a more progressive (and indeed more realistic) manner; however, this issue is inherent within the implicit solver and cannot be eliminated: the analysis would still abort once a completely damaged region exists in each layer, even though the structure may not have actually failed.

The key disadvantage of the explicit solver is its conditional stability [144,147,152]. This creates a limit on the maximum size of a time increment, defined in terms of the highest frequency of the system, and estimated via the following simple relationship [144]:

$$\Delta t_{max} = \frac{l_{el}}{v_d}$$

(23)

Where l_{el} is the shortest element length, and v_d is the dilatational wave speed of the material, given by:

$$v_d = \sqrt{\frac{E}{\rho}}$$

(24)

Where E and ρ are respectively the stiffness and density of the material. Typically, this maximum stable time increment will be very small – for composite materials with a properly refined mesh, this can be as small as $1e^{-9}$ s. The obvious consequence of this is that analyses with a long time step, such as quasi-static problems where a long duration is necessary to ensure a suitably low loading rate, become hugely demanding of computational resources as many thousands or millions of increments become necessary to solve the problem. As a result, it is usually necessary to manipulate the solution via artificial acceleration of the loading and/or by artificially increasing the density (‘mass scaling’) [144,147] to increase the stability limit and thus improve computational efficiency. Both of these approaches change the physics of the problem being studied by increasing inertial effects within the solution, and thus need to be used with care, and checks must be performed to ensure the validity of the results is not compromised. Additionally, accelerated loading cannot be used with rate-dependant materials [118]. The stable time increment can of course be increased by using larger elements, but care must be taken to avoid an overly coarse mesh, which could also cause inaccurate results, particularly if used with cohesive elements.

If the problem is artificially altered via accelerated loading or mass scaling for computational efficiency, the solution must be checked to confirm that the results can be considered true for a quasi-static problem. The usual method is to compare the kinetic energy of the system with the internal energy of the system at the end of the step. Ideally, the kinetic energy would be zero or close to zero for a truly quasi-static case. The typical rule of thumb suggests that if the kinetic energy is less than 5% of the internal energy, the solution can be considered to be quasi-static, as inertial effects are negligible at this energy level [144,146,147]. An additional guarantee of a quasi-static solution is to compare the loading rate to the lowest natural period of the structure [144,147]. By finding the lowest natural frequency of the structure, one can find the period for this mode by taking the reciprocal of that frequency. A quasi-static deformation will occur over a much longer time period than the natural period, so, providing that the loading rate is much lower than this (at least 10 times slower is recommended) then the solution can be considered quasi-static. Such manipulations of the problem to reduce the solution runtime are generally not required for truly dynamic events, since these transient events are necessarily of very short duration, and thus can be modelled in true time without difficulty.

2.4.2 Finite Element Selection

This section is specifically concerned with element selection for the composite skins on the sandwich panel. The choice of element is central to the quality of the model and will depend on the precise requirements of the analyst. Due to the geometry and material behaviour of the core, where the through-the-thickness properties are critical, and the fact that the core responses of interest are in the out-of-plane direction (for example, the indentation), using a solid element is the only acceptable option for core modelling. However, since composite laminates are thin relative to the in-plane dimensions, with typically poor through-the-thickness properties, the element choice becomes rather more involved. There is no right or wrong answer, and the ultimate choice is down to the requirements of the analyst. Simply put, a solid element will use a 3-dimensional state of stress, whereas a shell element will feature only the in-plane stresses. A third option is to use of continuum shells, which apply the 2-D kinematic behaviour of a shell element to a 3-D geometry, allowing for easy use of composite lay-up and laminate data, while providing enhanced through-the-thickness analysis results, including localised deformation, that conventional shells cannot. Continuum shells represent something of a compromise between solid and shell elements. Figure 13 shows examples of solid and shell elements.

Image hidden due to copyright restrictions.
Please refer to [144], figure 3-1

Figure 13: Typical solid and shell elements. The solid element here is a linear element, whereas the shell element, with the mid-point nodes, is a quadratic element. [144]

Image hidden due to copyright restrictions.
Please refer to [144], figures 4-2 & 4-7

Figure 14: Linear and quadratic shell elements, with a) full integration (top) and b) reduced integration (bottom) [144]

Another consideration concerns the use of linear or quadratic elements (or first- and second-order respectively), both of which are available for shell and solid elements, though not necessarily each solver. The element topology can also be varied, for example quadrilateral, tetrahedral and wedges are all available in *Abaqus*, with quadrilateral elements being perfectly appropriate for most purposes. Fundamentally, a linear element will have a node at each vertex (giving, for example, 8 nodes in a solid quadrilateral element), whereas a quadratic element adds additional nodes along each edge (usually, but not invariably at the mid-point of the edge). This would give, for instance, 8 nodes for a quadrilateral shell element, and 20 in a quadrilateral solid element. The user can also choose between full- and reduced-integration of the elements. This refers to *“the number of Gauss points required to integrate the polynomial terms in an element’s stiffness matrix exactly when the element has a regular shape”* [144]. There are two and three Gauss points in each direction in a linear and quadratic element respectively when fully-integrated. Reduced integration removes one Gauss point in each direction. By adding nodes to the element, the quadratic element is able to deform in a more natural, continuous manner, forming curved shapes rather than being restricted to quadrilateral forms as the linear elements are. Figure 14 shows the difference between linear and quadratic shell elements.

When selecting elements, it is also worth considering the potential influence of shear locking and hourglassing, which may manifest under complex loadings or when severe element distortions start to occur. Shear locking is a problem associated with fully-integrated linear solid elements, which causes the element to be too stiff in bending. This is caused by the edges of the element being unable to curve, resulting in spurious non-zero shear stresses in pure bending. This can be visualised in Figure 15 by observing that the angles between the vertical and horizontal dotted lines (passing through the Gauss points) do not equal 90º, indicating the presence of shear stresses. Figure 17 shows how this problem is avoided using quadratic elements: as the edges are able to curve in bending, spurious shear stresses cannot develop.

Image hidden due to copyright restrictions.
Please refer to [144], figure 4-5

Figure 15: Shear locking in a linear, fully-integrated element in pure bending [144]

Image hidden due to copyright restrictions.
Please refer to [144], figure 4-8

Figure 16: Hourglassing in a linear, reduced-integration element in pure bending [144]

Hourglassing is the opposite problem, affecting reduced-integration linear elements. This occurs due to zero strain energy being generated at the Gauss point under bending, resulting in an overly-flexible element. In coarse meshes of linear elements, this zero-energy mode can propagate and invalidate the results. The problem can be seen in Figure 16; the length and angle between the two dotted lines through the integration point are unchanged, indicating that, despite the applied bending moment, there is zero strain energy in the element. *Abaqus* applies hourglass control to these elements by default, via a small artificial stiffness. Both shear locking and hourglassing can be mitigated by using reduced-integration elements and a suitably refined mesh. Additionally, quadratic elements are not usually affected by these phenomena, but they are not available in *Abaqus/Explicit*, with exception of tetrahedral elements.

Image hidden due to copyright restrictions.
Please refer to [144], figure 4-6

Figure 17: Fully-integrated quadratic element in pure bending [144]

Many of the reviewed works have successfully used shell, and continuum shell, elements to model composite skins, with researchers using solid elements to model composites being in the minority. Additional to this, most researchers studying delamination will use interfacial cohesive elements, regardless of whether the skins are modelled as solids or shells. Individual plies, or blocks of plies may be modelled as discrete parts of the whole, with or without a layer of cohesive elements existing at the interface. It is perfectly possible to model every single interface in this manner, as is the case in the work of Gonzalez et al [42]. In fact, this method may be essential if one wishes to use an inhomogeneous material with solid elements, since *Abaqus/Explicit* is incompatible with such a model, though this will come with a dramatic computational penalty. It is possible to model only some of the interfaces, and perfectly bond the rest of the plies with tie elements, though this will also carry a computational penalty, and thus this method may prove to be of negligible benefit. Yet another approach is to partition a plate into multiple regions through the thickness, and apply the required material properties and orientations to each region separately. The use of discrete ply modelling may also overcome some of the problems associated with using shell and continuum shell elements, particularly the lack of through-the-thickness accuracy, by allowing more elements to be used in the thickness direction.

As previously mentioned, the Hashin criteria built into *Abaqus* works only for plane-stress elements, precluding the use of solid elements for composite modelling. However, determining the interlaminar stresses in a plate are essential if one wishes to consider delamination, since these are what govern their formation. This requires a 3-dimensional stress state and so a solid element is needed. As a result, the lack of a 3-dimensional failure criterion for composite laminates is a crucial problem. As discussed in an earlier section, a number of authors have produced their own failure criteria to resolve this issue, though it must be noted that this is by no means a trivial proposition. To use the user-defined subroutines capability in *Abaqus* would require significant careful effort and testing, as advised in the subroutines manual [154].

2.4.3 Material Data Requirements

One important additional aspect to consider is the implementation of the core material model. *Abaqus* can accept and use a stress-strain curve for plastic behaviour quite easily, though this carries one vital condition. If the material data is entered in a tabular form in *Abaqus*, this data will be automatically regularised by the software, whereby the user-defined curve is fitted by another curve composed of equally-spaced points [144]. The regularisation is difficult if the smallest interval on the user-defined curve is small compared to the range of the independent variable. These curves can be seen in Figure 18. The implication of this for core modelling is that it is difficult to capture the sharp load reduction at the onset of crushing. In preliminary models, entering this drop as exactly vertical caused the regularisation operation to fail, and so a small gradient had to be applied to the data. A possible alternative approach would model the honeycomb core as a crushable foam, using the compression yield stress ratio and the hydrostatic yield stress ratio. There is no information available at this stage to suggest whether or not this method would work, however.

Some experimental work is required to gather a complete set of material data for the skin and core, depending on the precise requirements of the model and the availability of complete data for the particular material being studied. Gathering this information can be done in parallel with the production and running of developmental models prepared using data in the literature. It is especially important to obtain an accurate stress-strain curve for the plastic and crushing behaviour or the core. Schwingshackl et al [155] provide a useful review of existing theoretical and experimental methods for the determination of honeycomb elastic properties, and propose a new dynamic approach. For the purposes of this project, the core response is an aspect of secondary importance. While it is necessary to capture core crushing, proper modelling of the intra- and interlaminar damage is more significant, and thus within the time constraints of this project, advanced modelling and experimentation into the minutiae of the core response is not possible.

The exact data requirements for the skins will depend on the failure criteria used, but will at the very least include fracture energies and strengths in both longitudinal and transverse directions for tension, compression and shear. A separate set of data will also be required for the interfacial cohesive model. Again, this will be dependent on the exact model used, but is likely to require at least the material properties of the resin or adhesive, or the mode I and II opening tractions. Taking the example of the LaRC03 criteria [69], the required material data includes the elastic modulus, tensile and compressive strength in the longitudinal and transverse directions, the longitudinal shear modulus and strength, the in-plane Poisson's ratio, the mode 1 and 2 fracture toughness (longitudinal direction) and finally, as optional properties, α_0 and η^L, which are the angle of the fracture plane and longitudinal *"coefficient of influence"* – relating to internal friction – respectively.

Images hidden due to copyright restrictions.
Please refer to [144], figures 10-5 & 10-6

Figure 18: Regularistion of material data. The left curve a) shows data that is easily regularised. The right curve b) is data that is difficult to regularise, due to the small interval in the low-strain region relative to the range of strain for this material [144]

2.4.4 Contact

A final aspect of the numerical model that has not yet been discussed is the use of contact. Contact algorithms in *Abaqus* enable interaction between multiple bodies within an analysis; in this instance, indenters and load platens in contact with a sandwich panel to apply loadings. The contact interaction of interest here is surface-based [144], whereby two or more surfaces in contact will interact in accordance to the defined interaction relationship, be it friction, 'hard' contact where the load in one component transmits to the other, etc. 'Hard' contact is typically relevant to the normal-direction component of the contact interaction between two surfaces, with the constraint coming into effect when the clearance between the two surfaces reaches zero. Friction and similar relationships relate to the tangential component of the contact interaction.

The surface-based contact interaction requires the definition of the various surfaces in contact with one another. In *Abaqus/Standard* (the implicit solver), these surfaces are defined manually, whereas in *Abaqus/Explicit*, a general contact interaction is available that automatically defines element-based surfaces for every body in the model, providing an 'all-with-self' contact relationship. This is very convenient, but comes at the cost of fine control, though this limitation is not an issue in the current work. The exception to the automatic surface definition is for analytical rigid surfaces. These are undeformable surfaces generated via mathematical relationships to provide simple shapes without the need for meshing, and are particularly useful in this present context as loading surfaces, since their motion, and resultant output (such as the reaction force) is controlled via a single reference point. As there is no need for meshing, these surfaces are also computationally efficient, but as a result, the surfaces used for contact interactions must be defined manually.

The automated general contact interaction uses a balanced master-slave relationship to enforce the contact constraints. Simply point, the mesh nodes making up the master surface may penetrate the space between nodes in the slave surface, whereas the slave surface cannot do the same to the master surface. This can potentially cause problems whereby the master surface penetrates some distance into the slave surface without the contact constraint being triggered. This issue is shown in Figure 19a. This problem can be resolved by using a properly refined mesh, but the balanced contact relationship also alleviates this effect by simply applying the master-slave approach twice, switching the master and slave surfaces the second time around, and making a correction to the solution as required based on this calculation (see Figure 19b).

Image hidden due to copyright restrictions.
Please refer to [144], figures 12-52 & 12-53

Figure 19: a) (left) penetration of slave surface by master nodes b) (right) balanced solution eliminating this difficulty [144]

Contact constraints may be enforced using a kinematic or penalty contact algorithm [118]. The former is a strict implementation, relevant to contact between defined surface pairs. This method makes a prediction as to the expected penetration of slave nodes into the master surface, and then applies additional accelerations to nodes violating the constraints, until a corrected configuration meeting the constraints is achieved. The penalty contact algorithm is a less-strict method by which contact is enforced, and is relevant to general contact of the kind used in this particular project. This approach searches for areas where slave node penetration has occurred, and applies forces that are a function of the penetration distance to the slave nodes to oppose this. The contact force and penetration distance are related by an applied additional stiffness, which can potentially increase the stable time increment, though this effect is generally insignificant. Where an analytic surface is used, equal and opposite forces are applied to this surface as well (hence why viewing the reaction force output of an analytical rigid surface is such a convenient method for establishing the load on a structure when displacement control is used, as the reaction force at the controlling node of the surface necessarily equals the sum of the nodal forces in contact).

Another benefit of using rigid surfaces in conjunction with a contact interaction is that it allows greater flexibility in defining load cases. For example, it is easy to trial different sizes of indenter simply by changing the parameters of the analytic rigid surface. However, one must be careful to avoid slave nodes moving so much as to fall behind a rigid surface (see Figure 20). This is easily avoided by simply extending the rigid surfaces.

Image hidden due to copyright restrictions.
Please refer to [144], figure 12-10

Figure 20: Preventing analysis errors by extending rigid surfaces. [144]

Chapter 3

Experimental Work

3: Experimental Work

In this section, an extensive experimental study gathering compression-after-impact data for sandwich panels with differing thickness skins on the distal side, at different levels of damage, is reported. The objective was to produce a good-quality set of strength data (primarily), as well as damage morphology measurements and material property data (to use as input data for the numerical model). As a result, repeat testing in the compressive testing phase was used extensively, resulting in a large study despite the relatively small number of configurations for the panel and damage state under consideration. This data is intended to provide further validation of the model presented in Chapter 5 (*"Sandwich Model Development"*) – the configurations produced and tested in this section will be modelled and discussed in Chapter 6.

3.1: Sample Preparation

Two panel configurations were tested here: one with skins of equal thickness (henceforth designated as 'symmetric'), using a quasi-isotropic lay-up of $[-45/0/45/90]_s$ for both skins. The second configuration used skins of unequal thickness (designated as 'asymmetric'), with the thicker skin having the same lay-up as for the symmetric panel skins, and thinner skin using a multi-directional lay-up of $[45/0/-45]_s$. In the case of the asymmetric panel, the thick skin was used as the impacted (and thus damaged) side. Both panel configurations used a 12.7mm (nominal; mean measured thickness of 12.163mm) thick aluminium honeycomb core (*HexWEB CRIII 3/16 5052 4.4*). The skins were produced, in all cases, from high-strength carbon fibre uni-directional prepregs, utilising an out-of-autoclave cured epoxy resin, and T700S carbon fibre reinforcement with 12K roving (*M77/42%/UD90/CHS*). The panel configurations and materials were based on (but not identical to) those used by Zhou et al [22-25]; the planar dimensions of the panels are based on the requirements of ASTM D7137 for the CAI testing of monolithic composite plates [38]. All material was supplied by Gazechim Composites.

The plies were individually cut from the roll of prepreg using a Stanley knife and a metal template for convenience and improved repeatability, and laid-up by hand. Cut plies were stored in the freezer until needed, and during cutting, the roll would be periodically returned to the freezer as well – the prepreg would get tacky as it warmed to ambient temperature, making it difficult to produce a clean cut. During laying-up, the laminate assembly would be debulked under vacuum for a period of time (10 – 20 minutes) every two or three plies to remove air bubbles in the laminate and improve consolidation. The M77 resin system is designed to have a short cure cycle at moderately high temperatures [156]. Additional consolidation is provided by the application of a weighted caul plate, providing 2.7 kPa of pressure. This is less than ideal (Hexcel recommend a minimum pressure of 0.1 MPa), but time constraints required that the plates were cured three-at-a-time, and only limited weight was available for consolidation. So, to ensure good quality plates, an alternative cure cycle has been used, with the laminates cured at 100ºC for 40 minutes, with a temperature ramp rate of 2ºC / minute. This produced acceptable plates in spite of the reduced consolidation pressure. The nominal ply thickness was given in the datasheet to be 0.103mm. Measurement of a sample of cured skins gives an average thickness of 0.853mm for the 8-ply quasi-isotropic skins, and 0.644mm for the 6-ply multi-directional skins, for actual ply thickness of 0.107mm.

Peel ply was used on the top surface of the plies to provide a rough surface for bonding to the aluminium honeycomb. A manufacturing error resulted in some of the symmetric plates requiring bonding on the smooth face of the plate. As a result, some of the sandwich panels have one skin bonded on the rough surface (the preferred option), and one skin bonded on the smooth side. This minor inconsistency in the manufacture was not expected to cause undue harm to the results – these plates still bonded well to the honeycomb, and as an additional measure, these plates were reserved for damage characterisation tests. The damaging event was still applied to the rough-side skin to ensure consistency with the CAI samples and it was expected that the influence of the bond on the distal skin will be minimal. This assumption is based on previous work for low-velocity impact tests, where the distal skin is shown to be unaffected by the damaging event. Prior work also suggests that, at these energy levels, skin-core bond failure is not expected.

The honeycomb was cut using a Stanley knife with approximately 20cm of excess material in each direction, to ensure that cells distorted by the cutting were not included in the final panel. The panels were assembled such that the W-direction of the honeycomb is parallel with the 0º fibre direction on the skins, and also the loading direction for the compressive tests. The skins were bonded to the honeycomb one side at a time, using Redux 609 adhesive. These were cured at 120ºC for one hour, with a temperature ramp rate of 5ºC / minute, in accordance with Hexcel’s recommendations [157]. Hexcel recommend a minimum curing pressure of 140 kPa, which is easily achieved for the honeycomb-plate bond using 12.5kg of applied weight, even when the panels are cured two-at-a-time.

The completed panels were carefully trimmed to size using a tile-cutting circular saw. The finished panels are squared to ±1º, and have nominal (planar) dimensions of 150 x 100 mm (±1mm). These tolerances are considered acceptable for hand-cut panels. The longer dimension is parallel to the loading direction. The ends of all panels were then reinforced by potting with resin. Gurit Prime 20LV epoxy resin (used in conjunction with ‘slow’ hardener) [158] was gravity-fed into a shallow channel cut into the honeycomb. Rudimentary, expendable reservoirs were built onto each panel to hold the resin. The pots are cured at room temperature for 24 hours after degassing in a vacuum chamber. Finally, once the resin was cured, the ends of the panels were machined to remove excess resin.

A total of 26 each of symmetric and asymmetric panels (plus spares) were produced, to perform the following tests:

- Damage characterisation using a pendulum-based impact jig, to determine the maximum loads and residual dents produced for three energy levels, as well as the extent of skin and core damage (1 test per energy level per panel configuration).

- Damage characterisation using quasi-static indentation. The test was performed for three levels of applied load/displacement, which were set to correspond with the observed load/displacement from the impact tests. This test checks that the skin and core damage produced in this manner is representative of the damage induced by impact. It was anticipated that, based on the observations of other authors, that the quasi-static tests will produce more extensive damage for a given load, providing a conservative estimate for the residual strength (1 test per load level per panel configuration).
- Edge compression tests for panels damaged with a quasi-indentation load corresponding with those in the damage characterisation test, as well as for an undamaged panel. Data spread in the ultimate strength is expected, so repeat tests will be used here (at least 5 tests per load level – including undamaged, per panel configuration, spread over a number of phases).

A small number of panels were instrumented with unidirectional strain gauges, with three gauges used per panel. One was mounted at the centre of the distal face, aligned parallel to the loading direction (*B0*). The other two were fitted to the impacted face, one parallel to the loading direction and offset from the centre by 25mm in the x-direction (*F0*), and the other perpendicular to the load and offset from the centre by 25mm in the y-direction (*F90*). This outset was necessary to avoid impinging on the damaged region. The exception is the virgin panels, where the *F0* gauge was, like *B0,* placed at the centre of the face. Figure 21 shows these locations schematically, and Figure 22 shows two instrumented panels prior to the CAI testing, showing the front and rear aspects of the panels.

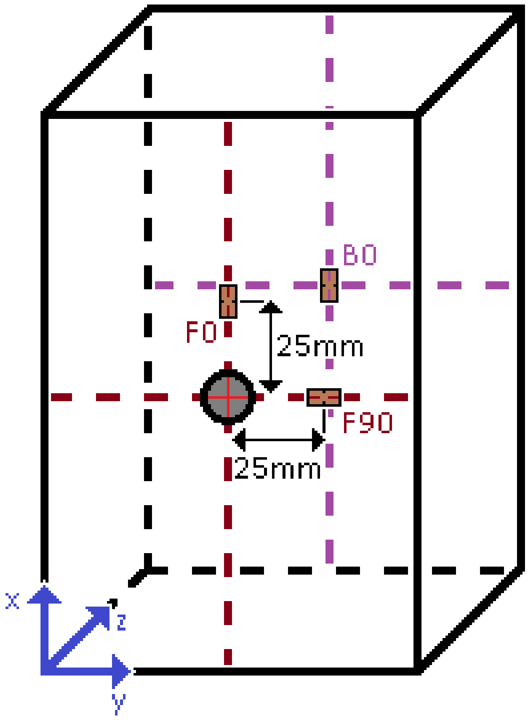

Figure 21: Schematic of instrumented sandwich panel (not to scale)

Aside from the sandwich panels, a number of uni-directional material specimens were prepared from the same roll of composite material to gather input data for the numerical model. Time and resource constraints meant that a complete set of data could not be collected. The tests performed were uniaxial tensile tests in accordance with ASTM D3039 [159], giving the elastic modulus and tensile strength in both longitudinal and transverse directions (E1, E2, σ1+ and σ2+), as well as the in-plane Poisson's ratio (ν12). A uniaxial compressive test using a sample from ASTM D3410 [160], modified to suit the supporting fixture specified in ASTM D695 [161] was also performed for the longitudinal compressive strength (σ1-). The results from these tests are provided in Appendix A.

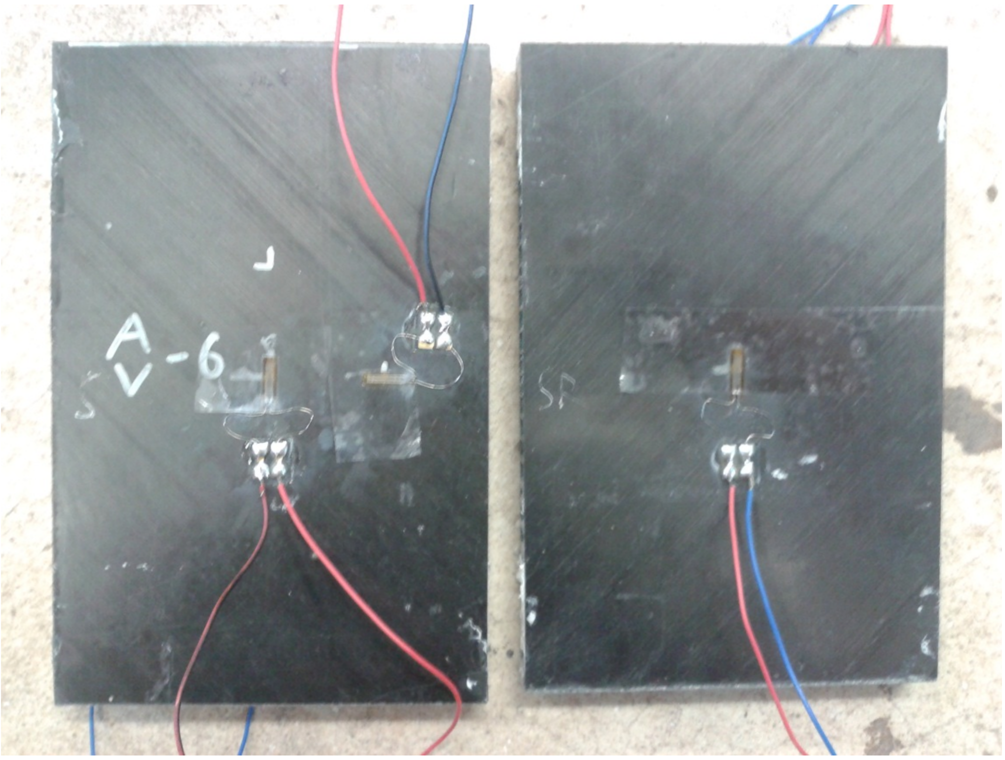

Figure 22: Two instrumented panels showing front aspect (left) and rear aspect (right). On a damaged panel, the front aspect corresponds with the impacted face.

3.2: Impact and Indentation Tests

A pendulum-type impact jig, equipped with a potentiometer to measure the angle of the arm and a force transducer behind the impact tip, was used for the impact tests. The jig is (theoretically) capable of a maximum impact energy of 16J – please see Appendices B and C for information on jig set-up and instrument calibration. The energy levels thus chosen for the impact tests were originally 4J (selected to be just over the threshold for barely-visible impact damage established by Zhou & Hill [17] for a very similar panel configuration), 10J and 16J. A forth configuration, impacting the panels at 7J was later added after initial testing showed extremely deep damage for the 16J impacts – the hammer became stuck in the asymmetric panel - with a broadly similar form to the 10J impact. This intermediate value, it was felt, would be more useful to the exercise, as the model is not intended to simulate very severe impact damage where the panel is nearly fully penetrated, with no further tests performed using the 16J energy level.

The impact test uses a ‘picture frame’ support fixture. This produces an ‘impact window’, giving an unsupported region of panel which is clamped around the periphery, with dimensions of 125 x 75 mm, aligned with the longer dimension parallel to the length of the panel. A hemispherical indenter, ø16 mm, is used as the impact tip. This set-up is broadly in accordance with ASTM D7136 [162], which is intended for drop-weight impact testing of monolithic composite plates. Table 3 gives the measured damage extents from both the impact and quasi-static indentation tests. Figure 23 shows the pendulum impact jig and Figure 24 shows the hammer in detail. Figure 25 to Figure 27 give the angle of the pendulum and the contact force on separate axes against time for various impact energies (the 16J impact test is omitted due to the very severe damaged induced, and is not considered further in this work). Note that in these figures, the initial kinetic energy and the absorbed energy can be found by considering the peaks on the left and right sides of the curve respectively. The energy can be found using this angle, and the guidance in Appendix B. The damage induced by the impact tests and the QSI tests for both panel configurations are shown in Figure 28 to Figure 31.

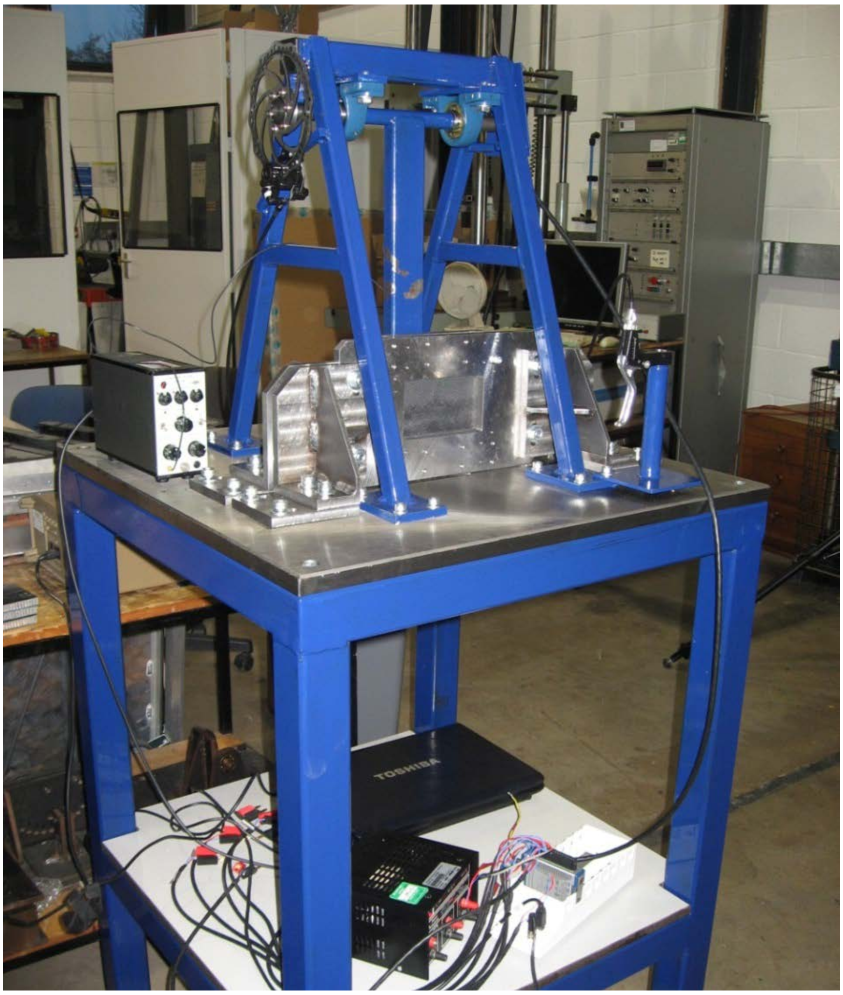

Figure 23: Pendulum impact jig

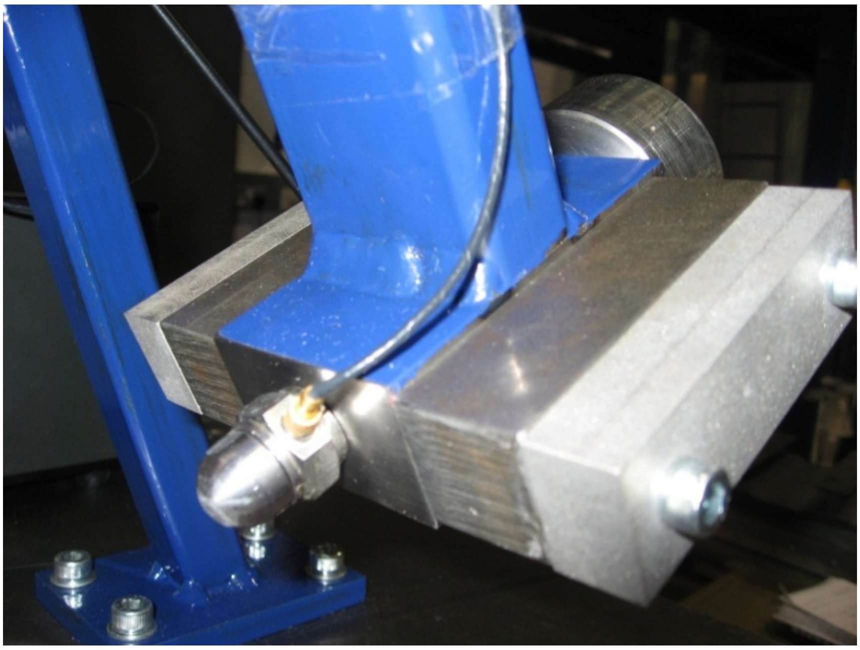

Figure 24: Hammer-head detail - the force transducer is mounted between the tip and the arm

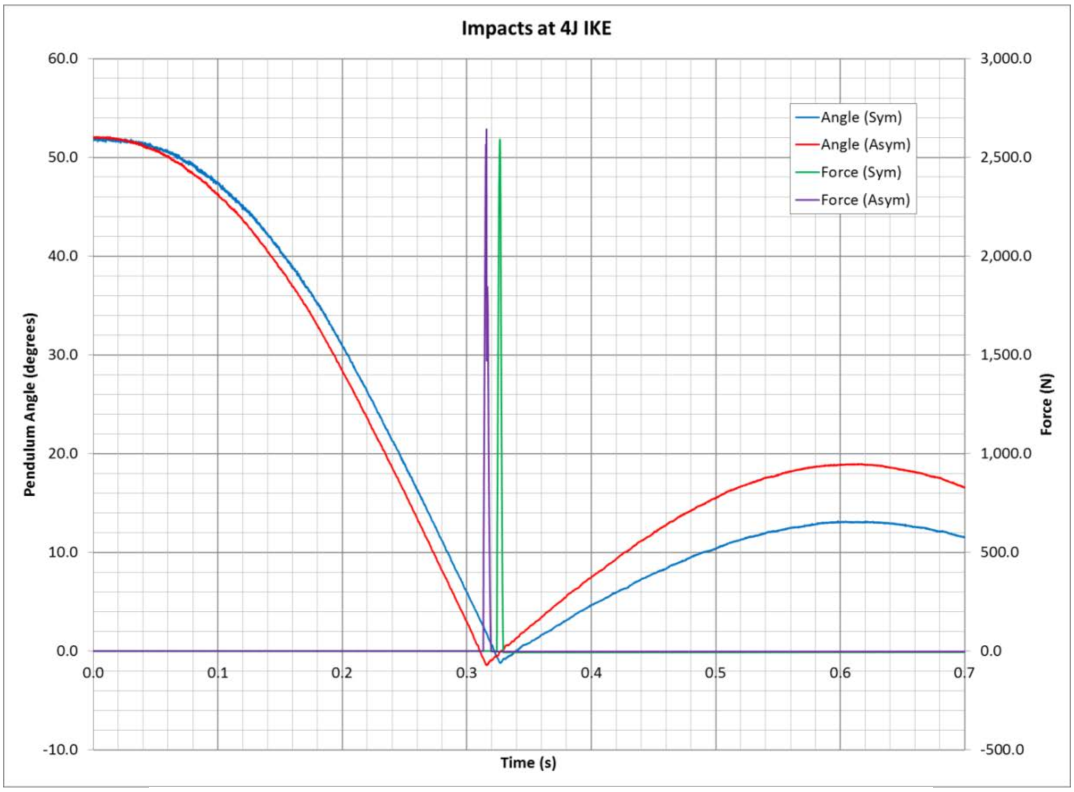

Figure 25: Angle and force curves against time for the 4J impacts on symmetric and asymmetric panels

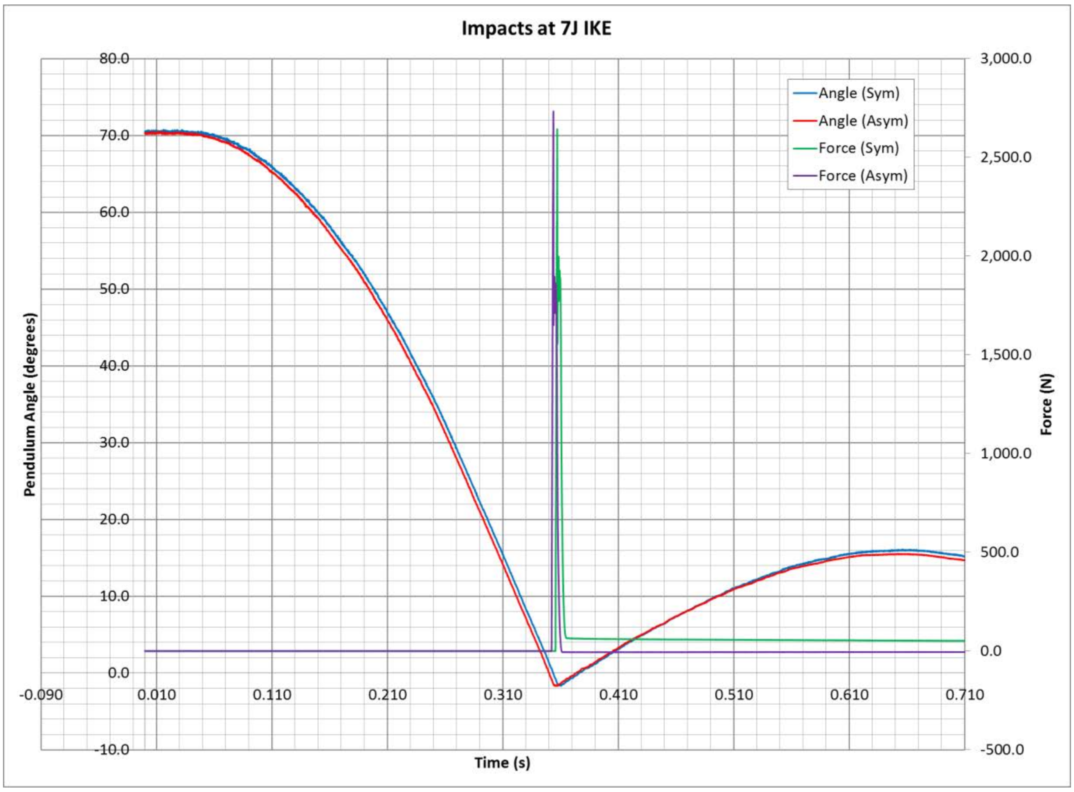

Figure 26: Angle and force curves against time for the 7J impacts on symmetric and asymmetric panels

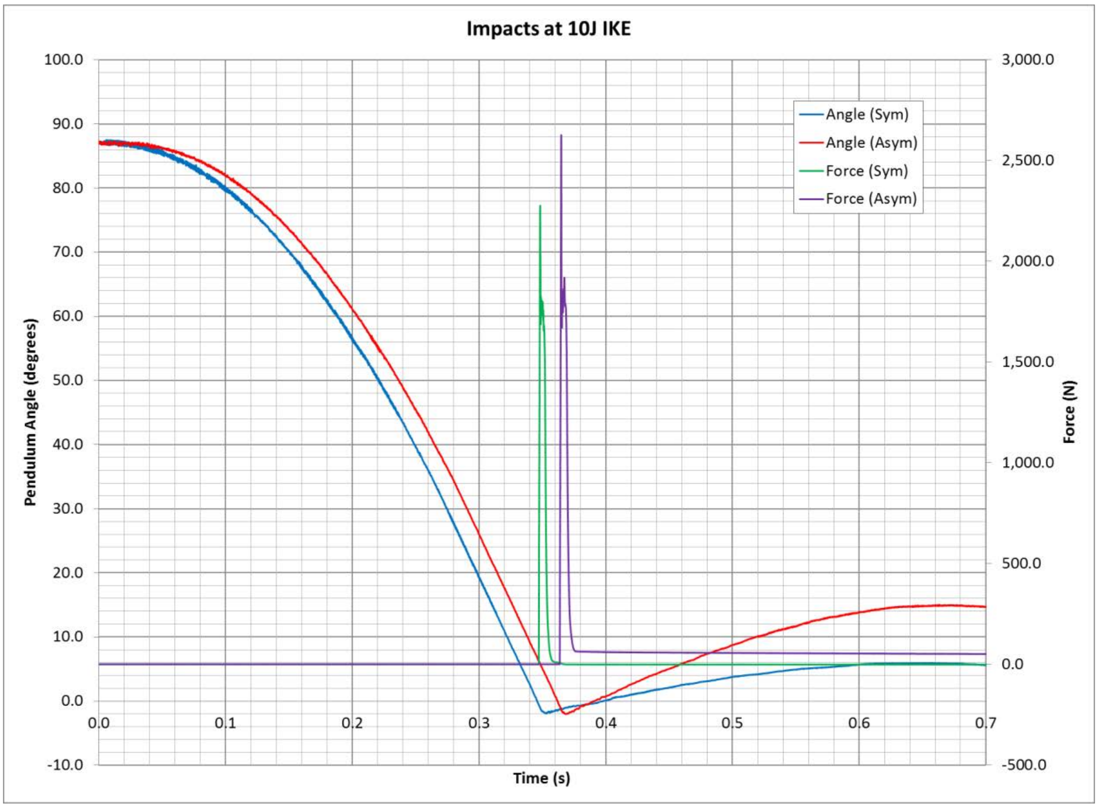

Figure 27: Angle & force curves against time for the 10J impacts on symmetric and asymmetric panels

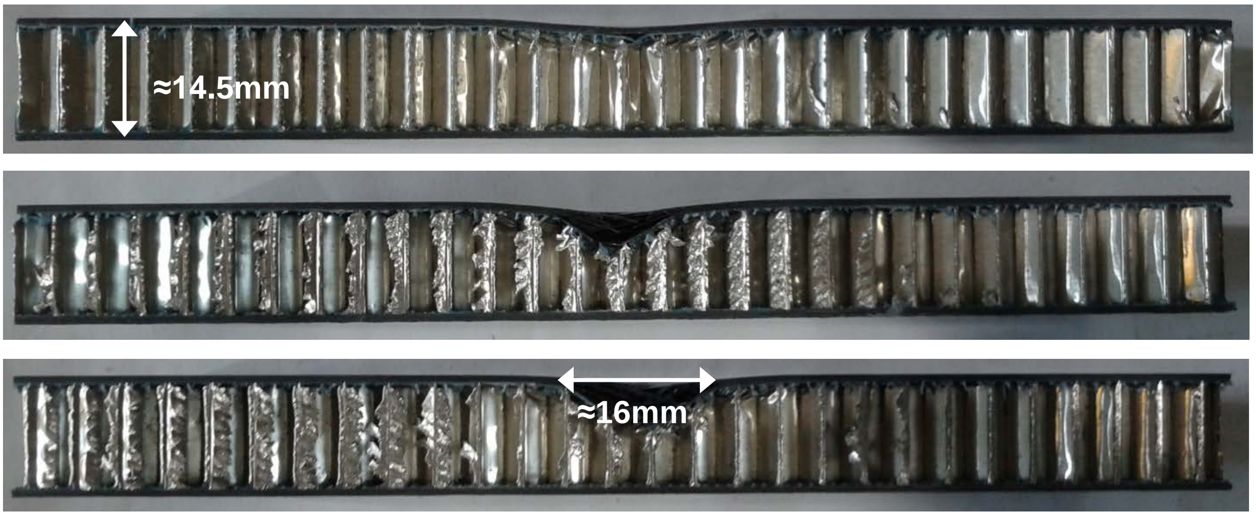

Figure 28: Sectioned symmetric panels after impact (from top) a) 4J, b) 7J, c) 10J initial kinetic energy

Figure 29: Sectioned symmetric panels after quasi-static-indentation (from top) a) 2.5mm, b) 5mm, c) 7mm applied displacement [2]

Figure 30: Sectioned asymmetric panels after impact (from top) a) 4J, b) 7J, c) 10J initial kinetic energy

Figure 31: Sectioned asymmetric panels after quasi-static-indentation (from top) a) 2.5mm, b) 5mm, c) 7mm applied displacement

Table 3: Measured damage magnitudes for skin damage and core crushing, for various impact and quasi-static indention tests

		P_{max} (N)		ø$_{dent}$ (mm)		ø$_{core}$ (mm)		d_{dent} (mm)		d_{fibre} (mm)		d_{core} (mm)	
		S	**A**	**S**	**A**	**S**	**A**	**S**	**A**	**S**	**A**	**S**	**A**
Impact IKE (J)	4	2592	2636	40	40	35	35	1	1.5	-	-	5	8
	7	2632	2733	40	40	37	37	2	2	5.5	6	7	7
	10	2276	2621	40	40	37	37	2	2	7	7.5	7	8.5
QSI Applied dent (mm)	2.5	2202	2307	40	37	37	35	1	1	-	-	5	5
	5	2909	2391	45	42	42	37	2	2	5.5	6	6.5	7
	7	3057	2528	50	40	45	39	2.5	2.5	8.5	8.5	9.5	12

Following the impact tests, quasi-static indentation tests were performed to try and approximate the results of the impact tests. The differing impact energy levels all gave a broadly similar peak force, due to the formation of damage in the skin (which on the damaged side is identical for both configurations, along with the core thickness and density), so the quasi-static indentation tests were performed under displacement control. The metric used for the applied displacement is the depth of the observed skin damage, as measured from the back face of the impacted skin on the sectioned panels (this is not to be confused with the dent depth indicated in Table 3, which measures from the flat surface of the panel to the exposed side of the dent). So, the applied displacements were 2.5mm, 5mm and 7mm, corresponding with the 4J, 7J and 10J impacts respectively. Note that there is no skin damage with the 4J impact, so the 2.5mm applied dent is an estimate whereby the average dent depth in the symmetric and asymmetric panels (considered comparable due to the identical impacted skin) is doubled, accounting for elastic strain recovery upon unloading. The peak impact force is not markedly different for the different impact energies or panel configurations, due to fibre fracture in the skin at the higher impact energies. The rebound energy of all the tests is around 0.5J for all tests, falling to less than 0.1J for the symmetric panel at 10J IKE. This indicates that most of the impact energy is being absorbed by the panel, with core crushing accounting for most of this absorption. The key trend here is that as the impact energy increases, the core crushing increases, as this is the primary energy absorption mechanism.

For the indentation tests, a load rate of 5mm/s is used, comparable with Lloyd’s quasi-static indentation tests on composite plates [163]. The same fixture and indenter is used for the quasi-static indentation test, to provide a direct comparison between the two approaches, though it must be noted that, as a result, the procedure deviates significantly from ASTM D6264 [164], for the quasi-static indentation of composite plates. However, in lieu of a standard for the indentation of sandwich panels, the method described here is an acceptable compromise that provides a good approximation of the impact event. Figure 32 shows the machine used for these tests, with the support fixture in place. Figure 33 shows close-up view of a test-in-progress.

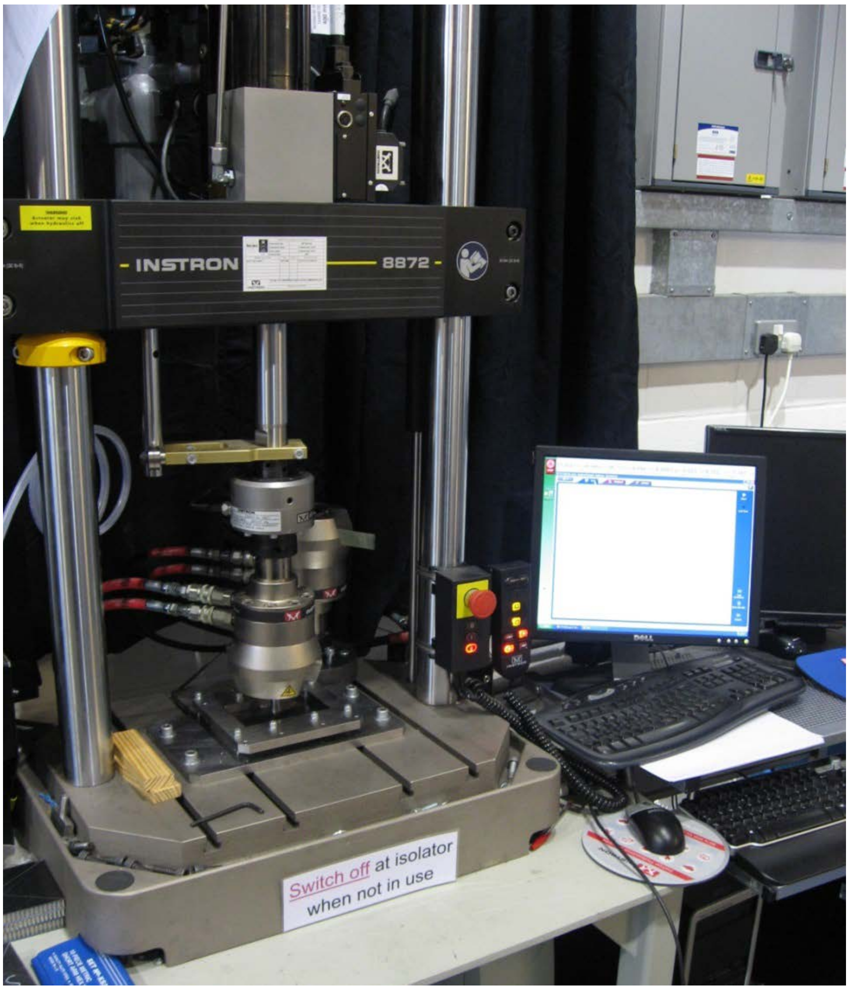

Figure 32: Instron 8872 testing machine ready to perform a quasi-static indentation test on a panel [2]

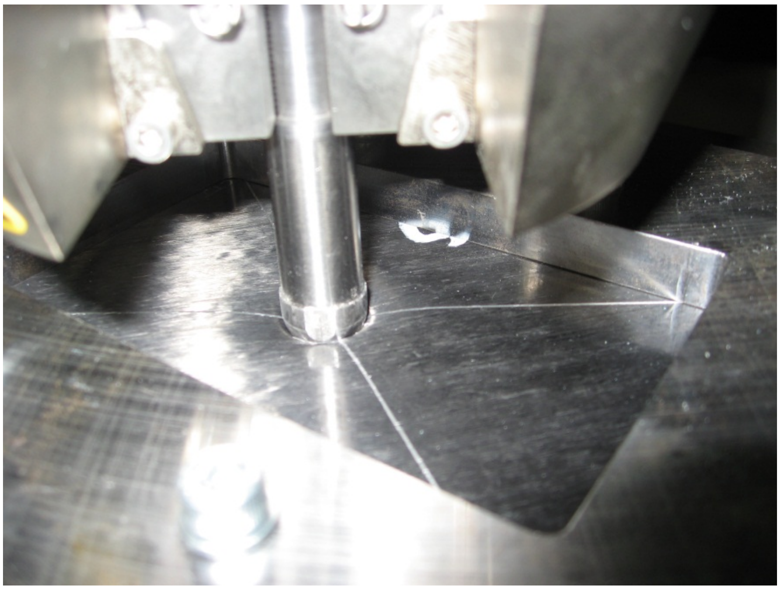

Figure 33: Close-up of a quasi-static indentation test in progress

From the force-displacement plots of the quasi-static indentation tests, shown in Figure 34 for the symmetric panel tests and Figure 35 for the asymmetric panel tests, one can see that the symmetric and asymmetric panels show slightly different responses, with the symmetric panels achieving a higher damage threshold force, followed by a sharper load drop, whereas the asymmetric panels exhibit a plateau at peak load before the load drop. The load drop in both cases is caused by fibre failure in the top skin, with the peak load plateau in the asymmetric panels prior to this (presumably) being due to delamination formation – however, this would need to be confirmed by additional testing using non-destructive imaging techniques, which weren't available for use in this project. The difference in these responses is due to the higher bending stiffness of the symmetric panel, which has the thicker distal skin.

The constant load plateau after fibre failure is due to progressive core crushing. The core crushing load is around 1750 N for all panels. This is expected, as the only difference in the configurations relates to the distal skin, which remains unaffected in these tests. The 2.5mm applied indentation cases are exceptions here, as damage is not created for such a small indentation. The QSI tests tend to generate higher forces before damage creation in the symmetric panels, and lower for the asymmetric panels, than the equivalent impact tests. Additionally, the force is lower for both of the 2.5mm indentation tests than the 4J impact test. The lack of inertial effects in the quasi-static indentation tests explains this discrepancy. However, the difference is not overly significant, and as with the impact tests, fibre fracture in the top skin does seem to impose a limit on the maximum load.

The primary purpose of the damage characterisation study is to confirm that the quasi-static indentation used in the CAI experiments and the numerical model produces a damage state representative of low-energy impact. Thus, comparison of the measured damage sizes (see Table 3) show that the quasi-static indentation tests produce a reasonable approximation of the low-energy impact tests. The main difference is in the diameter of the dent, and thus also the core damage, in the quasi-static indentation tests, due to the load being distributed over a greater area. The depth of core damage is also greater, presumably as the core absorbs more energy under the lower rate of loading. The magnitude of the damage, particularly the dent depths and extent of fibre fracture, is very similar for both tests. In all metrics, the agreement between impact and QSI degrades as the energy increases, due to the increasing contribution of inertial effects to the panel response. Destructive sectioning of the 2.5mm panels show no obvious skin damage, only core crushing. Non-destructive imaging of the panels may reveal damage (particularly delamination) that isn't readily visible, but it is not inconceivable to imagine that, should the impacted skin be separated from the crushed core, that it would recover its usual, flat shape. As far as a thorough damage characterisation study goes, a more focussed, dedicated effort that expands on the investigation presented here would need to be performed, since insufficient data has been generated to make any additional conclusions beyond those already offered.

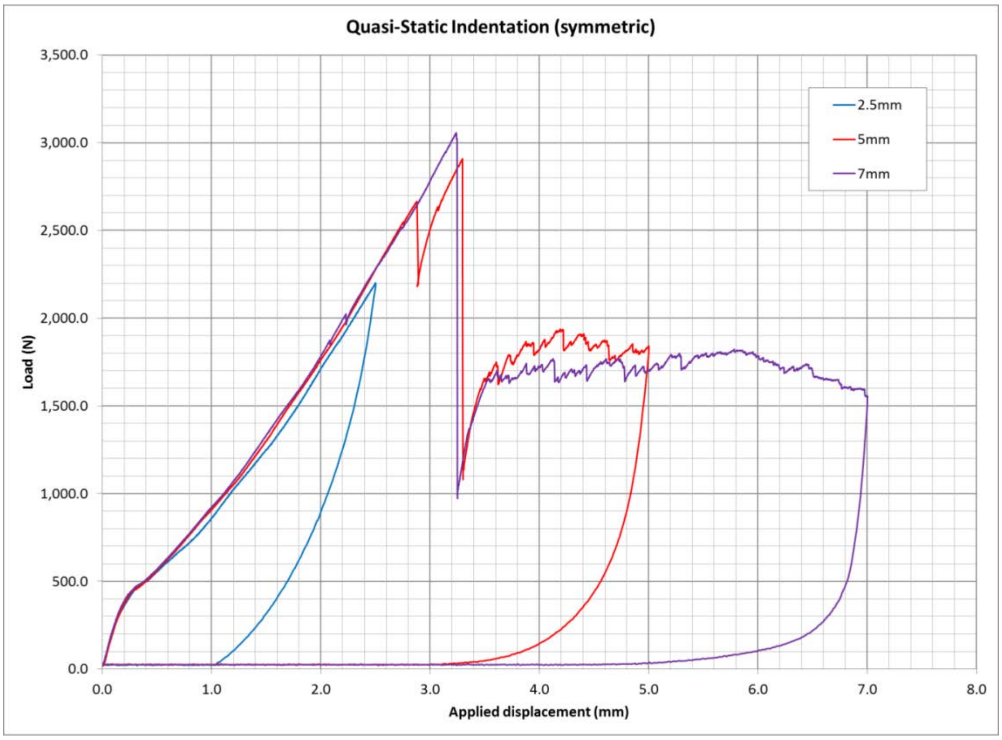

Figure 34: Force-displacement plot for the quasi-static indentation tests performed on symmetric panels

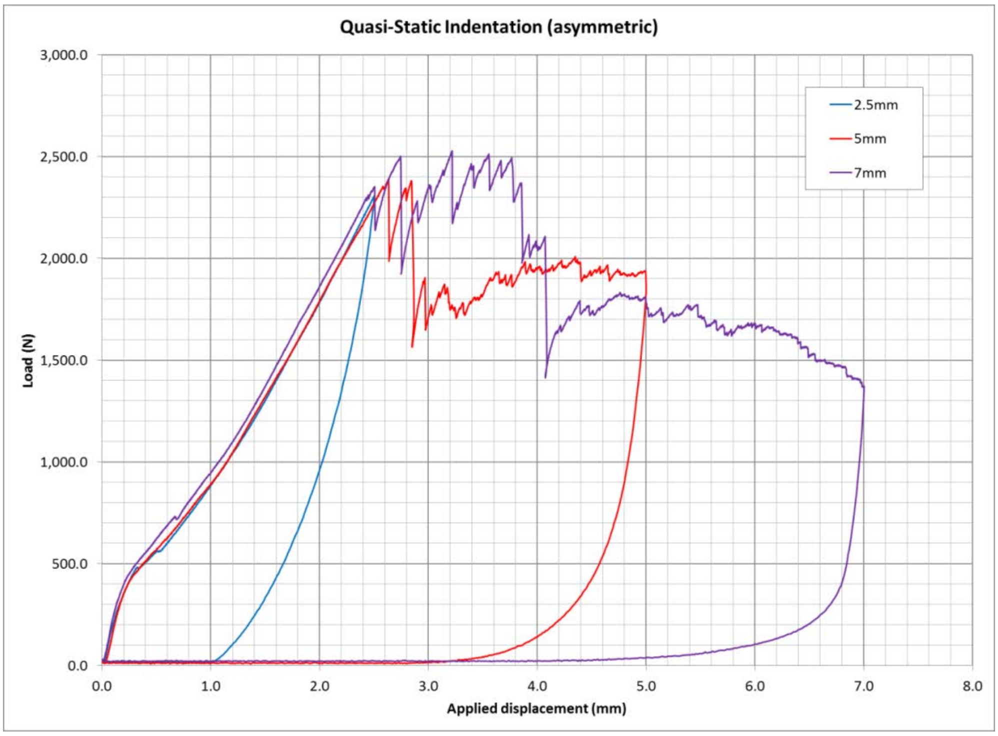

Figure 35: Force-displacement plot for the quasi-static indentation tests performed on asymmetric panels

3.3: Compression-after-Impact (CAI) Tests

The main experimental effort went into performing compression-after-impact tests on indented sandwich panels. The required indentations were induced in the panels using the same procedure described for the quasi-static indentation damage characterisation tests. There is no standard method for the CAI testing of sandwich panels, so for this study, a modified version of ASTM D7137 [38] for the CAI testing of monolithic composite plates is used, with the panel support jig design being slightly altered to accommodate the thicker panel. This approach was chosen rather than using a modification of ASTM C364 [39], which is the standard edge compression test for undamaged sandwich panels, since the latter approach does not includes support for the unloaded edges of the panel, which in turn makes the panel vulnerable to failure via global buckling. The load was applied in an Instron 5500R universal testing machine. A spherical bearing was used to provide self-alignment during load application, reducing the risk of inducing unwanted bending moments. The fixture is shown fitted to the machine, with a panel inside, in Figure 36. The majority of tests only collected force-displacement data, using a 100 kN load cell mounted behind the spherical bearing unit on the jig (the large cylindrical section seen at the top of Figure 36). The weight of the bearing unit hanging from the load cell (and thus resting on top of the panel prior to load application) has to be accounted for in the calculations; a correction of 49.2N is thus added to all of the force data. A small number of panels were also strain gauged, to give an indication of the bending moment in the panels under compression, as previously stated.

A single 'control' test was performed prior to testing the panels proper, to find the displacement of the fixture itself under loading. This makes it possible to correct for the displacement of the fixture when finding the strain-to-failure and stiffness of the panels. By assuming a simple linear relationship from the origin to the peak load (thus eliminating the non-linearity due to bedding-in during this test, which if not accounted would also result in an over-estimate for panel displacement), the corrected displacement for a panel is found to be:

$$\delta_{panel} = \delta_{total} - (1.4661e^{-5}P)$$

(25)

This correction is applied to all displacement data to ensure a representative stress-strain curve, with the displacement given in mm and the load given in Newtons. An abridged table of results is presented in Table 4. Please refer to Appendices D and E for a comprehensive set of data for symmetric and asymmetric panels respectively. Note that a small number of panels failed via brooming at the ends. These are treated as invalid results and are disregarded in the calculation of the mean results – these results are marked in red in the appendices. All load, strength, strain and stiffness results are compressive. The peak indentation force is also included in the results (the average value given here includes the forces found in the damage characterisation study, which are not quoted in the raw results).

Figure 36: A panel loaded into the compression-after-impact support fixture, ready for testing [2]

Table 4: Abridged table of results from the compression-after-impact tests [2]

Panel	Applied dent (mm)	Mean peak indentation load (kN)	Mean peak CAI load (kN)	Mean CAI strength (MPa) *(range)*		Mean residual strength (%)	Mean strain at failure (%)	Mean Youngs Modulus (GPa)	Typical failure mode and location
SV	0	-	45.06	**259.9**	-38.1 +36.1	-	1.27	31.19	D, E
S2.5	2.5	2.22	42.10	**245.4**	-47.7 +55.7	94.4	1.20	29.24	D, E
S5	5	2.92	37.98	**219.8**	-10.2 +10.8	84.6	1.02	29.33	K, C
S7	7	2.93	34.92	**204.3**	-11.0 +11.1	78.6	0.98	28.04	K, C
AV	0	-	36.37	**239.9**	-71.2 +35.1	-	1.18	29.79	K, E
A2.5	2.5	2.26	38.50	**254.7**	-27.2 +31.1	106.2	1.04	30.42	K, E
A5	5	2.54	33.08	**216.2**	-22.3 +14.8	90.1	0.97	29.58	K, C
A7	7	2.66	31.06	**206.6**	-17.9 +24.5	86.1	0.91	30.14	K, C

Failure codes: K = kink-band, D = delamination buckling
E = near-end, C = center

The results for the symmetric panels show a clear reduction in compressive strength with increasing dent depth, as expected. The failure mode switches to kink-band formation for the 5mm and 7mm indentations, as the localised fibre fracture induced by these events creates an obvious weak-point from which damage propagation can originate (note that the 2.5mm indentation events only result in a permanent dent, with no obvious damage being induced). The peak indentation load is limited by the bending strength of the upper skin, hence the very similar maximum load between the 5mm and 7mm indentation cases, though it must be noted that there is notable variation in the indentation load once skin damage starts to form, due to the unpredictable nature of precisely when fibre damage forms. A similar, but weaker trend is shown for the asymmetric panels, with reduced peak indentation load due to the slightly reduced global bending stiffness of the asymmetric panels. Examples of delamination buckling and kink-band failures are shown in Figure 37, for symmetric panels. The displayed failure modes are representative of their type for both panel configurations.

The inclusion of asymmetry in the panel has a profound influence on the CAI strength. As expected, the virgin panels show reduced strength as compared to the symmetric panels, which are identical aside from the slightly thicker distal skin on the symmetric panels. This difference is due to a stiffness imbalance which allows for the formation of additional bending moments in the asymmetric panels during the compressive loading. However, when

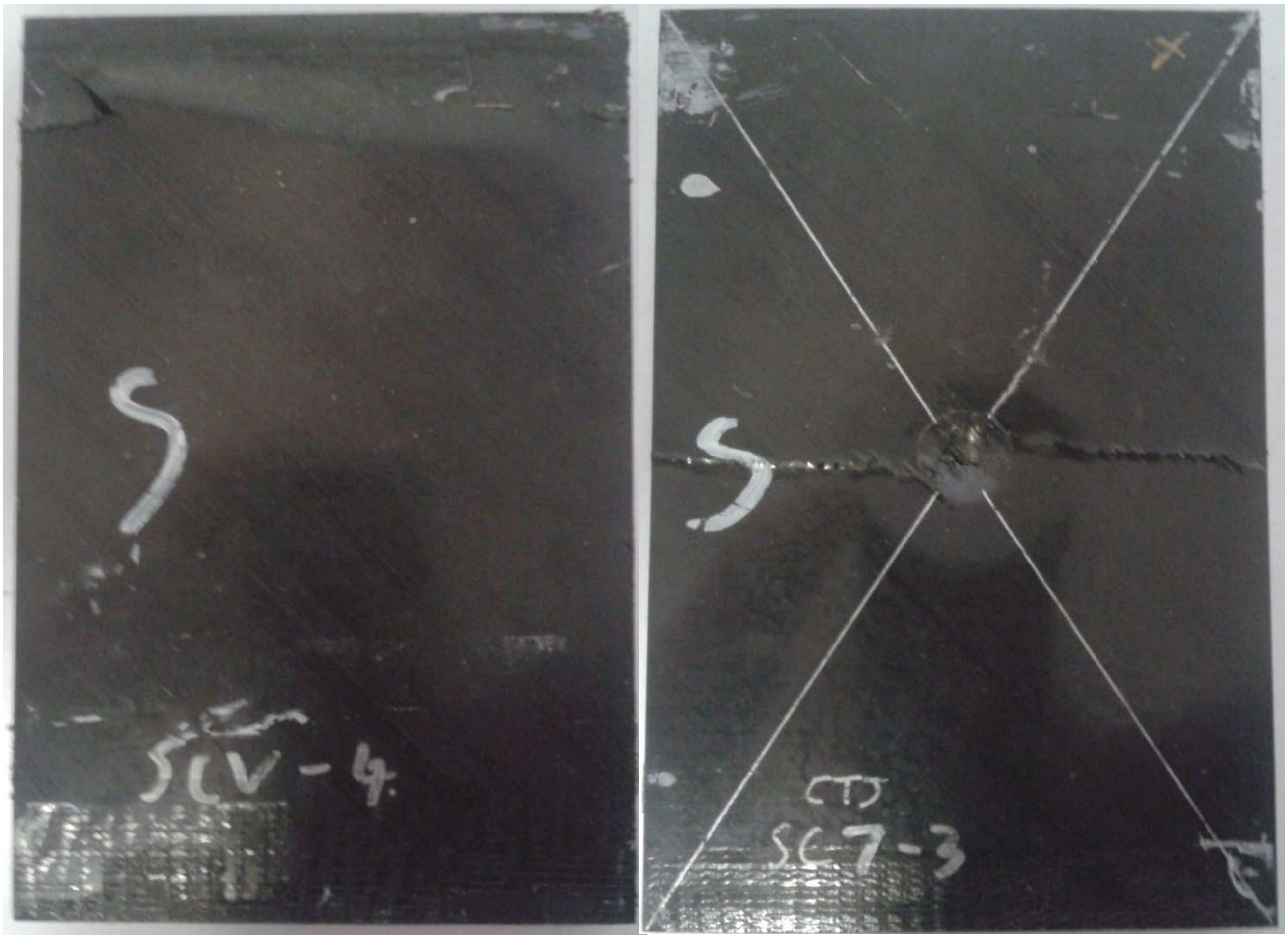

Figure 37: Failure of sandwich panels a) (left) delamination buckle towards the top end of the panel, b) (right) kink-band propagation originating from the damaged region [2]

a small dent is produced (*A2.5*), the average compressive strength actually becomes greater than the virgin strength, as the instability produced by the dent negates the instability due to the stiffness imbalance between the impacted and distal skins. This agrees with the findings of Zhou et al [24]. Of further interest is that the strength of the *A2.5* panels is on average only marginally lower than the strength of the ‘virgin’ (undamaged) symmetric panels (*SV*). This finding may have very interesting implications in terms of design efficiency; if it were possible to induce mild geometric imbalances in a repeatable manner, it might be possible to produce more efficient structures by reducing the amount of material required in their construction. However, it should be noted that the absolute load-carrying capacity of the asymmetric panels is lower than the symmetric panels at all damage levels, due to the lower overall cross-sectional area of these panels. The strain-at-failure reduces for both configurations with increasing damage.

To illustrate this effect, a simple analysis is performed to calculate the stresses on the impacted and distal faces for these panels, accounting only for the geometric differences of the two panels. For a beam under axial compression, when the compressive load is applied on a line offset by a distance of e from the centroid of the beam, the stress at a location y on the beam is given by [165]:

$$\sigma_y = \frac{P_x}{A} + \frac{P_x e y}{I_x}$$

(26)

Where:

P_x = axial compressive load in the x-direction (N)
A = cross-sectional area of the beam (m^2)
I_x = moment of inertia (m^4)

In the case of the sandwich panel, the beam is assumed to comprise only of the two skins, separated by 12.7mm. The gap represents the core, which is assumed to have no other contribution to the behaviour of the beam (obviously, this is not true in reality, but the analysis illustrates the effect of asymmetry adequately despite this simplification). The skins are assumed to be made of 6 or 8 plies (orientation irrelevant) for the asymmetric and symmetric skins respectively, with a ply thickness of 0.103mm, and a width of 100mm, representing the perfect nominal case. The geometry of the beam is illustrated in Figure 38. Note that the first term on the left-hand side of this equation is the elementary expression for axial stress, with the second term providing the stress due to the bending moment induced by the eccentricity of the axial load. The moment of inertia for the beam is given by:

$$I_x = \sum (I_i + h^2 A)$$

(27)

This is the sum of moment of inertias of the sections that make up the beam, in this case, the two rectangular sections of the skins. Thus:

$$I_i = \frac{bd^3}{12}$$

(28)

h is the distance between the centroid of a given section $\bar{y}$ (which for this structure is the geometric centre of each section relative to the stated origin, which in this case is the bottom of the impacted skin, see Figure 38) to the centroid of the structure $\bar{Y}$. The centroid of the structure, also relative to the origin is given by:

$$\bar{Y} = \frac{\sum \bar{y} A}{\sum A}$$

(29)

with $\bar{y}A$ being calculated for each section in the structure. Note that the location y is also found relative to the structural centroid $\bar{Y}$. Finally, the offset of the axial load can be found, by finding the difference between the structural centroid and the geometric centre of the beam. With this information, results can be calculated for four cases: virgin and damaged symmetric and asymmetric panels. For simplicity, damage is assumed to create an open hole in the impacted skin of ø16mm, broadly analogous to the 5mm and 7mm indentation cases performed in the experiments, though obviously neglecting stiffness degradation, core damage, and geometric non-linearity induced in the skin at the periphery of the damage. This, at its most basic, reduces the cross-sectional area of this skin. The load P_x is assumed to be 1kN for all cases.

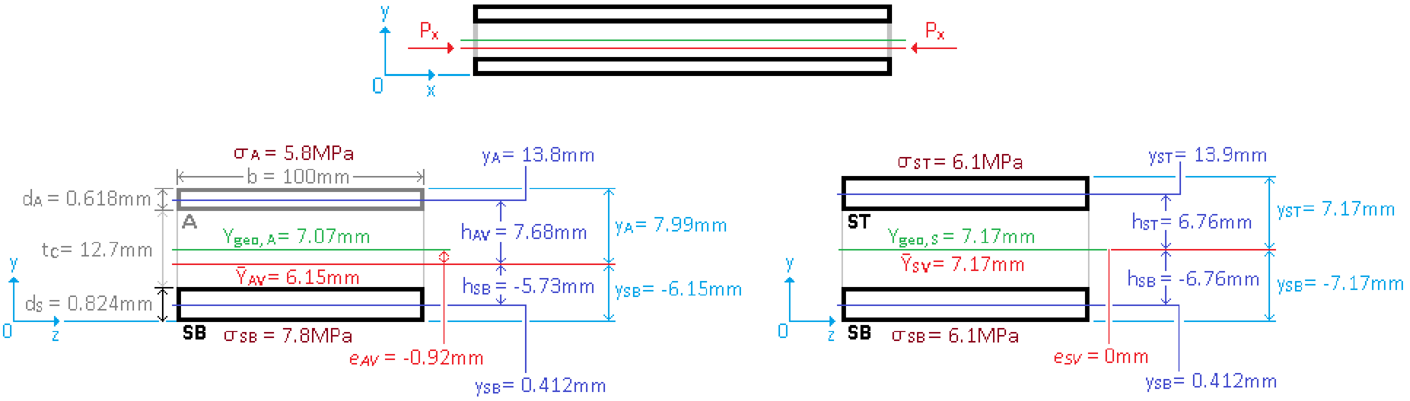

Figure 38: Stress analysis of undamaged sandwich beams: a) (top) loading direction, b) (left) asymmetric panel, c) (right) symmetric panel

For the virgin panels, the offset e between the geometric centre and the centroid of the asymmetric panel is approximately 0.9mm towards the 'impacted' (thicker) face due to the stiffness imbalance caused by the thinner skin, whereas there is no offset on the symmetric panel, as expected. This results in stresses of 5.8MPa and 7.8MPa on the thinner and thicker skins of the asymmetric panel respectively – for a difference of 2MPa, with the offset biasing the stress distribution so that the surface closest to the centroid (the stiffer skin) experiences greater stress. Each skin on the symmetric panel experiences approximately 6MPa. This is illustrated in Figure 38.

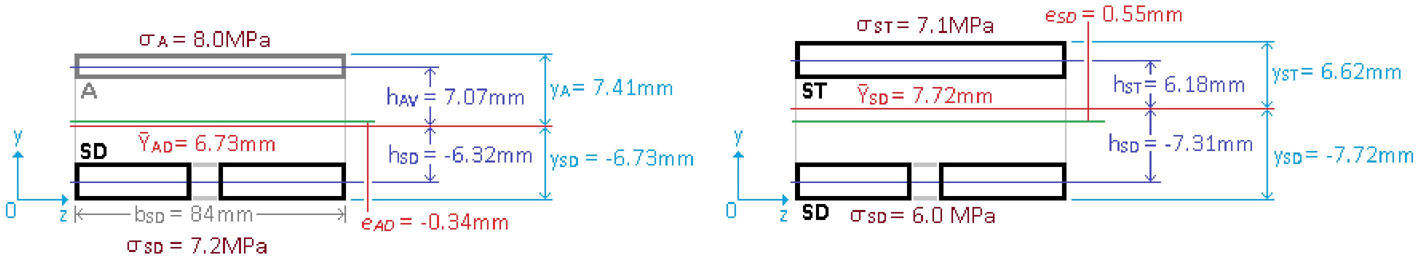

Figure 39: Stress analysis of damaged sandwich beams (a) (left) asymmetric panel, b) (right) symmetric panel

When damage is induced, the offset in the asymmetric panel is reduced to 0.3mm towards the impacted face, and the symmetric panel exhibits an offset of 0.6mm towards the undamaged distal face. This supports the conclusion that the damage removes some of the existing instability in the asymmetric panel, as the stiffness of the thicker skin is reduced with damage, reducing the offset of the centroid and thus improving post-damage performance. The stress in the damaged asymmetric panel is now 7.2MPa and 8.0MPa on the thinner and thicker skins respectively (a difference of 0.9MPa, half that of the undamaged asymmetric case). In the damaged symmetric panel, the stresses on the impacted and distal skins are 6MPa and 7.1MPa respectively, for a difference of 1.1MPa. This indicates an increasing instability in the symmetric panel, supporting the findings of the experiments, as the stiffness imbalance due to damage produces a case not dissimilar to the undamaged asymmetric panel. This is illustrated in Figure 39.

Obviously, as the load increases, so the skin experiencing the greater stress will fail first, all other aspects being equal. The asymmetric panels still experienced a greater peak stress compared with the symmetric panels due to the smaller overall cross-section of the asymmetric panel. Note that this is a limited analysis of the conditions created by the experiments, with the effects of lay-up, damage, geometric imperfections and the presence of the core all being neglected. This will inevitably have an effect on the failure stress and the response of the panel.

The failure modes seen for the asymmetric panels are the slightly different when compared with the symmetric panels, with the majority of panels appearing to fail via kink-band formation regardless of the amount of damage. The failure locations, however, remain the same as the symmetric panels, with the failure shifting from near the end of the panel to the centre only when fibre damage is evident in the indented skin. In the low/no damage panels, the thinner distal skin almost invariably fails first (*AV-1* being the only clear exception). The interesting thing to observe here, for the *A5* panels, is that there appears to be a degree of competition between the two failure modes for this level of damage. One panel (*A5-3*) failed at both the centre and near the end near simultaneously – it was not possible to establish in this instance which kink band controlled the ultimate failure of this particular sample. Another panel (*A5-4*), while failing via delamination buckling, was showing clear evidence of kink-band formation; in this case, the kink-band does not reach the critical length before the panel failed.

The stress-strain plots for all panels, ordered by configuration (symmetric and asymmetric) and then by damage from undamaged to maximum damage, are given in Figure 40 to Figure 47. The ‘mean’ stress-strain response of the panels, given by the green dashed line in each plot, is based on these plots, using the mean Young’s modulus and strength for each configuration presented. The mean response is idealised, removing the initial non-linear ‘bedding-in’ section of the experimental responses and any small load drops due to damage development prior to final failure, but will be useful for comparison with the numerical model results. The responses shown by a dotted line (*SV-1*, *S7-2* and *A2.5-1*) are ‘invalid’ tests that failed via end crushing, and have not been used in the calculations for the mean properties of the panels, as previously stated. The stiffness of both panel configurations remains more-or-less unaffected by the damage, with the symmetric panel showing a slight decrease in stiffness as the damage level increases; no trend is apparent for the asymmetric panels. The response of all panels remains linear up until ultimate strength, which is expected, due to the brittle nature of CFRP.

On the whole, the responses of the different panels are fairly consistent between repeat tests, but there are some notable outliers in the data, which can be clearly seen from the stress-strain plots presented here, and also in the range indicated in Table 4. *AV-1* sticks out as an especially significant outlier, showing a noticeably lower stiffness and ultimate strength when compared with its fellows. The *S2.5* tests also show a very large amount of spread, with *S2.5-1* also showing low stiffness. On the other hand, some other data sets, particularly *A7* and *S7* are remarkably consistent, most likely because the large induced damage is providing such a significant weakness that it negates the imperfection sensitivity that dogs the undamaged and moderate-damage cases. The 5mm indentation cases are also fairly consistent, for the same reason. From Table 4, the data spread at higher damage levels is smaller for the symmetric panels, perhaps due to the inherent instability of the asymmetric panels. The variation in strain-to-failure seen in all tests is an inevitable consequence of differing degrees of bedding-in required for each panel at the start of loading. This could be reduced in future test programs by the progressive application and removal of small amounts of load before proceeding into the test proper. A number of tests did exhibit subsequent load increases after the initial failure, suggesting that the distal skin was taking some more load, but as the ultimate strength had already been achieved, these tests were invariably terminated.

Strain gauge data was collected for a small number of the panels tested, and is presented in Table 5. The two critical gauges are B0 and F0, positioned at or close to the centre of the panel. By comparing the strains measured by these gauges, the amount of bending in the panel can be determined. Unfortunately, due to the very small sample size used here and the significant variation in the data, no meaningful trends can be readily observed from this data, and so no concrete conclusions can be made. Particularly, the *SV* panel appears to show greater bending than the *AV* panel, which is contrary to the expectation of the symmetric panels showing no bending at all – this particular result is most likely due to imperfections in the test of the *SV* panel. Ideally, the difference between the two gauges for *SV* should be 0, but in practice, imperfections in the loading and panel make achieving this impossible. A tenuous inference can be made by considering the results of the *S5* and *A5* gauge pairs, that the asymmetry between the impacted and distal skins is indeed negating some of the instability due to the damage, due to the lower level of bending seen in the *A5* panel, but this is by no means conclusive, due to the difficulties already stated. Further extensive testing is required to see if this effect continues at the higher damage level, and also to confirm whether the asymmetry does indeed increase the instability of the virgin panel. Time and resource constraints prevented more extensive gauging of panels for this particular study, but the results do suggest that this could be an interesting avenue for further work.

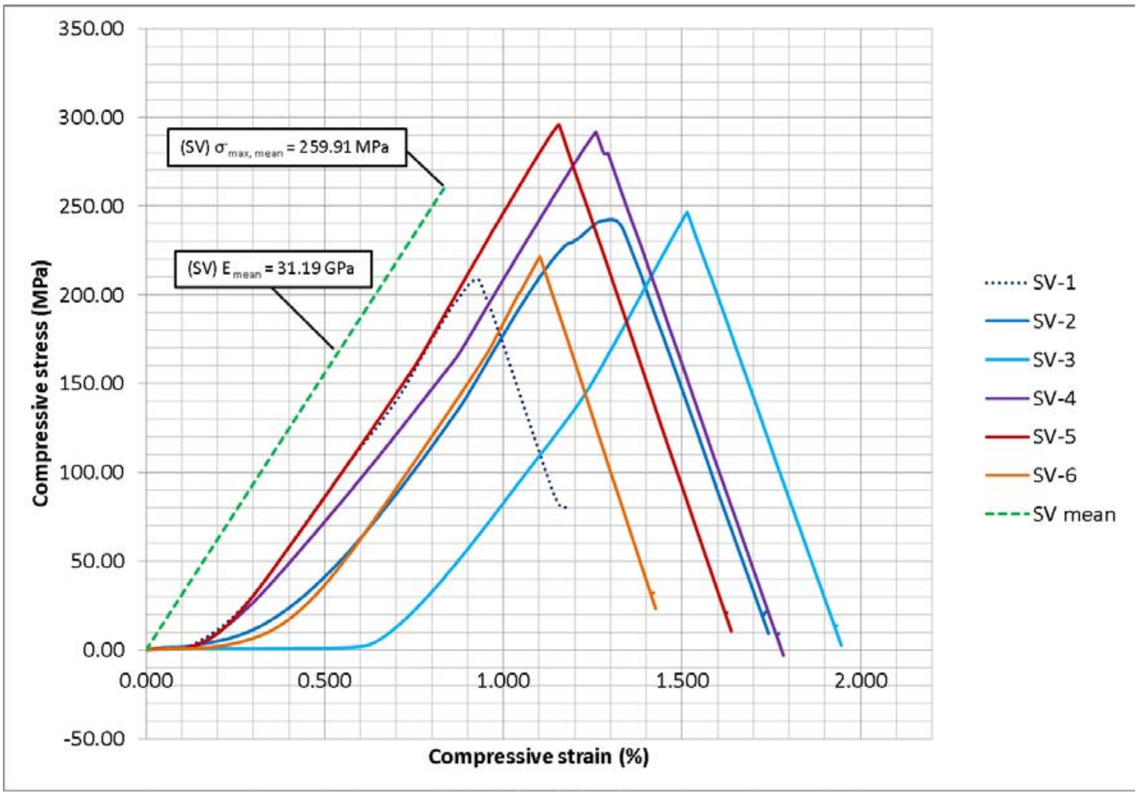

Figure 40: Stress-strain plots for undamaged symmetric panels

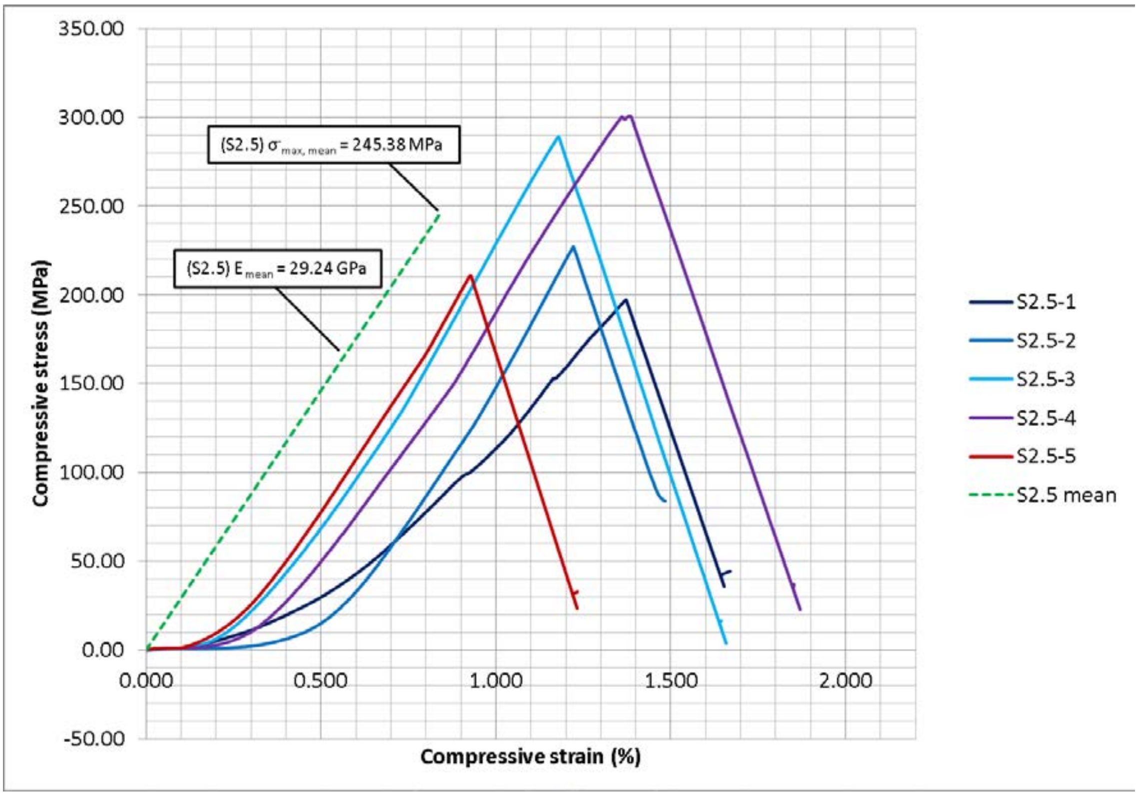

Figure 41: Stress-strain plots for damaged symmetric panels (2.5mm QSI)

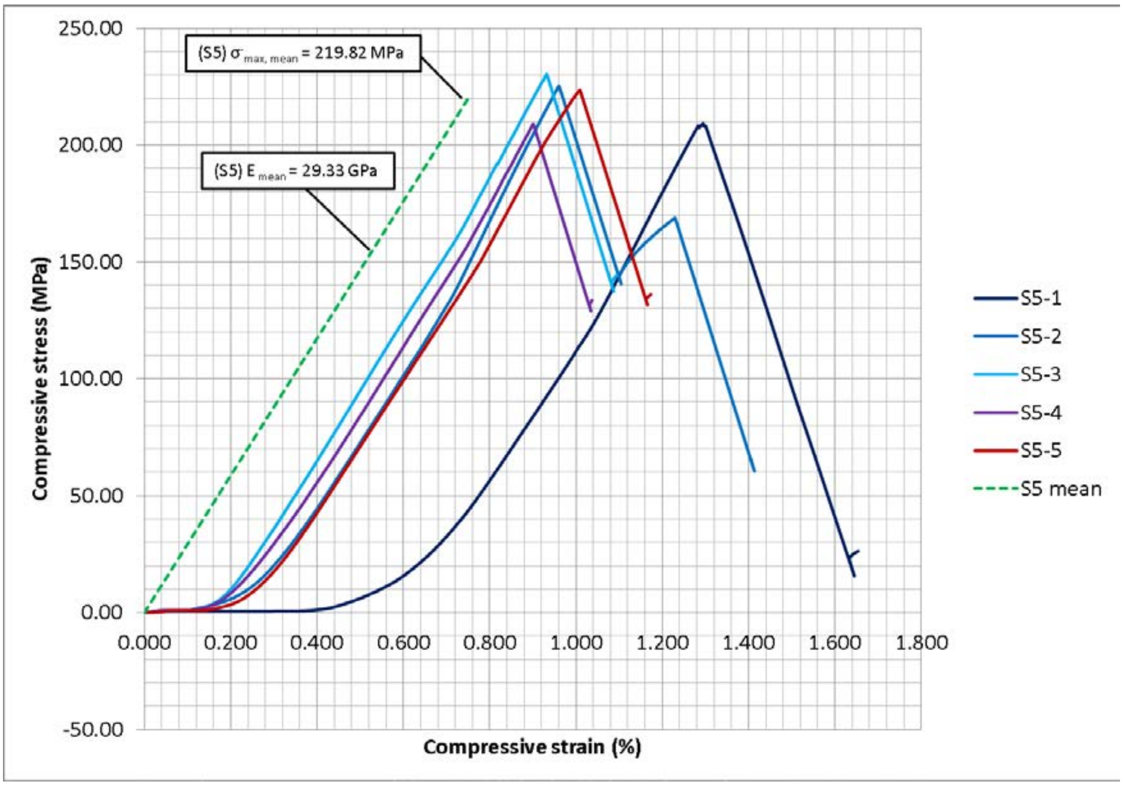

Figure 42: Stress-strain plots for damaged symmetric panels (5mm QSI)

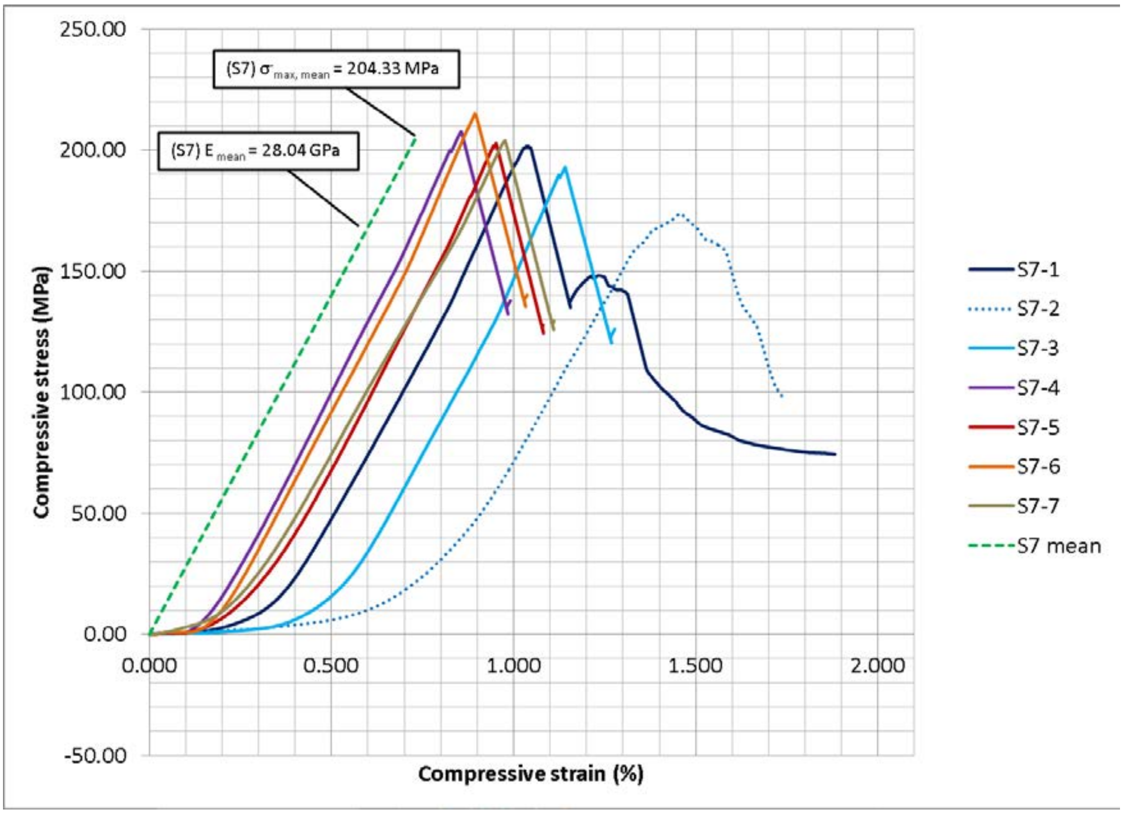

Figure 43: Stress-strain plots for damaged symmetric panels (7mm QSI)

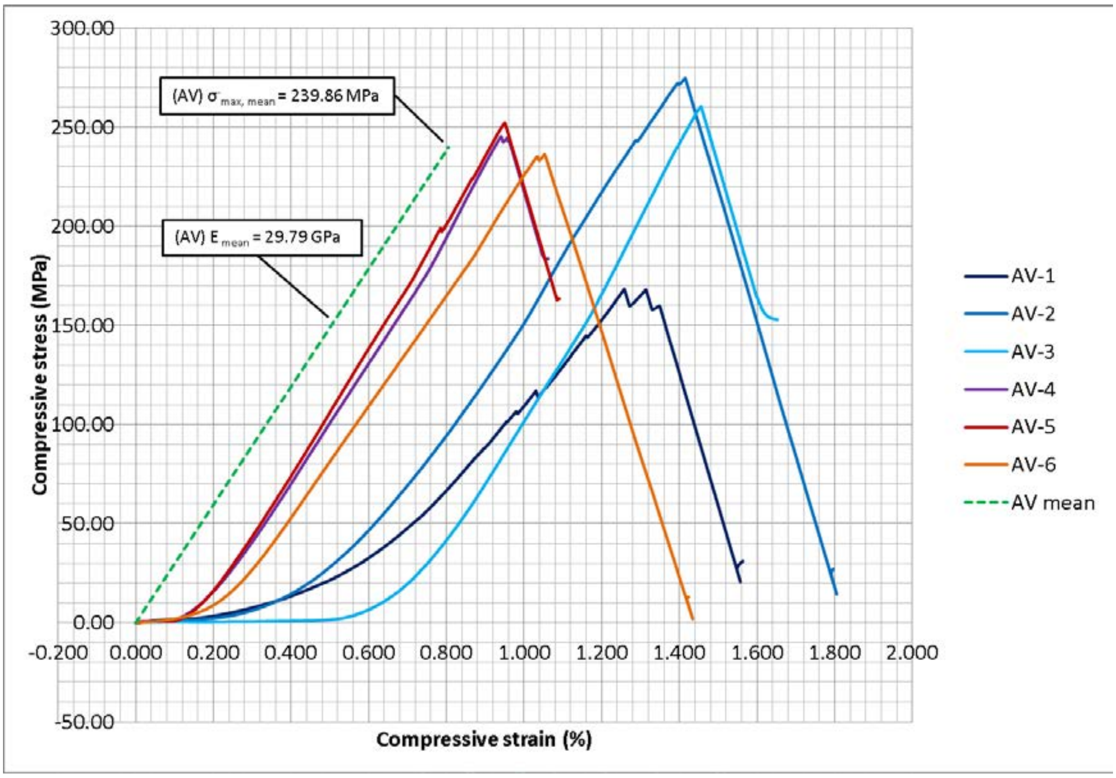

Figure 44: Stress-strain plots for undamaged asymmetric panels

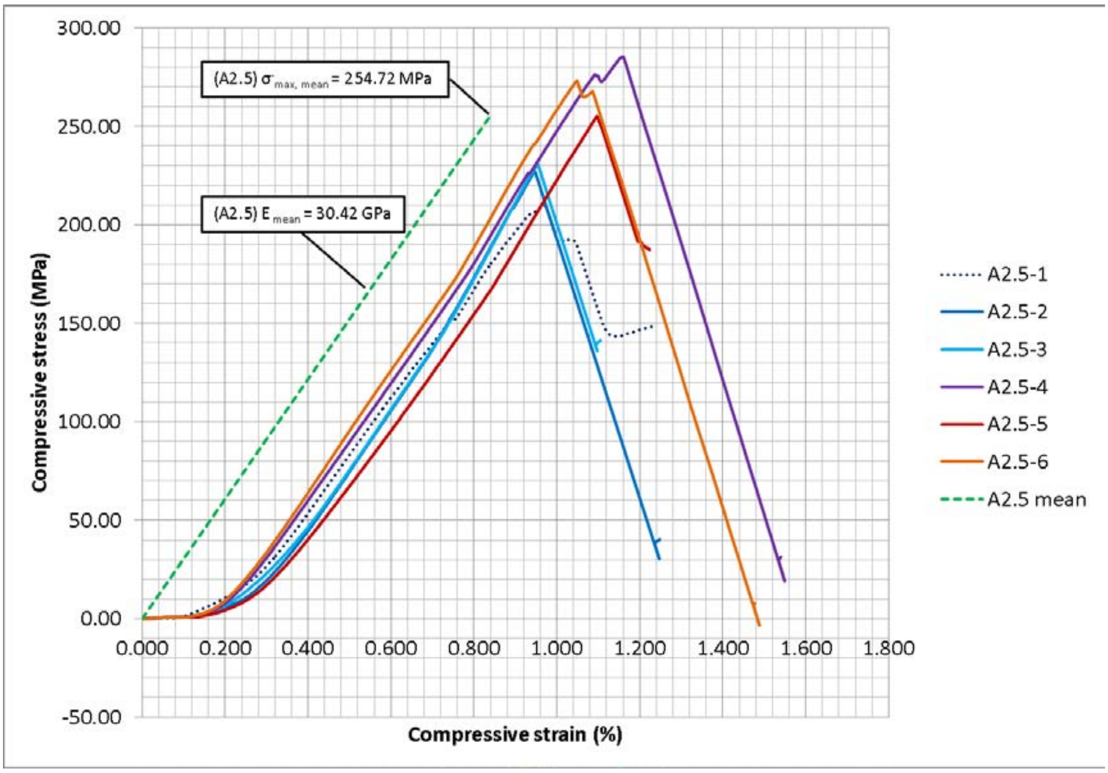

Figure 45: Stress-strain plots for damaged asymmetric panels (2.5mm QSI)

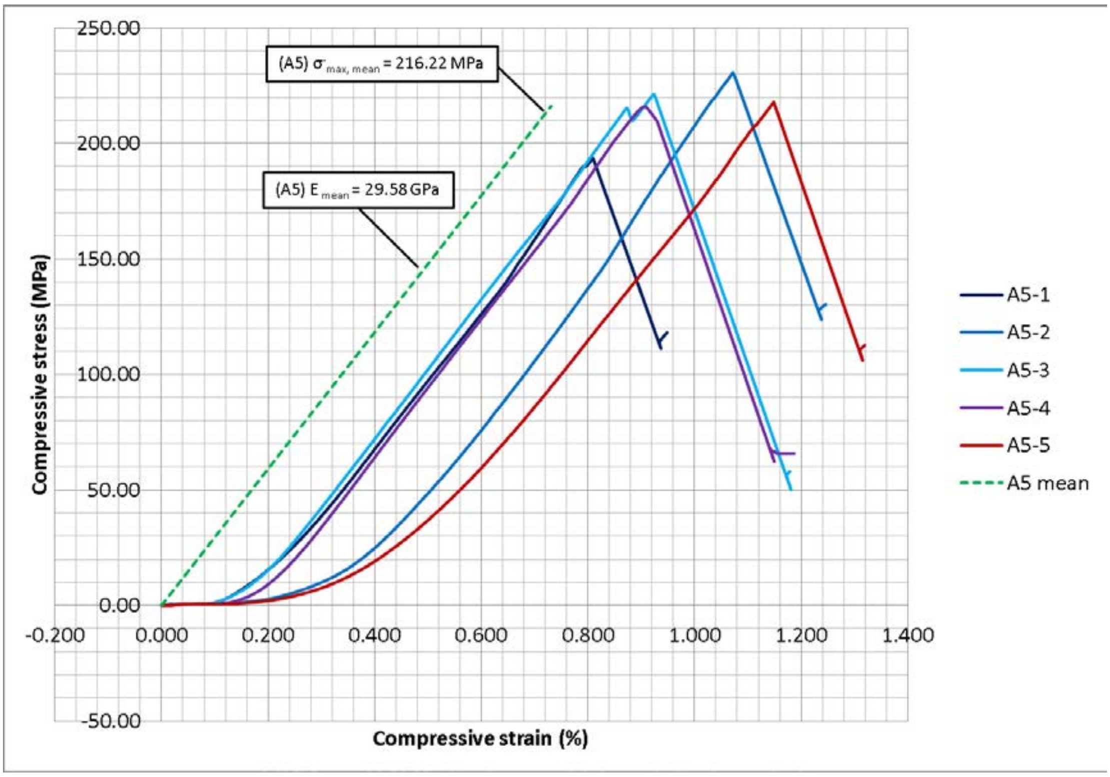

Figure 46: Stress-strain plots for damaged asymmetric panels (5mm QSI)

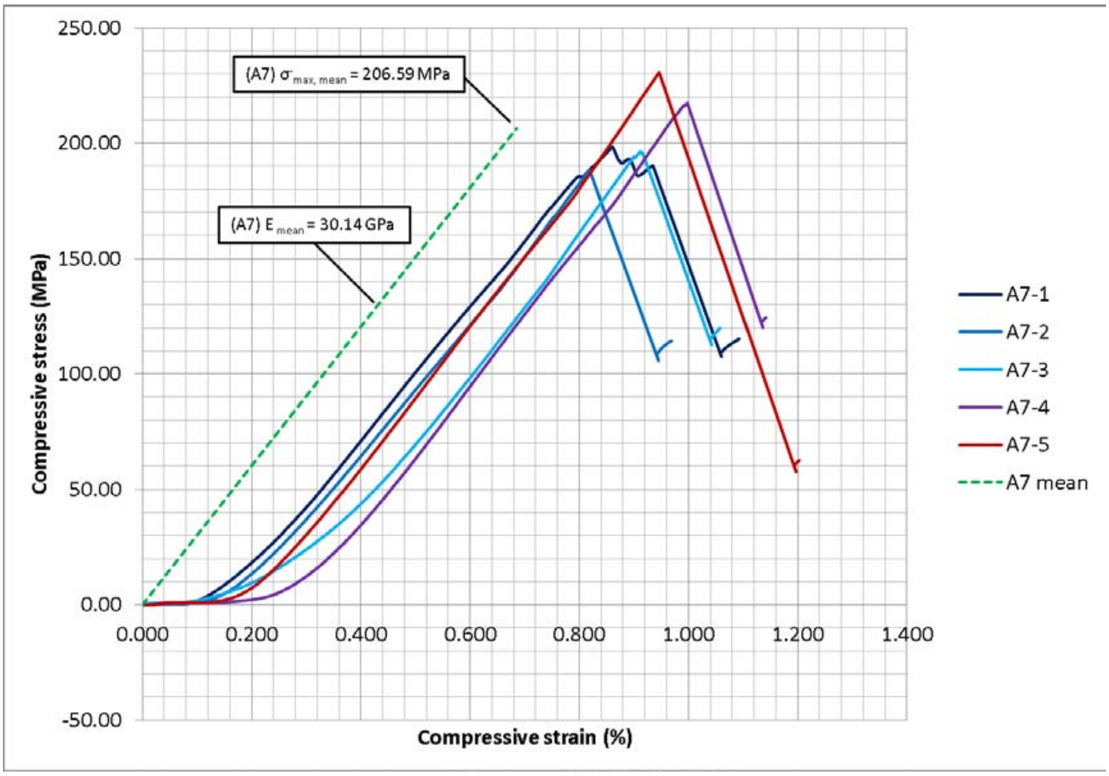

Figure 47: Stress-strain plots for damaged asymmetric panels (7mm QSI)

Taking the average of the B0 and F0 gauges provides a second estimate for the stiffness of the panels. Again, the *SV* result is rather suspect, but the remaining data show, as with the displacement-derived results in Table 4, that the damage does not significantly affect the stiffness. For some panels, the strain gauge data shows a higher stiffness than the displacement-based data would suggest. This is particularly apparent for the 5mm and 7mm indentation cases. As mentioned previously, the very small sample size used here means that this data must be treated with some caution.

Table 5: Strain gauge data from instrumented panels

Panel	**Strain at failure (με)**			**Δ F0-B0**	$\mathbf{E}_{\mathbf{gauges}}$ *Mean (F0,B0)*
	B0	**F0**	**F90**		
SV	-3104	-2836	1446	268	81.94
S2.5	-5673	-6590	2182	-917	37.29
S5	-5630	-4336	1832	1294	42.79
S7	-4702	-4140	1333	562	46.31
AV	-7055	-7141	2509	-86	33.31
A2.5	-5552	-6483	2068	-931	38.04
A5	-5118	-4045	1487	1073	42.92
A7	-6066	-3703	7660	2363	41.03

The compression-after-impact study presented here supplies a good-quality set of strength data which can now be used to further validate the model developed in Chapter 5 (‘*Sandwich Model Development*’). Significantly, the hypothesis that a small amount of asymmetry can improve the strength retention factor of damaged panels has been supported by the experimental and accompanying calculations. The strain gauge and damage morphology data may also be used for cautious comparisons, but is too limited to make any decisive conclusions. Future work should focus on these two aspects, using non-destructive testing methods to study the damage (particularly delamination), and extensive strain gauging of the panels to get a thorough view of the strain field and bending that is occurring in the panels under loading.

Another useful addition to the experimental effort would be to choose composite lay-ups such that both symmetric and asymmetric panels have the same overall cross-sectional thickness, so that any change in strength would be purely due to changes in the neutral axis rather than simple differences in thickness. As it stands, the two configurations used here have differing cross-sectional thicknesses which have an obvious effect on the absolute load-carrying capacity of the two panels. While the strength calculations inherently account for this, the influence this has on the results should be eliminated in future studies to ensure proper isolation of the effect the movement of the neutral axis has on the response of these panels.

Chapter 4

Skin Model Development: Quasi-Static Indentation of a Composite Plate

4. Skin Model Development: Quasi-Static Indentation of a Composite Plate

In this Chapter, a composite plate with a 16-ply quasi-isotropic lay-up subjected to a quasi-static transverse indentation is numerically modelled for deformation in the elastic region of behaviour only, and then later with strength data applied to capture damage and failure. These results are compared with experimental results from Lloyd [163]. This exercise forms part of the familiarisation process with *Abaqus*, demonstrating and validating various numerical techniques and solutions that will later be used for the modelling of compression-after-impact on sandwich panels, including the use of contact algorithms with rigid surfaces, the dynamic/explicit solver, and implementations of the Hashin criteria and cohesive zone model.

4.1 Problem Description

Only a single test case is available for comparison, since in this section of his investigation, Lloyd was primarily interested in the quasi-static response of fabric composite plates. The experiment had the following parameters:

- The plate is circular (diameter 40 mm), with 2 mm nominal thickness
- The indenter used is hemispherical, with diameter 20 mm
- The plate is clamped around the entire outer edge.
- T700 uni-directional carbon-epoxy is used, with a lay-up of $[45/90\text{-}45/0]_{2S}$. The material data required is (predominantly) taken from Lloyd [163], with additional fracture energy data, required for damage evolution as discussed previously, taken from Maimi et al [64], and presented in Table 6. The fracture energies are not for this exact material, but rather are for a similar CFRP system (T300), and can be considered representative for the purposes of this study. Mass data is required later when the explicit solver is used, thus the density of a typical carbon-epoxy is used [166].
- The data in Table 7 is for the cohesive layer introduced later on in this section. There is little data available in Lloyd that is applicable to the bond, with exception of the normal opening and shear opening fracture energies, and the interlaminar shear strength. The rest of the required data is gathered from Camanho & Davila [75] for a similar carbon-epoxy material. The mode-mix ratio used in the Benzeggagh-Kenane Criterion for fracture propagation is also taken from Camanho & Davila. The elastic properties and the density are respectively divided by and multiplied by the cohesive layer thickness – the density is representative of a typical epoxy resin [166]. The data provided assumes a cohesive layer of 10 microns thick. Note also that the strength data is given in terms of stresses. As discussed previously, this directly relates to the opening tractions required by the cohesive model. All the material data here is used as direct inputs into *Abaqus.*

Two experimental samples using these conditions were tested by Lloyd. The first sample exhibited first damage at 1.33 kN, with a central strain reading of 7714 με. Reading from Figure 48 (*Sqps-1*), this strain can be seen to coincide with an indenter displacement of approximately 0.48 mm. For the second sample (not shown in Figure 48 – the second curve, *Schl*, refers to a fabric composite not relevant to the current discussion), damage occurred at 1.49 kN, with a strain of 7620 με. Assuming a constant ratio for this material of ε/δ, this coincides with a displacement of approximately 0.474 mm. Delamination was found to be the source of the initial softening, with the hardening response at higher strain being due to membrane effects. Plate failure occurs at 8.99 kN and 8.52 kN for the first and second samples respectively, due to plate penetration causing fibre fracture in all plies. For the first plate, this occurs at a displacement of approximately 3.7 mm. The approximate force-displacement data from Lloyd is given in abridged form in Table 8 (read directly from Figure 48) and will be used for comparisons with all the numerical models that follow.

Image hidden due to copyright restrictions.
Please refer to [163], figure 3.8

Figure 48: Experimental results for quasi-isotropic plate under quasi-static load [163]

Table 6: Material data for T700 CRFP

E_{11} (GPa)	E_{22} (GPa)	v	G_{12} (GPa)	G_{13} (GPa)	G_{23} (GPa)
129.6	8.8	0.3	5.4	4.7	4.7
σ_{lt} (GPa)	σ_{lc} (GPa)	σ_{tt} (MPa)	σ_{tc} (MPa)	τ_l (MPa)	τ_t (MPa)
1.9563	1.032	48	129.7	72.5	72.5
G_{lt} (kJ/m^2)	G_{lc} (kJ/m^2)	G_{tt} (kJ/m^2)	G_{tc} (kJ/m^2)		ρ (kg/m^3)
89.83	78.27	0.23	0.76		1800

Table 7: Material data for cohesive layer

K_{E3} (Pa/m)	K_{G1} (Pa/m)	K_{G2} (Pa/m)		ρ_{coh} (kg/m^2)
1.1 *e15*	6 *e14*	3.7 *e14*		0.013
σ_n (MPa)	τ_2 (MPa)	τ_3 (MPa)		mode-mix
45	66.3	66.3		2.284
G^C_1 (J/m^2)	G^C_2 (J/m^2)	G^C_3 (J/m^2)		
275	940	940		

Table 8: Lloyd's Experimental Data (abridged) [163]

P (kN)	δ (mm)
0	0
1.49	0.47
1.8	1.0
2.3	1.5
3.0	2.0
4.3	2.5
6.5	3.0
8.7	3.4
8.1	3.5
9.1	3.7
3.6	3.75

4.2 Elastic Response

The first stage considered the elastic response of the plate only, to validate the modelling techniques to be used in the second phase modelling the inelastic response of the plate. Firstly, the method for load application will be established, the options under consideration being displacements applied directly to relevant nodes, or via a rigid indenter pressing into the plate, using a contact interaction between the two parts. Secondly, a study of the response of different elements will be performed, considering conventional and continuum shells. Finally, a comparison of the two available solvers, implicit and explicit, will be made for the linear region of the plate’s response.

4.2.1 Load Application

The displacement field of the indentation is determined using the basic equation for a circle with an arbitrary centre:

$$(x-a)^2 + (y-b)^2 = r^2$$

(30)

Where: x = radial position of interest on the plate – in-plane (mm)
y = y-coordinate for the edge of the indenter – out-of-plane (mm)
a = x-coordinate for centre of indenter (mm) = 0
b = y-coordinate for centre of indenter at peak displacement (mm)
= $r - \delta_{max}$
r = radius of the indenter (mm)
δ_{max} = maximum applied displacement (mm)

This expression is solved for *y*. The displacement at point *x* is then given by:

$$\delta_x = y - 2b \tag{31}$$

δ_x will always equal the applied displacement δ_{max} when $x = 0$. This analysis assumes that the indenter is penetrating the plate, and that no change in the curvature of the plate occurs. Eventually, for a sufficiently large value of x, $\delta = 0$, defining the boundary of the contacted region of the plate for the given displacement level. The size of this boundary can never exceed the radius of the indenter. This is shown in Figure 49.

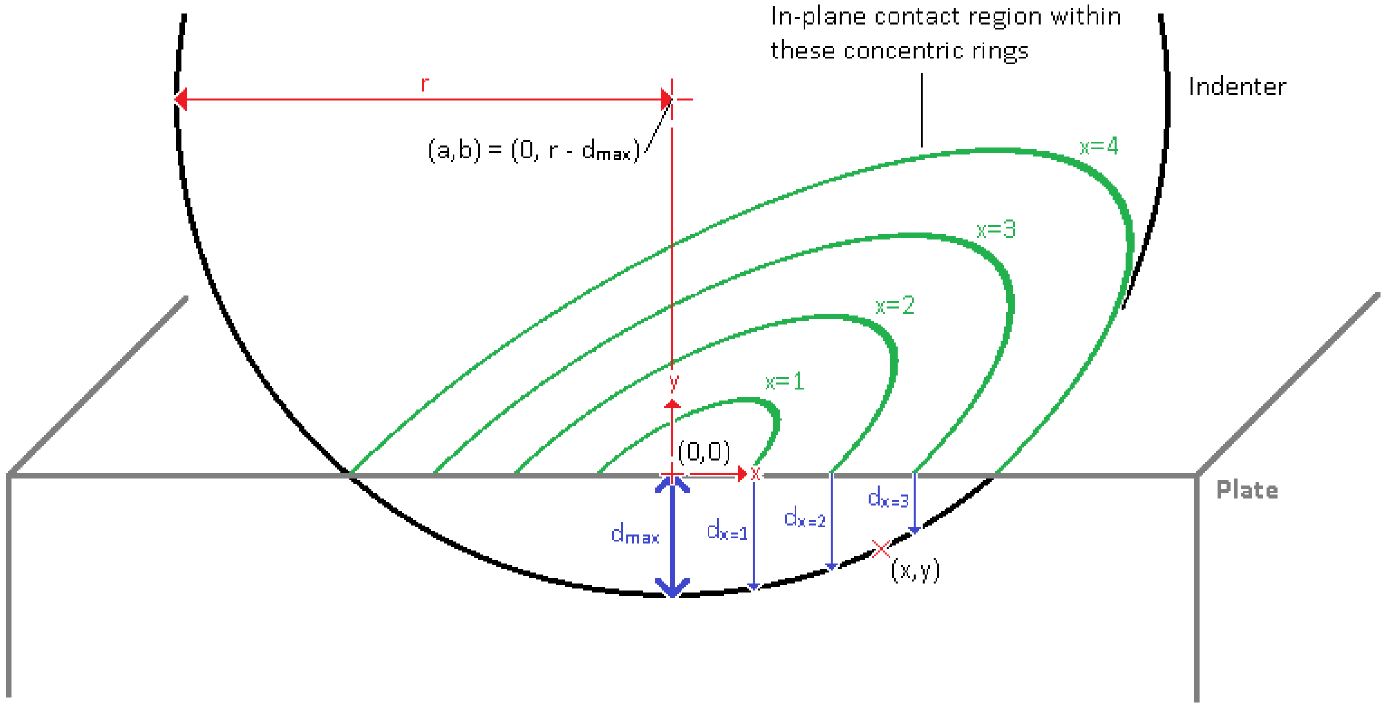

Figure 49: Schematic representation of the indenter on the plate

Based on the experimental results, δ_{max} = 0.5mm, therefore b = 9.5mm. The displacements are found for concentric in-plane rings spaced at 1mm originating from the centre of load application. So, for this test case, the y coordinate of the edge of the indenter for various values of x is given by:

$$y_{x=0} = \sqrt{r - x^2} + b = \sqrt{100 - 0} + 9.5 = 19.5\,mm$$
$$y_{x=1} = 19.450\,mm$$
$$y_{x=2} = 19.298\,mm$$
$$y_{x=3} = 19.039\,mm$$
$$y_{x=4} = 18.665\,mm$$

From these values, the displacements at these locations can be found thus:

$$\delta_{x=0} = y - 2b = 19.5 - 19 = 0.5\,mm$$
$$\delta_{x=1} = 0.450\,mm$$
$$\delta_{x=2} = 0.298\,mm$$
$$\delta_{x=3} = 0.039\,mm$$
$$\delta_{x=4} = -0.335\,mm$$

This indicates the boundary of the contacted region is between $x = 3$ and $x = 4$. It is not important at this stage to determine its precise limit. These displacements are applied directly to the relevant nodes in the central contacted region of the plate.

The alternative approach is to model the indenter as a part in its own right. A part modelled as a rigid (i.e. non-deformable) surface may be controlled by applying displacements to a single reference point on the part. All output data, such as the reaction force, is also collected from this node. This approach is clearly much more convenient from a modelling perspective as there is no need to determine the displacement field prior to setting up the model. Additionally, it is a more flexible approach: the plate mesh and indenter geometry can be modified as required without having to redefine the displacements. However, a contact relationship does need to be established between the two parts, to capture the interaction between the two – in this case, the indenter pressing into and deforming the plate. Without this interaction, the two parts would remain entirely independent of each other, and the indenter would simply pass through the plate. This first model, a node-to-surface contact algorithm (whereby the master surface is set as the surface of the indenter, contacting with a set of slave nodes on the top face of the plate) is used. A general 'all-with-self' contact algorithm is available in the explicit model, which doesn't require contact surfaces to be defined separately, but comes at the expense of fine control. A friction coefficient of 0.3, as used by Gonzalez et al [42] for friction between steel and CFRP, is applied between the indenter and plate for all the rigid indenter models discussed in the section.

These two approaches are applied to a plate modelled using 4-node linear shell elements with reduced integration (S4R). The mesh is identical for both models, with a clamped boundary condition applied to the nodes around the outer edge of the plate. Both analyses are performed with the implicit solver, using a step time of 6s. The applied displacement is 0.5mm, corresponding with the linear elastic region of the experimentally-observed response. For the applied step time, this corresponds to a quasi-static loading rate of 5 mm/min. Figure 50 and Figure 51 show the meshed plate and the indenter model assembly respectively, with the lay-up of the plate presented in Figure 52. The force-displacement response is output directly from the numerical model, and is shown for both of these models (amongst others to be discussed later) in Figure 53; the ‘directly-applied displacement’ model *Disp-WF* is indicated by the red line and the ‘rigid indenter’ model *Indt-WF* by the blue line. The experimental result from Lloyd is indicated by the green dashed line. Figure 54 shows the displacement profile through a section of both plates local to the indenter. Figure 55 and Figure 56 show the displacement fields for the direct displacement and rigid indenter models respectively.

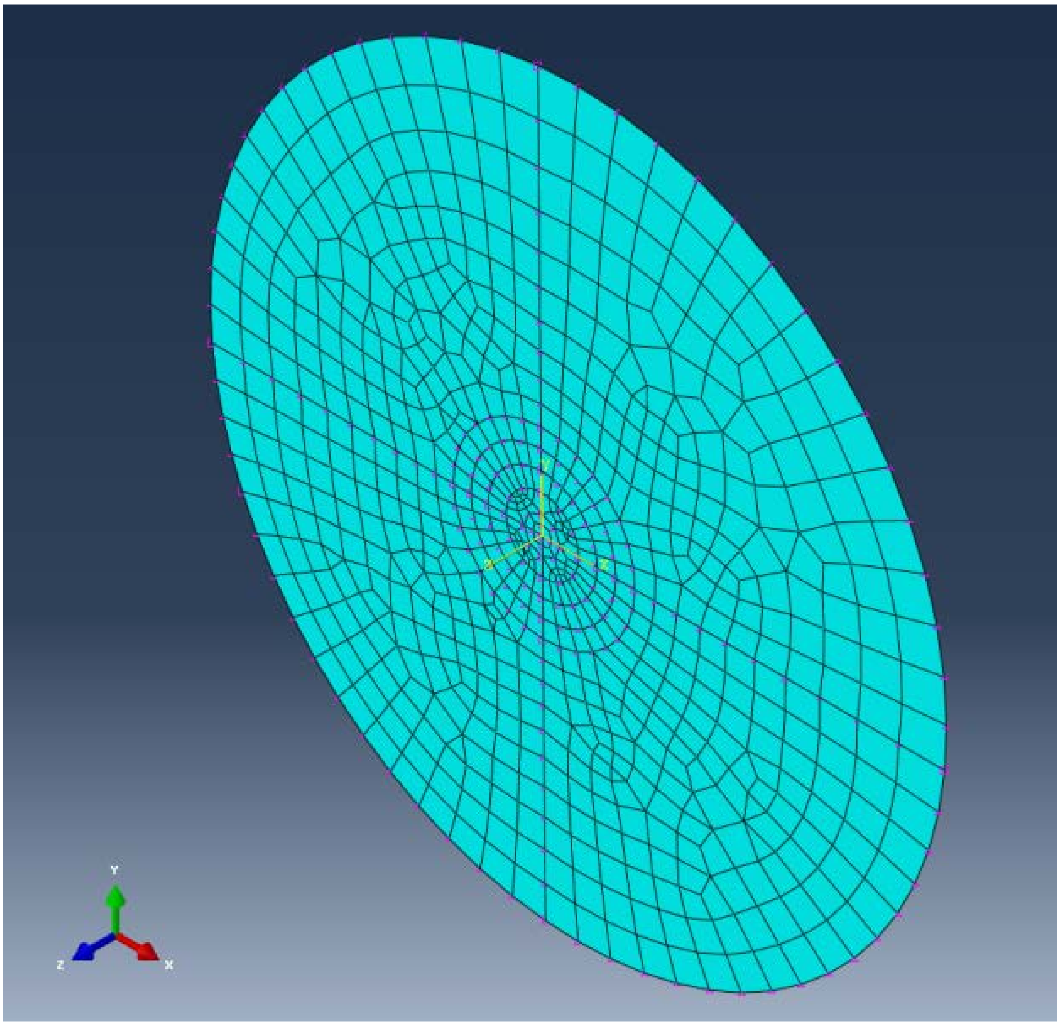

Figure 50: Meshed conventional shell model

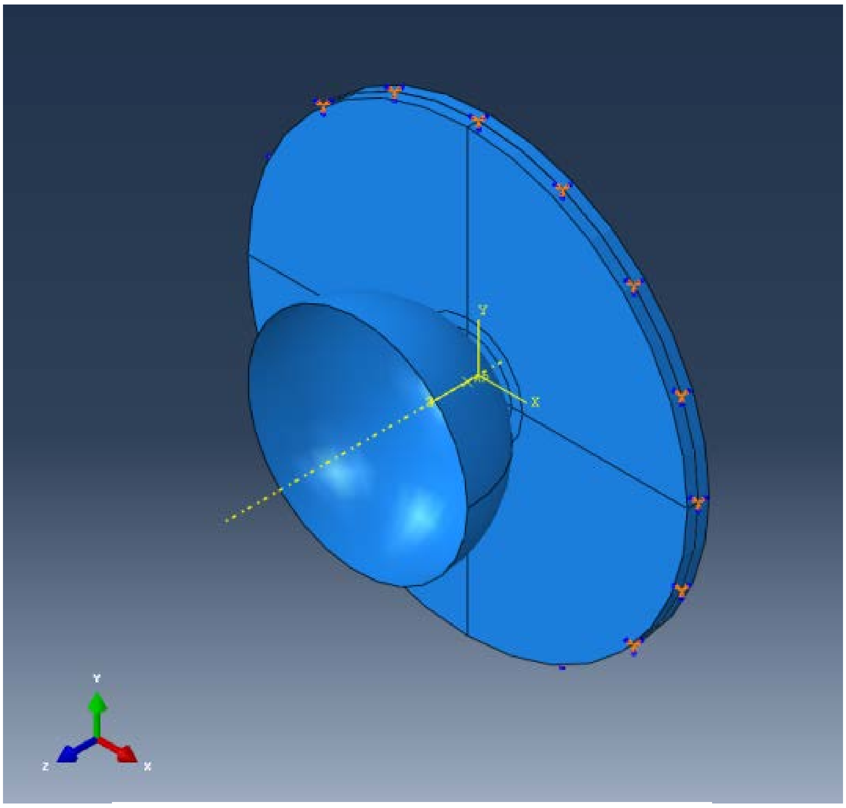

Figure 51: Indenter and plate assembly (shell thickness rendered)

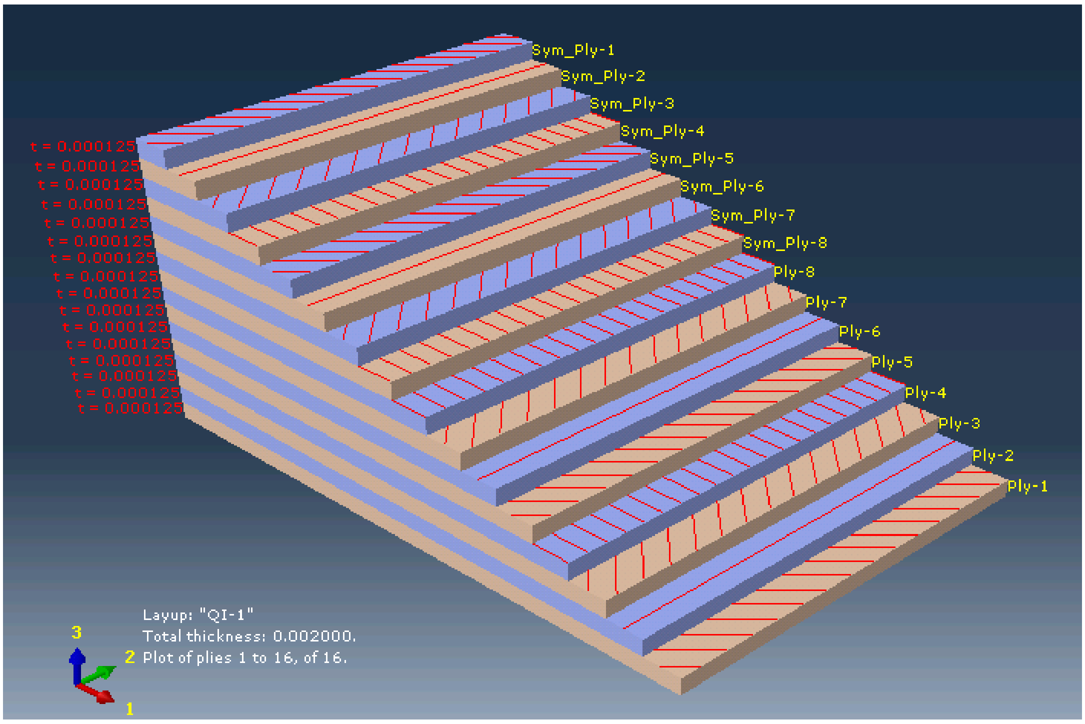

Figure 52: Ply stack plot showing lay-up of the plate

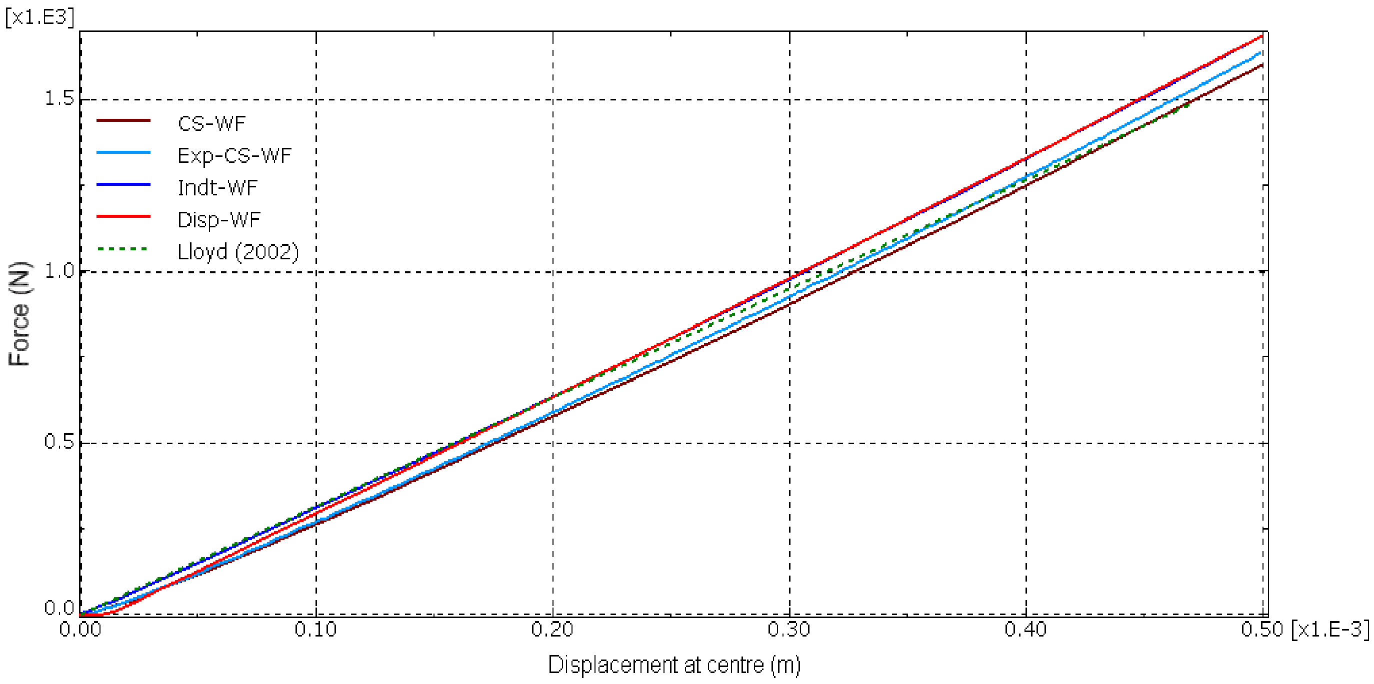

Figure 53: Force-displacement response of all elastic models

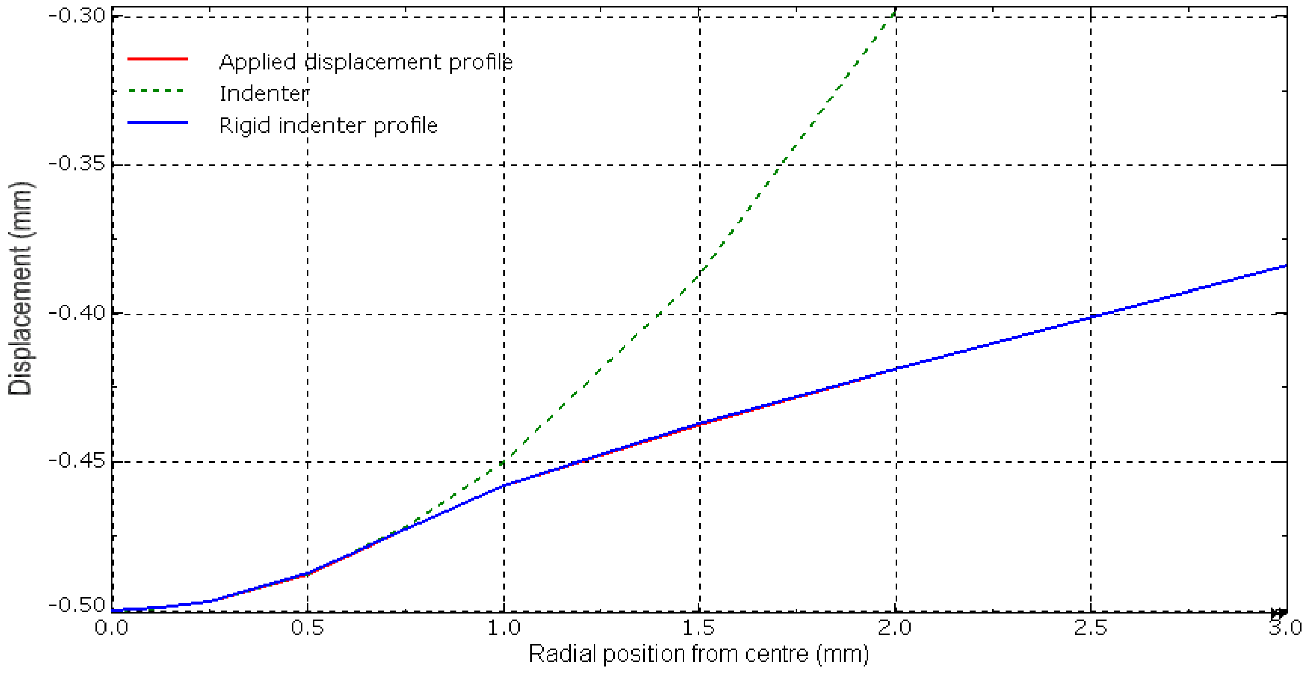

Figure 54: Local displacement profile along line x=0 for applied displacement and indenter models

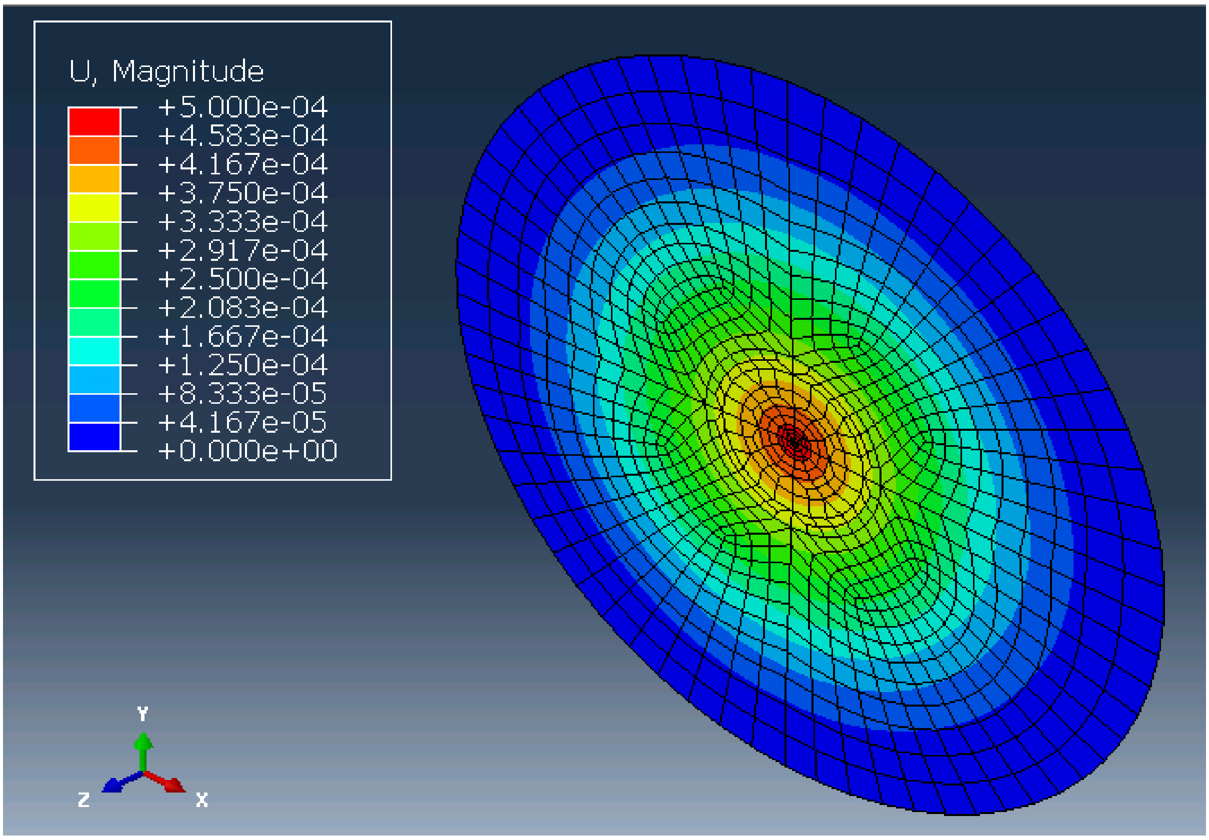

Figure 55: Displacement field for the applied displacement model

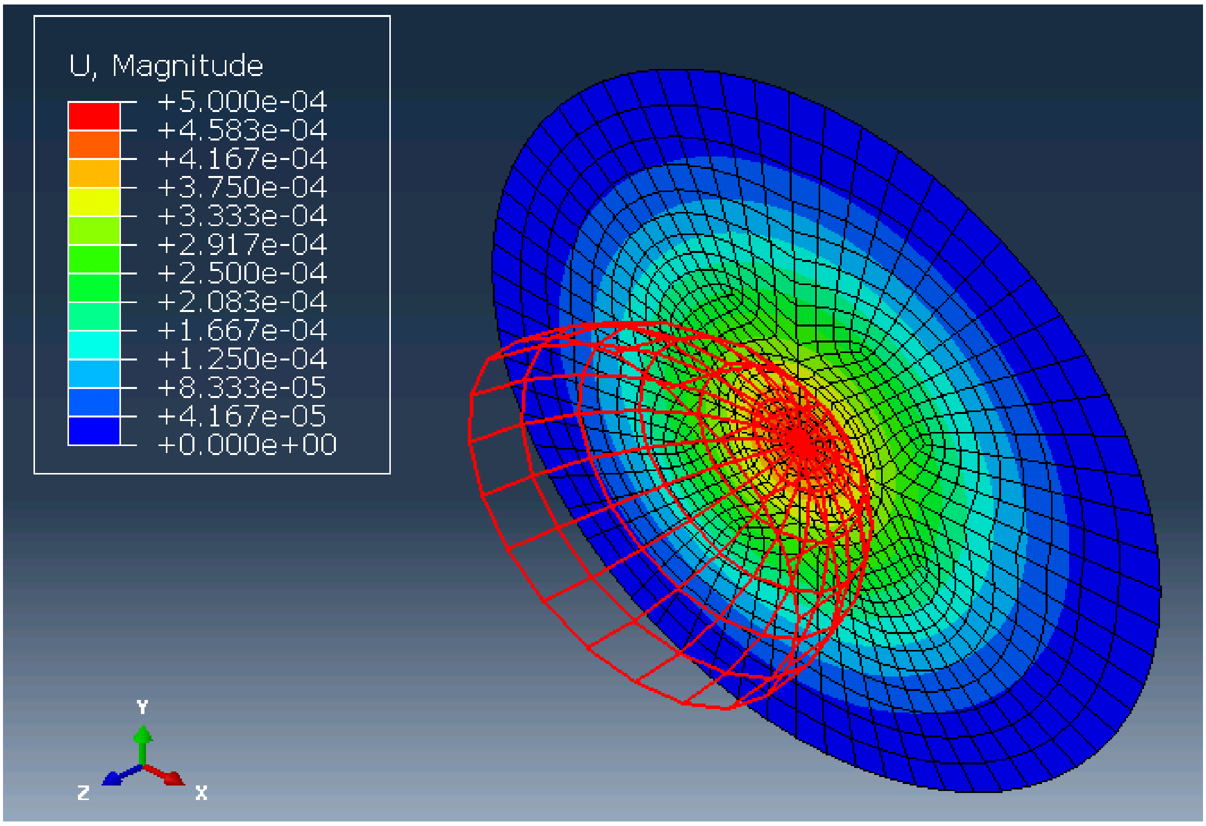

Figure 56: Displacement field for the rigidly indented model

From the force-displacement plot, it is clear that both approaches agree very well with the experimental results, and also each other. At 0.47 mm displacement, after which point damage is observed in the experimental results at load level of 1490 N, the rigid indenter model predicts an indenter load of 1579 N, and the applied displacement model predicts a total force (analogous to the indenter load) of 1581 N. This gives a maximum overestimate of 5.76%. Additionally, the displacement profile in the indented region shows very good agreement between the two models, and also confirms that the contact algorithm used in the rigid indenter model is functioning correctly. There is a slight non-linearity in the applied displacement model at the start of loading. This is due to the element geometry and the inability to correctly represent the initial contact load, resulting in a slight delay in the load response. The displacement field plots confirm the global response of the plates is correct, with the maximum displacement observed at the centre, falling to zero at the boundary.

4.2.2 Element Comparison

This section compares conventional and continuum shell elements, with the load applied using the rigid indenter method just discussed. Solid elements were not considered here, since there was no data for through-the-thickness elastic modulus or Poisson’s ratio, and thus it would not have been possible to produce accurate results for comparison. Additionally, since there is no feature in *Abaqus* for treating material damage and failure in a solid composite model, it would not in any event have been possible to use these elements once strength data was to be applied (at least not without producing custom sub-routines). The continuum shell used here, and throughout the rest of the work in this chapter, is an 8-node linear, reduced-integration element (SC8R).

The force-displacement response for the continuum shell model is included with the other curves in Figure 53 (*CS-WF*, indicated by the crimson line). The indenter force at 0.47 mm displacement for this model is 1497 N, giving an overestimate for this model of less than 0.5%. This extremely good agreement, which is considerably better than that provided by the conventional shell model, is due to the improved through-the-thickness fidelity of the continuum shell. Figure 57 shows a section through the deformed plate, showing the (very small) local indentation that the conventional shell is unable to capture.

Stress data is collected for both conventional and continuum shell models as a further check that the model is behaving correctly in the elastic regime. Figure 58 shows the refined mesh at the centre of the plate used to find the normal force distribution. The highlighted elements are used, along with all other elements along the radial line, to find the stress in the x-direction, analogous with the radial stress. The mesh was seeded in this manner to ensure that all of the elements in direct contact with the indenter were of very similar, if not the same, size, to allow for an accurate through-the-thickness normal stress distribution. The normal stress is found by taking the sum of the nodal force for each element and dividing that by the area of the element. The precise elemental area is found with ease from output of the element volume, divided by the plate thickness. This approach is necessary, since despite the 3-D geometry of the continuum shell elements, they are not capable of directly capturing through-the-thickness stresses due to their 2-dimensional kinematic behaviour.

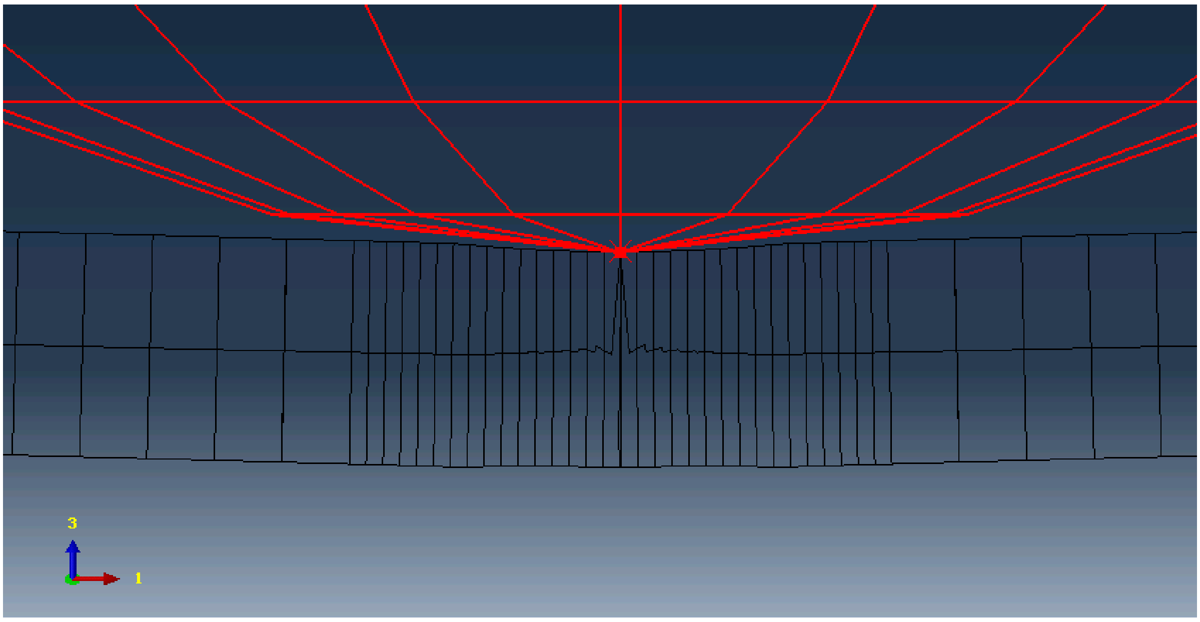

Figure 57: Section of the continuum shell model local to the indenter, showing local indentation

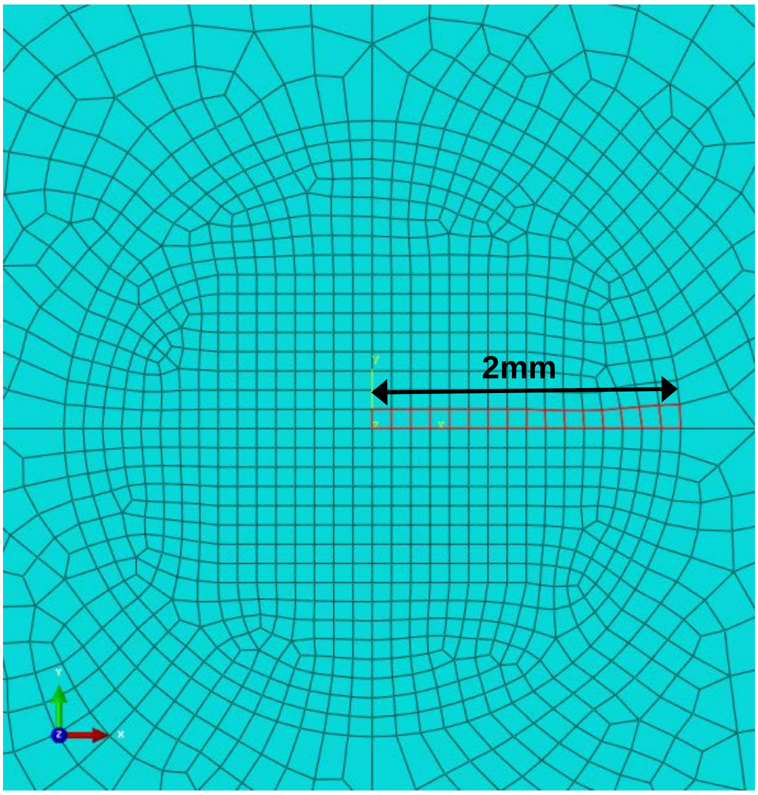

Figure 58: Refined central region of the plate. The radius of the inner section is 2 mm, so each element in this area is 0.25 mm across.

The distribution of the radial stress from the centre of the plate to the boundary is shown in Figure 59 for the tensile and compressive faces of the plate (*St*- and *Sc*- respectively) both the conventional shell (-*Sh*) and continuum shell (-*CS*) models. The distribution is largely the same for both element types. The key difference between the two models is in the indented region on the compressive side of the plate. Here, in the region of local indentation captured by the continuum shell there is a small degree of material stretching that counteracts the overall compressive stress generated on this face, due to friction in the contact area between plate and indenter. This effect could not be captured by the conventional shell model. Note the reversal of the stress on both faces towards the edge of the plate, caused by membrane stretching at the periphery, present in both models. Focusing on the contact area of the continuum shell, the normal stress distribution (Figure 60) shows that the greatest stress is at the centre of the loaded region, reducing towards zero in a parabolic manner as the boundary of the contact area is approached. This behaviour is also clearly seen in the normal force distribution (Figure 61). Note that normal stress falls to zero outside of the contacted area, as expected.

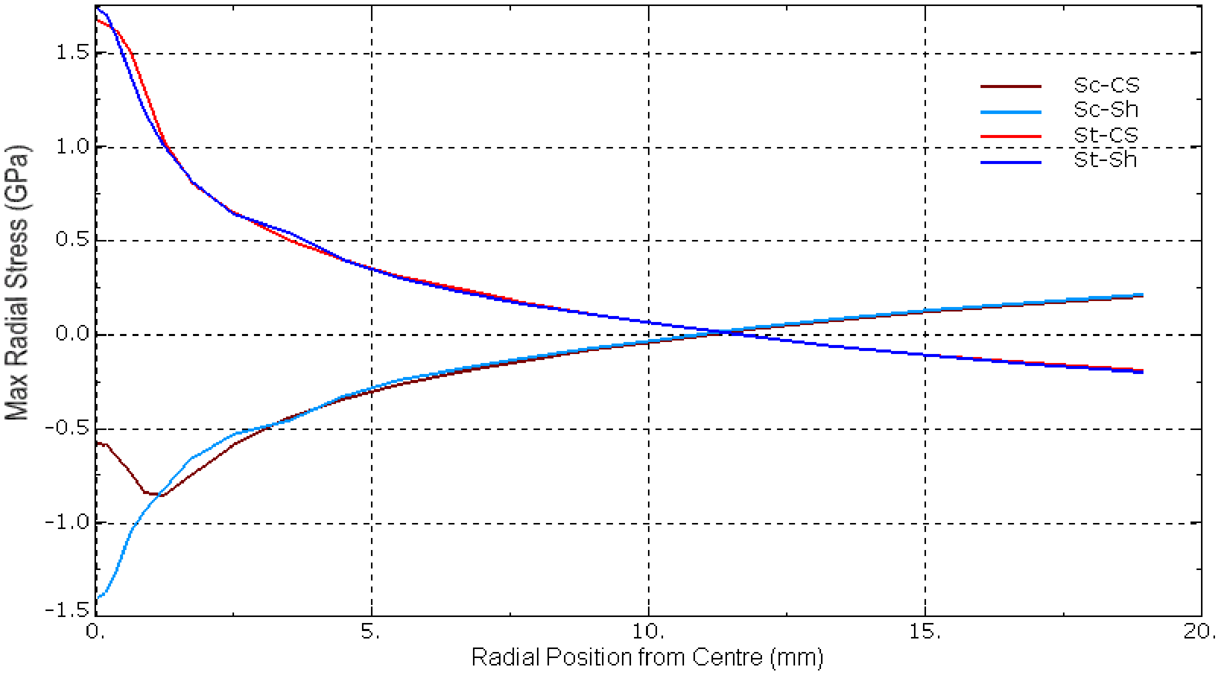

Figure 59: Stress distribution in x-direction (corresponding with radial stress)

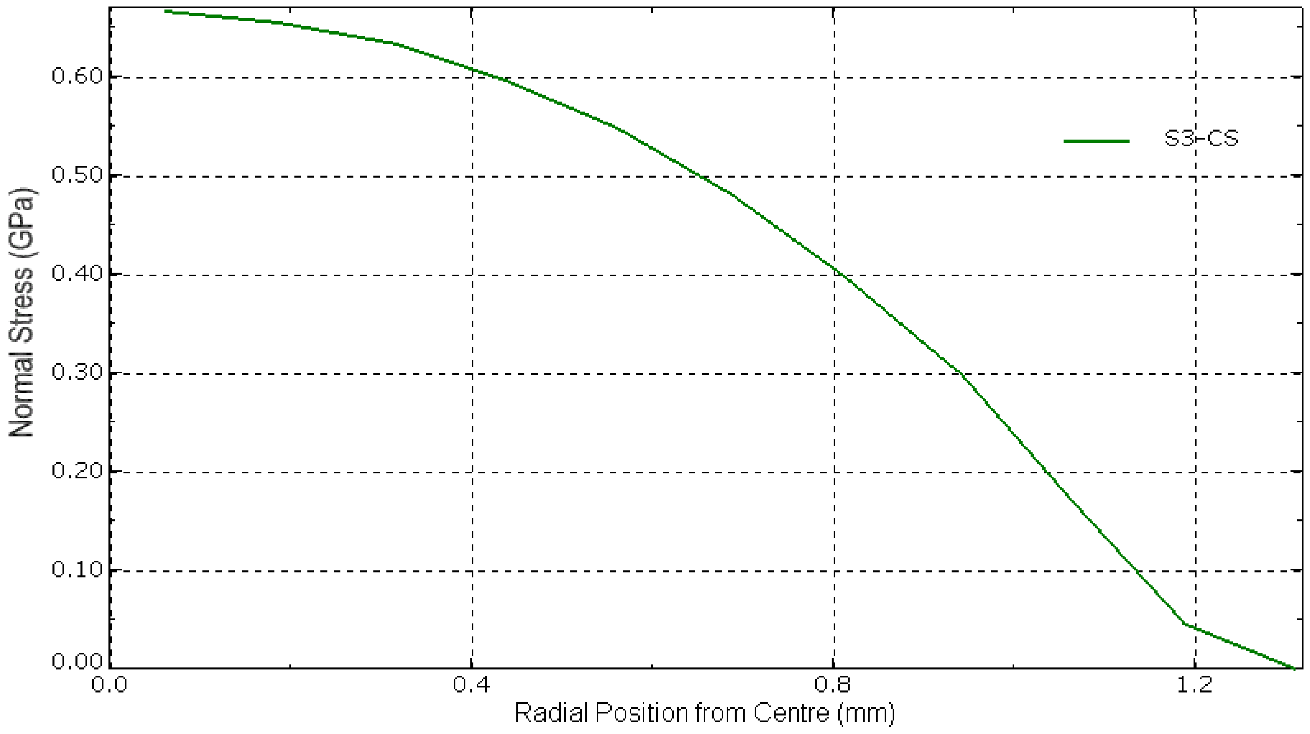

Figure 60: Normal stress distribution in contact region.

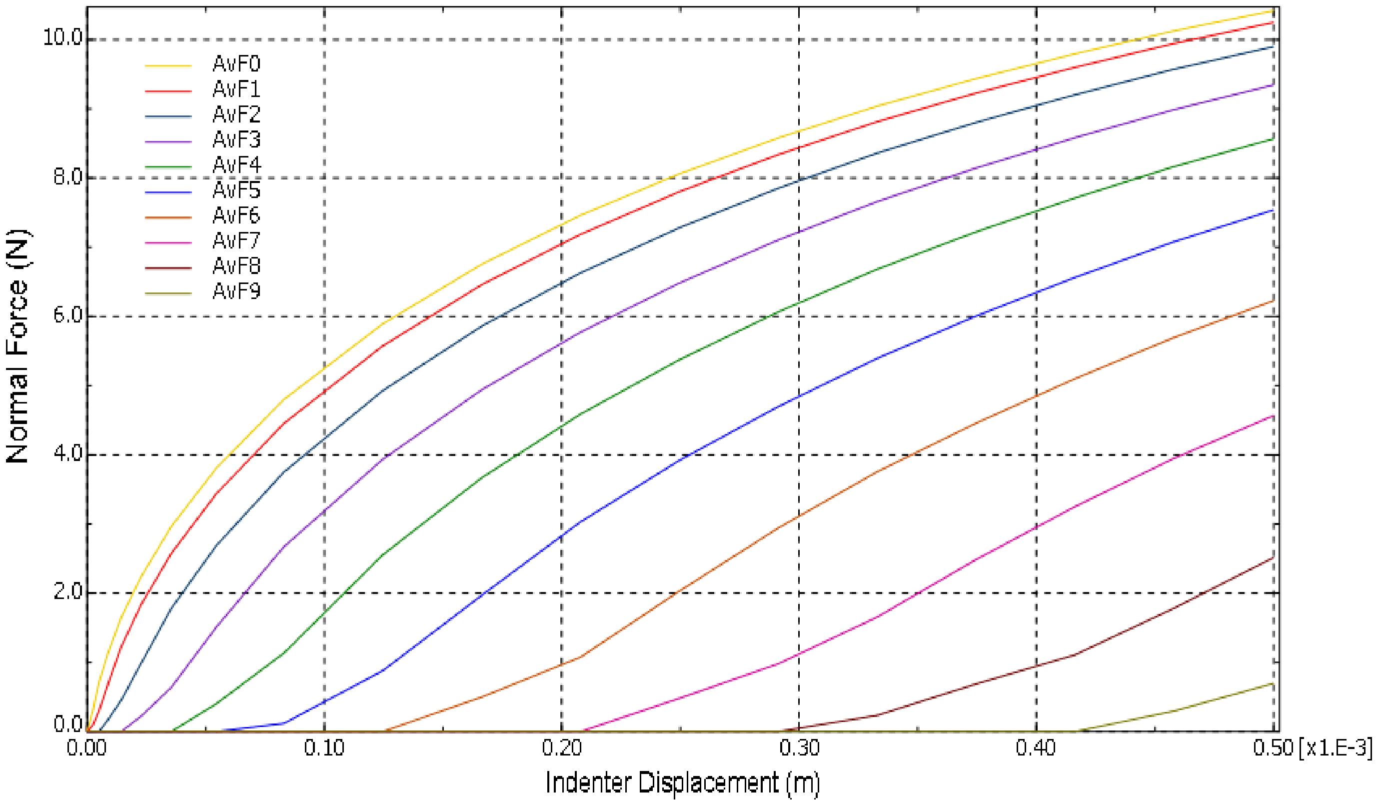

Figure 61: Normal force distribution in contact region (continuum shell) from the centre of the contact region (peak displacement, F0) to the outside edge of this region (F9)

4.2.3 Solver Comparison

The continuum shell model is rerun for the elastic regime using the explicit solver. As previously mentioned, mass data is required in the explicit model. The indenter is given a mass of 0.01 kg, to minimise the kinetic energy. A frequency analysis is performed in order to set an appropriate time step. The lowest natural frequency is found via frequency extraction to be approximately 11 kHz for this particular plate, for a period of the order of 1e^{-4}s. The displacement is applied over a 5 ms time step, giving a loading rate which is considerably lower than this time period, thus the response can be presumed to be quasi-static. By way of confirmation, Figure 62 shows the energy balance for the system. The kinetic energy (indicated by the blue line *Exp-WKE*) is clearly seen to be approximately zero, supporting the conclusion that the simulation is quasi-static. Figure 53 shows the force-displacement response for this model (*Exp-CS-WF*, indicated by the cyan line) along with the responses of the models discussed previously, showing very good agreement with both the previous analyses, all produced with the implicit solver, and also the experimental results. The force at 0.47 mm displacement is determined to be 1531 N, overestimating the experimental result by 2.7%.

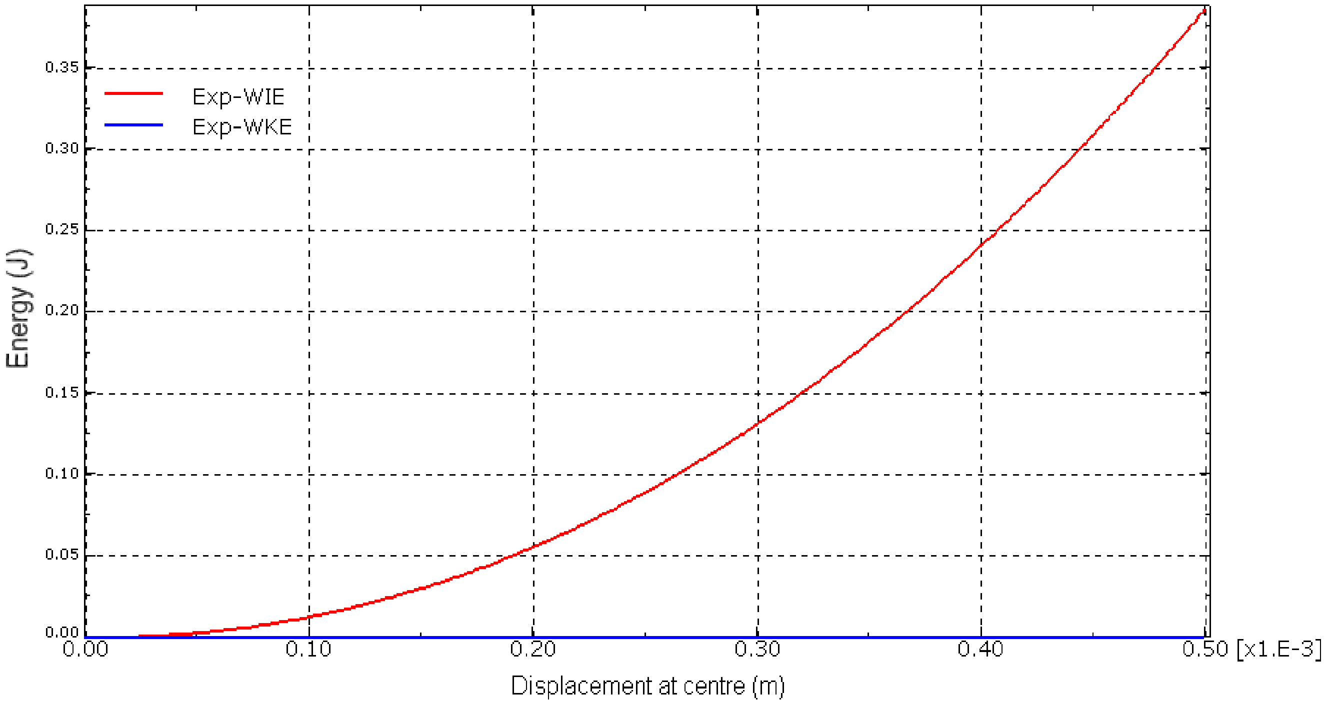

Figure 62: Energy balance of explicit model

From this work with the elastic model, it is possible to conclude that using a rigidly modelled indenter is preferred to applying displacements directly to nodes on the meshed plate, for modelling convenience and flexibility. The continuum shell is the preferred element for modelling the plate, since it provides some of the through-the-thickness fidelity of the solid element, while permitting the use of composite-specific material properties and constitutive behaviours. Finally, it is confirmed that both the implicit and explicit solvers will provide results of excellent quality for the linear elastic region of behaviour under quasi-static loading, though for these linear analyses, with no material damage and very limited geometric non-linearity, the implicit solver is a much more efficient solver.

4.3 Inelastic Response

The inelastic response (in this instance, this is taken to mean the inclusion of damage initiation and propagation rather than plastic behaviour) of the plate is studied in three stages. First of all, the initiation of intralaminar damage is considered, to demonstrate the use of various numerical techniques for solving the highly non-linear problem that results from this. Next, the initial load drop observed in Lloyd's experimental data is modelled, through the use of a layer of cohesive elements using a traction-separation law. Finally, once this effect is captured, intralaminar damage is taken into account using the Hashin criteria, to capture the complete load history of the plate up to and including the final failure. It is important to state at this stage that a true reproduction of the experimental results is not expected from this work, due to the limitations of the material data and very small experimental sample size. Particularly, the fracture energies for both the intra- and interlaminar damage are not truly representative of the plates produced by Lloyd, and due to the sensitivity of the numerical model to these values, matching the numerical curve to the experimental curve cannot be reasonably achieved. Instead, this section is better viewed as a 'proof-of-concept', demonstrating the use of the techniques for composite skin modelling that will eventually be applied to the sandwich models this project ultimately seeks to produce.

4.3.1 Solution of the Non-Linear Problem

The force-displacement response for a plate with skin strength data, and varying degrees of damage stabilisation, applied is presented first in Figure 63, plotted against the experimentally-derived curve produced by Lloyd as seen in Figure 48, shown as a green dashed line. These curves are intended to show the initiation of damage – to this end the damage evolution energy is set at an extremely low value (three orders of magnitude less than the actual fracture energy for matrix and fibres). Neglecting the damage evolution is not an option, since in *Abaqus*, this would only affect the output data, and not show any change in the force-displacement response [118]. Damage for fibre-reinforced materials in *Abaqus*, as discussed earlier in the report, is based on the work of Matzenmiller et al [117], and utilises the well-established damage initiation criteria of Hashin & Rotem [103,104]. Please refer to Chapter 2 ('*Numerical Modelling of Damage in Composite and Sandwich Structures*') for details.

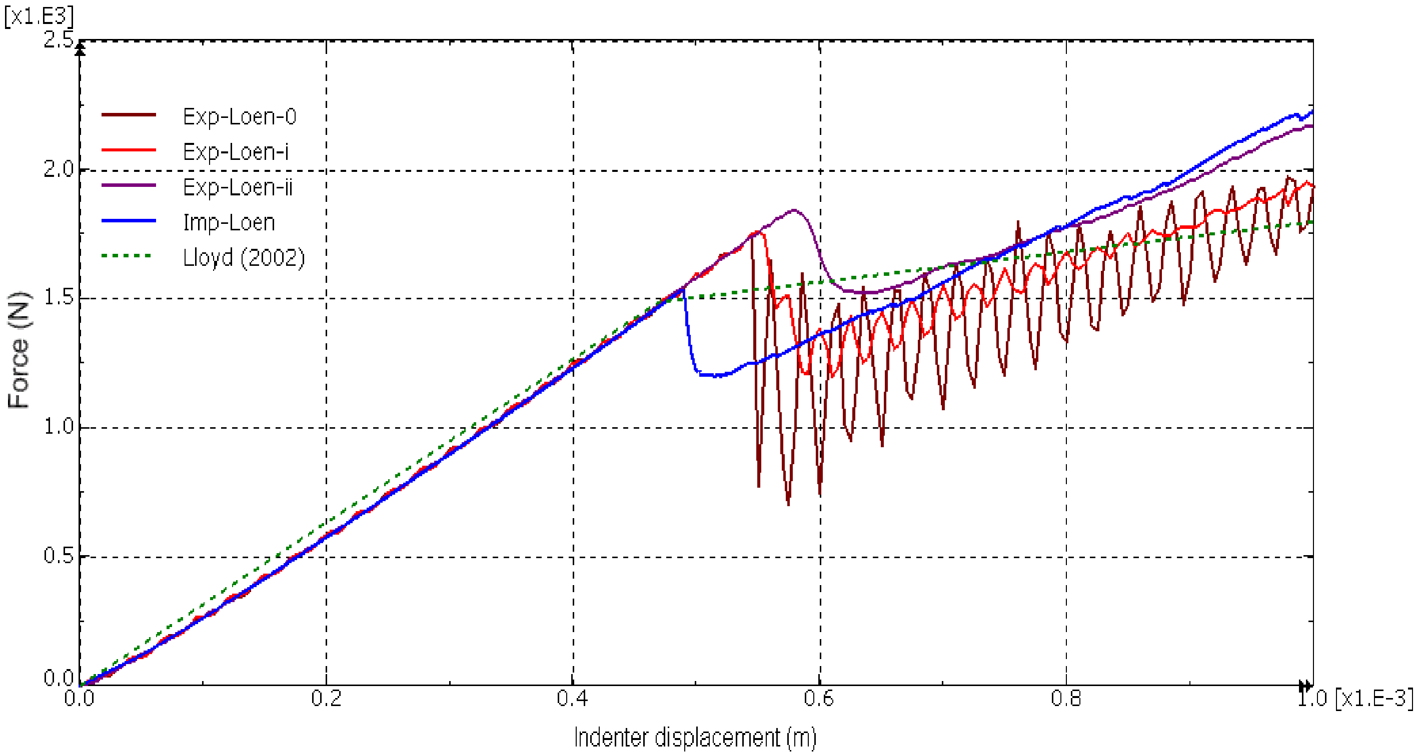

Figure 63: Force-displacement response for plates featuring damage initiation

All curves are produced using the explicit solver, with exception of the blue curve (*Imp-Loen*), which is generated using the implicit solver. The crimson (*Exp-Loen-0*), red (*Exp-Loen-i*) and purple (*Exp-Loen-ii*) curves have damage stabilisation (the application of a small artificial viscosity to prevent convergence difficulties – refer to Section 2.1.2) set to 0, 1e^{-6} and 1e^{-5} respectively. Additionally, *Exp-Loen-ii* used a longer step time of 4 ms, whereas the other two curves used a step time of 2 ms. The longer step time results in a slower load application, which reduces the inertial effects. The explicit models are otherwise identical. The implicit analysis used damage stabilisation set to 2.5e^{-4} – analyses ran with a lower level of damage stabilisation aborted prematurely at a load level of approximately 500 N due to convergence failure at the first instance of complete material property degradation, in this instance in the matrix on the tensile face of the plate. The results are also displayed in Table 9; the two failed implicit runs are indicated in the table as *Imp-Loen-0* and *Imp-Loen-i*, using damage stabilisation set to zero and 1e^{-4} respectively. The '*% difference*' is calculated as the difference between the numerical and experimental results. The suffix *Loen* applied to each of these results denotes 'low energy', to separate these results, using artificially low fracture energies, from later models using the true fracture energies, and *Exp* and *Imp* denote models solved using the explicit and implicit solvers respectively.

Table 9: Results for plates with damage initiation

Model	At load-drop…			
	Displacement (mm)		Load (N)	
	Numerical	% difference	Numerical	% difference
Exp-Loen-0	0.545	13.8	1755	15.1
Exp-Loen-i	0.550	14.6	1762	15.4
Exp-Loen-ii	0.580	19.0	1842	19.1
Imp-Loen	0.489	3.9	1534	2.9
Imp-Loen-0*	0.178	-	504	-
Imp-Loen-i*	0.175	-	494	-
Lloyd (2002)	0.47	-	1490	-

**Analysis not completed*

The implicit model agrees very well with the experiment for the point of damage initiation. However, the high level of damage stabilisation required to complete the analysis successfully casts some doubt on the validity of the results. The results from the explicit model do not agree as well with the experiment. Damage stabilisation is useful in the explicit model to eliminate some of the noise in the post-damage onset response (compare *Exp-Loen-0* and *–i*), but clearly, too much stabilisation creates a potentially unsafe overestimate of the force at damage onset (see *Exp-Loen-ii*). The longer time-step shows a slightly smoother response overall, though this is due to the reduced resolution of the output history, rather than any meaningful change in the physical response.

One modelling aspect not fully considered here is temporal convergence. This is akin to mesh refinement as applied to the temporal domain, and relates to the size of the increments used by the solver. *Abaqus/Explicit* uses automatic incrementation, but it is possible to make the time increments even smaller than that chosen by the solver (based on the minimum stable time increment) to gain greater accuracy. Implicit solvers will reduce the time increments as much as necessary to ensure convergence. Spatial discretisation (mesh refinement) tends to have greater influence on the solution accuracy, but a particularly thorough study would include the temporal convergence as well.

It is essential to note once again that in the experiment, the first load drop was caused by delamination, which is not yet considered in this model. However, delamination and matrix cracking have been seen to be related [71,133,134], so the fact that these models agree well with the damage initiation load while only featuring intralaminar damage lends some support to these observations made by other researchers. It should be noted that the two faster explicit analyses had kinetic energy above the 5% quasi-static threshold, up to 18.6% of internal energy by the end of the load step. The slower model's (*Exp-Loen-ii*) kinetic energy was at 4.2% of the internal energy, and so can be treated as a valid quasi-static solution. It is illuminating to note that while the faster solutions were rather noisy, the accuracy of the results does not appear to be harmed. This is not unexpected, as low-velocity impacts result in an approximate quasi-static equilibrium state in the material [18], and thus remain representative of Lloyd's experiments.

4.3.2 Initial Load Drop – Delamination

To implement cohesive elements, a discrete ply model was prepared by modelling the top and bottom halves of the plate as separate 1 mm thick ply blocks, with a single 10 micron cohesive layer introduced as its own part between the two halves. Each ply block has half of the total plate layup applied using the usual composite layup tool, so that together, the two ply blocks produce the desired symmetric laminated structure. The cohesive layer was then joined to the mating faces of each ply block using tie constraints, which constrain the motion of nodes on the selected slave surface to have the same motion as the nearest node on the master surface [118]. Care must been taken to ensure that the nodes defining the tie constraints are not involved in the boundary condition definition, as this results in analysis errors. This becomes particularly relevant at the two loaded ends of a panel in edge compression, such as in the sandwich panels presented later in this report. Additionally, the cohesive elements must also be unconstrained – that is to say, not included in the boundary conditions. Although the use of cohesive layers necessitates a degree of discrete ply modelling, even if not necessarily going to the extent of modelling each ply individually (a perfectly plausible proposition), discrete ply modelling does have a useful side benefit of increasing the through-the-thickness fidelity of the model, due to the increased number of elements in the thickness direction. It also assists in accurate modelling of progressive failure, as the multiple through-the-thickness elements allow each ply block to fail individually, rather than the unrealistic situation presented by the equivalent single ply model used thus far wherein all plies essentially fail all at once.

The cohesive layer is meshed with 8-node cohesive elements (COH3D8), using the material data given in Table 7. The quadratic maximum stress criterion is used for damage initiation in conjunction with energy-based damage evolution, which includes mixed-mode behaviour with linear softening. As before, the explicit solver is used for solving the non-linear problem, to prevent convergence difficulties when the interfaces start to fail, and damage stabilisation in the interface of $1e^{-6}$ is applied to the interface model. Taking the requirements for mesh refinement into due consideration (as discussed in Chapter 2) the bond layer contains approximately 23,000 elements, giving around 5 elements per mm. The plate has a much coarser mesh, approximately 1000 elements. Finally, element deletion for failed elements is suppressed in the bond. This is to prevent numerical problems due to severe element distortion, which can result from removing elements that are tied to other elements, as exists in this particular model.

This model just described is used to produce all the following results, with the different responses produced via changes to the material data. Due to time constraints, and the considerable computational demands of the cohesive model, significant load acceleration is used here, with the step time being of the order of milliseconds. This is likely to invalidate the quasi-static loading assumption, though this is not considered important at this stage in the exercise, due to the reasons previously stated – these models are for proof-of-concept only. Initially, only the elastic response of the model is considered, and compared with the explicit model *Exp_Loen_i* from section 4.3.1, which confirmed that the model is responding correctly for the elastic region. Then, the damage parameters are applied to the cohesive layer, but not the composite laminates. For comparative purposes, results generated using other damage evolution laws are also presented here. Figure 64 shows the single-bond cohesive model force-displacement response (*One bd*, red) compared with a benchmark explicit model (*Exp-Loen-i* from the previous section, shown here in blue) and the experimental data (green). Note that the benchmark data has been smoothed using an exponential moving average [167] with a smoothing factor of 0.2 applied to eliminate the noise in the post-damage region for clarity – this operation has no significant effect on the load peak. Figure 36 also shows the response of a two-layer cohesive model (*Two bd*, purple), where a second cohesive layer is introduced at the midplane of the upper (that is to say, the side in contact with the indenter) block of plies.

The single-layer cohesive model with mixed-mode fracture and linear softening (*One bd*, red) shows a load drop at approximately 1810 N, for a displacement of approximately 0.595 mm. This provides a very interesting result when compared with the benchmark numerical model – recall that this model, *Exp-Loen-i*, gave a load drop at 1762 N and 0.55 mm displacement. The benchmark model only featured intralaminar damage and the cohesive model only includes failure in the interface – the similarity of the load and displacement at the onset of damage lends some credence to the suggestion that matrix damage and delamination are connected [71,133,134], and is worthy of closer investigation. The onset of damage in the interface agrees reasonably well with the experimental result, with the error being predominantly due to the limitations of the available material data, and the assumptions that have been required as a result in order to run the model successfully. Note also that the use of two cohesive layers does not have a significant effect on the results, with the two-layer model showing a slightly less stiff response, but with damage onset occurring at approximately the same load as the single-layer model. This result is useful, as it could potentially allow for good results with only a single cohesive layer, which would offer considerable benefits in terms of computational expense.

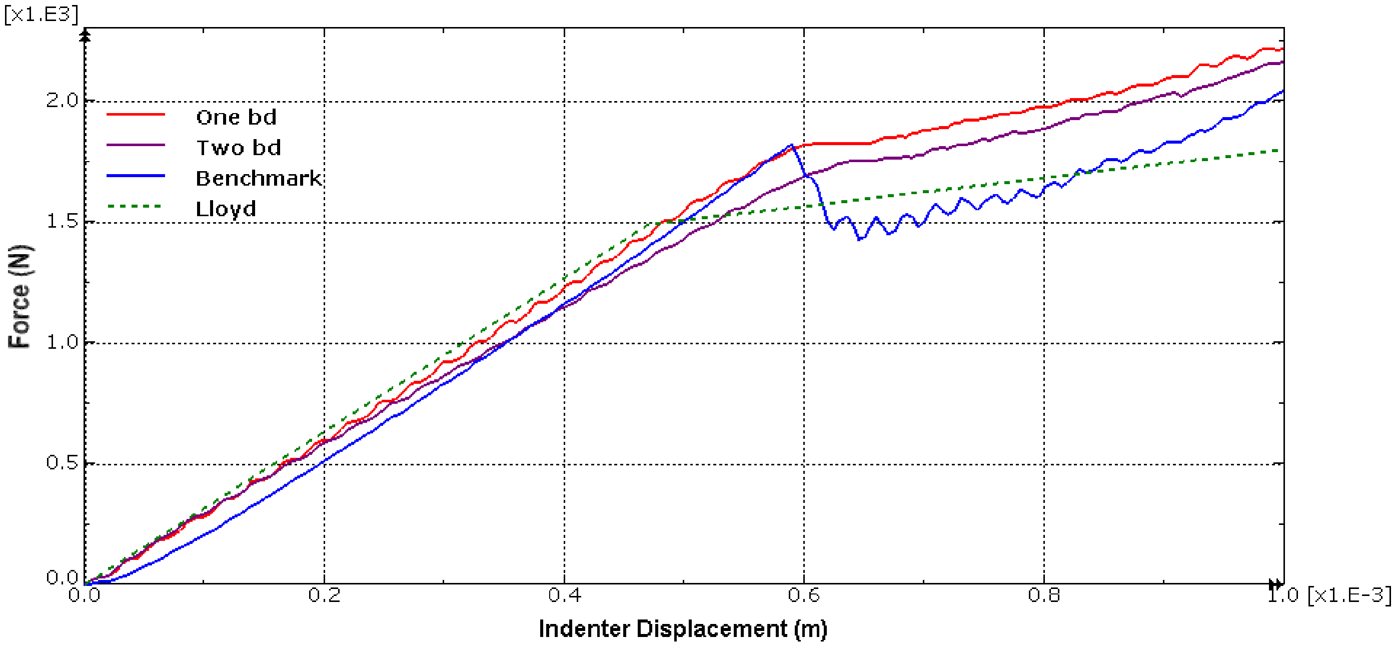

Figure 64: Force-displacement response of cohesive models against experimental and numerical benchmarks

Figure 65 shows the response of the same single-bond model with different damage evolution parameters. The original model uses mixed-mode fracture behaviour with linear softening, as mentioned previously, and it is compared here with mode-independent fracture - *Mode 1* using 275 J/m^2 for normal-opening fracture only, and *Mode 2* using 940 J/m^2 for shear-opening fracture only, shown by light cyan and dark cyan curves respectively - and against results for mixed-mode fracture with exponential softening (*Exp,* purple).

The responses shown in Figure 65 demonstrate the significance of using mixed-mode fracture in generating accurate results. The use of mode-independent fracture fails to take into account the interaction between normal opening and shear opening of cracks – selecting the lower of the fracture energies, associated with mode 1 normal opening (light cyan) results in significantly premature damage onset. The higher fracture energy, associated with mode 2 shear opening (dark cyan) produces a result similar to that including mixed-mode fracture, suggesting that shear opening is the dominant fracture mode in this case. The linear softening law used in the main model is the preferred option, as the use of exponential softening (*Exp,* purple) appears to suppress the load drop that should arise at the onset of damage.

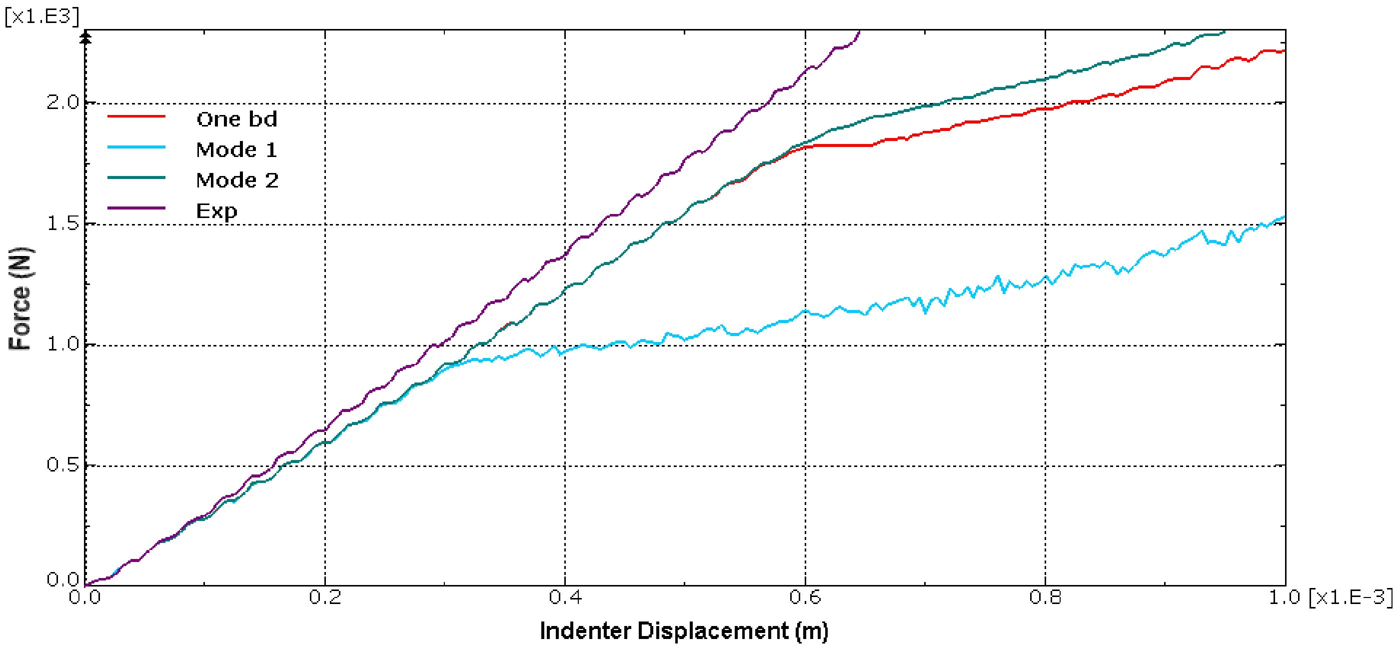

Figure 65: Force-displacement response of single-layer cohesive model with different damage evolution strategies

4.3.3 Damage Evolution – Intralaminar Damage

As previously stated, after the onset of delamination in Lloyd's experiment, the load in the plate is increased, with membrane stiffening being observed, until the plate eventually fails due to fibre fracture. To model this behaviour, damage initiation and evolution is now reintroduced into the composite material model for the plate with the cohesive element layer.

Numerical difficulties were experienced here, due to the mismatched bond and ply meshes. Recall that for this model, a highly-refined layer of cohesive elements is tied to two ply blocks, which use a much coarser mesh. This had been intended to improve computational efficiency by avoiding the use of an overly refined mesh in the plies, while retaining the fine mesh required for a correct cohesive model response. The problem arises just over half-way through the analysis run, as the interactions between the tied meshes causes severe element distortion in the bond layer, resulting in premature analysis failure. Altering the meshes and the loading rate do not appear to solve the problem; rather, it appears to be a fundamental difficulty in using tied constraints with a cohesive layer in this particular problem, as the elements in the cohesive layer are failing due to shear sliding, rather than normal opening. More work is required to achieve a thorough understanding of this particular problem. The force-displacement plot for this model is included in Figure 66 (*Tied*, red). Up to the point of analysis failure, the overall shape of the response is very promising, with initial softening due to delamination, followed by a load increase due to membrane stiffening. As previously noted, the numerical response doesn't fit the experimental curve particularly well, due to the necessary assumptions made in the material data.

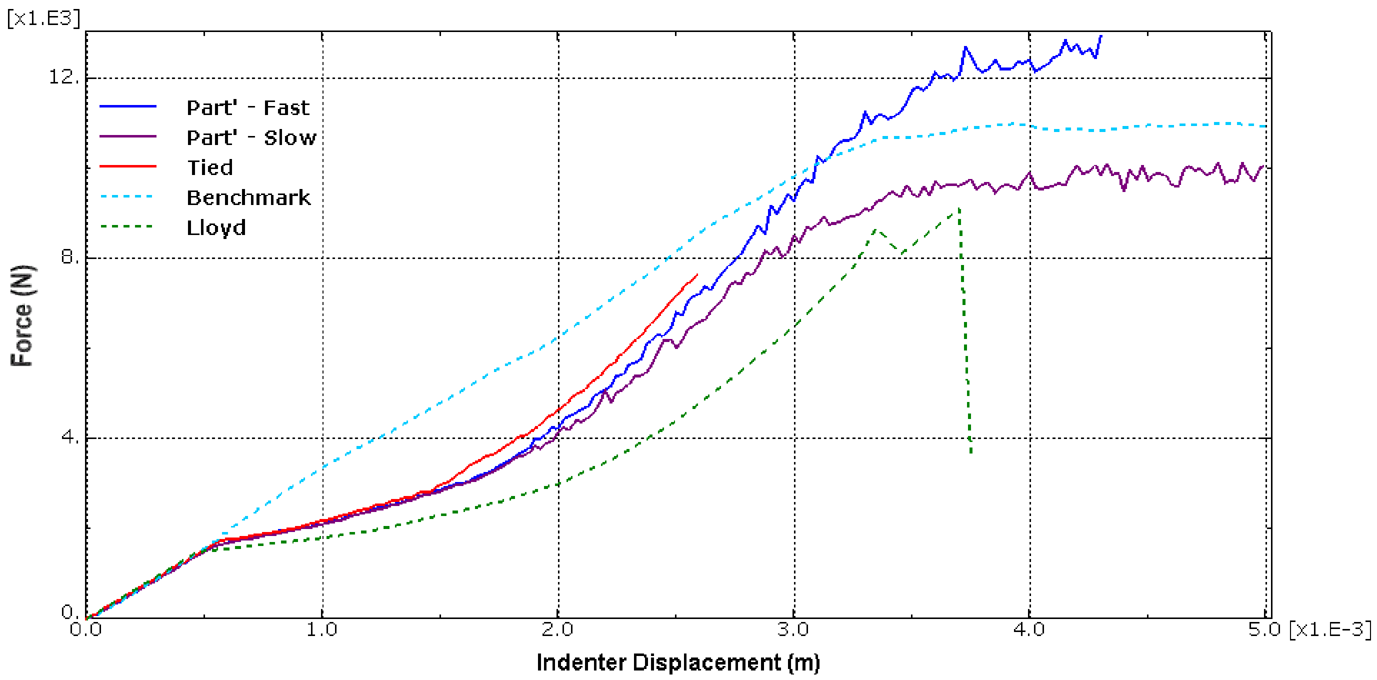

Figure 66: Force-displacement responses of models with a single, central cohesive layer, with intralaminar damage included

As a consequence of this analysis issue, a change of tack was required. A different approach to discrete ply modelling was adopted, whereby the whole plate is modelled as a single part, partitioned into different geometric regions (for this model, one unique region through-the-thickness per ply block and/or bond layer is used). The required material properties and orientations are then applied to each region. In this instance, the two ply blocks are treated as individual composite laminates, mated together to provide the required symmetric layup, as before – in the case of each layer of the laminate being modelled separately, the composite layup tool would not be required, and the orientation of each ply would simply be applied directly. The use of this approach eliminates the issue of mismatched meshes experiencing severe distortion under heavy loading via imposed constraints. The downside however is that the significant mesh refinement required in the cohesive layer is necessarily copied through the thickness of the part, with a corresponding increase in computational effort; it has not been established whether different mesh densities can be produced for a part modelled in this manner.

Figure 66 shows the response of both the initial discrete ply model, using tie constraints, that was used in the previous section (red) and the modified model utilising a partitioned model (*Part'-Fast*, blue). This is compared with the experimental results (green) and a modified version of the benchmark model discussed previously and shown in Figure 64, which is indicated here by the dashed cyan line. This new benchmark model uses intralaminar fracture energies set to their 'true' values – it is worth reiterating that these energies are estimated based on the values found for a different material, and thus may not necessarily be correct for this material system. Otherwise, the old and new benchmark models are identical, and lack any kind of cohesive layer, and so do not experience delamination. Finally, a 'slow' partitioned model, using a 10 ms step time, but otherwise identical to the one generating the blue curve (with a step time of 5 ms), is shown here by the purple curve.

The first thing to note here is how critical it is to allow for delamination onset and propagation in the numerical model. With the correct fracture energy applied to the benchmark model, there is no meaningful change to the force-displacement response at the point of damage onset, as the material stiffness does not degrade particularly quickly. As a result, this model produces a response more reminiscent of the elastic-plastic behaviour of, say, an aluminium alloy. Introducing the cohesive layer allows the model to capture the stiffness degradation due to delamination correctly. The response of the tied model at delamination onset has already been discussed, and the responses of the partitioned models are broadly the same. The partitioned models deviate from the tied model at approximately 2.9 kN, and thereafter gives a slightly better (but still fairly poor) estimation of the experimental response in the membrane stiffening phase of loading.

The fast partitioned model, like the tied model, does not complete the analysis, suffering from severe element distortion late in the run. However, the element distortion in this case is due to the complete degradation of the material in the ply blocks – indeed, at this point in the analysis, very extensive fibre damage is observed in all plies. Thus, this model can be considered successful. The slow partitioned model completes the analysis without fatal errors. The other key difference between the partitioned models and the tied model is that the former models starts to exhibit gradually worsening noise in the response after about 4 kN. This corresponds with complete degradation of the entire cohesive layer in the model, indicating total separation of the two halves of the plate, at least within the clamped boundary. Figure 67, representative of both partitioned models, shows the cohesive layer in isolation (the two ply blocks are hidden) at 0.5 mm and 1 mm indenter displacement (*a* and *b* respectively). The parameter *SDEG* is the stiffness degradation in the layer, with a value of 1 indicating a fully degraded (failed) element.

The initial stiffness reduction occurs at approximately 0.5mm displacement, and this is confirmed by Figure 67a. The initial delamination is fairly extensive, with a diameter of approximately 7.5 mm (estimated from the mesh density). This then grows very rapidly, covering more than half of the plate at 1mm displacement (Figure 67b). Both analyses eventually terminate due to fibre failure, as mentioned previously, but show the load reaching a plateau as opposed to the sharp drop seen in the experimental result. This plateau occurs at approximately 12.7 kN for the fast model, which is clearly a much higher load than the failure load of 9.1 kN seen in the experiment, with a percentage error of 39.6%. Curiously, this model produces a more significant overestimate than the benchmark model without a cohesive layer, despite using a slightly longer step time. The slow partitioned model produces a far more promising result – though it is still non-conservative compared to the experimental result, it is much closer, with the plateau occurring at approximately 9.9 kN, for a percentage error of 8.8%.

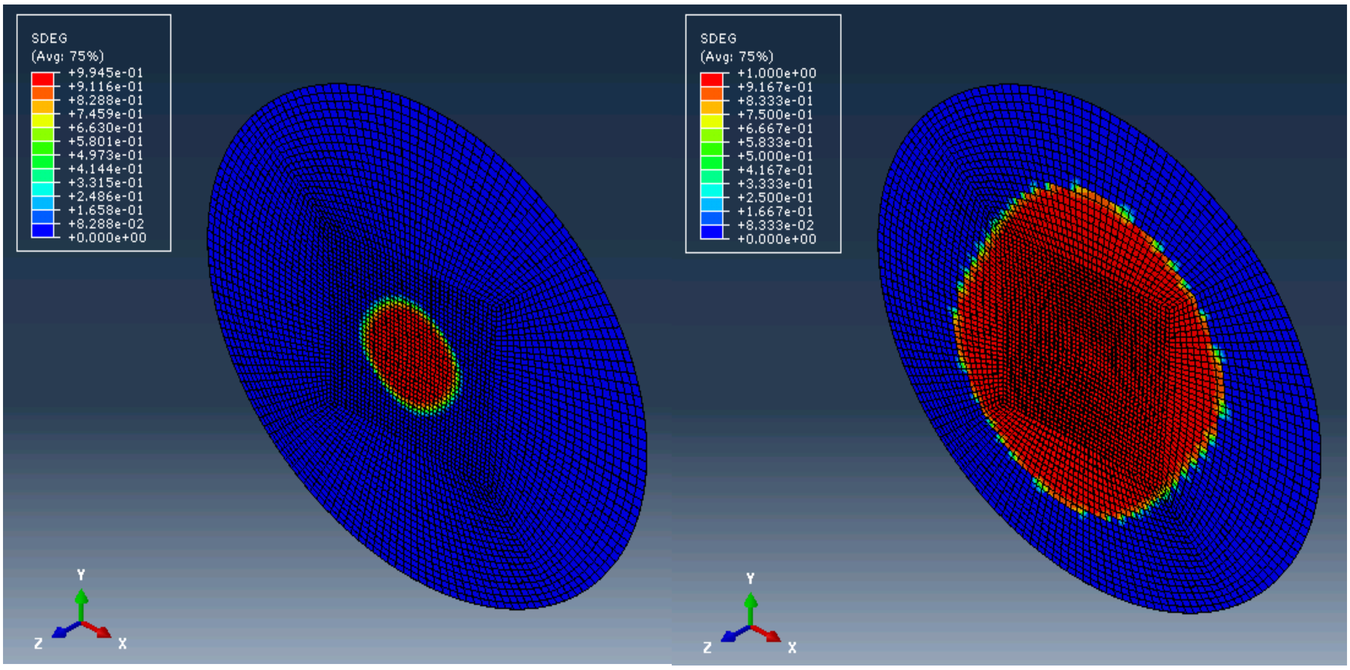

Figure 67: Degradation of the cohesive layer at (a, left) 0.5mm and (b, right) 1mm indenter displacement

While the predicted severity of the delamination is suspect, and the failure load showing a plateau rather than a sharp drop is not ideal, that the cohesive layer is showing the onset and propagation of delamination, and that this has a subsequent effect on the load-displacement response of the plate, is a very encouraging result, which will be extremely valuable for the sandwich panel models to follow. The close agreement for the ultimate strength using the slow model is also very useful.

The final consideration is the effect of mass scaling, an additional modelling technique that has been hitherto neglected. As mentioned in Chapter 2.4.1, this is a technique specific to the explicit solver used to improve the computational efficiency of dynamic analyses, by selectively increasing the elemental mass density to reduce the stable time increment. This technique is trialled here. Figure 68 shows the fast partitioned model (blue, denoted as *'No MS'*) compared with an otherwise identical model with variable mass scaling applied (gold), both over a shortened analysis run (1mm displacement). The mass scaling function is set to achieve a minimum time increment of 1e^{-8} s, by automatically increasing the mass of critical elements in the mesh. The positive effect on the run time is indisputable – the scaled mass model completes the analysis in 3 hours, as opposed to the unscaled model which takes 12 hours (both use two processors). For completeness, note also that the slow model just discussed completed the analysis in around 14.5 hours, using four processors. The mass scaling used here has a significant negative effect on the results, producing a response almost identical to the mode-independent fracture response (Mode 1) from Figure 65 (cyan). This is an obvious deviation from the expected behaviour, though it is unclear why the response suddenly seems to become dominated by a normal opening fracture mode when all other aspects of the two models are the same. Additional work here is appropriate, since the runtime benefits of using mass scaling are too significant (and potentially useful) to abandon the technique altogether - while good results have been shown to be achievable, the computational requirements may prove problematic. All this said, producing good quality results remains the priority, and the work presented in this chapter provides a very solid foundation upon which the sandwich panel models can be developed. Crucially, the use of rigid surfaces in conjunction with a contact algorithm for load application, the explicit dynamic numerical solver for the analysis, and the Hashin criteria and the cohesive zone model have all been shown to work effectively in modelling load and damage in composite structures.

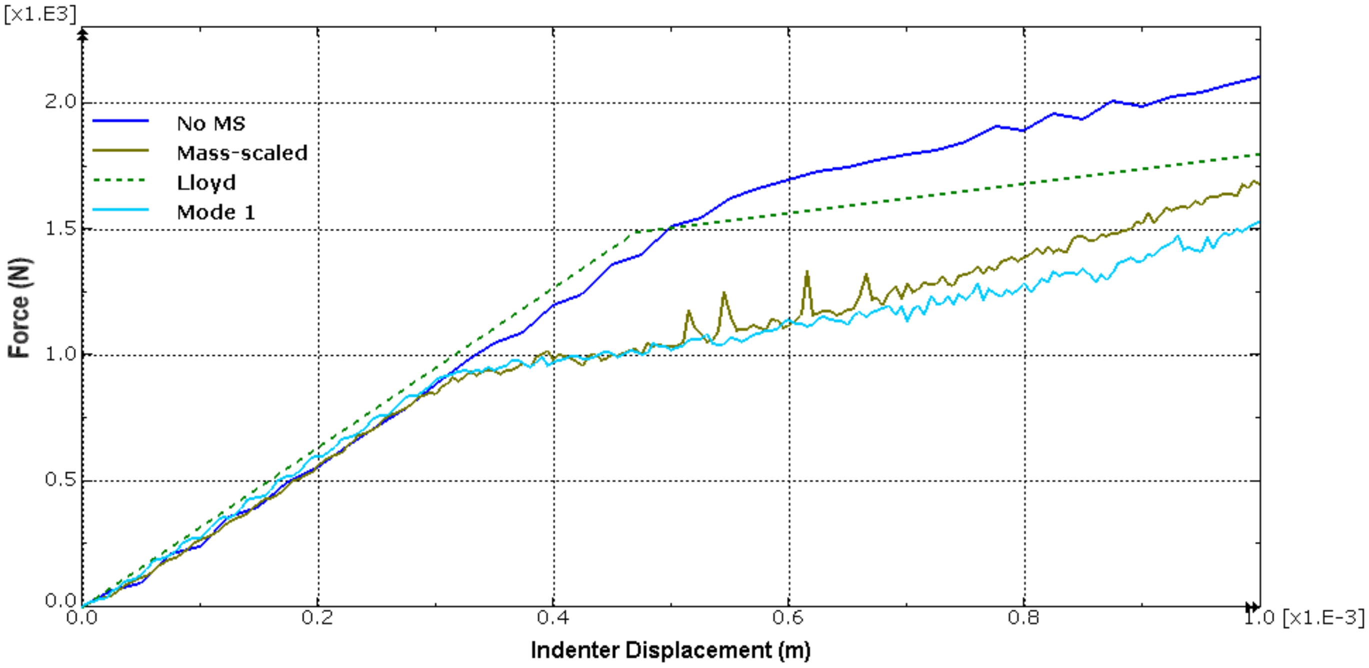

Figure 68: Load-displacement response of mass-scaled and unscaled models

Based on the work presented in this Chapter, it is shown that delamination and intralaminar failure in composite plates can be successfully simulated using the cohesive zone method and Hashin criteria. This necessitates the use of the explicit solver in *Abaqus* to ensure robustness once the material behaviour becomes highly non-linear. The use of a rigid surface in combination with a general contact algorithm is a convenient method for applying the load and extracting the force-displacement data. Continuum shell elements are suitable for meshing the plates, as it may be readily applied to a 3-dimensional geometry (useful for sandwich panel construction, where multiple components may need to be assembled) and allow improved through-the-thickness fidelity over their conventional 2-D counterparts. The sandwich panels developed in the following Chapters will thus implement all of these features.

Chapter 5

Sandwich Model Development

5: Sandwich Model Development

The numerical model for a sandwich panel representative of the experimental work described in Chapter 3 is developed and presented herein, using the skin model developed in Chapter 4. The model allows for the formation and propagation of delaminations in the impacted skin of a sandwich panel subject to a quasi-static indentation (which serves as an approximation of a low-velocity impact), followed by edge compression. The influence of this damage mechanism is used in conjunction with the Hashin composite failure criteria, and a simple plasticity model to capture core crushing. This model is prepared using material and panel configuration data from an experimental study by Czabaj et al [33,40]; the results from this study are used for comparative purposes. The predicted and measured damage extents will also be compared, to ascertain whether there is a link between the quality of the damage prediction and the accuracy of the strength estimate.

5.1: Czabaj, Singh et al Experimental Studies

A number of panel configurations and layups were studied by Czabaj et al [33,40], using panels with carbon-epoxy skins (IM7/8552) and aluminium honeycomb core (HexWeb CR-III, 3.2mm cell size, 5052 aluminium alloy). This model simulates the the*'Q1-C1'*, *'Q1-C2'* and *'Q2-C1'* configurations indicated in Czabaj et al. *Q1* and *Q2* relate to two of the quasi-isotropic lay-ups used by Czabaj et al, with lay-ups of $[45/0/-45/90]_S$ and $[45/-45/0/90]_S$ respectively. *C1* and *C2* correspond to two of the cores used in the Czabaj et al study, both with density 49.7 kgm^{-3}, but with thicknesses of 25.4mm and 16.5mm respectively. The planar dimensions are 178 x 152 mm for all panels. Only the cross-sectional area of the skins is used for the strength calculation: with a nominal ply thickness of 0.127mm, this gives a skin thickness of 1.016mm, for a total cross-sectional area of 3.08864 $x10^{-4}$ m^2. The ribbon direction of the honeycomb core and the 0º plies in the skins are parallel to the longer of the panel's planar dimensions. This is also parallel to the loading direction in compression. Panels damaged with the smaller indenter tended to show lower residual strengths in the experimental investigation, perhaps due to fibre fracture during indentation, which was not caused by the larger indenter.

The initial damage is produced via quasi-static indentation due to an applied load, recreating the damage induced in sandwich panels during an experimental study by the Singh et al [168]. Two sizes of indenter, both hemispherical, are used here, with a suitable load applied to correspond with the onset of Barely Visible Impact Damage (BVID). For the 76.2mm indenter, this load equalled 2,800 N. The smaller 25.4mm indenter required a 1,300 N load for BVID. Both cases are modelled here for each of the panel configurations stated above, as well as the undamaged (virgin) panels for each configuration, for nine models in total. During the quasi-static indentation, the panel was rigidly supported – that is to say, it was placed on a solid surface, with no additional constraint necessary. For the subsequent edge compression, the free edges of the panel were left unconstrained. The strength results from this study are included with the predicted strengths from the model in Table 13. Failure in the virgin panels tests was usually via microbuckling, shear fracture, or a combination thereof in the 0° plies with subsequent fracture in the rest of the plies in a direction perpendicular to the loading direction [40]. The nature of the damage caused by the QSI varied depending on the skin and core configuration; from Singh et al [168], the *Q2* lay-up experienced more delamination than the *Q1* lay-up, due to the presence of 90° changes in ply orientation. The panels with the thinner *C2* cores also experienced more delamination then those with the *C1* core, due to reduced load redistribution resulting in an effectively stiffer structural response. Finally, the larger indenter induced larger delaminations, though this conclusion is based on qualitative rather than quantitative assessments.

5.2: Model Description

The final form of the model developed in the current work has the following features:

- The panel model has a single symmetry plane parallel to the compressive loading, so for efficiency, a half-model is used, with a symmetric boundary condition ensuring correct model behaviour. Note that in post-processing, the reaction forces must be doubled to give a true representation of the structural response.
- The analyses are performed as multistep analyses. A quasi-static transverse indentation is applied first, under load control. The indenter is then withdrawn and finally, after a pause step to facilitate redefinition of boundary conditions, a quasi-static edge compression is applied via displacement control to find the residual strength of the damaged panel.
- All steps use a dynamic explicit solver, due to the highly non-linear structural response arising from material damage and failure. The indentation load is applied at a rate of 1MN/s, and the compression-after-impact (CAI) displacement is applied at a rate of 0.5m/s. The use of load control in the indentation phase is not ideal, but in lieu of displacement information for this phase, ramping the load to the stated target load must suffice. These loading rates represent a significant acceleration of the problem as compared to a true quasi-static analysis. The rule-of-thumb for simulating quasi-static loadings with a dynamic solver assumes that the response of the structure is quasi-static provided that the kinetic energy does not exceed 5% of the system internal energy [147]. The ratio between kinetic and internal energy falls well below this accepted threshold for these loading rates – a typical example here, *Q1-C1-lg-3,* has an energy balance of 0.02% in the indentation phase and 0.33% in the compression phase - so the quasi-static loading assumption can be considered valid. The peak load is taken as the point of reference in both steps, as the kinetic energy will inevitably spike at ultimate load, due to a loss of system equilibrium.
- Both the initial indentation and compression-after-impact loading are applied via rigid surfaces using a general 'all-with-self' contact interaction. This allows the load and displacement history for both steps to be generated by monitoring a single node that defines the surface. The rigid surfaces have small masses applied to the controlling

nodes, to enable their use with the explicit solver, while minimising the effect of inertia.

- The cohesive surface interactions between surface pairs, forming the interlaminar interfaces for delamination prediction, are defined within the general contact definition, using the material data given in Table 10. There are two locations for the cohesive interface: configuration *1* places the surface at the third interface from the indented surface in the indented skin (between the -45º and 90º plies in the *Q1* lay-up, and the 90º and 0º plies in the *Q2* lay-up). This surface is denoted as 'cohesive surface 1' in Figure 41. Configuration *2* places the interface at the fifth interface from the indented surface (between the 90º and -45º plies in the *Q1* lay-up, and the 0º and 90º plies in the *Q2* lay-up); this surface is denoted in Figure 69 as 'cohesive surface 2'. There is also a third configuration presented here, which includes both of the above-mentioned cohesive surfaces. These locations have been chosen because delamination is expected to occur at a location where there is a change in fibre orientation [168].
- The skins are perfectly bonded to the core using tie constraints. The sets used to define the tied regions are selected such that a region around the edges of the mated parts are treated as unconstrained, to avoid clashes with the boundary condition definitions.
- All boundary conditions are applied to sets defined at the assembly level. For convenience, these sets are defined by geometry.
- Skins are meshed using 8-node general-purpose continuum shell elements with reduced integration (SC8R). The composite lay-ups are defined using *Abaqus'* lay-up tool, with Hashin criteria used to model laminate damage initiation and evolution [118]. The core is modelled as a solid, using a homogenous orthotropic core model with crushing behaviour applied via a simple plasticity response. It is meshed using 8-node linear solid elements with reduced integration (C3D8R). Hourglass control is applied to all elements by default, preventing spurious compliances under loading.
- Damage in the cohesive interface is initiated via the quadratic traction criteria and damage evolution controlled by the energy-based Benzeggagh-Kenane criteria with linear softening behaviour.
- The indented skin (which is split into two or three blocks to allow for the inclusion of the cohesive surface, depending on the configuration) has approximately 1 element every 0.46mm on average, with the mesh density increasing significantly towards the indented region. This level of refinement is necessary for the cohesive surface to provide a reasonably accurate description of the initiation and propagation of the delamination. Indeed, to improve the delamination prediction would require even greater mesh refinement; for composite materials, the cohesive zone whereby damage is developing will typically be tenths of a millimetre in length, and it is recommended to have at least three elements in this region to produce an accurate cohesive response [122,125]. The mesh size chosen is a compromise solution, giving an acceptable load-displacement response without requiring excessive computational resources, which was verified via a brief mesh sensitivity study, performed by trialling the preliminary models with different mesh densities (presented in the next section). The two cores

are meshed with approximately 1 element/mm in the through-thickness-direction to ensure a good representation of the core crushing behaviour. The distal skin has a relatively coarse mesh, as its response is only of secondary importance in this particular model. In total, the models contain approximately 113,000 elements; the exception is the *Q1-C2* model, which has approximately 94,000 elements, due to the thinner core. Model configuration *3*, with the additional cohesive layer, has between approximately 138,000 and 119,000 elements, depending on the core thickness.

- The key data output is the reaction force and displacement at the compression surface's controlling node, and the system's kinetic and internal energies. The force and displacement of the indenter is gathered to confirm the required load level for the damaging event is reached. Full-field data is collected for the out-of-plane displacement, the stiffness degradation in the cohesive surface, indicating delamination, and intralaminar damage. This data is used to predict the extent of the damage induced by the indentation.

A small number of preliminary models were produced and analysed before the final form described above was settled upon, based upon the *Q1-C1-lg* configuration only. These approaches are as follows:

P1: A single cohesive element layer introduced to the mid-plane of the top (impacted) skin only.

  i. A variant of this model uses a cohesive surface interaction, which provides a cohesive interaction without needing a separate layer of element, between the two ply blocks, as opposed to a layer of cohesive elements. Two versions of this model are trialled, using moderately refined and highly refined meshes. These will be distinguished using the suffixes *–mid* and *–hi* respectively.

P2: A single layer of cohesive elements added to the mid-plane of both skins. Both models using cohesive elements are added by the use of partitions in the part model, and are meshed using 8-node cohesive elements (COH3D8).

P3: Three cohesive surface interactions are added to the top skin, dividing the top skin into pairs of plies. Two versions of this model, using coarse and refined meshes, are trialled, designated using the suffixes *–lo* and *–hi* respectively.

The final model is shown schematically in Figure 69, showing load directions, boundary conditions, material orientations and interfaces. The meshed model (*Q1-C1-lg-1*), also showing the rigid surfaces used to apply the loadings, is shown in Figure 70. Note that degrees-of-freedom *1, 2* and *3* and displacements *u, v* and *w* act in the directions of the *x, y* and *z* coordinates respectively.

The material data used in the model is given in Table 10. The data is predominately taken from Czabaj (the 'corrected' data stated in [40] is used here). Some data has had to be taken from other sources, namely the core ultimate and crush strengths, taken from Hill [4], and the cohesive layer properties. There is no data provided by Czabaj for the interlaminar behaviour of this particular material, so the required data is predominately gathered from Camanho &

Davila [75] for a similar carbon-epoxy material. The exception is the normal opening and shear opening fracture energies, and the interlaminar shear strength, which are taken from Lloyd [163] for another carbon-epoxy composite. The mode-mix ratio used in the Benzeggagh-Kenane criterion for fracture propagation is also taken from Camanho & Davila, for yet another material system. This lack of consistency in the interlaminar material data must be regarded as a potential source of error, though it should be noted that the interlaminar performance of these different materials is reasonably similar. The data provided assumes a cohesive layer of 10 microns thick. Damage stabilisation is applied to the skin and cohesive models to ensure smooth behaviour. This is set at $1e^{-6}$ for all stabilisation parameters, to prevent stabilisation having an undue influence on the solution. Note in Table 10 that the numbers *1*, *2* and *3* correspond directly with the same numbers in Figure 69. For the strength directions, the first letter (*L* or *T*) refers to the longitudinal (*1*) direction or transverse *(2)* direction respectively. The second letter (*T* or *C*) denotes tension and compression respectively.

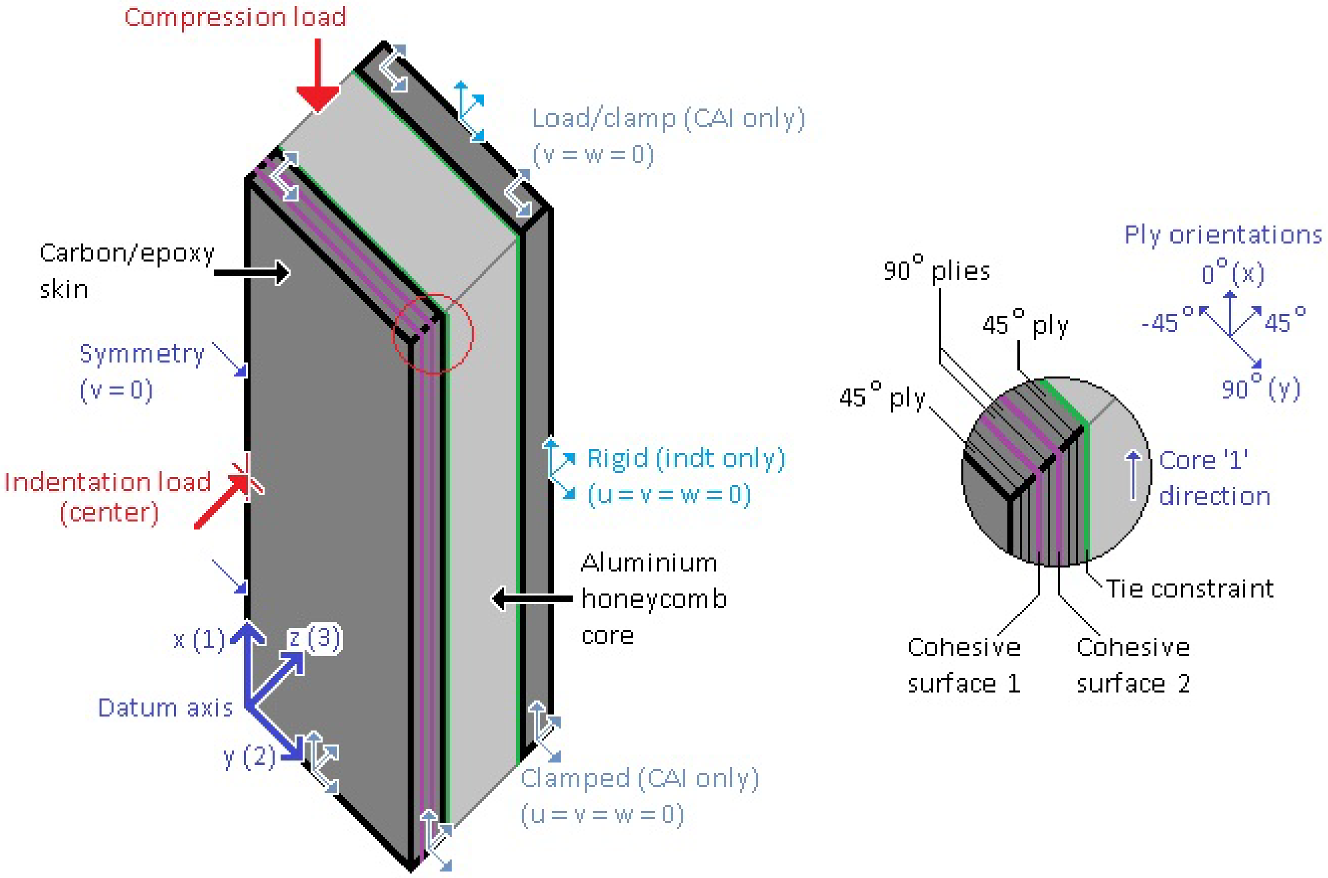

Figure 69: Schematic representation of the composite sandwich model, including boundary conditions, load and material directions and interfaces [1,2]

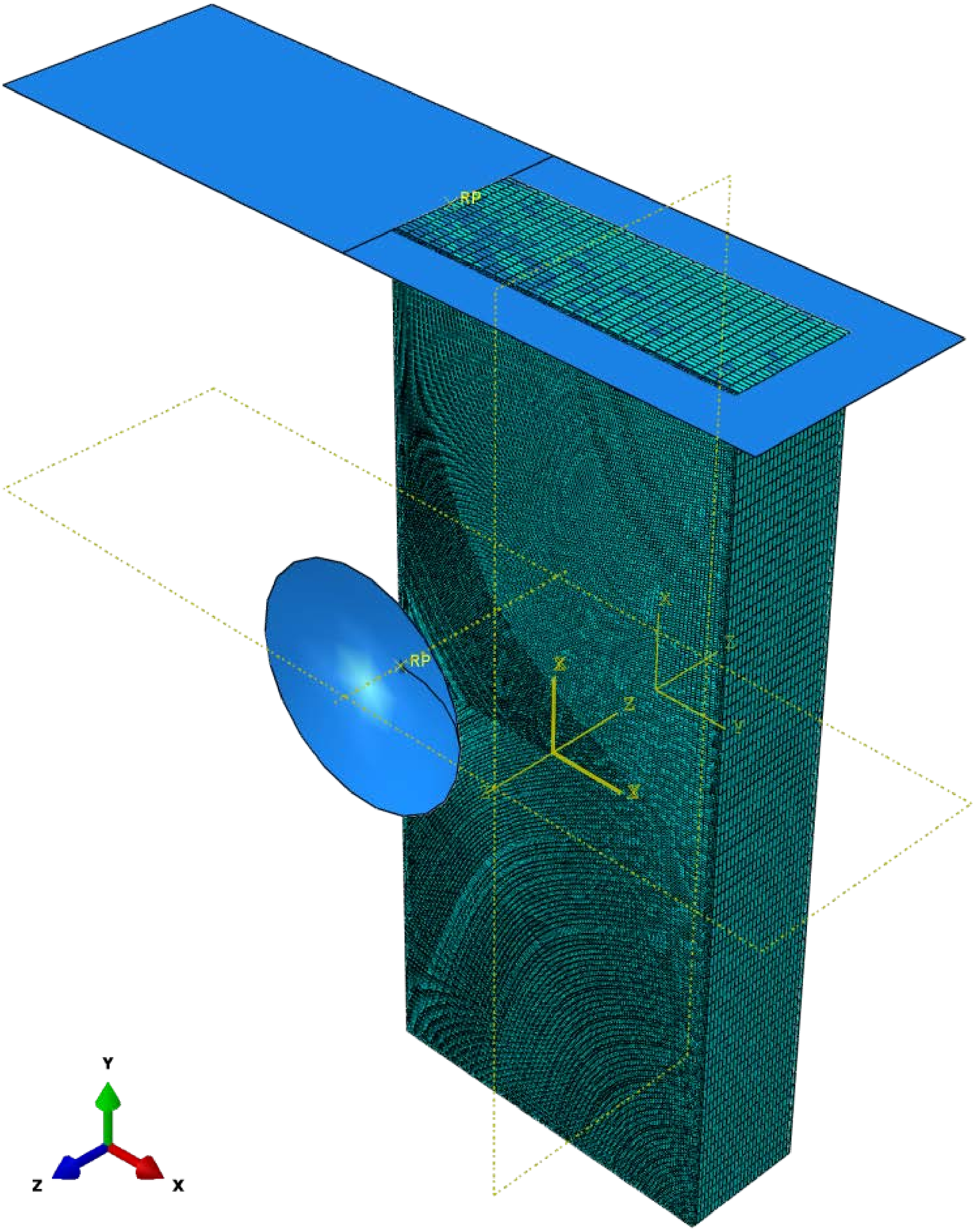

Figure 70: Meshed sandwich including rigid surfaces for load application (Q1-C1-lg-1) [1]

Table 10: Material Data for Czabaj Numerical Model [1]

		C-E skins	Al HC core	Bond
t (mm)		0.127 (ply)	25.4 or 16.5	0.01
ρ (kg/m^{-3})		1,770	49.7	-
E (GPa)	**1**	143	1.48 x10^{-4}	
	2	12.9	1.47 x10^{-4}	
	3	-	1.1	
K_{E3} (TPa/m)			-	1,100
G (GPa)	**12**	4.13	8.9 x10^{-5}	-
	13	4.13	0.17	
	23	3.98	0.127	
K_G (TPa/m)	**m2**	-	-	600
	m3			370
ν	**12**	0.32	1	-
	13	-	1 x10^{-5}	
	23		1 x10^{-5}	
σ (MPa)	**LT**	2,323	-	
	LC	1,200		
	TT	160.2		
	TC	199.8		
	Ult	-	2.3	
	Crush		0.9	
	mode 1		-	45
τ (MPa)	**L**	130.2		-
	T	151.7		
	m2	-		66.3
	m3			66.3
G_C (N/m)	**LT**	81,500		-
	LC	106,300		
	TT	277		
	TC	788		
	m1	-		275
	m2			940
	m3			940
Mode-mix ratio				2.284

The Czabaj et al investigation used composite skins produced from uni-directional prepregs rather than fabric composites, such as used by Hwang & Lacy [11,12]. Thus, using *Abaqus's* composite layup tool is more likely to produce an accurate result for this material configuration. The material of the honeycomb is also significant. Modelling a nomex honeycomb as an orthotropic solid with elastic-plastic behaviour to simulate crushing may not be ideal, as the aramid paper that the core is made from is itself an anisotropic material, with failure under compressive loading occurring via fracture rather than cellular buckling [139]. Czabaj et al induced damage via quasi-static indentation, so in this model there is no need to try to and approximate the dynamic impact event; as well as potentially improving the accuracy of the results by removing the influence of inertia and strain-rate dependency, it is also more efficient from a modelling perspective, as the damage event does not require calibrating in terms of finding a level of applied displacement that will produce a state of damage representative of that produced via impact. The key departures of the current model from the Czabaj et al exercise include the use of a homogenous orthotropic core throughout in the current model, whereas Czabaj et al included a region under the indenter with an explicitly modelled honeycomb geometry. Additionally, Czabaj et al used skins meshed with solid elements, without a prediction method for delamination initiation and growth, whereas the current model utilises continuum shells, with the cohesive zone method providing delamination simulation.

The models are all run on a 64-bit Intel Xeon supercomputing cluster due to their size. Note that wall time is defined as the real time the problem is run for. CPU time is the equivalent time a single CPU would require to complete the run, and the parallelisation efficiency of the run is provided by dividing the wall time by the CPU time, and then dividing this number by the number of cores used for the analysis. The supercomputing cluster is split into 161 processing nodes, with each node containing two six-core Intel Westmere Xeon X5650 CPUs, for a clock speed of 12 x 2.66 GHz. As far as the author is aware, it is not possible to split an analysis over multiple nodes. This, combined with a hard limit on the wall time of 100 hours, creates a limit on the amount of CPU time available for a single analysis of 1,200 hours. It is possible to run analyses for longer than 100 hours of real-time via the use of *Abaqus'* restart functionality, but this was not used here to avoid over-use of available resources.

5.3: Preliminary model results

Table 11 gives the strength results from the preliminary sandwich models described in the previous section. The numerical result is compared with the maximum strength result given by Czabaj's experiments [40] for this panel configuration. Table 12 gives the runtime data for these models, so the computational performance of the analysis can be assessed. Note that virgin panel models were not produced for every model configuration. In these, and all following cases, the strength is found by simply dividing the peak force output by the numerical model by the cross-sectional area of the skins, which was previously given as 3.08864 e^{-4} m^2 for every panel configuration under consideration in this Chapter.

From these tables, it is clear that introducing a cohesive layer to the impacted skin alone provides a very good estimate for the strength of the panel, provided that the mesh is sufficiently refined to allow the cohesive zone model to behave correctly. Including the cohesive layer on both skins results in a large over-estimate of the CAI strength. Model *1-i-hi* and *3-hi* both show very good agreement with the experimental result for the damaged model, with the former model being nearly as accurate as the latter model, while requiring less than a quarter of the computational resources, despite being less than half the size in terms of the number of elements. This difference is due to the number of cohesive interactions: even though these relationships do not contribute to the element count, computational effort is still required to solve them, so obviously increasing the number of cohesive surfaces increases the computational effort.

Table 11: Numerical results for the preliminary Czabaj sandwich models

Model	Virgin strength (MPa)	CAI strength (MPa)	% error (CAI)
P1	465.34	347.27	+6.99
P1-i-mid	-	271.13	-19.1
P1-i-hi	506.01	319.49	-1.1
P2	-	413.6	+21.91
P3-lo	-	359.13	+10.1
P3-hi	460.63	324.59	+0.49

Table 12: Runtime data for preliminary models

Model	Problem size (elements)	Cores used	Wall time (hours, mins)	CPU time (hours, mins)	Parallelisation efficiency (%)
P1	116,328	12	40h 16m	471h 44m	97.6
P1-vir	116,328	8	3h 29m	25h 21m	91.0
P1-i-mid	80,612	6	30h 13m	167h 37m	92.5
P1-i-hi	156,642	6	45h 41m	256h 59m	93.8
P1-i-hi-vir	156,642	12	6h 30m	63h 42m	81.7
P2	205,816	12	50h 25m	588h 15m	97.2
P3-lo	70,016	12	33h 12m	372h 33m	93.5
P3-hi*	146,464	12	90h 1m	1063h 48m	98.5
P3-vir	146,464	12	18h 0m	207h 58m	96.3

**Did not finish; wall-time allocation for run exceeded*

The results for the virgin models are more questionable when compared with the experimental results. *1* and *3-hi* are both outside experimental variation, but are within 10% of the upper end of this range. *1-i-hi* gives a result that over-estimates the maximum experimentally observed virgin strength, for a percentage error of +19%, as compared to the upper limit of the experimental range (425.4 MPa). However, it is noteworthy that the three virgin models give results within 10% of one another. It should also be reiterated that scatter in experimental data for edge compression of panels is a well-recognised problem, due to its sensitivity to geometric imperfection, and the models assume a perfect panel, so these results cannot be discounted out of hand, even though these limitations cannot be ignored either. One observation worth making is that the elements at the boundary between the core and the bottom (un-impacted) face show considerable deformation, as the distal skin tries to buckle away from the core. This suggests that skin-core debonding may be a valuable inclusion in the model at this location, though it should be noted that panel failure occurs before this deformation is observed, so the apparent debonding seen here may be a consequence of panel failure, rather than influencing the failure itself. Based on these above results, model *P1-i-hi* will be carried forward for the modelling of the experiments.

The preliminary models form a mesh sensitivity study of sorts as well. The computational demands of the analysis mean that performing a full mesh sensitivity analysis would consume too many resources, especially due the model being made up of numerous components, the refinement of each part undoubtedly having its own influence on the overall mesh sensitivity of the model. The number of elements in each variation is obviously governed as much by the structure of the model as the mesh refinement. Direct comparisons are possible with *1-i* and *3*. *1-i-mid* and *1-i-high* have 80,612 and 130,407 elements respectively, and *3-lo* and *3-hi* have 70,016 and 146,480 elements respectively. Clearly, and intuitively, increasing the mesh refinement improves the accuracy of the results. The highly-refined models showed very good agreement with the experiments so there was no need to further refine the mesh, as the increase in computational effort would not be worth the marginal improvements in accuracy. The accuracy of the solution drops quite quickly with coarser meshes; this is particularly clear with *3-lo*, despite the notionally more accurate structure of the model. This will at least partly be due to inaccuracies in the cohesive model response with the coarser meshes.

The loading rates applied result in significant acceleration of the problem. Both the indentation and the edge compression are quasi-static loadings in actuality. The reader is reminded of the rule-of-thumb for simulating quasi-static loadings with a dynamic solver, which assumes that the response of the structure is quasi-static provided that the kinetic energy does not exceed 5% of the system internal energy. It is difficult to determine whether this criterion is met during the indentation phase, as the indentation is applied via load control rather than displacement control, resulting in a non-linear displacement-time response, and consequently a complex relationship between kinetic energy and internal energy. Considering *1-i-hi*, the peak displacement, corresponding to the peak load occurring at 5.6ms, is 4.313mm, giving a peak kinetic energy for the indentation phase of 0.297J. The system internal energy at this time is 7.271J, giving an energy balance (the ratio of kinetic energy to internal energy) of 4.09%. This falls comfortably within the threshold for a quasi-static response. Next, the edge compression phase is considered up to 9.08ms, where panel failure occurs (the loss of system equilibrium inevitably causes a spike in the kinetic energy here). At this time, the kinetic energy is 0.64J and the internal energy is 30.17J. This gives an energy balance of 2.12% for the compression phase, which is also well within the 5% threshold. The energies are easier to interpret here, as the edge compression is applied via displacement control. Also, at the start of the compression phase, the internal energy is non-zero, due to residual strain energy from the indentation phase.

On the whole, it is more efficient (defined in this context as (CPU time / number of processors) / real time) to use a higher number of processors - the relatively low efficiency of the *1-i-hi-vir* run standing out as an obvious anomaly, due the overall brevity of this particular analysis - but software licensing constraints mean that it is often not possible to make full use of the hardware. Longer runs also tend to be more efficient, as the supercomputer requires a certain amount of time to get up to speed. One factor that does stand against the use of 6 cores in the supercomputing cluster is that a single core of the cluster is slower than a single core in the available desktop machines, so using 6 cores in the cluster is not appreciably quicker than using the maximum available 4 cores on a desktop. Using the desktop for the analysis runs would create separate difficulties of its own however, as the machine would become unavailable for routine usage. It should be noted that the final model is based on *P1-i*, with a mesh refinement roughly between that of the *–mid* and *–hi* variations. It should also be reiterated that the position of the cohesive surface is moved to boundaries between dissimilar ply orientations, to produce a more realistic response.

5.4: Residual Strength Prediction

The residual strength results from the final-form models are presented in Table 13. The models are all run on the supercomputing cluster mentioned previously (with exception of *Q1-C2-lg*, which is run on an office desktop computer, see asterisk). Included in this table are the mean CAI strengths for the configurations considered, as presented in the experimental results from Czabaj [40]. The suffixes *vir*, *lg* and *sm* indicate the virgin tests, and the CAI tests using damage induced by the large and small indenters respectively. Table 14 shows the strain-to-failure and stiffness predictions from the models, as compared with the experimental results.

The CAI strength results vary between very good-to-fair depending on the panel, loading configuration and model configuration. For the purposes of this discussion, a “good” result has a percentage difference, as compared to the experiments, of 10% or less, and “very good” is 5% or less. These values are based on the experimental variation in the experimental data; 5% is within experimental variation for most of the experiments, and 10% is within the maximum variation across all tests. Model configuration *1* gives the best residual strength predictions for the large indenter configurations whereas configuration *2* gives the best results for the small indenter configurations, and also the undamaged panel models. Perhaps unsurprisingly, configuration *3*, using both cohesive surfaces, offers a ‘best of both worlds’ solution, with generally good agreement with the experiments for both CAI configurations, albeit at a significant computational cost (the runtimes using configuration *3* are approximately double that of the other two configurations). What is interesting to note is that the percentage residual strength prediction, if not necessarily the absolute strength values, is generally conservative, with the agreement between the numerical and experimental percentage residual strengths sometimes becoming weaker as the agreement between the absolute strength results becomes stronger. However, the residual strength prediction is necessarily dependant on the accuracy of the undamaged strength prediction. The model seems to perform best with the *Q2-C1* configurations, as the presence of the cohesive surfaces at a 90º ply boundary (where delamination is more likely) produces a physically more accurate response. The strength results tend to be non-conservative, as the model is an idealised representation of actual structures (that is to say, the geometry, loading and boundary conditions are all assumed to be perfect), and so lack the imperfection sensitivity present in real structures.

Table 13: Residual strength results from numerical models and Czabaj et al experiments [1]

Model*			**CPU time (hrs, mins)**	**Pmax (kN)**	**σ_{CAI} (MPa)**			**% residual strength**		
					Num	**Exp**	**% error**	**Num**	**Exp**	**% error**
Q1-C1	**vir**	**1**	143h 28m	144.5	**467.8**	400.1	***16.9***	-		
		2	297h 52m	101.5	**328.7**		***-17.8***			
		3	289h 23m	150.4	**486.8**		***21.7***			
	lg	**1**	276h 19m	101.5	**328.7**	322.7	***1.9***	70.3	80.7	*-12.9*
		2	263h 1m	76.2	**246.9**		***-23.5***	75.1		*-6.9*
		3	472h 29m	104.2	**337.2**		***4.5***	69.3		*-14.1*
	sm	**1**	157h 48m	116.4	**376.7**	293.6	***28.3***	80.5	73.4	*9.7*
		2	271h 41m	86.6	**280.3**		***-4.5***	85.3		*16.2*
		3**	403h 4m	83.7	**271.0**		***-7.7***	55.7		*-24.1*
Q1-C2	**vir**	**1**	147h 40m	143.9	**466.0**	348.3	***33.8***	-		
		2	125h 42m	102.3	**331.3**		***-4.9***			
		3	282h 24m	149.8	**484.8**		***39.2***			
	lg$^+$	**1**	160h 29m	79.2	**256.3**	274.7	***-6.7***	55.0	78.9	*-30.3*
		2	146h 13m	75.9	**245.8**		***-10.5***	74.2		*-5.9*
		3	278h 19m	85.6	**277.2**		***0.9***	57.2		*-27.5*
	sm	**1**	211h 52m	93.1	**301.3**	247.3	***21.8***	64.7	71.0	*-8.9*
		2	203h 24m	76.3	**247.2**		***0.0***	74.7		*5.2*
		3	434h 3m	76.5	**247.5**		***0.1***	51.1		*-28.1*
Q2-C1	**vir**	**1**	152h 45m	148.0	**479.3**	444.1	***7.9***	-		
		2	134h 02m	139.3	**450.1**		***1.6***			
		3	291h 18m	157.4	**509.6**		***14.7***			
	lg	**1**	276h	100.6	**325.7**	299.1	***8.9***	68.0	67.3	*0.9*
		2	279h 47m	98.7	**319.5**		***6.8***	70.8		*5.2*
		3	442h 43m	103.6	**335.6**		***12.2***	65.8		*-2.2*
	sm	**1**	165h 57m	124.0	**401.5**	312.4	***28.5***	83.8	70.3	*19.1*
		2	221h 10m	107.5	**348.0**		***11.4***	77.2		*9.7*
		3	441h 20m	104.8	**339.4**		***8.6***	66.6		*-5.3*

**1 = cohesive surface 1 only;*
2 = cohesive surface 2 only;
3 = both surfaces

*** Minor adjustments to the mesh required for Q1-C1-sm-3 to avoid element distortion issues.*

$^+$ *All Q1-C2-lg models run on a desktop machine using 3 cores.*

Colour code for percentage errors:

<5%	**<10%**	**<15%**	**>25%**	**>35%**	**>50%**
🟩	🟩	🟦	🟧	🟥	⬛

Table 14: Strain and stiffness results from models and experiments

Model			Strain-to-Failure (%)			Stiffness (GPa)*		
			Num	**Exp**	**% error**	**Num**	**Exp**	**% error**
Q1-C1	**vir**	**1**	0.81	0.77	5.1	65.4	52.0	25.8
		2	0.54		-30.0	65.6		26.2
		3	0.88		14.6	55.2		6.1
	lg	**1**	0.56	0.56	-0.7	59.1	57.6	2.6
		2	0.41		-26.8	60.2		4.5
		3	0.57		2.3	58.8		2.2
	sm	**1**	0.63	0.51	24.5	59.3	57.6	3.0
		2	0.45		-11.9	62.4		8.3
		3	0.46		-10.8	59.6		3.4
Q1-C2	**vir**	**1**	0.81	0.70	15.6	59.2	49.8	19.0
		2	0.55		-21.3	64.1		28.8
		3	0.88		25.2	55.3		11.1
	lg	**1**	0.44	0.49	-9.4	57.7	56.1	2.9
		2	0.40		-17.5	60.8		8.3
		3	0.47		-4.8	59.4		5.9
	sm	**1**	0.51	0.42	20.4	59.6	58.9	1.2
		2	0.40		-3.7	61.1		3.8
		3	0.41		-2.4	60.4		2.5
Q2-C1	**vir**	**1**	0.87	0.85	2.4	62.7	52.3	19.8
		2	0.76		-10.1	55.5		6.1
		3	0.96		13.0	53.0		1.4
	lg	**1**	0.55	0.51	8.0	59.2	58.7	0.8
		2	0.53		4.6	59.9		2.0
		3	0.56		10.2	59.7		1.8
	sm	**1**	0.68	0.53	28.3	59.1	58.9	0.3
		2	0.57		8.1	60.7		3.1
		3	0.57		7.1	59.8		1.6

*Stiffness calculation assumes linear response up to final failure

On the whole, the predictions for the undamaged panel strengths are moderately good at best when compared with the experimental results, becoming quite poor for the *Q1-C2* panel; all the same, the numerical model produces strength predictions well within the 1.4 factor of safety recommended by NASA for uniform composite structures [169]. Generally, the undamaged strength predictions are noticeably less accurate than the CAI results produced using the same model set-ups. The already-mentioned problem of scatter in experimental data for edge compression of panels may be an influencing factor in this error. One peculiar result in Czabaj's study is that the compressive strength of the undamaged panels seems to be dependent on the lay-up in a manner that is not expected, as the *Q1* and *Q2* lay-ups have identical numbers of plies oriented to the 0/45/-45/90º axes [40]; this may be due to the increased likelihood of delamination in the *Q2* lay-up. Additionally, the Czabaj panels had skins co-cured with the cores, resulting in some waviness of the plies closest to the core, which in turn induces a degree of imperfection for which the model does not allow. It may therefore be more appropriate to treat the virgin panel numerical results as a theoretical upper-limit for panel strength. The noteworthy exception already identified is model configuration 2, which shows good agreement with the experimental strength results.

Considering Table 14, it can be seen that the numerical strain-to-failure estimates are moderately good, though with considerable variation between indenter and structural configurations. The panel stiffness estimates provided by the model are generally very good for the indented panels. The stiffness estimates for the virgin panels are generally significantly overestimated, due to the significantly non-conservative estimates for the ultimate strength of these panels. However, it is encouraging that these values are generally accurate, as it demonstrates that the model is capturing the structural response of the panels correctly, as well as the ultimate strength. The stress-strain responses for all 18 models are shown in Figure 71 to Figure 79. Each figure compares the performance of the three different model set-ups for each structural configuration against each other, and an idealised stress-strain response derived from Czabaj’s experimental data (indicated in each plot by the suffix *Exp*). These plots clearly show the generally good agreement between the models and the experimental work. Encouragingly, every model exhibits the classic linear-elastic-brittle structural response, with little or no softening of the structure being observed prior to the severe load-drop that indicates failure. The post-failure response varies between models. Most drop to a very low near-constant stress value. Others, particularly the small indenter models, show some degree of progressive failure prior to the strength degrading to a constant value. It is noteworthy that the virgin panel models show greater stiffness than the experimental results would suggest, while the damaged models capture this very well, and on the whole the response of the models is largely independent of the specifics of their configuration.

A key limitation with all the models is the simple, homogenised core response. Singh et al [168] note that the core is the primary controller of the QSI indentation response, so inaccuracies in the core behaviour will inevitably affect the state of the damage prior to the CAI loading, and thus influence the ultimate strength. In spite of this, the CAI results are consistently good using model configuration *3*, regardless of panel and load configuration. Instead, the deficiency in the core model may be more significant in explaining the relative weakness of the model at predicting the undamaged strength of the panels, as the response of the virgin panels may be more sensitive to flaws in the core response in lieu of a pre-existing delamination. Future work is required to address this deficiency in the core model. Singh et al also note that, for the small indenter configurations, delaminations tend to be deeper in the plate, at the 5th, 6th and 7th interfaces. This may explain why model configuration *2*, with the cohesive surface set deeper into the panel, gives improved results for the small indenter load cases over configuration *1*, where the cohesive surface is placed closer to the indented surface

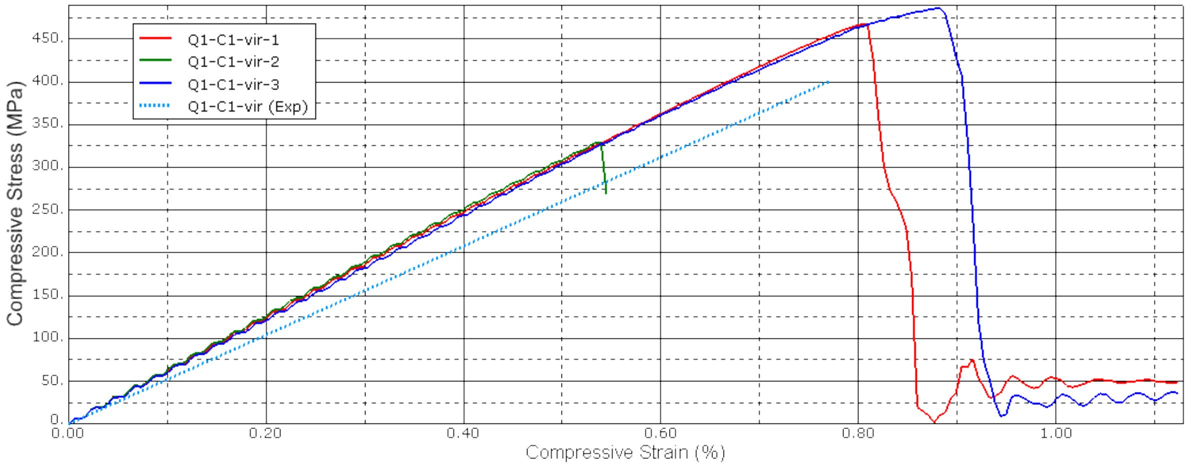

Figure 71: Stress-strain responses for the Q1-C1-vir panel models [1]

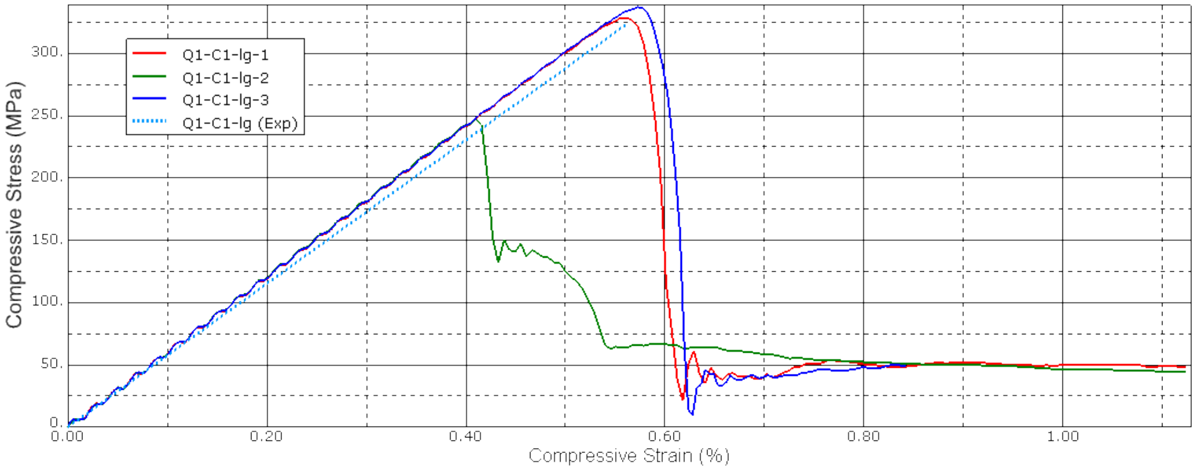

Figure 72: Stress-strain responses for the Q1-C1-lg panel models [1]

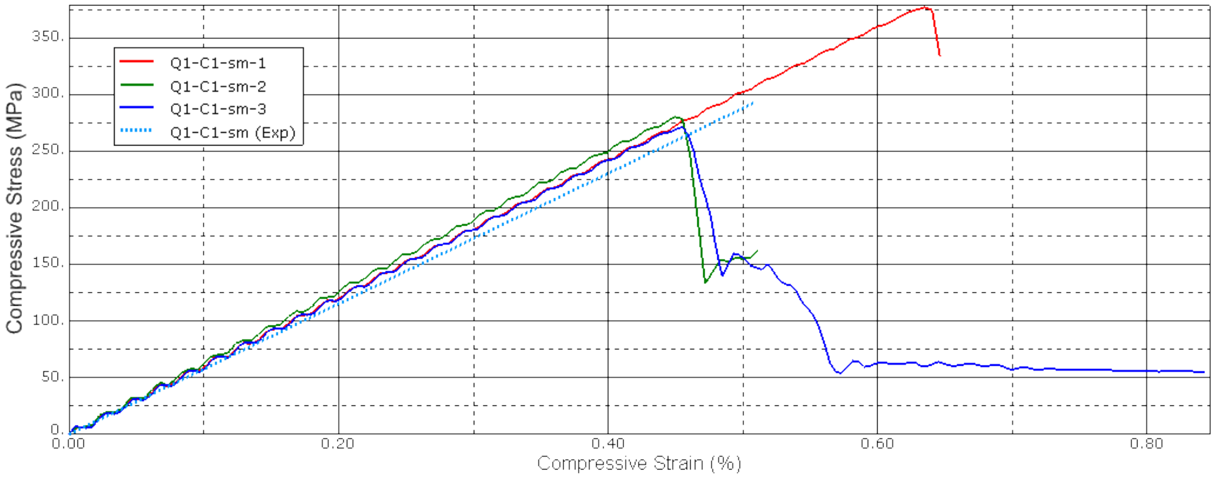

Figure 73: Stress-strain responses for the Q1-C1-sm panel models [1]

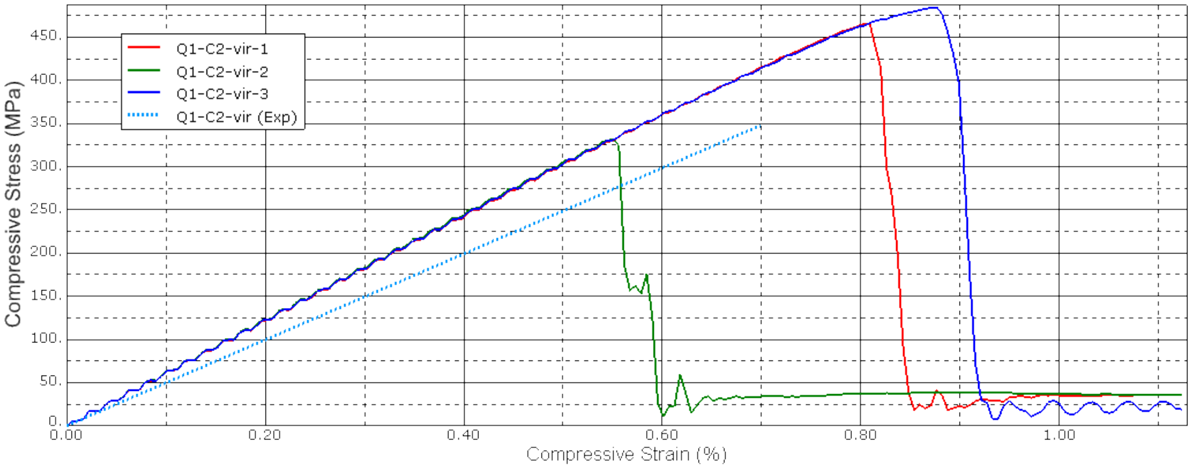

Figure 74: Stress-strain responses of Q1-C2-vir panel models [1]

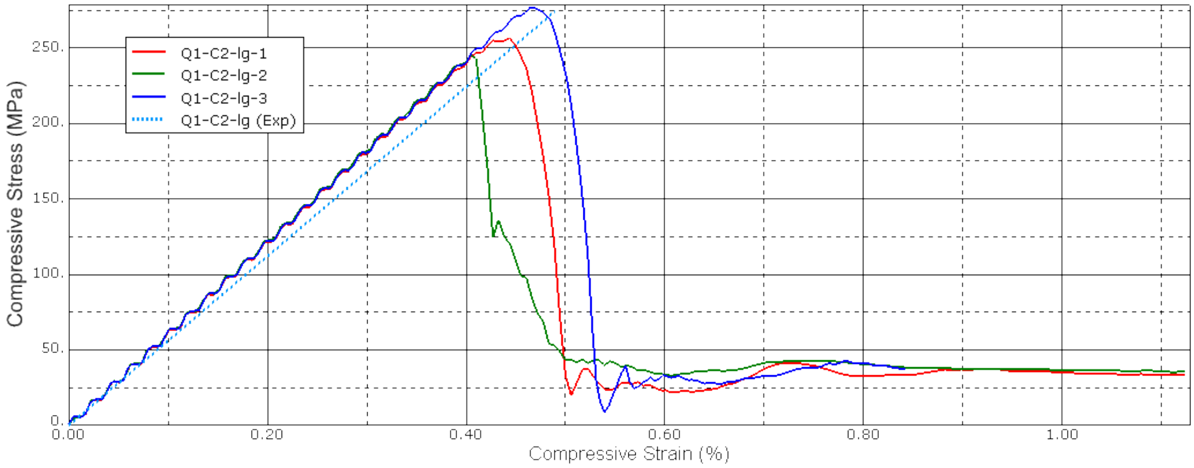

Figure 75: Stress-strain responses of Q1-C2-lg panel models [1]

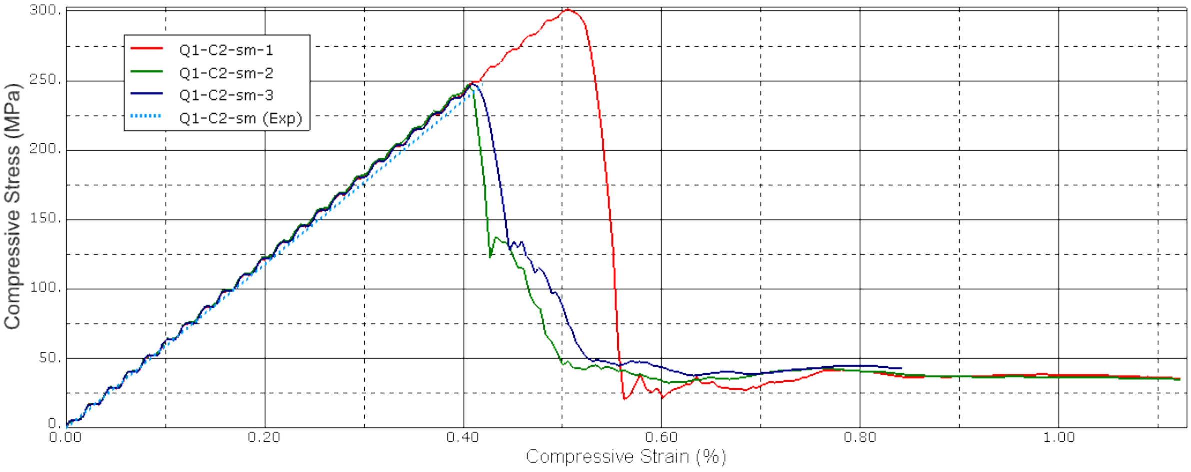

Figure 76: Stress-strain responses of Q1-C2-sm panel models [1]

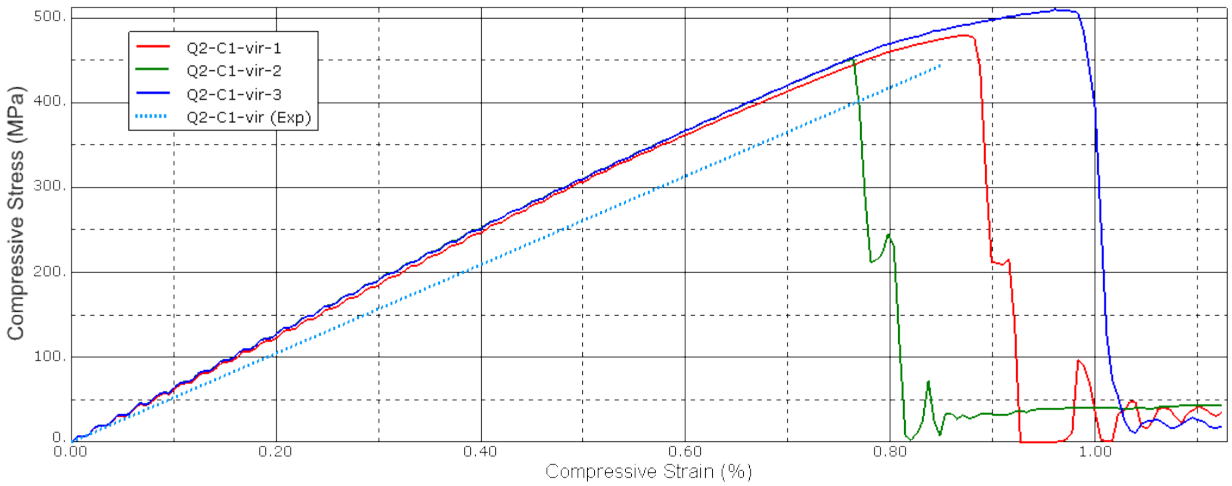

Figure 77: Stress-strain responses of Q2-C1-vir panel models [1]

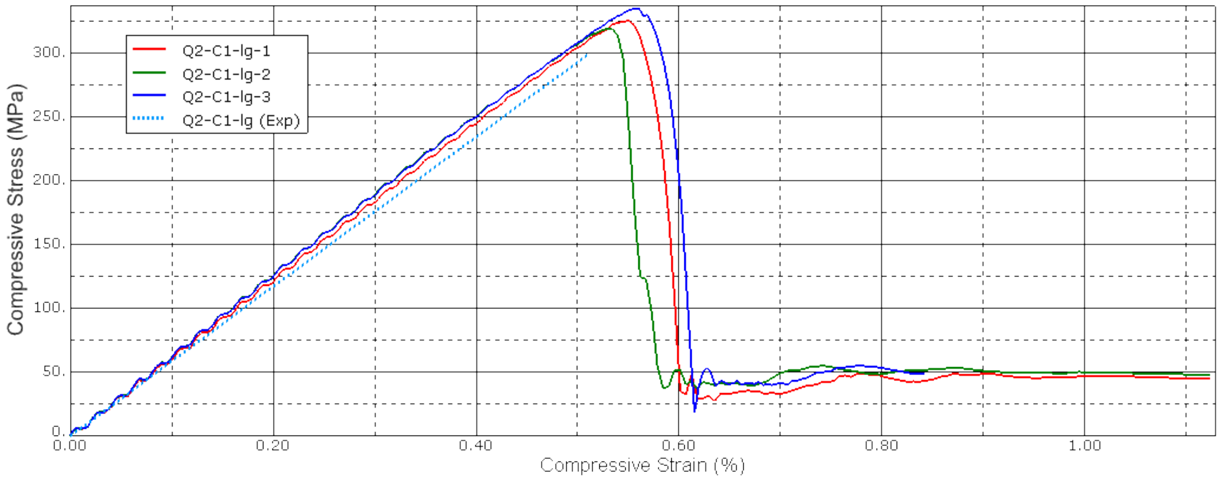

Figure 78: Stress-strain responses of Q2-C1-lg panel models [1]

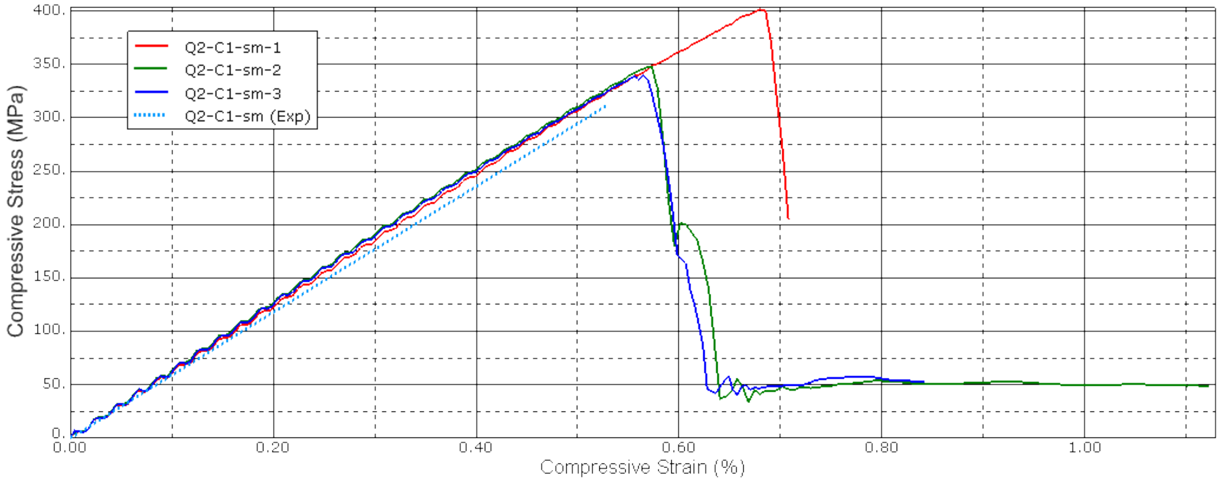

Figure 79: Stress-strain responses of Q2-C1-sm panel models [1]

of the panel. Based on the improved results for the large indenter load cases using configuration *1*, one could hypothesise that, for these cases, the delaminations that control the response of the panel occur closer to the indented surface. Without experimental data for the large indenter cases, it is not possible to state conclusively whether or not this is in fact true.

Regarding the failure mechanism, it is difficult to observe the propagation of damage due to the relatively low resolution of the field data output. However, for most configurations studied here, the model appears to show indentation growth (that is to say, the dent is becoming deeper, rather than wider) prior to final failure. Failure seems to usually occur via a rapid propagation of delamination across the width of the panel, resulting in delamination buckling. An example of this is shown in Figure 80a, for configuration *Q1-C1-lg-1* (the top ply block is removed to show the cohesive surface). In a couple of cases, the dent depth gets smaller, but this does not appear to influence the final failure. Some panels also appear to undergo localised longitudinal compressive failure, as seen by a continuous line of elements across nearly the whole width of the panel that suddenly exceed the Hashin criteria's limit for this damage mechanism; this is shown for *Q2-C1-sm-1* in Figure 80b. It is unclear for these panels whether it is the ubiquitous delamination growth or the local compressive damage that initiates final failure. As far as the model allows, the predicted onset and propagation of failure appears to agree well with the experimental observations for the panels studied.

5.5: Damage Extent Prediction

To get a better understanding of the behaviour of the model, the percentage difference between the predicted and experimentally measured damage geometries are presented in Table 15 (complete data in Appendix F). Delamination is presented by Czabaj [40] by area for the small indenter cases only, and no core damage metrics are provided by Czabaj. The mean values from Czabaj for damage magnitude are presented here for comparison. Delamination is considered to have occurred in the model when the scalar stiffness degradation in the cohesive surface equals one, indicating complete separation of the two faces at that location. The diameter of the dent is determined by considering the region where the depth of the dent exceeds 0.25mm (the visible threshold for BVID is accepted at 0.5mm [17], however, a smaller threshold is required here due to the small maximum dent sizes). The same lower limit is used to establish the depth and diameter of the crushed core region, as this approximately corresponds with the generation of significant plastic strain in the core, indicating permanent deformation in the core. The numerical damage sizes are estimated from the element sizes; based on the mesh seeds, 1 element approximately equals 0.46mm in the skin, and 2.5mm in the core. The core also has approximately 1 element/mm through-the-thickness. Due to the use of biased meshing to increase the mesh density in the indented region, these measures are average sizes and so are not perfectly accurate, but adequate for making broad comparisons between the experiments and the models.

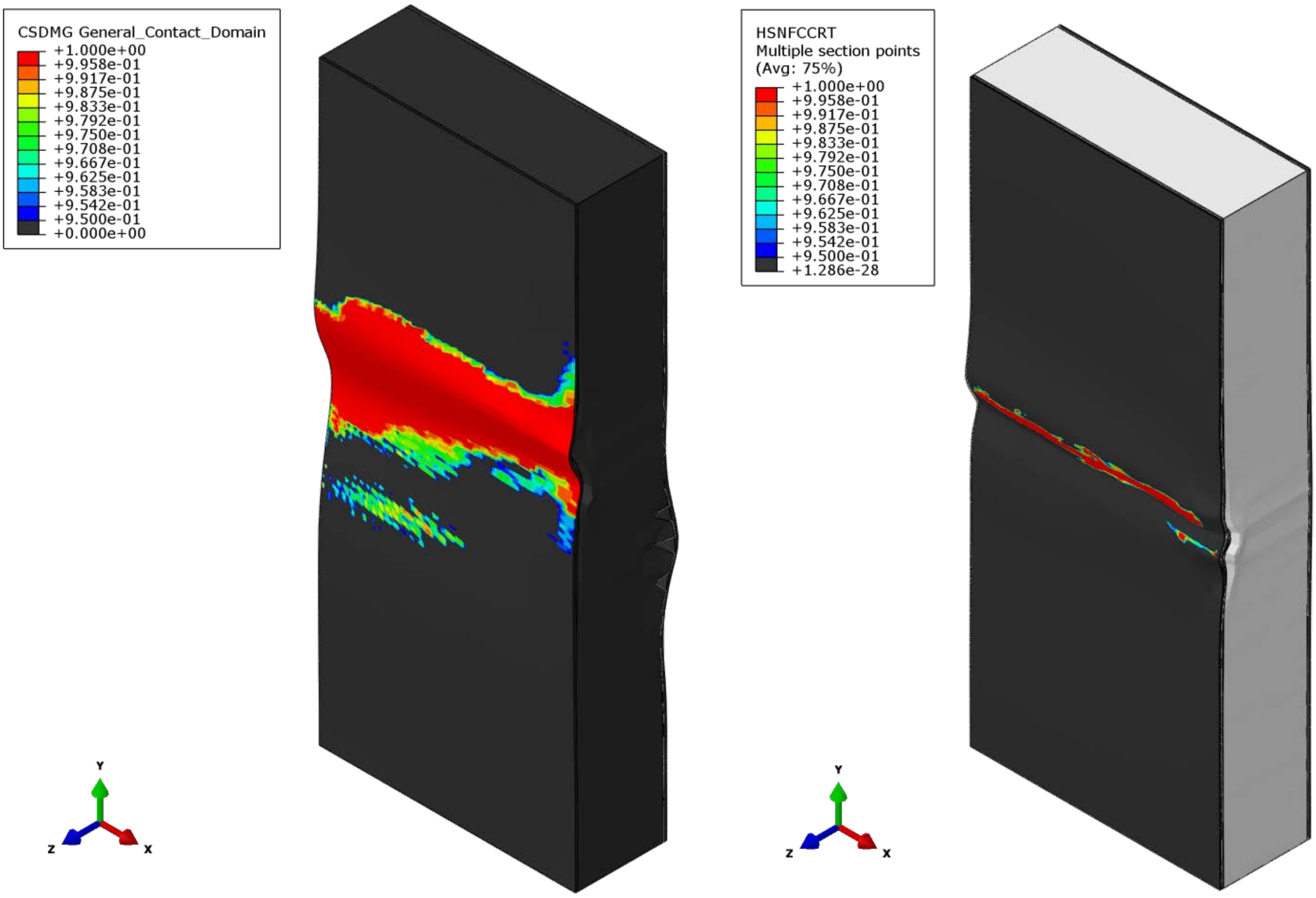

Figure 80: Sandwich panels at the point of final failure. [1]
a) (left) Q1-C1-lg-1, showing typical delamination propagation and buckling – delamination occurs when CSDMG = 1.
b) (right) Q2-C1-sm-1, showing compressive failure of the fibres – fibre failure in compression occurs when HSNFCCRT = 1.
(Note that the abbreviations here correspond with those in the Figure)

As with the strength results, the estimates for damage extent from the models vary significantly between configurations. The large indenter configurations generally show the best agreement with the experimental results for dent depth and extent, with model configuration *1* providing the best agreement across all panel configurations; as previously discussed, the large indenter models also tended to have the strongest agreement with the experiments for the residual strength, regardless of which model configuration was used. This suggests that the response of these configurations is controlled more by the damage in the skins, but without experimental data for delamination extent in the large indenter configurations, or core damage in general, this observation is by no means conclusive.

Table 15: Percentage error between predicted and measured damage extents in the sandwich panels at the end of the quasi-static indentation phase

Model			Dent depth % error	Dent ø % error	Delamination area % error
Q1-C1	**lg**	1	*1.0*	*7.6*	-
		2	*37.5*	*15.5*	
		3	*26.9*	*10.7*	
	sm	1	*-24.1*	*-4.7*	*175*
		2	*-8.6*	*68.2*	*454*
		3	*136*	*55.6*	*436*
Q1-C2	**lg**	1	*-24.2*	*6.7*	-
		2	*-20.2*	*8.9*	
		3	*-15.2*	*8.9*	
	sm	1	*4.3*	*24.9*	*47.0*
		2	*23.4*	*41.0*	*76.8*
		3	*25.5*	*52.9*	*188*
Q2-C1	**lg**	1	*0*	*2.3*	-
		2	*7.4*	*6.0*	
		3	*9.0*	*3.7*	
	sm	1	*-55.9*	*-35.9*	*35.4*
		2	*-35.3*	*2.3*	*121*
		3	*138*	*58.7*	*317*

The small indenter models show poor agreement with the experiments for dent depth and extent, with the thick-core models (*Q1-C1* and *Q2-C1)* being particularly poor. However, the model still produces acceptable strength results for this loading configuration. The discrepancy is particularly stark with model configuration *3*, which shows very poor agreement for the dent depth and magnitude for most small indenter models, and yet in the main produces good agreement with the experimental results for residual strength. The small indenter case is also the only one where there is quantitative experimental data for the delamination extent; the model invariably over-estimates delamination by a significant amount. This leads one to conclude that the response of the small indenter configurations may instead sensitive to the accuracy of the core response model; without experimental data for the core damage extent, no comparisons are possible at this stage. Improving the core response was previously identified as an area for improvement (see *section 5.4, 'Residual Strength Prediction'*). In any case, it is clear that poor predictions for the damage magnitude at the QSI phase of the analysis do not necessarily correlate with poor accuracy in the compression-after-impact strength estimates; *Q1-C1-sm-3* and *Q2-C1-sm-3* are good examples of this point, as the damage extents estimated by these models are extremely poor, yet the ultimate strength estimates for both models fall within 10% of the experimental results.

Singh et al [168] state that, based upon qualitative assessment, the larger indenter induces a greater size of delamination than the small indenter, so it is possible that numerical delamination prediction is better for the large indenter models. Additional work is necessary to support this hypothesis. It is also noteworthy that the model does not capture the shape of the delamination accurately. Considering configuration *Q1-C1-sm-1,* it can be seen that the delamination in the model is approximately circular (see Figure 81), whereas in the experimental study it is broadly elliptical (see Figure 82 – taken from Singh et al [168] - *'interface 3'*). This is to be expected, as the response of the other interfaces isn't captured, thus removing their influence on the response of the interface under consideration here. Additionally, recall that the mesh may not be sufficiently fine to ensure an accurate estimate of the delamination size and shape (see *section 5.2, 'Model Description'*). The model is unable to capture any asymmetry that may be present in a delamination due to the use of a half-model geometry, which necessarily assumes that the structure behaves in a symmetric manner.

For model configuration *3*, the delaminations in both interfaces tend be more of a 'squashed circle' shape, closer to the shape seen in the experiments, but all the same, the minor dimension in the numerically-derived delamination is much larger than the experimental results would suggest. It is interesting to note that with this model configuration, no delamination is detected after indentation for any of the large indenter models in the first interface (near the surface), and the deeper, second interface delamination is always the larger one in the small indenter models. This seems to contradict the experimental findings of Hwang & Liu [37], who note that the near-surface delamination should be the largest after an impact event. Also noteworthy is the fact that the residual strength predictions for configurations *1* and *2* clearly demonstrate that the position of the cohesive surface (and thus the delamination) influences the strength, yet this effect seems to be negated once multiple delaminations are able to form. It should be restated that the material data for cohesive surface is taken from different sources for different materials, and thus may not be entirely representative for this particular material system.

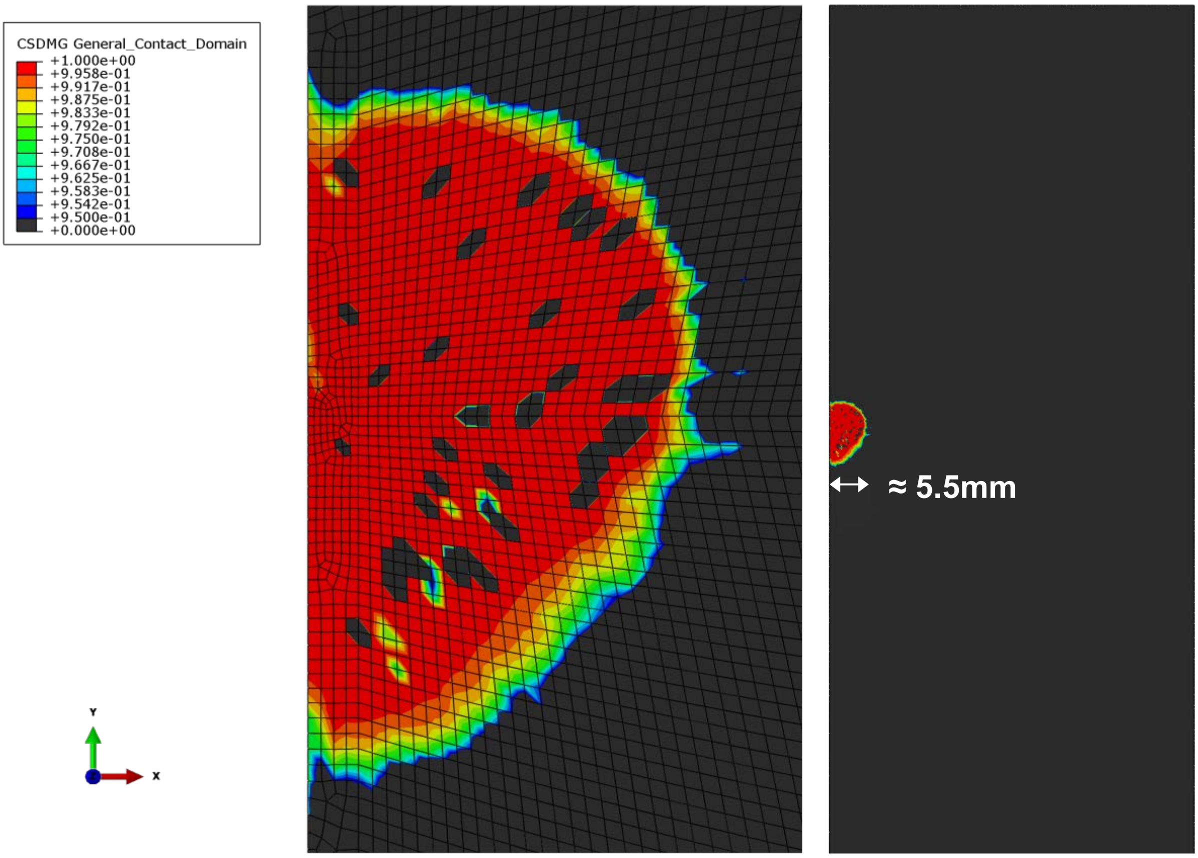

Figure 81: delamination in Q1-C1-sm-1 after QSI (right: full panel view) [1]

Image hidden due to copyright restrictions.
Please refer to [168], figure 6

Figure 82: 3D damage map of the Q1-C1 specimen [168]. The delamination shown in Figure 81 corresponds with ‘interface 3’

5.6: Parametric Study – Effect of Inaccuracies in Material Data Input

A parametric study is presented investigating the effect of inaccuracies in the material data input to the model. A large amount of data is required for this particular model to work, including skin, core and cohesive interface, for 39 entries in total (not including material thicknesses). All of these values are subject to inaccuracy: some entries may be difficult to acquire, or not have an agreed standard test for measuring the quantity. A good example of this is the fibre fracture energies required for damage evolution using the Hashin criteria for intralaminar failure within *Abaqus*, which may be determined by a combined experimental and numerical procedure recently proposed by Pinho et al [120]. Often, some data will have to be gathered from a literature source, possibly for a similar (but still different) material; indeed, this was necessary for the model just discussed. With this in mind, the sensitivity of the model to these inaccuracies, particularly the strength and fracture energy is investigated. The out-of-plane stiffness of the core is also included. Additional to the material properties, this study looks at the sensitivity of the model to inaccuracies in the material orientations. Laying-up of composite plies by hand is a laborious process, subject to error, and the orientations of the plies (and also the core) may well be offset from their required positions by some margin.

In the first instance of this study, each of these quantities is varied individually by ±20% of the nominal value included in Table 10. For the plies and core orientation, the offset is 18º, corresponding to a 90º ply offset by 20% of its nominal value. A value is considered ‘sensitive’ if the difference between the baseline numerical results for the compressive strength discussed previously in this chapter (case *0*) and the strength result given by the modified model exceeds 5%; a change of 5% or more will cause the strength result to exceed the variation for most of the compression-after-impact experiments. For those cases where either the positive or negative value change results in a percentage difference of more than 10%, which exceeds the observed experimental variation across all tests, this change is regarded as significantly sensitive and an additional test is performed for a parameter variation of ±10% from the nominal value (9º for the angular parameters). If the percentage difference for a given variation is less than 1%, this parameter is considered insensitive.

Some additional variations are performed for the structural parameters (i.e. ply and core orientations). A variation of ±20% for the material properties, while quite large, is not unrealistic; 20% is incidentally almost exactly the variation between maximum and minimum values for the longitudinal tensile strengths determined in the experiments discussed in Chapter 5 (*‘Experimental Work’*). However, deviation of more than a few degrees in the ply and core orientations would justifiably cause alarm in a production context. So, three analyses, varying the orientation of the 0º and ±45º plies and the core by 1º, are performed, reflecting a change representative of typical manufacturing tolerances. Four ‘special case’ models are also performed. Test *#7* offsets the ±45º plies by -45º, producing a cross ply lay-up of $[0, 0, 90, 90]_S$. Test *#8* continues with this theme, using a cross-ply lay-up of $[0,90]_{2S}$. Finally, two different core orientations are trailed: test #12 with an unorthodox core orientation of +45 º, and test #13, which rotates the core by 90º, thus, making the ribbon direction perpendicular to the load direction. These tests will demonstrate the ability of the model to handle parametric studies as relevant to design, where small changes to the configuration of the basic structure may be necessary to optimise the structure for a given application.

All of these tests are performed for the *Q1-C1-…-1* model, for the virgin and large indenter configurations. For the honeycomb core material properties, the small indenter configuration is also included to test the hypothesis offered in the previous section that some of the configurations studied were more sensitive to the core properties than offers. Time and resource constraints prevent this study from being a comprehensive investigation of all properties for all load and lay-up configurations. The results of the study are presented graphically in Figure 83 and Figure 84, showing the compressive strength of the panel for each of the variations performed as compared with the original numerical result (case *0*), for the virgin panel and large indenter damage cases respectively. The complete list of these variations is given in Table 16. A complete set of data is given in Appendix G, and an abridged data set, giving just the percentage difference between each test and case *0* is presented in Table 17.

Table 16: Summary of tests performed in the parametric study

Region	#	Property	Change (from nominal)
-	**0**	Base model *(Q1-C1)*	N/A
Structure	**1**	0° fibres (offset)	+1°
	2		+9°
	3		+18°
	4	±45° fibres (offset)	+1°
	5		+9°
	6		+18°
	7		-45°
	8	Cross-ply lay-up $[0,90]_{2s}$	
	9	90° fibres (offset) +18°	
	10	Core orientation (offset, planar)	+1°
	11		+18°
	12		+45°
	13		+90°
Skin (strengths)	**14**	σ_{LT}	+20%
	15		-20%
	16	σ_{LC}	+20%
	17		-20%
	18		+10%
	19		-10%
	20	$\sigma_{TT\ \&\ TC}$	+20%
	21		-20%
	22	$\tau_{L\ \&\ T}$	+20%
	23		-20%
Skin (energies)	**24**	G_{LT}	+20%
	25		-20%
	26	G_{LC}	+20%
	27		-20%
	28	$G_{TT\ \&\ TC}$	+20%
	29		-20%
Bond	**30**	σ_{m1}	+20%
	31		-20%
	32	$\sigma_{m2\ \&\ m3}$	+20%
	33		-20%
	34	G_{m1}	+20%
	35		-20%
	36	$G_{m2\ \&\ m3}$	+20%
	37		-20%
	38	Mode-mix ratio	+20%
	39		-20%
Core	**40**	σ_{ult}	+20%
	41		-20%
	42	σ_{crush}	+20%
	43		-20%
	44	E_3	+20%
	45		-20%

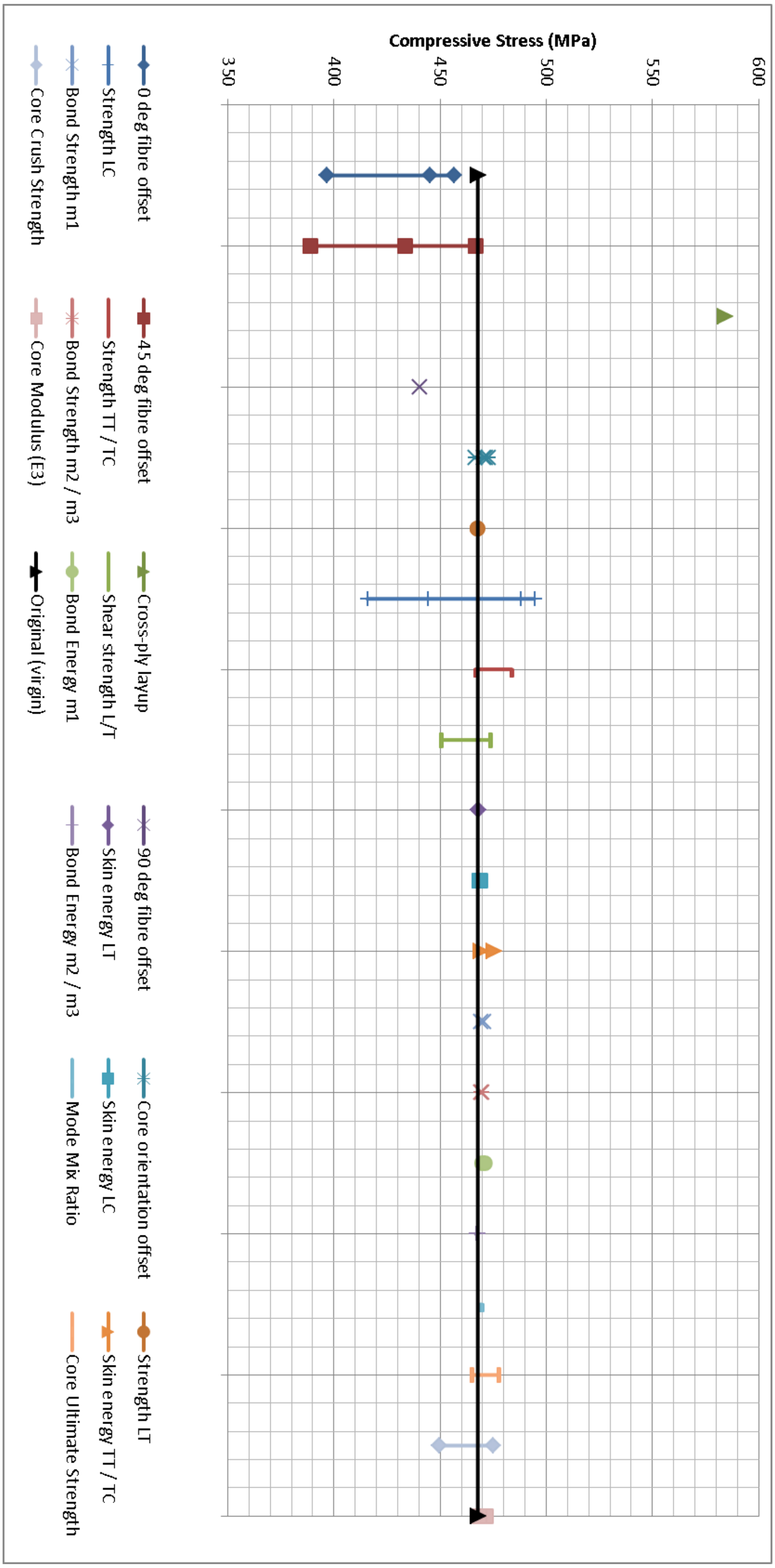

Figure 83: Compressive stress of all virgin model variations

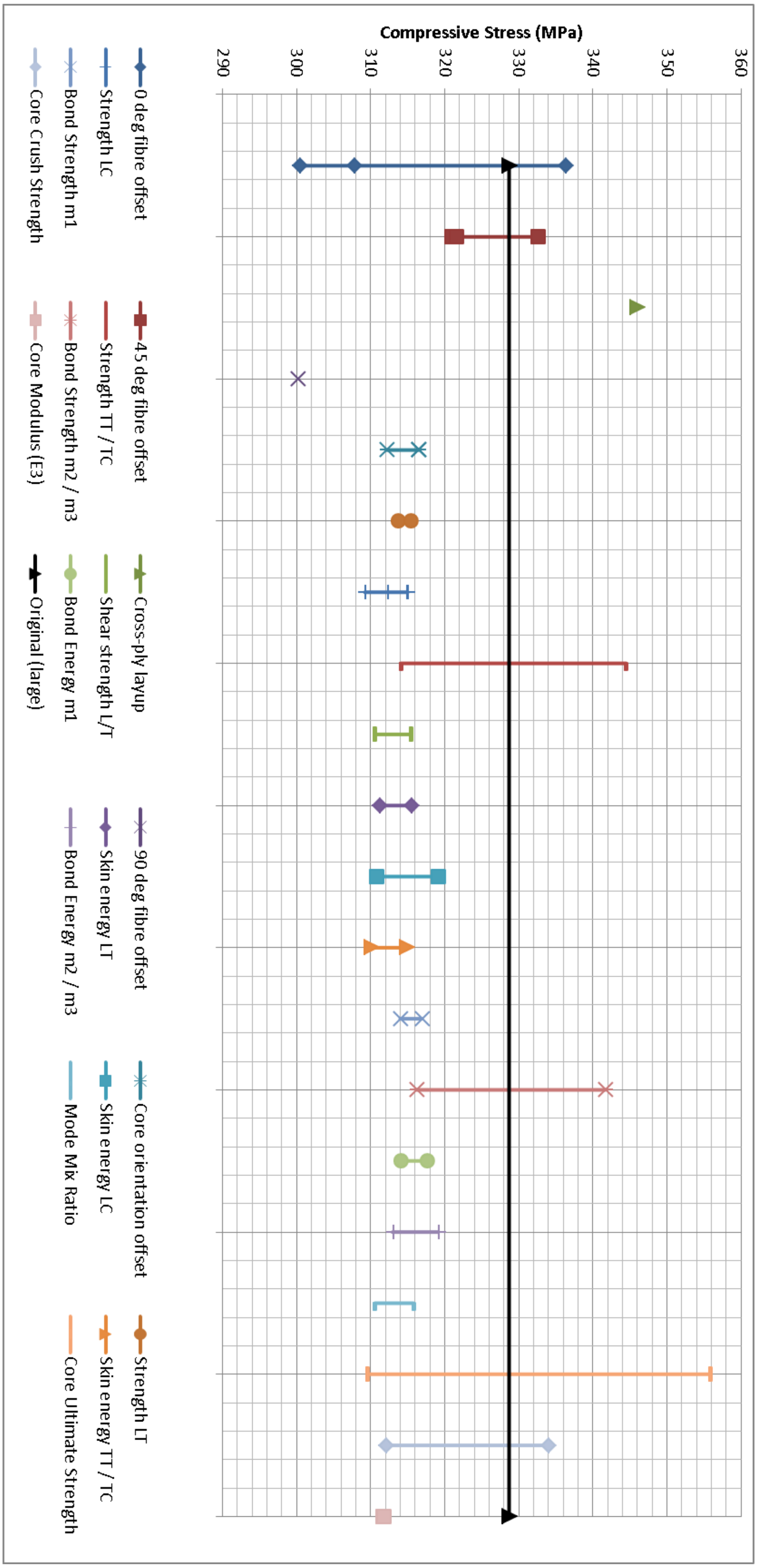

Figure 84: Compressive strength of all large indenter model variations

Table 17: Percentage difference in strength between base models and variations

#	% error		#	% error		#	% error		
	virgin	large		virgin	large		virgin	large	small
1	-2.5	2.3	14	0.0	-4.5	30	0.3	-3.6	-
2	-4.9	-6.4	15	0.0	-4.0	31	0.5	-4.5	
3	-15.2	-8.6	16	5.7	-4.2	32	0.2	4.0	
4	-0.2	-2.3	17	-11.1	-4.2	33	0.4	-3.8	
5	-7.3	-2.2	18	4.3	-5.9	34	0.5	-3.4	
6	-16.8	1.2	19	-5.1	-5.0	35	0.7	-4.4	
7	13.8	-4.3	20	-0.2	4.8	36	0.0	-2.9	
8	24.8	5.2	21	3.4	-4.5	37	-0.2	-4.8	
9	-5.9	-8.7	22	1.3	-5.5	38	0.2	-5.5	
10	1.0	-3.7	23	-3.7	-4.0	39	0.4	-3.9	
11	0.5	-5.0							
12	0.7	-4.6	24	0.0	-4.0	40	2.1	8.3	-7.6
13	-0.3	-8.0	25	0.0	-5.3	41	-0.6	-5.8	-4.3
			26	0.2	-2.9	42	1.5	1.6	8.5
			27	0.2	-5.4	43	-4.0	-5.1	0.7
			28	1.5	-4.2	44	0.8	-5.2	-0.1
			29	0.3	-5.7	45	0.2	-5.1	6.2

Colour code for percentage errors (parametric study)

<1%	>5%	>10%	>25%
🟩	🟧	🟥	⬛

This study reveals a few key trends. Firstly, the indented model is moderately sensitive to most of the parameters, with the percentage difference from the base model usually being around ±4 – 6%. However, the indented models never show ‘significant’ (>10% change) sensitivity. Contrast this with the virgin panel models, which are insensitive to the majority of the applied changes, particularly the changes to fracture energies for intra- and interlaminar failure. This comes as something of a surprise, as the fracture energy is regarded as a parameter that has a significant influence on the accuracy of delamination prediction in particular [19]. For these parameters, the insensitivity is likely down to the strength of the panel being governed by the ultimate intralaminar strengths; with little progressive damage to speak of, changes in the parameters governing progressive damage are of negligible effect. However, where the virgin model is sensitive, it is usually significantly so, with the orientation of the 0° fibres, the ±45° fibres and the longitudinal compressive strength all being particularly sensitive parameters for the undamaged model especially. This is not overly surprising, given the nature of the problem; the panel is loaded in uniaxial compression, so clearly the strength and orientation of the primary load-bearing fibres, nominally parallel to the loading direction, will have a profound effect on the strength of the structure. Altering the orientation of the 0° and ±45° fibres and the core by only a small amount does not affect the ultimate strength of the panel to a serious extent, whether it is damaged or not.

It is less clear why the indented panels are less sensitive to the intuitively crucial strength and orientation of the 0º fibres. One possibility is that the presence of damage moderates the imperfection sensitivity inherent to the edge compression problem. Since the weakness is induced in the panel becomes the feature controlling eventual failure, changes to any single parameter become less important. Additionally, changing many of the parameters will often increase the strength of the virgin panel, and reduce the strength of the indented panel, regardless of whether the parameter is increased or decreased. An obvious example is the fracture energies and the bond properties, which when changed almost invariably increase (albeit very marginally) the undamaged panel strength, and reduce the strength of the indented panel. In fact, most parameter changes will reduce the strength of the damaged panel. It appears that increasing one parameter seems to create a peculiar competitive situation whereby other failure mechanisms come into play, resulting in reduced panel strength. These unexpected results suggest a good deal of interaction between various properties in a manner not yet fully understood, and perhaps worthy of further study. What can be said for certain is that, based on this study, that no one parameter seems to have particular control over the ultimate failure of the damaged panel.

Regarding the core parameters, it is seen that the virgin panel is fairly insensitive to the out-of-plane properties of the core. However, the sensitivity of the panel to the core properties does vary depending on whether the panel is indented with the small or large indenter. On the whole, it appears the large indenter model is the slightly more sensitive of the two configurations, but both models are generally moderately sensitive to the core data input. The difference in sensitivity between the damaged and undamaged models is due to the change in stabilisation provided by the core. As previously suggested, the strength of the virgin panel is governed primarily by the ultimate intralaminar strengths, so the other parameters are less important. Once damage is induced in the panel, the stabilisation provided by the core is more significant. This is particularly apparent when considering the ultimate and crushing strengths of the core. Increasing or reducing other property tends to produce a noticeable increase or decrease in the ultimate strength of the damaged panel, though paradoxical results still occur with the small indenter model. While considering only the out-of-plane data for a sample of the configurations, these paradoxical results perhaps indicates that the core model itself is the ‘weak link’ in the model, though it is just as possible that these unexpected results are products of the complex interaction of failure modes inherent to composite and sandwich structures. It is pertinent to reiterate at this stage that the original virgin model and particularly the small indenter model gave fair to poor agreement with the experimental results; it is not inconceivable that an improved model might demonstrate different levels of sensitivity to various parameters.

The final discussion point relates to the four ‘special case’ models: the two cross-ply lay-ups and the two alternative core orientations (tests *7*, *8*, *12* and *13*). The two cross ply lay-ups, not surprisingly, were considerably stronger for the virgin test cases, due to the greater number of plies parallel to the loading direction. This was particularly pronounced for the $[0,90]_{2S}$ lay-up (test *8*), as the removal of the ply-clustering will have improved its delamination resistance, even though the number of interfaces vulnerable to this effect increased [35]. This trend is further apparent when these panels were indented, with the panel with ply-clustering (test *7*) showing reduced strength compared to the (quasi-isotropic) base model, and the non-clustered panel (test *8*) showing higher strength. The indented model showed a smaller change in strength as compared to the virgin model. It must be stressed that these results do not suggest that the cross-ply lay-up is superior, as its ultimate strength will obviously be harmed should the load be applied in a different direction (for example, in shear) due to the absence of the ±45° plies. Changing the core orientation does not influence the strength of the virgin panel to any appreciable extent, but it does influence the strength of the damaged panel. It is difficult to say for certain what is causing this effect, due to the simplicity of the core crushing response. Changing the orientation does change the effective action of the shear stiffness however. This may be changing the support given to the damaged skin to a greater or lesser degree, but further work is necessary for this assessment to be conclusive.

It must be stated that this study has only looked at changing a single parameter at a time, and makes the assumption (in lieu of better data) that the rest of the data is perfectly accurate. Clearly this assumption is not representative of reality, otherwise it is likely that there would be little or no difference between the experimental strength results and the numerical model predications for any of the configurations tested, as opposed to just some of them. The significance of this is that, given the large amount of independent variables required by the model, the effect of cumulative errors could potentially become very significant. Indeed, the build-up of small errors, which may have little influence on their own, could explain some of the weaker strength predictions presented in this chapter, and highlight the need for a comprehensive and reliable experimental program to gather a complete set of material data.

To investigate the effect of the core and the bond parameters more closely, the change in crushing and delamination extent induced by the indentation is considered next. As with the strength results, the size of damaged estimated by each altered model is compared with the results from the base model, and sensitivity determined using the same percentage difference thresholds. An additional threshold is added for when the percentage difference exceeds 25% indicating a very severe deviation from the base models. Complete results may be found in Appendix H, and Table 18 gives an abridged presentation of the results, giving the percentage difference from the base model. The percentage difference in the strength result given in Table 16 is also provided, to assess the influence of the change in damage size on the change in ultimate strength.

From Table 18, it’s clear that changes to the various material parameters generally have a dramatic effect on the predicted damage extents produced by the indentation, with the effect being especially profound in the core depth prediction (though in this latter case, the effect may be at least partially due to the use of a relatively coarse mesh in the through-thickness direction). The large indenter models experience greater changes in the core crush depth, whereas the small indenter models tend to exhibit greater changes in damage diameter. A simple explanation for this could be the smaller load applied in the small indenter models. The delamination extent observed is also rather sensitive to changes in the material data, but not nearly to same extent as the core damage. The fracture energy for the shear opening delamination modes is the major exception, being very sensitive to change (test *36*). The same applies, to a lesser extent, to the shear-opening strength (test *32*). Curiously, changing the normal opening strength noticeably increases the delamination extent, as does decreasing the mode-mix ratio, which increases the influence of the shear-mode fractures in the B-K criterion. These results suggest that the delamination is dominated by the shear-opening mode (which is intuitive, due to the local bending) but there remains a considerable amount of competition between normal mode and shear mode fracture.

Table 18: Percentage difference for QSI damage extents between base models and variations

#	Delamination area % error	Core crush diameter % error		Core crush depth % error		Strength % error	
		lg	sm	lg	sm	lg	sm
30	10.1	-	-	-	-	-3.6	-
31	17.4					-4.5	
32	-8.3					4.0	
33	25.5					-3.8	
34	7.5					-3.4	
35	5.2					-4.4	
36	-8.9					-2.9	
37	32.3					-4.8	
38	1.4					-5.5	
39	11.6					-3.9	
40	-	-2.4	-30.0	-21.3	-14.3	8.3	-7.6
41		14.1	51.7	82.5	71.4	-5.8	-4.3
42		8.8	10.0	112.5	14.3	1.6	8.5
43		2.4	-5.0	-21.3	28.6	-5.1	0.7
44		13.6	0.0	70.0	20.0	-5.2	-0.1
45		12.0	10.0	71.3	0.0	-5.1	6.2

There doesn’t appear to be any obvious correlation between the extent of the damages observed and the ultimate strength of the panel in the compression step. This is particularly obvious in the case of delamination. Paradoxically, the parameter change that influences the size of the delamination the least has the biggest effect on panel strength (test *37*). This test increases the mode-mix ratio, favouring normal-opening fractures. Though it is not possible to state for certain, this particular result may indicate that normal-opening delamination starts to predominate in the compression step. Again, this is a fairly intuitive conclusion, supported by the experimental work presented in the next chapter, as the delamination will start to buckle in the out-of-plane direction, driving further delamination growth. The panel strength is more sensitive to changes in the core parameters, as already noted, but the change in strength seems fairly minor when the considerable changes in the extent of core damage are considered. It can only be assumed that, while both core damage and delamination are important to the response of the panel, changing their material inputs will not dramatically influence the global behaviour of the panel, as other factors, such as the intralaminar material strengths, are ultimately the controlling factors in panel failure.

5.7: Summary

In this chapter, a numerical model for the behaviour of composite sandwich panels tested by Czabaj et al [33,40] is developed and compared with their experimental data. Inter- and intralaminar skin damage are accounted for in this model, using cohesive surface interactions and the Hashin criteria respectively. A simple plasticity model is used to capture core crushing. The use of a cohesive surface interaction to capture the onset and propagation of interlaminar delamination within the skin of a sandwich is a novel feature that to the best of the author's knowledge has not been implemented in a numerical model for sandwich panels prior to this effort. The compression-after-impact strength predictions are generally good, but tend to become weaker for the undamaged panels. The strain-to-failure predictions by the model are reasonably accurate, and the stiffness estimates are also very good, but become weaker for the virgin panels due to the over-estimated strength for this configuration. Table 19 restates the percentage error between the numerical model and the experiments for these structural performance metrics, by way of a summary. This table also includes a statement of 'overall [model] quality' – refer to the notes for details on how this has been calculated. The calculation emphasises the accuracy of the strength estimate in the overall quality assessment, as the ultimate strength prediction is the key performance metric for this model.

The predictions for the damage extent resulting from the quasi-static indentation phase are usually quite poor, though there doesn't seem to be a correlation between the accuracy of the damage extent and the accuracy of the ultimate strength estimate. The simple core response used for this model is identified as a potential source of error. Additionally, the model assumes a geometrically perfect panel, which will not be representative of reality, a limitation compounded by the sensitivity of the panel to these very same imperfections when compressively loaded.

Additionally, a parametric study is performed, revealing that the undamaged model is particularly sensitive to the longitudinal compressive strength of the skins and the correct orientation of the 0° plies, but little else. The damaged panel, however, shows moderate sensitivity to most of the material data. This exercise, though not comprehensive (due to time constraints) highlights the importance of using correct material data, as the cumulative effect of small errors in the data could potentially result in large errors in the ultimate strength prediction, as seen for some of the models presented here. Despite the limitations however, the model presented here represents a promising basis for further development, which may ultimately prove useful for design work.

Table 19: Summary of the % errors between models and experiments

Model					% errors		
			Strength	% residual strength	Strain-to-failure	Stiffness	Overall quality
Q1-C1	vir	1	16.9	-	5.1	25.8	**0**
		2	-17.8		-30.0	26.2	**-1**
		3	21.7		14.6	6.1	**1**
	lg	1	1.9	-12.9	-0.7	2.6	**3**
		2	-23.5	-6.9	-26.8	4.5	**1**
		3	4.5	-14.1	2.3	2.2	**3**
	sm	1	28.3	9.7	24.5	3.0	**1**
		2	-4.5	16.2	-11.9	8.3	**2**
		3	-7.7	-24.1	-10.8	3.4	**2**
Q1-C2	vir	1	33.8	-	15.6	19.0	**-1**
		2	-4.9		-21.3	28.8	**1**
		3	39.2		25.2	11.1	**-2**
	lg	1	-6.7	-30.3	-9.4	2.9	**2**
		2	-10.5	-5.9	-17.5	8.3	**1**
		3	0.9	-27.5	-4.8	5.9	**2**
	sm	1	21.8	-8.9	20.4	1.2	**1**
		2	0.0	5.2	-3.7	3.8	**3**
		3	0.1	-28.1	-2.4	2.5	**3**
Q2-C1	vir	1	7.9	-	2.4	19.8	**2**
		2	1.6		-10.1	6.1	**3**
		3	14.7		13.0	1.4	**2**
	lg	1	8.9	0.9	8.0	0.8	**3**
		2	6.8	5.2	4.6	2.0	**3**
		3	12.2	-2.2	10.2	1.8	**2**
	sm	1	28.5	19.1	28.3	0.3	**0**
		2	11.4	9.7	8.1	3.1	**2**
		3	8.6	-5.3	7.1	1.6	**3**

Quality measure	<5%	<10%	<15%	>25%	>35%
Strength	+5	+3	+1	-3	-5
Others	+3	+2	+1	-1	-2

The overall quality of a model is determined by assigning the above values to each metric based on the error for that metric. These 'scores' are then averaged across all metrics to give the model quality, rounded to the nearest integer.

Chapter 6

Numerical Modelling of the Experimental Work

6: Numerical Modelling of the Experimental Work:

6.1: Model Description

The model developed and discussed in Chapter 5 (*'Sandwich Model Development'* – henceforth referred to as the 'Czabaj model', after the experiments this model was based on) will now be used to attempt to recreate the results of the experimental study in Chapter 3, henceforth referred to as the 'James model'. To reiterate from Chapter 3, all panels have planar dimensions of 150 x 100mm, and use the same 12.7mm thick (nominal) aluminium honeycomb core (*HexWEB CRIII 3/16 5052 4.4*). The skins are produced from T700S carbon fibre reinforced pre-pregs with an out-of-autoclave cured epoxy resin (*M77/42%/UD90/CHS*). The symmetric panels use 8-ply quasi-isotropic skins with a $[-45/0/45/90]_s$ lay-up on both sides. The asymmetric panels use the same 8-ply skin on the impacted face, and have a 6-ply multi-directional skin, using a $[45/0/-45]_s$ lay-up, on the distal skin. The mean ply thickness (derived from the measured skin thicknesses) of 0.107mm is used for all plies. A core thickness of 12.815mm is used in the model, which includes the thickness of the adhesive layer. This value is found by subtracting the ply thickness multiplied by the number of plies from the mean measured total panel thickness of the experimental panels. For additional realism, the measured mean planar dimensions are also used in the model, giving dimensions of 149.65 x 99.635 mm.

The damage is induced via a quasi-static indention using a ø16mm hemispherical indenter to the centre of an unsupported 125 x 75mm region of the panel (clamped around the periphery) before the compression-after-impact step, which adds simple supports to the unloaded edges of the panel, as well as the usual clamped conditions on the loaded ends. The geometric partitions used to apply the boundary conditions are altered to accommodate this. Note that the side supports used on the experimental CAI fixture are not included in the numerical boundary conditions, as in practice these exist only to provide a means to secure the knife-edges used to provide the simple-support. Including them in the model would result in an overly stiff response. The QSI and edge compression displacements in the numerical model are applied at rates of $1ms^{-1}$ and $0.5ms^{-1}$ respectively. Otherwise, the James model is constructed in the same manner as the Czabaj model, with a single cohesive layer in the impacted skin, displacements applied via rigid surfaces and a similar mesh density, using the same elements and analysed using the explicit/dynamic solver. Please see Chapter 5 for a complete description of the model. Of course, the material data is different for this model, as a different composite material system and honeycomb core was used; this data is given in Table 20.

Initially it was felt that 'configuration 2' from Chapter 5, with the cohesive surface placed closer to the core, would be the better option for this phase of the investigation, since this set-up gave better results for the small indenter cases in the Czabaj study, which are more representative of the indenter used in the experimental study. However, this configuration failed to give results for the worst damage cases, with the analysis failing very early into the compression step due to extreme element distortion in the ply block close to the core. Thus, ‘configuration 1’ is used for this part of the study. The total problem size is 51840 elements, for all panels.

Table 20: Material Data for James Numerical Model [2]

		C-E skins	**Al HC core**	**Bond ^{C}**
t (mm)		0.107 (ply)	12.771	0.01
ρ (kg/m^{-3})		1,800	70	-
E (GPa)	**1**	106.45* (tensile) *or* 92.76* (compressive)	1.48 x10$^{-4\ C}$	
	2	5.918*	1.47 x10$^{-4\ C}$	
	3	-	1.0	
K_{E3} (TPa/m)			-	1,100
G (GPa)	**12**	5.4	8.9 x10$^{-5\ C}$	-
	13	4.7	0.21	
	23	4.7	0.47	
K_G (TPa/m)	**m2**	-	-	600
	m3			370
ν	**12**	0.27*	1 ^{C}	-
	13	-	1 x10$^{-5\ C}$	
	23		1 x10$^{-5\ C}$	
σ (MPa)	**LT**	2,032.21*	-	
	LC	439.688*		
	TT	45.509*		
	TC	129.7		
	Ult	-	4.1	
	Crush		1.72	
	mode 1		-	45
τ (MPa)	**L**	72.5		-
	T	72.5		
	m2	-		66.3
	m3			66.3
G_C (N/m)	**LT**	89,830		-
	LC	78,270		
	TT	230		
	TC	760		
	m1	-		275
	m2			940
	m3			940
Mode-mix ratio				2.284

It should be made clear that this section of the investigation is not ‘more of the same’ as compared with the Czabaj study: the heavy damage induced by the 5mm and 7mm applied displacements place high demands on the numerical model, as significant ply damage, including fibre failure, is generated by the indentation steps. Conversely, the indentation used in the Czabaj models only generated BVID, with little ply damage (excluding delamination) being caused by the indentation step. Furthermore, the inclusion of the unusual asymmetric panel configuration is also a noteworthy addition.

As with the Czabaj model, the material data for the model had to be gathered from multiple sources. Some material property tests were performed to collect some of the skin data; these entries are denoted by an asterisk in Table 20. The remainder of the strength and shear data for the skin is taken from Lloyd [163], as are the skin fracture energies. The cohesive layer properties and the in-plane properties of the core are the same as those used in the Czabaj model; all properties carried over from the Czabaj study are denoted by a superscript ‘^{C}’. The out-of-plane core properties (including shear in the 13 and 23 directions, but excluding Poisson’s ratio) and the core strength data are taken from Hill [4].

One significant difference between the present model and the developmental model in Chapter 5 is the use of mass-scaling. This technique was discussed in Chapters 2 and 4 as a means to reduce the computational effort required in using the dynamic explicit solver, by using selective increases in the elemental mass to reduce the stable time increment. This technique is now used here to improve the efficiency of the model – usually only a small number of critical elements are responsible for the small minimum time increment, so in this instance, the solver is set to scale the mass of only those elements whose stable time increment is less than $2.5e^{-8}$ s. The solver will rescale the elemental mass as required every 4,000 increments, to ensure that damage progression does not result in a sudden dramatic decrease in the time increment.

6.2 Numerical Modelling Results

The results from these numerical models are now presented. All of the models are run twice using either the compressive or tensile values for the ply longitudinal Young’s Modulus, since the material property experiments performed provided both values. These variations are denoted *E1C* and *E1T* respectively (indicated by a *–c* or *–t* suffix in the tables for brevity). The models simulating higher levels of damage, with the 5mm and 7mm applied indentations, had rather noisy load-displacement responses and thus the data was smoothed via a Butterworth filter with a cut-off frequency of 35Hz. A summary of the results from the James models are presented alongside the mean results from the experimental study in Table 21 and Table 22, for the compressive and tensile values for the longitudinal ply modulus respectively.

The CAI strength prediction show strong agreement with the experimental results for the symmetric panels at all damage levels. The strength prediction is weaker for the asymmetric panels, particularly for the low- and no-damage states, though even here the agreement with the experiments is not so poor as to compromise the validity of the model. For this configuration, the agreement with the experiments is much better at the higher damage levels, becoming comparable with (and sometimes better than) the symmetric models. The asymmetric models do not capture the increase in strength for the dented *A2.5* panels as compared with the virgin panel observed in the experiments, instead showing what would be better described as insensitivity to the induced damage, even when the damage becomes highly significant. This is best seen in the negligible reduction in strength between *A2.5* and *A5*, whereas the strength reduction between *S2.5* and *S5* is much more noticeable, particularly for the *E1C* variation. From these results, one can conclude that the model does capture the same tendency for improved tolerance to the damage induced observed in the experiments for the asymmetric panels when compared with the symmetric panels. The percentage residual strength for the asymmetric panels is generally higher than for the symmetric panels, so the stabilising effect of the thickness asymmetry is clearly having some effect in the numerical analysis. That being said, it is also clear that the instability induced by this asymmetry has a significantly exaggerated influence in the model for lightly dented and undamaged panels.

Table 21: Results from the numerical models of the James experiments (E1C)[2]

Model	**P_{max} (kN)**	**σ_{CAI} (MPa)**				**% residual strength**		
		Num	**Exp**	**% error**		**Num**	**Exp**	**% error**
SV-c	41.4	**242.8**	*259.9*	**-6.6**		-	-	-
S2.5-c	40.8	**239.2**	*245.4*	**-2.5**		98.5	*94.4*	4.3
S5-c	36.4	**213.6**	*219.8*	**-2.8**		88.0	*84.6*	4.0
S7-c	30.1	**176.3**	*204.3*	**-13.7**		72.6	*78.6*	-7.6
AV-c	30.3	**202.7**	*239.9*	**-15.5**		-	-	-
A2.5-c	29.7	**198.7**	*254.7*	**-22.0**		98.0	*106.2*	-7.7
A5-c	29.5	**197.9**	*216.2*	**-8.5**		97.6	*90.1*	8.3
A7-c	28.4	**190.5**	*206.6*	**-7.8**		87.9	*86.1*	9.1
	$\delta_{failure}$ (mm)	**Strain-to-Failure (%)**				**Stiffness (GPa)**		
		Num	**Exp**	**% error**		**Num**	**Exp**	**% error**
SV-c	1.89	**1.26**	*1.27*	**-0.9**		37.4	*31.19*	20.0
S2.5-c	1.60	**1.07**	*1.20*	**-10.8**		37.4	*29.24*	28.0
S5-c	1.11	**0.74**	*1.02*	**-27.6**		37.0	*29.33*	26.0
S7-c	0.78	**0.52**	*0.98*	**-47.0**		35.5	*28.04*	26.8
AV-c	1.65	**1.10**	*1.18*	**-6.5**		41.3	*29.79*	38.7
A2.5-c	1.20	**0.80**	*1.04*	**-23.2**		40.9	*30.42*	34.4
A5-c	0.90	**0.60**	*0.97*	**-38.5**		39.2	*29.58*	32.5
A7-c	0.81	**0.54**	*0.91*	**-40.6**		39.8	*30.14*	32.0

The use of the tensile value for the Young's modulus usually increases the ultimate strength of the panels (with the notable and unexpected exception of *A7-t*) as the elastic stability is increased for these panels, delaying the onset of buckling. This results in slight overestimates for the failure strength in some of the symmetric panels and improves the predictive ability of the model for the asymmetric panels, though the effect of this change on the strength of these panels is marginal (excluding *A7-t*, as already stated). The percentage residual strength prediction is also good for both panel configurations and longitudinal stiffness inputs. This is aided by the good prediction of the undamaged panel strength for the symmetric panels, but it is noteworthy that the weaker strength estimate for the undamaged asymmetric panels does not harm the percentage residual strength estimate, further supporting the conclusion that the use of the thinner distal skin does indeed produce a balancing effect in the damaged panels.

The stress-strain response of the numerical models is not representative of the experiments. The stress-strain responses are presented in along with the idealised, averaged stress-strain responses from the panel experiments in Figure 85 to Figure 88 for the *E1C* and *E1T* variations of the symmetric and asymmetric panel models respectively. First of all, the stiffness of the panels is hugely overestimated by the models, in some cases being 50% greater than the stiffness calculated via the experimental load-displacement responses when using the tensile longitudinal ply stiffness. The overestimate in the overall stiffness is significantly reduced using the longitudinal compressive modulus, but the error still remains rather high. It should be noted that the overall panel stiffness found by considering the (admittedly small) sample of strain gauged panels is considerably higher than that calculated from the force-displacement curves, so it is possible that the stiffness predicted by the numerical models is actually not as inaccurate as it may appear at first glance. Indeed, the stiffness of some of the models agrees very well with the strain gauge stiffness data, with a percentage difference between the two values of less than 10% for half of the models considered.

Table 22: Results from the numerical models of the James experiments (E1T)[2]

Model	**P_{max} (kN)**	**σ_{CAI} (MPa)**				**% residual strength**		
		Num	**Exp**	**% error**		**Num**	**Exp**	**% error**
SV-t	42.8	**249.6**	*259.9*	**-4.0**		-	-	-
S2.5-t	42.3	**248.2**	*245.4*	**1.1**		99.4	*94.4*	*5.3*
S5-t	40.7	**238.5**	*219.8*	**8.5**		95.5	*84.6*	*13.0*
S7-t	30.9	**181.4**	*204.3*	**-11.3**		72.7	*78.6*	*-7.6*
AV-t	31.0	**207.7**	*239.9*	**-13.4**		-	-	-
A2.5-t	30.0	**201.1**	*254.7*	**-21.0**		96.9	*106.2*	*-8.8*
A5-t	29.9	**200.1**	*216.2*	**-7.5**		96.4	*90.1*	*6.9*
A7-t	27.3	**182.6**	*206.6*	**-11.6**		87.9	*86.1*	*2.1*
	$\delta_{failure}$ (mm)	**Strain-to-Failure (%)**				**Stiffness (GPa)**		
		Num	**Exp**	**% error**		**Num**	**Exp**	**% error**
SV-t	1.57	**1.05**	*1.27*	**-17.2**		42.6	*31.19*	36.7
S2.5-t	1.57	**1.05**	*1.20*	**-11.9**		41.4	*29.24*	41.7
S5-t	1.27	**0.85**	*1.02*	**-17.2**		41.7	*29.33*	42.3
S7-t	0.73	**0.49**	*0.98*	**-49.7**		42.5	*28.04*	51.6
AV-t	1.56	**1.04**	*1.18*	**-11.6**		45.5	*29.79*	52.6
A2.5-t	1.17	**0.78**	*1.04*	**-25.2**		45.2	*30.42*	48.5
A5-t	0.87	**0.58**	*0.97*	**-40.5**		44.6	*29.58*	50.8
A7-t	0.70	**0.47**	*0.91*	**-48.7**		44.0	*30.14*	45.9

What is of greater concern is that the models do not exhibit the expected linear elastic response leading directly into a sharp load drop due to brittle failure, as observed in the experiments. The symmetric panels show bilinear, and occasionally even tri-linear, stress-strain behaviour, with all panels showing a drop in an the overall panel stiffness to a stiffness slightly less than that seen in the experiments at a strain of around 0.5% for the *E1C* models or 0.4% for the *E1T* models. This drop occurs at this strain level regardless of damage level, except for the highly damaged *S7* models, where the stiffness reduction approximately coincides with failure. This initial softening appears to be caused by the formation of highly localised compressive matrix damage, and the initial formation of partial compressive fibre damage and cohesive surface damage. *SV* and to a lesser extent *S2.5* also show a plateau in the stress at around 0.9% strain. Aside from the changes in strength and stiffness already discussed, using the tensile longitudinal ply modulus has no significant influence on the response of the symmetric panels, except that the strain-to-failure of the undamaged panel is markedly reduced using this higher stiffness value.

The asymmetric panels usually show a plateau in the stress at around either 0.5% or 0.45% strain for the *E1C* and *E1T* model variations respectively. The length of this plateau gets shorter with increasing damage, until it is essentially non-existent for *A7*. The strain-at-failure is usually significantly underestimated for all models as well, getting lower with increasing damage. Like the symmetric panel models, changing the ply modulus has no significant influence on the response of the asymmetric models. As with the experiments, it appears that none of the numerical models experience any appreciable reduction in the initial panel stiffness due to the induced damage. Additionally, the model shows a considerable amount of global out-of-plane deformation from the indentation, which was not observed the experiments. The peculiar behaviour of the models may be due to the nature of the damage criteria used in the model, whereby damage propagates due to energy release upon reaching the specified strength thresholds. Additionally, as only a small amount of data for this particular material was collected experimentally, with the rest gathered from the literature, there is a distinct possibility that the input data is inconsistent, thus creating these anomalous stress-strain responses. Both of these factors will be investigated and discussed later in this chapter. It is important to note that the deviation from the usual elastic-brittle strain-strain response for composite materials becomes less severe for all panels with increasing damage, becoming insignificant or non-existent for the *S7* and *A7* cases.

It was previously mentioned that mass-scaling has been used in this particular model to improve the computational efficiency. To check the validity of this approach, the mass-scaled models for the virgin and 2.5mm indentation cases (both symmetric and asymmetric) are compared with the results from non-mass-scaled versions of these models. The strain-strain responses from this exercise are shown in Figure 89 and Figure 90 for the symmetric and asymmetric panels respectively. The use of mass scaling in this investigation has a negligible effect on the response of the panels. Crucially, the ultimate strength and the response up to this point is not changed to any appreciable degree, though the strain at the load drop does occasionally vary. Without mass scaling, the stable time increment for these panel models is typically of the order $1e^{-8}$ s, so the mass scaling used here is very minor from a physical perspective, but has a significant effect on the run time. For the virgin models, the analysis is as much as 1.5 hours faster with mass scaling, and 5 to 7 hours faster for the 2.5mm indentation models. The maximally damaged models complete the analysis in approximately 20 hours, whereas preliminary, non-mass-scaled models with this amount of damage required nearly twice that. As a final check, the ratio of kinetic energy to system internal energy is checked. In the compression phase, the energy balance is always less than 0.1%, and in the indentation phase the ratio does not exceed 0.5% (and is usually lower, as the internal energy is higher for the more deeply indented panels, while the kinetic energy remains effectively constant). This is well within the accepted 5% threshold for a valid quasi-static solution [147].

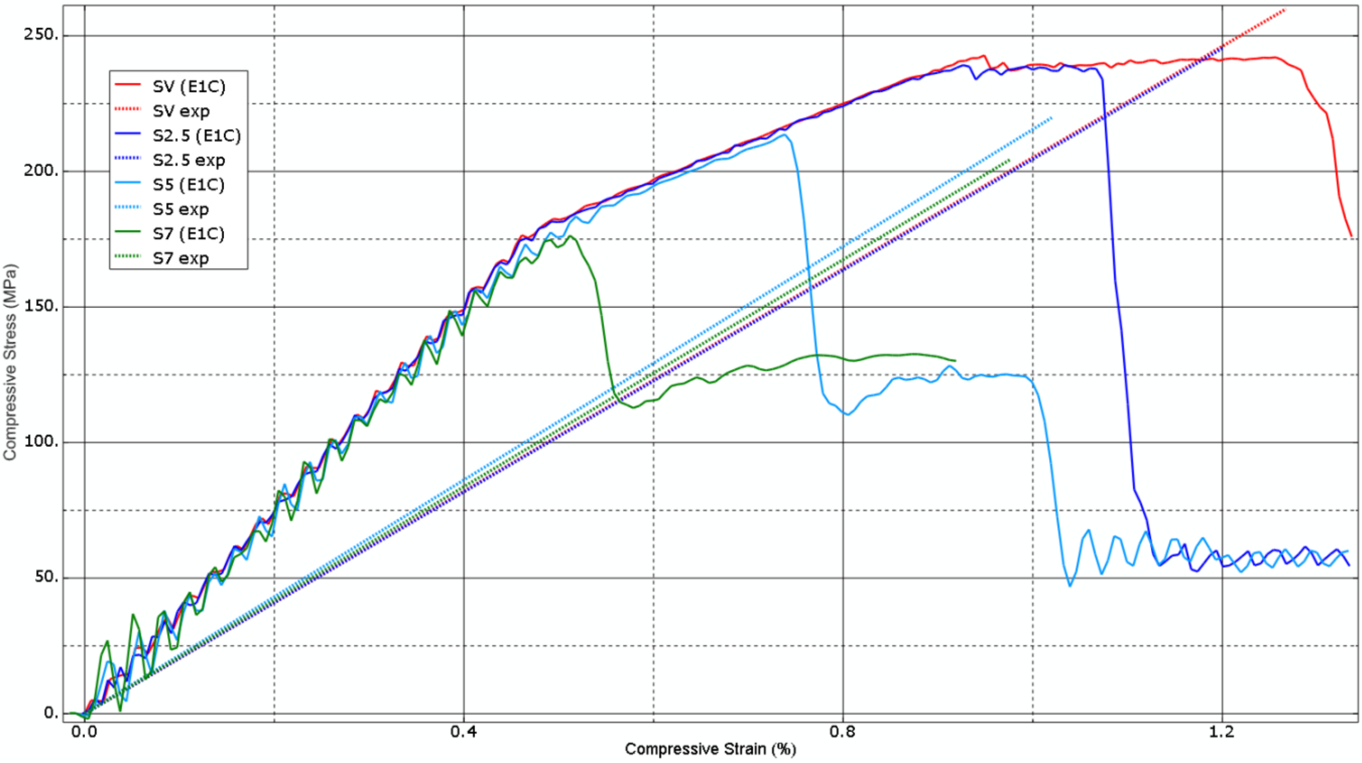

Figure 85: Stress-strain response from the models of the James experiments (symmetric, E1C) [2]

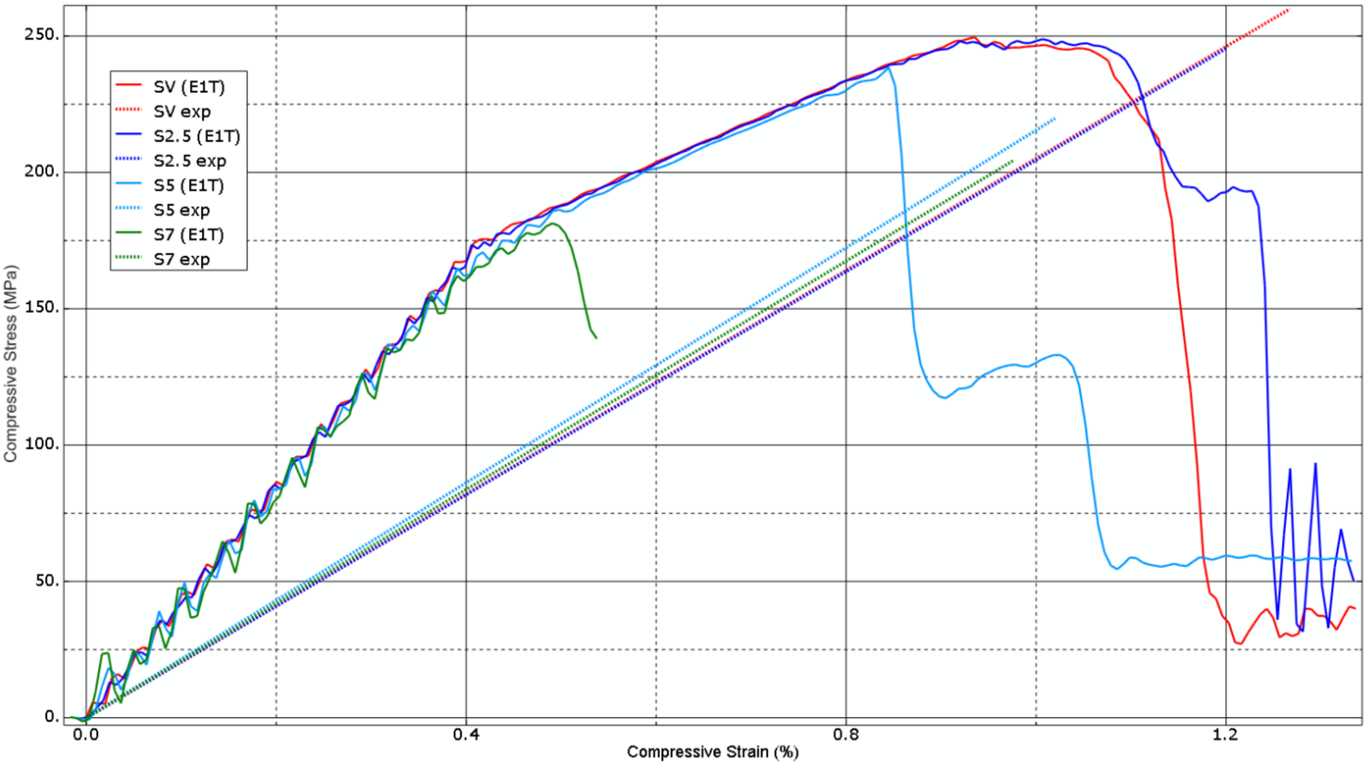

Figure 86: Stress-strain response from the models of the James experiments (symmetric, E1T) [2]

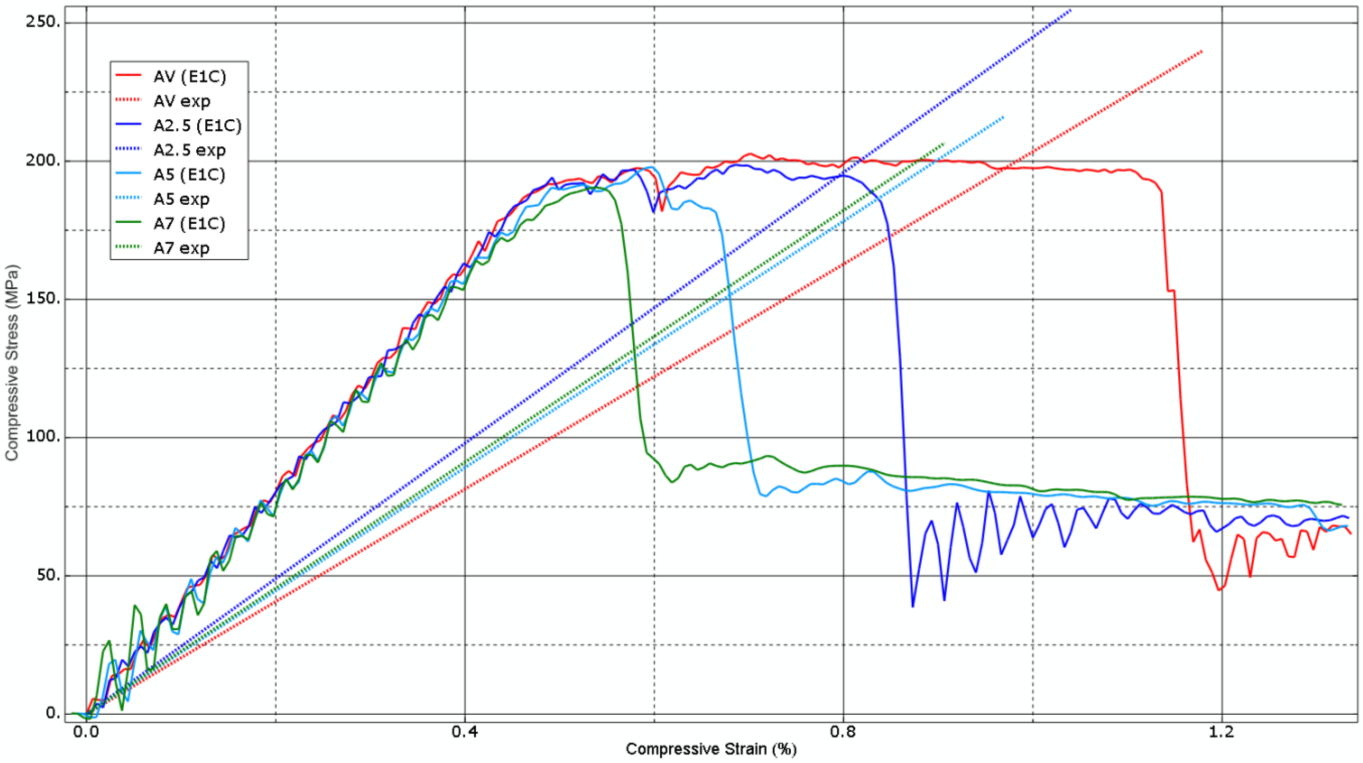

Figure 87: Stress-strain response from the models of the James experiments (asymmetric, E1C) [2]

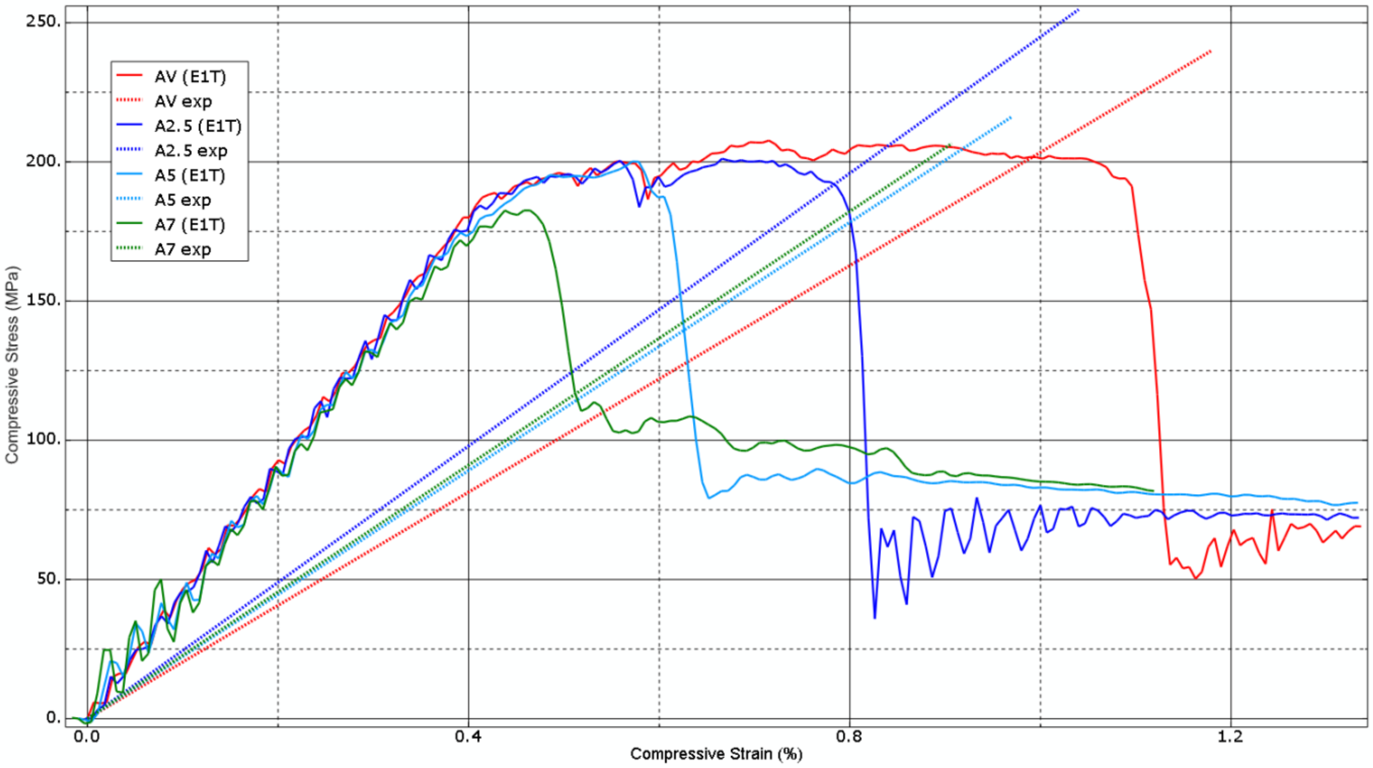

Figure 88: Stress-strain response from the models of the James experiments (asymmetric, E1T) [2]

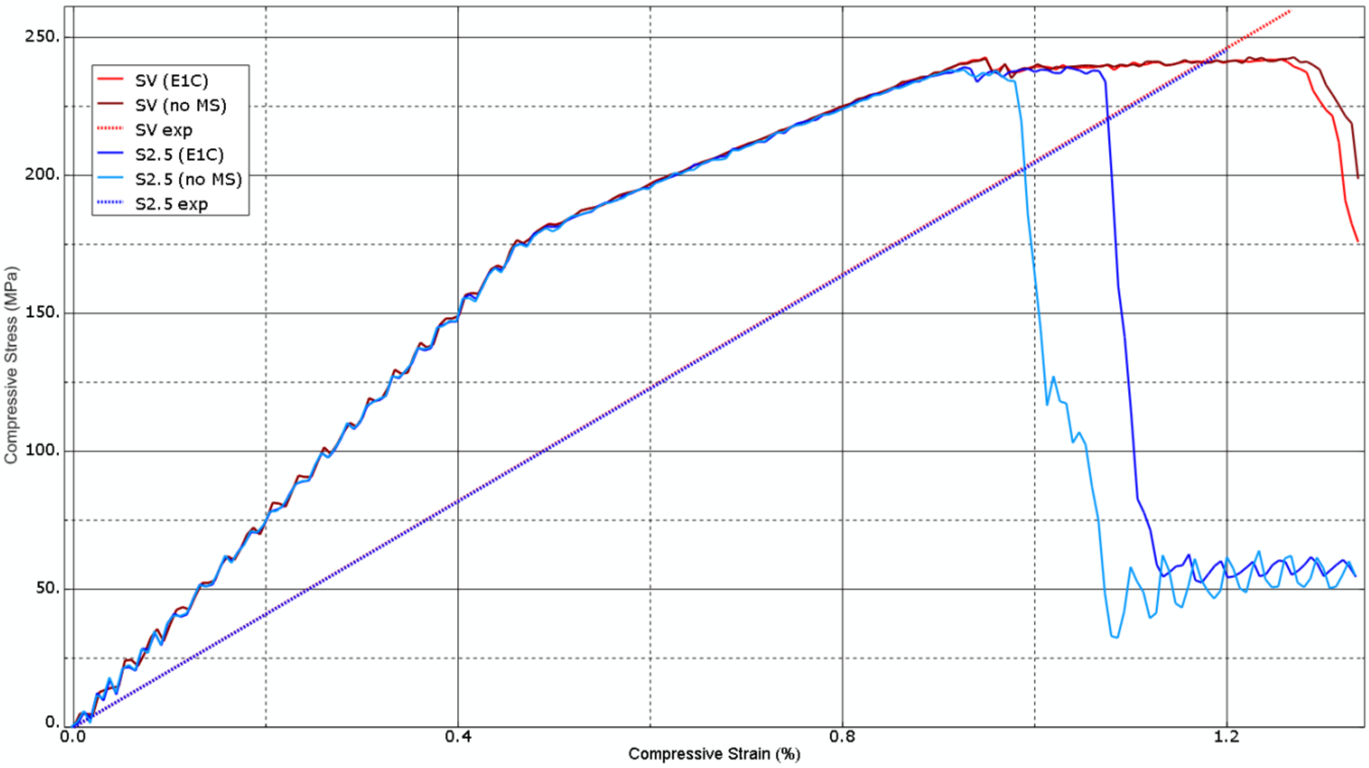

Figure 89: Comparison of mass-scaled and non-mass-scaled symmetric panels

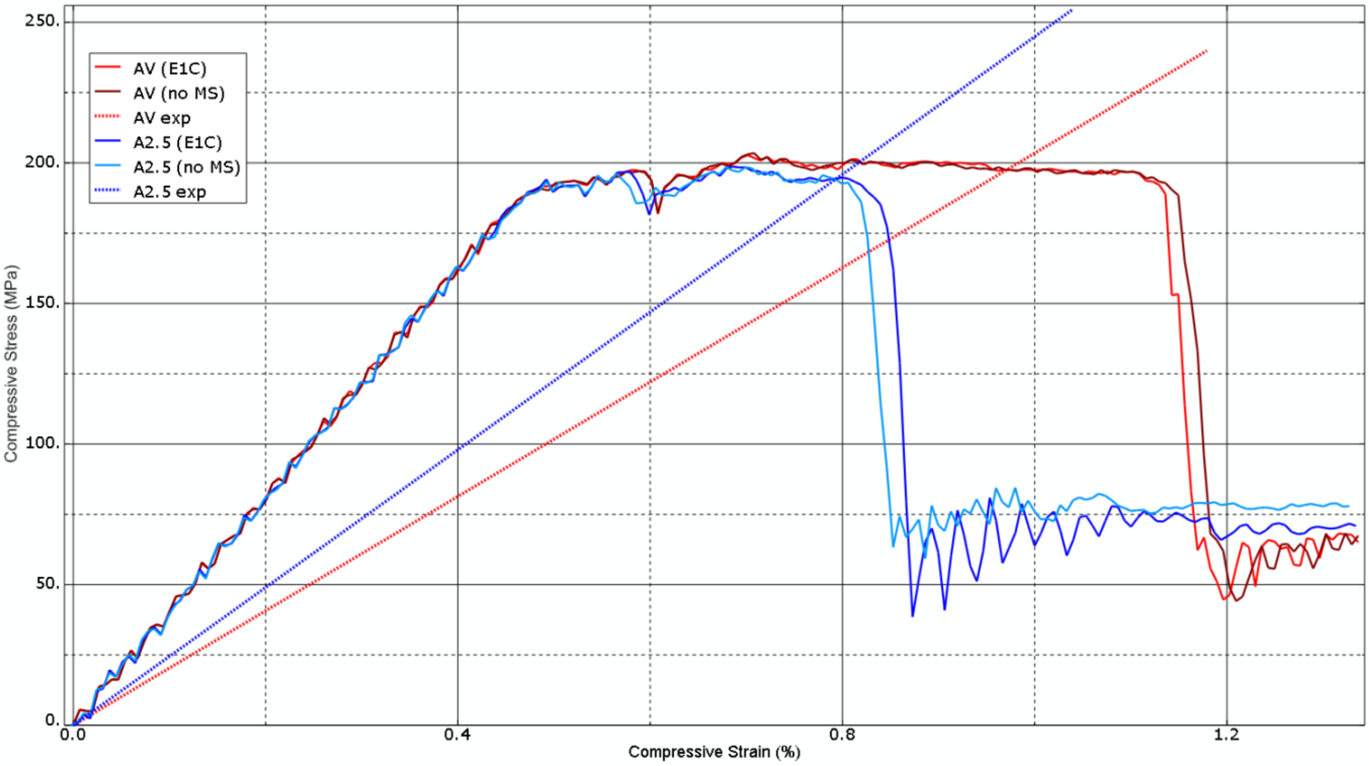

Figure 90: Comparison of mass-scaled and non-mass-scaled asymmetric panels

6.3 Damage and Failure Progression

The undamaged symmetric panels fail via a delamination buckle forming near the end of the panel, as seen in the experiments. However, the damaged symmetric panels all fail via the propagation of delamination buckling originating at the damaged region in the centre of the panel, with no evidence of extensive fibre damage that would indicate kink band formation. The propagation of the delamination buckle seen in the model is shown in Figure 91 for *S7-C*, and is representative of all of the panels failing in this manner. The undamaged asymmetric panel fails in a similar manner to the damaged panels, with the delamination buckling originating at a random location between the loaded end and the centre line. *A2.5* and *A5* are also more interesting cases, with the delamination buckle originating at the damaged region as in the other damaged panels, but propagating at an angle, rather than perpendicular to the load direction. This tendency is shown in Figure 92 for *A2.5-C*. *A7* fails in the same manner as the damaged symmetric panels. The use of the higher longitudinal modulus in the plies does not change the nature of the final failure, though in the case of *SV-T*, the delamination at the loaded end seems to be somewhat exaggerated, resulting in a rather dramatic peeling of the free surface of the top skin (see Figure 93). Generally, the failures seen in the numerical models are a deviation from the experiments, which typically showed failure via kink band formation for the 5mm and 7mm indented panels, and via delamination buckling at the end for the undamaged and 2.5mm indented panel. Thus, it would appear that delamination is perhaps overly influential in this particular model.

Figure 91: Delamination propagation in S7-C. The leftmost frame shows the panel just prior to final failure, with the delamination growing outwards from the damaged region to the fully-developed state in the rightmost frame. The failure propagated fully in less than 0.2ms. [2]

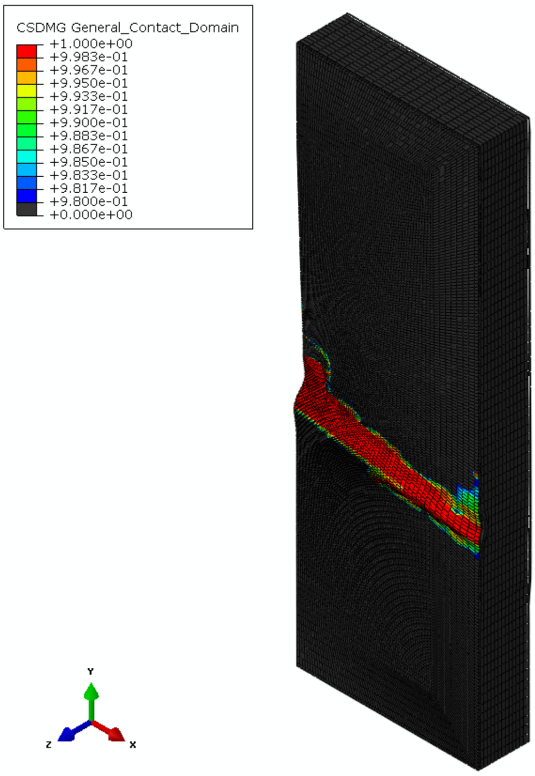

Figure 92: Failure of A2.5-C, showing angled propagation of the delamination buckle.

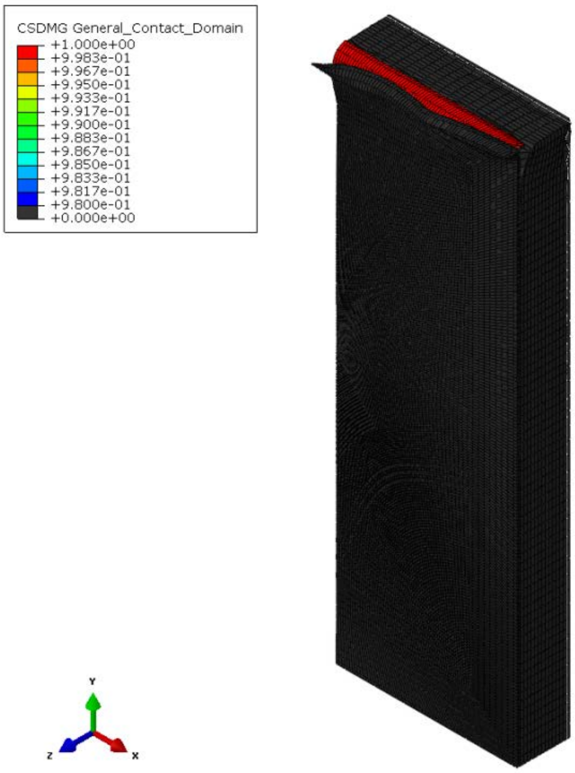

Figure 93: Severe delamination of SV-T, resulting in skin peeling.

Next, the accuracy of the estimates of damage magnitude from the QSI phase of the analysis is considered by comparison with the experimental QSI results, with the damage extents measured from the numerical models presented in Table 23 to Table 25.

As with the Czabaj model, delamination is considered to have occurred in the model when the scalar stiffness degradation in the cohesive surface equals one. Delamination extent predicted by the model is included here, though there is no experimental data available to verify the accuracy of this estimate. The diameter of the dent is determined by considering the region where the depth of the dent exceeds 0.5mm. It is not really practical to consider a separate measure for the depth of fibre damage, as the thickness of the skin in the model does not change any by any appreciable amount under indentation. Another curious effect is that the dent often bulges outwards after the indenter is withdrawn, complicating the estimate of the dent depth. The peak displacement in the top face of the indented skin will be used for this measure, but it should be noted that this may not necessarily be at the centre of the panel.

The core damage extent is determined differently from the Czabaj model. The key driver for this change is the global deformation caused by the indentation, so simply setting a universal lower bound on the out-of-plane core displacement is inadequate for estimating the onset of crushing. Additionally, the threshold displacement for the onset of core crushing is altered, by calculating the strain at crushing using the out-of-plane stiffness and the ultimate strength, and then multiplying this by the core thickness. This gives a displacement at crushing onset of 0.052mm for this configuration. The lower bound for core damage is thus this displacement plus the peak global displacement of the core for the panel in question. This change should give a better estimate for the predicted core crushing, which when coupled with the availability of core crush measurements from the experiment, makes a more rigorous assessment of the effectiveness of the core material model possible. As with the Czabaj model, the numerical damage sizes are estimated from the element sizes; based on the mesh seeds for this model, 1 element approximately equals 0.55mm in the skin, and 2.5mm in the core. The core also has approximately 1 element/mm through-the-thickness, as in the Czabaj model. Figure 94 to Figure 96 show the dent and core displacement profiles for *S2.5-C*, *S5-C* and *S7-C*, which are used as a proxy to estimate the extent of the panel damage. The profiles shown here are representative of the damage at these three indentation levels for both the symmetric and asymmetric panels, and for both values of longitudinal ply modulus.

First of all, it is noteworthy that the ‘cup’ of damaged fibres observed in the experiments is not recreated by the model, and there is little evidence of extensive fibre damage even in the most severely damaged cases. Without significant fibre damage in the indented region where the indenter starts to penetrate the top skin, there is no suitable initiation point for kink-band formation, which would explain why the numerical panel models fail exclusively via delamination buckling. The same difficulty was seen in Chapter 4, where the skin model is developed from Lloyd’s results of a composite plate loaded to failure via quasi-static indentation [163] – recall how the numerical model of this case resulted in a load plateau at peak load rather than the expected load drop due to localised fibre failure (see Figure 66, section 4.3.3). It has already been noted that the dent bulges outwards in all cases, indicating a degree of elastic recovery in the damage skin that simply wasn't present in the experimental 5mm and 7mm indentation cases, due to lack of local fibre breakage. The presence of the global panel deformation may also be attributed to this deficiency in the skin damage model. The relatively minor global deflection seen in the 2.5mm indentation cases may actually be plausible - after all there is a fairly large unsupported region in the panel during the indentation phase - but when the amount of indentation increases, the global deformation also continues to rise as the indenter fails to penetrate the top skin and create the severe localised damage that is expected. The global deflection may contribute to the tendency of the model to underestimate the ultimate strength, as the resultant geometric imperfection causes a reduction in the elastic stability of the panel, and thus increasing the likelihood of buckling.

Table 23: Skin damage metrics from numerical model (compressive longitudinal modulus)

Model	**δ_{global} (mm)**	**$P_{max,\ indt}$ (N)**			**Dent depth (mm)**			**Dent ø (mm)**		
		Num	**Exp**	**% error**	**Num**	**Exp**	**% error**	**Num**	**Exp**	**% error**
S2.5-c	0.94	1162	2219	-47.6	1.3	1	30.0	24.8	40	-38.0
S5-c	2.33	2333	2916	-20.0	3.1	2	55.0	33.6	45	-25.3
S7-c	2.63	2939	2928	0.4	4.4	2.5	76.0	34.1	50	-31.8
A2.5-c	0.97	1158	2264	-48.9	1.3	1	30.0	24.8	37	-33.0
A5-c	2.58	2345	2539	-7.6	3.0	2	50.0	33.6	42	-20.0
A7-c	2.84	2939	2662	10.4	4.5	2.5	80.0	34.1	40	-14.8

Table 24: Skin damage metrics from numerical model (tensile longitudinal modulus)

Model	**δ_{global} (mm)**	**$P_{max,\ indt}$ (N)**			**Dent depth (mm)**			**Dent ø (mm)**		
		Num	**Exp**	**% error**	**Num**	**Exp**	**% error**	**Num**	**Exp**	**% error**
S2.5-t	0.84	1224	2219	-44.8	1.3	1	30.0	23.9	40	-40.3
S5-t	2.45	2480	2916	-15.0	3.0	2	50.0	33.3	45	-26.0
S7-t	2.61	3063	2928	4.6	4.4	2.5	76.0	34.1	50	-31.8
A2.5-t	1.04	1201	2264	-47.0	1.3	1	30.0	25.3	37	-31.6
A5-t	2.64	2406	2539	-5.2	3.0	2	50.0	33.6	42	-20.0
A7-t	2.81	3030	2662	13.8	4.4	2.5	76.0	34.1	40	-14.8

Table 25: Core damage and delamination metrics from numerical model

Model	**Crush depth (mm)**					**Crush ø (mm)**					**Delamination area (mm^2)**	
	Exp	**Num**		**% error**		**Exp**	**Num**		**% error**			
		C	T	C	T		C	T	C	T	C	T
S2.5	5	3.4	4.4	-32.0	-12.0	37	12.5	13.8	-66.2	-62.7	1996	2121
S5	6.5	12.3	11.8	89.2	81.5	42	15	13.8	-64.3	-67.1	2591	2651
S7	9.5	12.3	12.3	29.5	29.5	45	17.5	17.5	-61.1	-61.1	3969	3914
A2.5	5	2.9	3.4	-42.0	-32.0	35	12.5	12.5	-64.3	-64.3	2053	1819
A5	7	12.3	11.8	75.7	68.6	37	13.8	12.5	-62.7	-66.2	2680	2501
A7	12	11.8	11.8	-1.7	-1.7	39	16.3	17.5	-58.2	-55.1	3748	3803

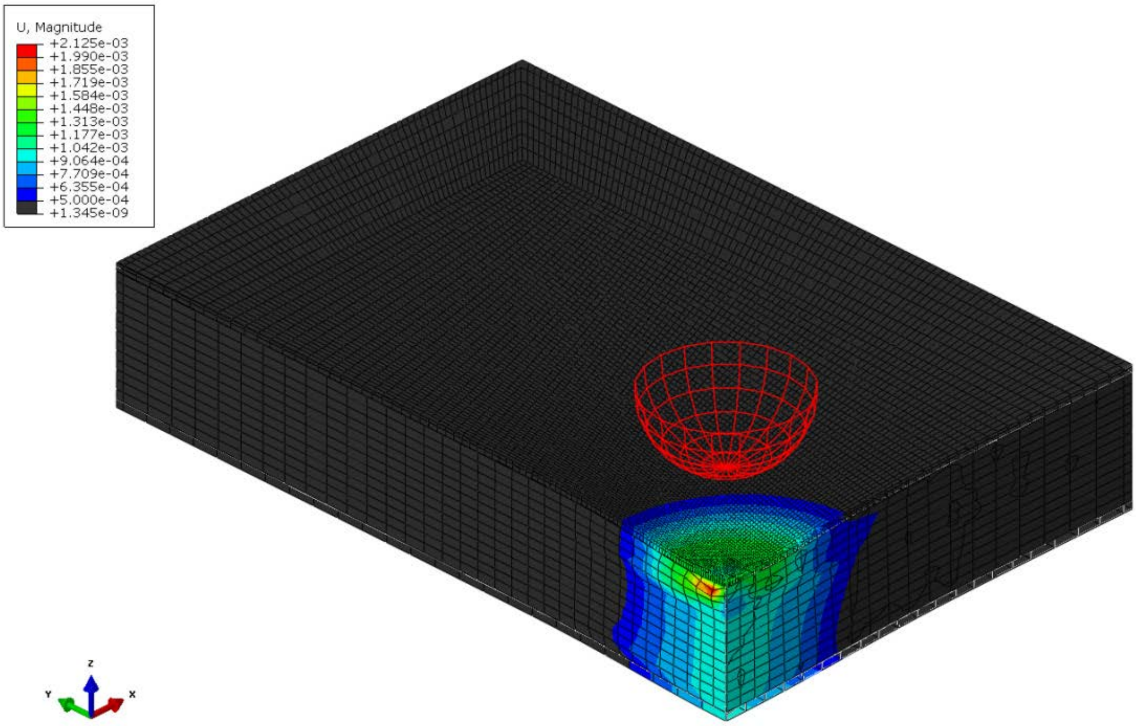

Figure 94: Damage profile for S2.5-C

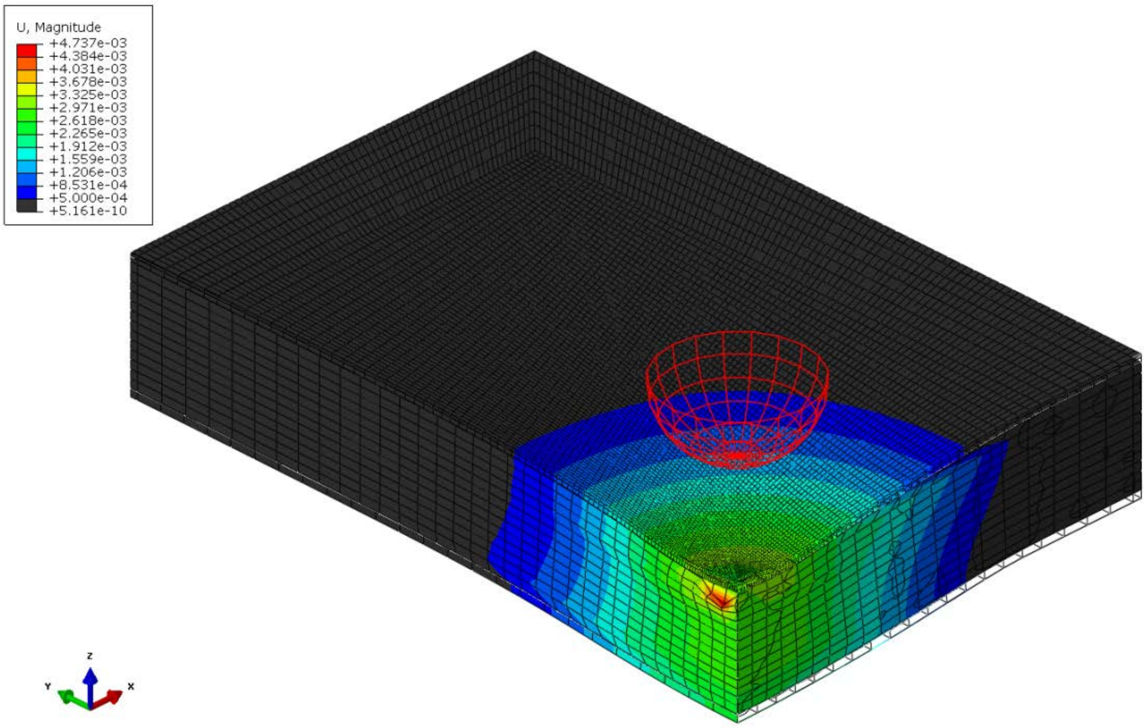

Figure 95: Damage profile for S5-C [2]

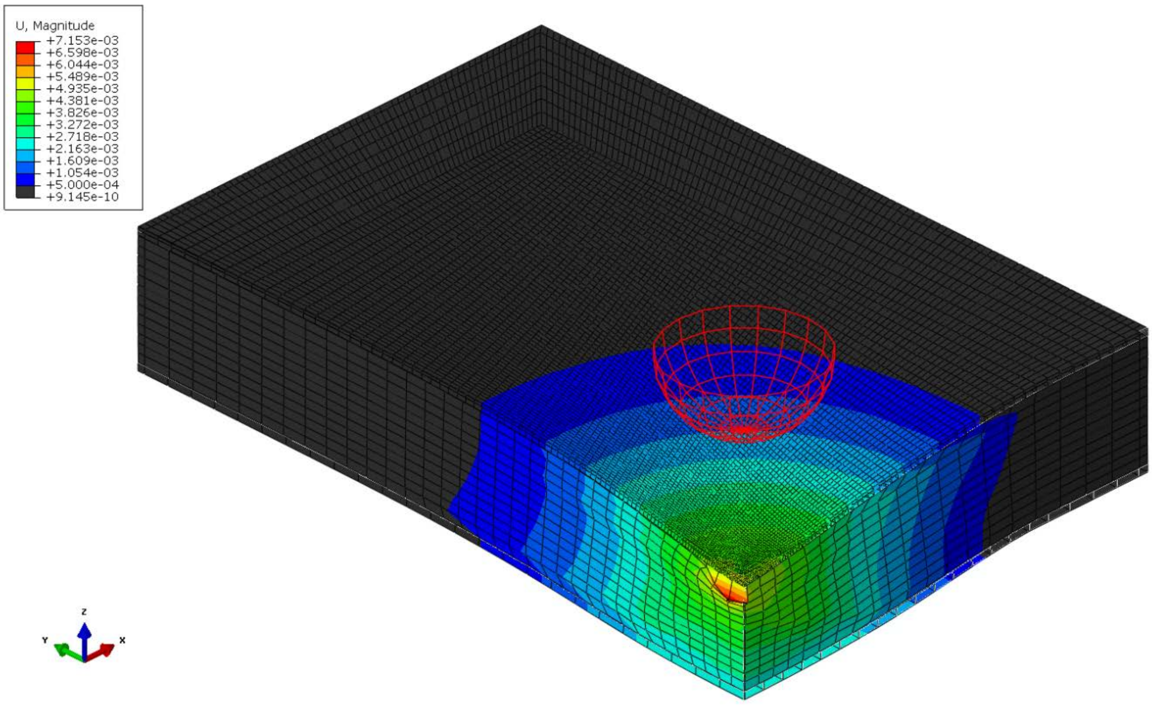

Figure 96: Damage profile for S7-C

As with the Czabaj models, the prediction of damage magnitude is again very poor. The depth of the dent and core damage is usually over-estimated, often severely so, whereas the dent diameter and particularly the core damage diameter are considerably underestimated. The prediction for the peak indentation load varies with the applied dent, significantly underestimating the load for the small indentation, and overestimating the load for the largest indentation. These errors are likely due to the global deformation (as in bending the whole panel is less stiff than the localised portion of well-supported skin in contact with the indenter) and the inability of the model to capture the localised fibre damage, respectively. There is no significant difference in the damage metrics between the symmetric and asymmetric panels, though the latter does show slightly higher global deformation and slightly lower peak indentation forces, due to the reduced bending stiffness of the asymmetric panels. This is expected based on the experimental observations, where the insensitivity of the damage metrics to panel configuration is due to the identical thickness and lay-up of indented skin between the two configurations. The use of the tensile longitudinal ply modulus causes a minor increase in the overall panel stiffness, notable in the slight reduction in global deformation and marginally increased peak indentation forces, though this change does not change the damage extent in any appreciable way.

The delamination produced by the indentation is, as with the other damage metrics, effectively independent of panel configuration. The delamination after indentation is shown for *S2.5* in Figure 97. The delamination after indentation and just prior to ultimate failure are shown in Figure 98 and Figure 99 for *S5* and *S7* respectively, showing the growth in the delamination with the compressive loading. These images are representative of the delamination present at these damage levels for both panel configurations and longitudinal moduli. Typically, panels with 2.5mm and 5mm of indentation show an elliptical delamination with the major axis being parallel with the panel transverse direction. For the 7mm indentation case, the major axis switches to become parallel to the longitudinal direction. The largest delamination also starts to deviate from the elliptical form, with lobes forming in the longitudinal direction. In all cases, the dimension of the axis parallel to the transverse direction remains approximately constant, with only the longitudinal dimension of the delamination changing. As the compressive load is applied, the delaminations formed by the 5mm and 7mm indentations show uniform growth prior to the propagation of delamination buckling. This is particularly prominent in the 7mm case, with the delamination induced by the indentation nearly doubling in size prior to ultimate failure. The 2.5mm indentation case does not exhibit this growth in the delamination prior to failure, with the delamination buckling propagation occurring suddenly with no warning. As the delamination grows, dark regions are seen in the images which perhaps suggests that the cohesive layer is reforming in this region, though that is not possible as the option for the cohesive bond to reform after failure and separation (in a manner akin to Velcro) is not selected in the numerical pre-processor. Thus, the meaning and reason behind this remains unclear. It is possible that these dark regions indicate that the two ply blocks are coming back into contact with the compressive loading, but not rebonding. In any event, the delamination buckle still propagates in the expected manner. Again, note that the delamination extent was not measured in the experimental study, so the form and size of the delamination predicted by the numerical model still requires experimental validation.

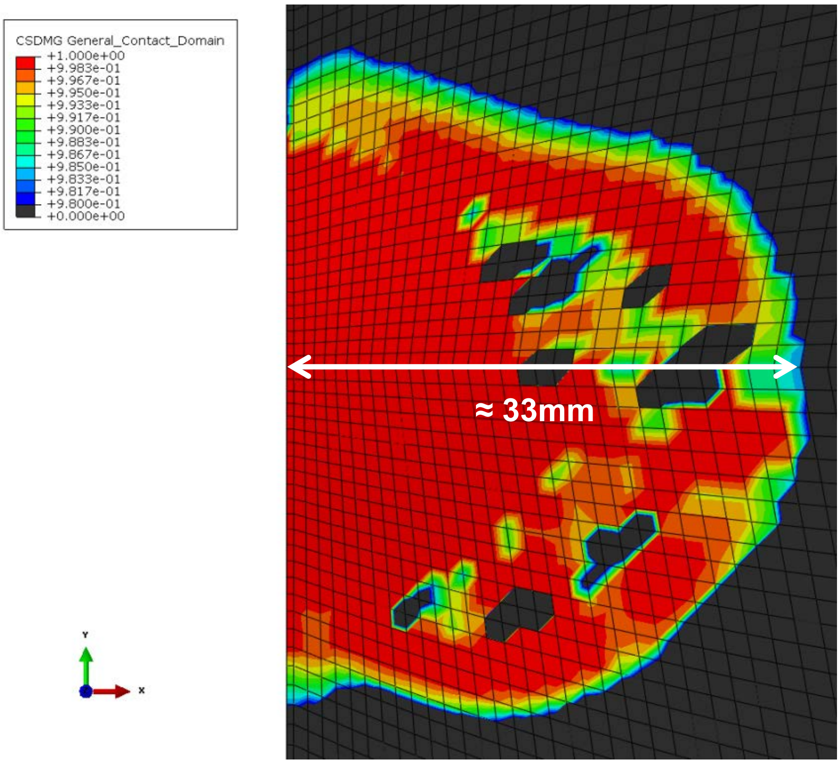

Figure 97: Delamination after indentation for S2.5

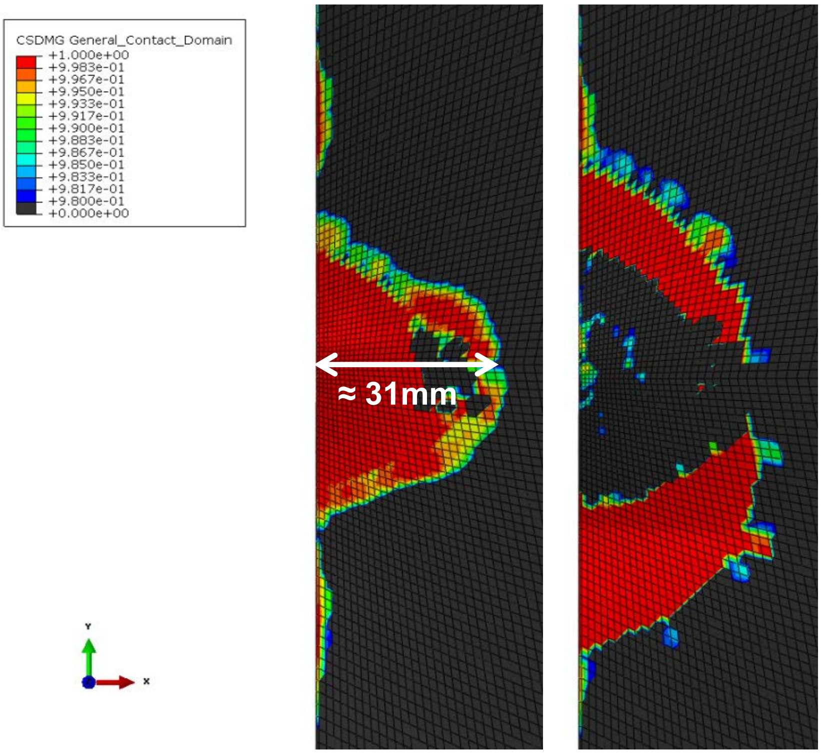

Figure 98: Delamination in S5 a) (left) after indentation and b) (right) immediately prior to ultimate failure

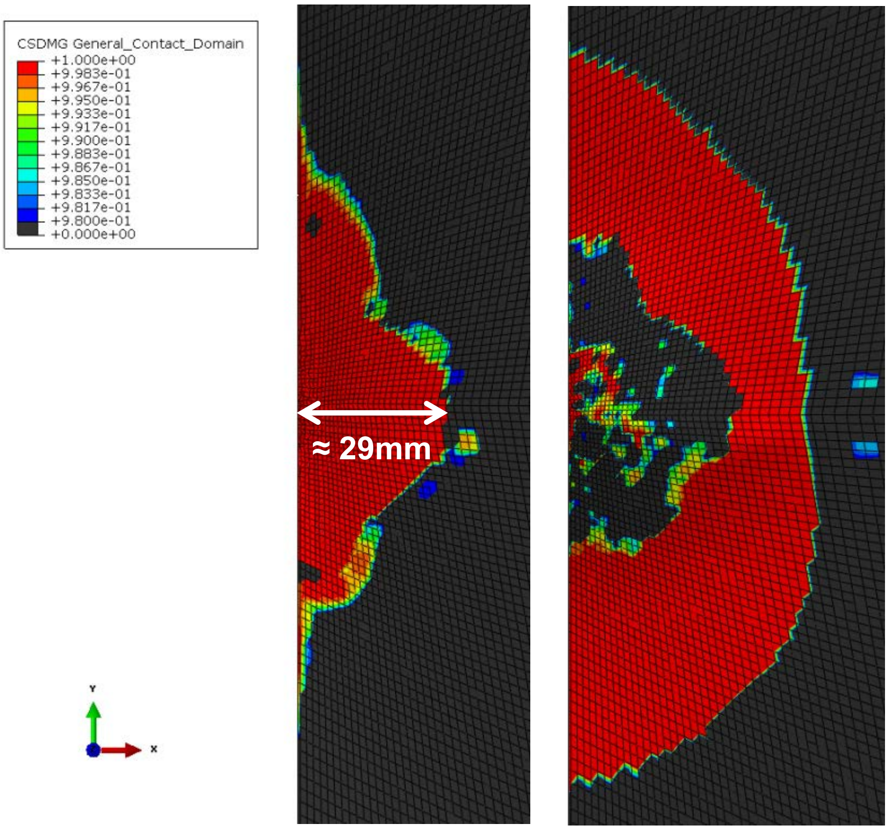

Figure 99: Delamination in S7 a) (left) after indentation and b) (right) immediately prior to ultimate failure

6.4 Investigation of the Unexpected Stress-Strain Response

The unexpected stress-strain response is investigated next, in a manner similar to the parametric study shown in Chapter 5. Of particular interest are the quantities not found experimentally, especially the shear strengths and stiffness, which are felt to contribute to the error in the stiffness prediction, and the fracture energies of the skin and bond layer, which may be contributing to the multi-linear stress-strain response and load plateaus seen in some of the models. The variations discussed in this section are for the virgin symmetric and asymmetric panel model, as these models showed the biggest deviation from the expected experimental shape. The original models, as presented previously in this chapter, are henceforth referred to as the *'benchmark'* models, and use the same designation in the graph legends as before.

By comparison of the material used for this particular model (Table 20) and the data used in the Lloyd and Czabaj models (Table 6 and Table 10) one quantity that sticks out as questionable is the longitudinal compressive strength σ_{LC}. The experimental value has been used in this model, as previously stated, but is approximately 2.5 times smaller than the other values, while the other experimentally-derived values used here are broadly comparable with those in the other data sets. Thus, the first variation trialled here changes only σ_{LC}, using the value from Lloyd instead (σ_{LC} = 1,032 MPa [163]). This variation is also trialled for the maximally damaged 7mm applied indentation models, as these represent the 'worst case' situation as far as damage is concerned, though it should be reiterated that these panels did not deviate from the usual elastic-brittle strain-stress response to any significant extent, if at all. The results of this change for both the symmetric and asymmetric models are shown with the experimental result and the benchmark model results in Figure 100 to Figure 103, for both values of the longitudinal modulus that were found in testing.

It is clear from these plots that the markedly lower longitudinal compressive strength is the key parameter resulting in the flawed response of the benchmark models. This is particularly obvious for the virgin symmetric panels, where the use of the higher σ_{LC} value gives an almost-textbook demonstration of the elastic-brittle behaviour expected of composite materials, and which has been observed in the experiments (see the purple traces in Figure 100 and Figure 101). The modified asymmetric panel models (the purple traces in Figure 102 and Figure 103) do not mimic the experiments quite as well, showing evidence of progressive failure that was not observed in the experiments (or at least, not nearly to the same extent), though this is still clearly a marked improvement on the plateau seen in the benchmark asymmetric models (red traces). Progressive failure of this nature, with multiple load drops prior to ultimate failure, is entirely consistent with the known behaviour of composite materials. Indeed, many of the experiments did show evidence of continued loading after the main failure, as the distal skin appeared to start carrying more load. Based on the original strain-strain plots, it is fair to presume that 2.5mm and 5mm indentation models using the increased longitudinal compressive strength value would fit somewhere between the undamaged and 7mm indentation cases presented here.

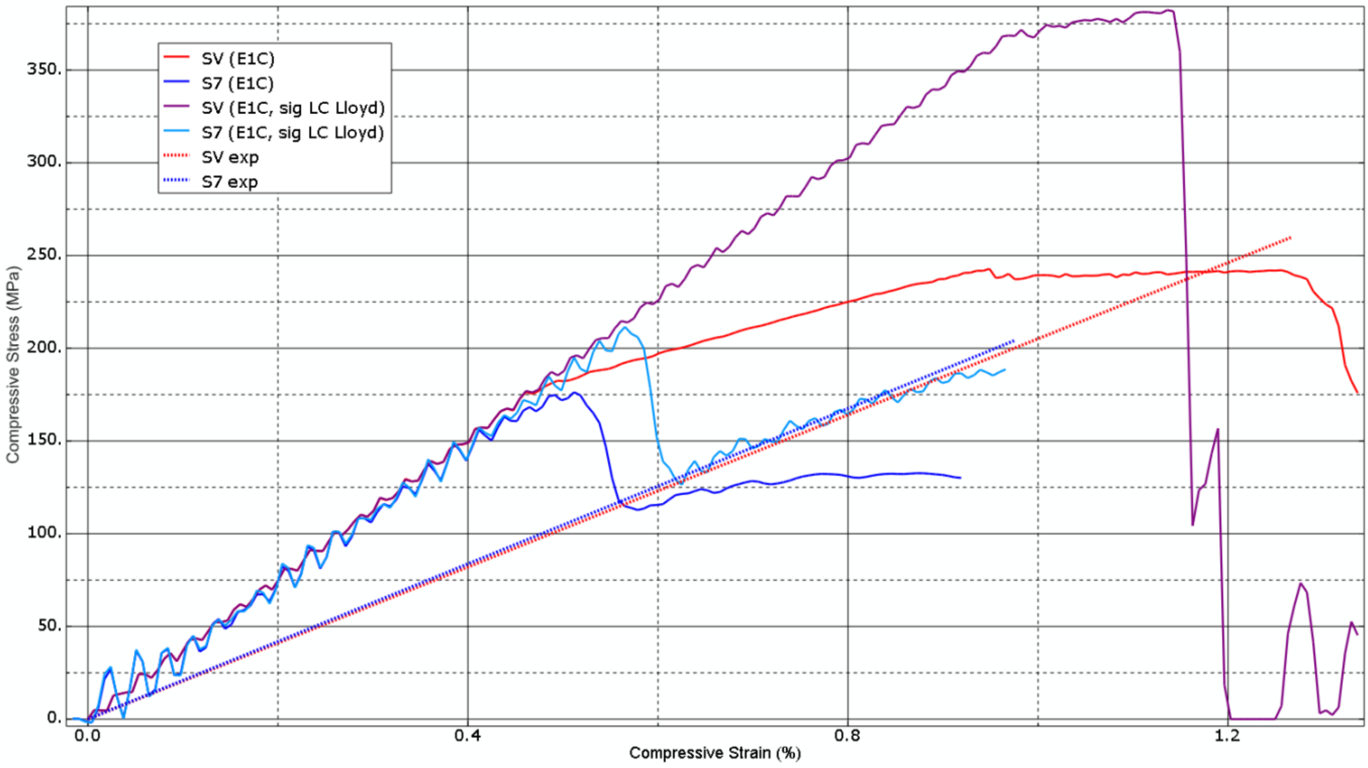

Figure 100: Stress-strain responses of symmetric panels using increased longitudinal compressive strength and compressive longitudinal stiffness [2]

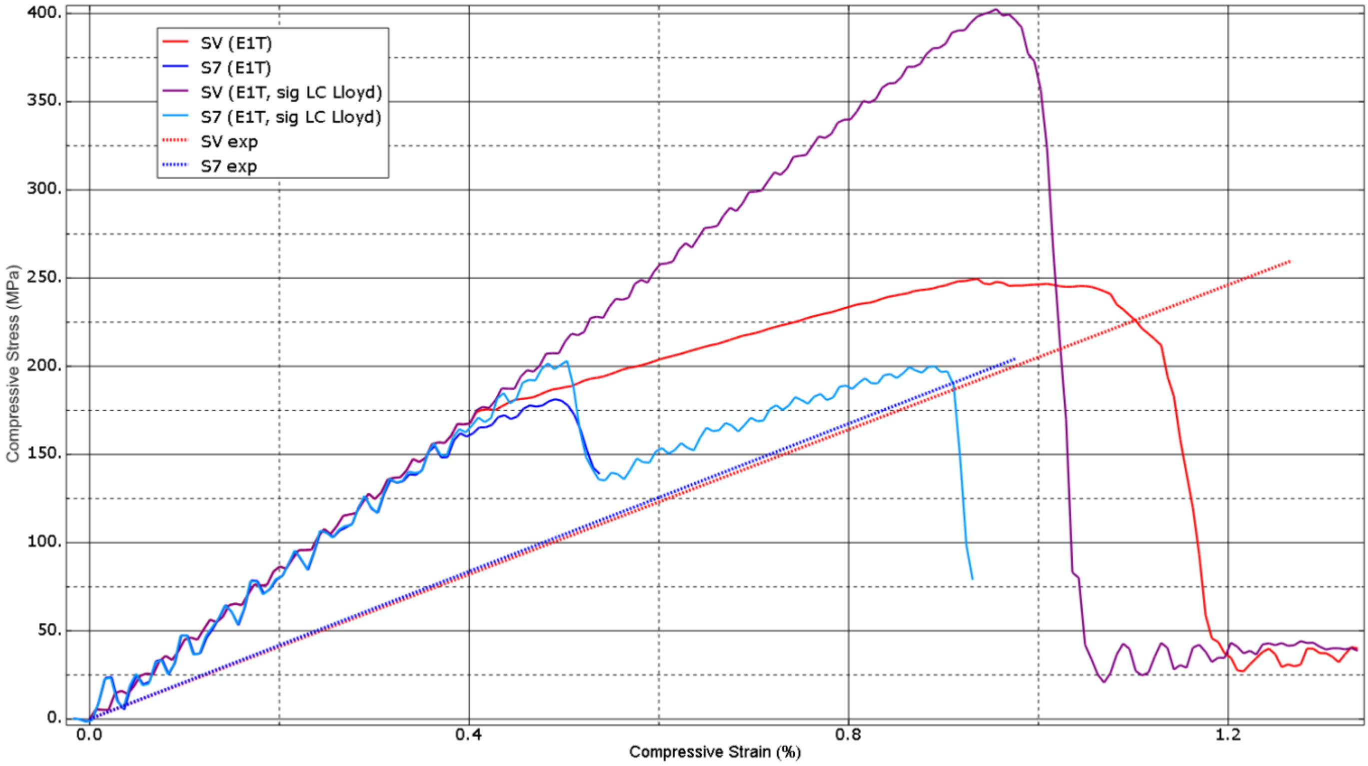

Figure 101: Stress-strain responses of symmetric panels using increased longitudinal compressive strength and tensile longitudinal modulus [2]

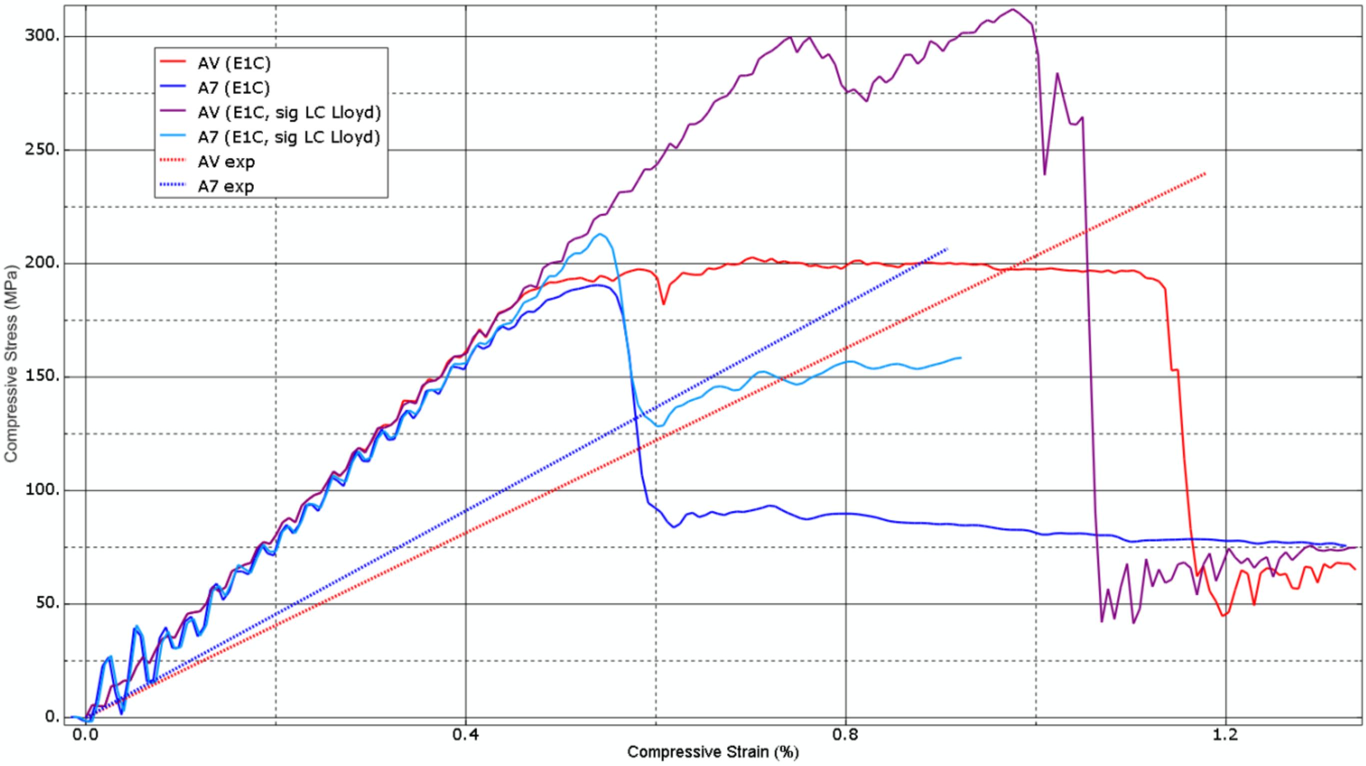

Figure 102: Stress-strain responses of asymmetric panels using increased longitudinal compressive strength and compressive longitudinal modulus [2]

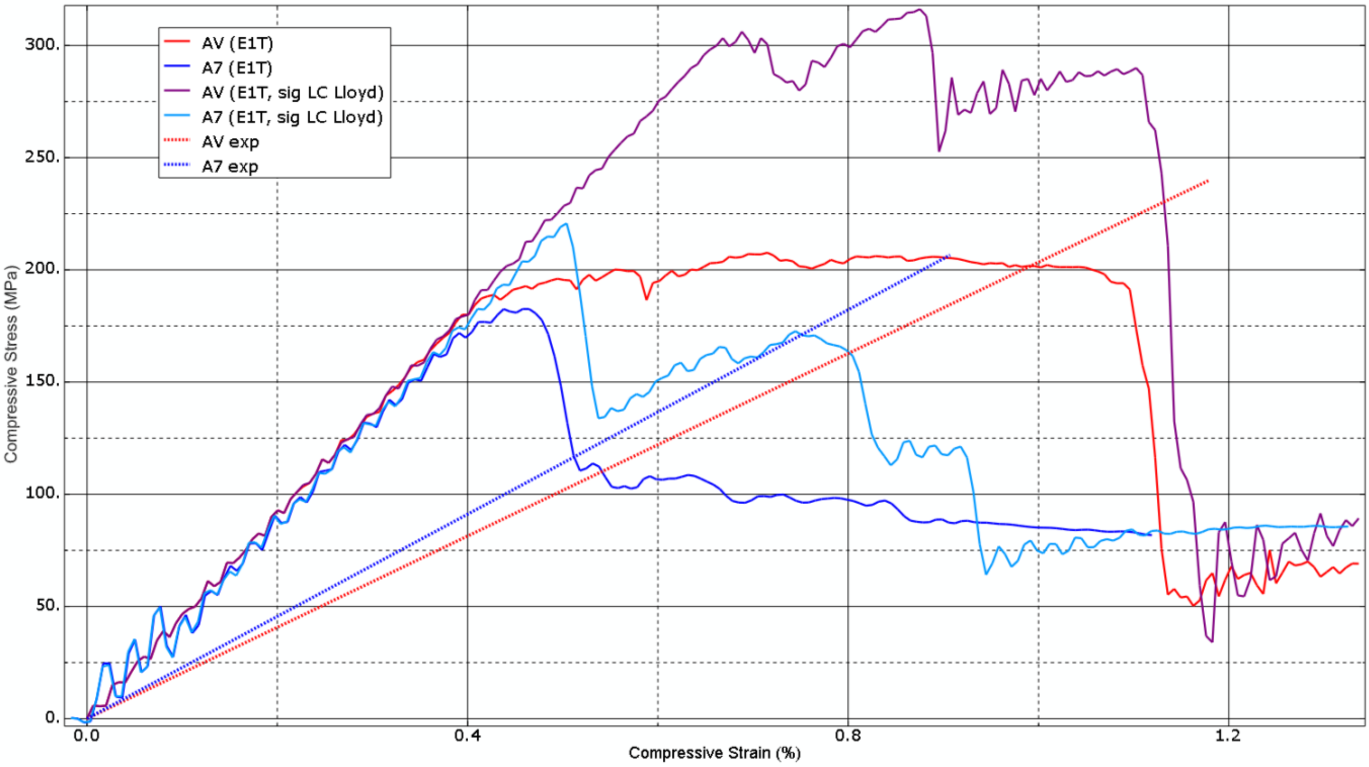

Figure 103: Stress-strain response of asymmetric panels using increased longitudinal compressive strength and tensile longitudinal modulus [2]

The difficulty arises from the fact that, while increasing σ_{LC} to a level consistent with the literature sources does result in a more realistic stress-strain response, this modification also causes the ultimate strength of the panel to far exceed that seen in the experiments. The benchmark models, as stated previously, do agree well with the experiments on the ultimate strength of the panels at all damage levels. This suggests that the compressive strength value found via experimentation and given in Table 20 is in fact representative of the material system used for the experiments, and actually it is the inconsistency between this and the rest of the material data gathered from external sources that is causing the erroneous structural response seen in the benchmark models. This effect is particularly significant for the symmetric models. Interestingly, the increased value for the longitudinal compressive strength has only a limited effect on the ultimate strength of the highly-damaged panels, with the modified models producing only a small over-estimate in this property when compared with the benchmark models and experiments, as the failure of these panels is dominated by other damage mechanisms, such as delamination and fibre fracture in the indentation phase. Even so, these models still show a different response to the benchmark cases, with progressive damage and failure becoming much more prominent in the modified panel models.

As the longitudinal stiffness and strength values were also found by experimentation, and thus may also be treated as representative for this material, the transverse compressive strength (σ_{TC}) of the material is considered next, as well as the shear stiffness (in-plane and out-of-place) and shear strength. Additionally, models are trialled using reduced fracture energies in the skin and cohesive layer. As damage propagates according to the fracture energy given in the material data after the specified threshold strength is reached, it is believed that an overly-high fracture energy value is causing damage to propagate too slowly prior to ultimate failure, resulting in the load plateau observed in the benchmark models. The normal-opening and shear-opening strengths are also changed in some models for the sake of completeness, though it is expected that this will have little effect, due to the previously observed insensitivity of the normal-opening mode to changes in a virgin model (see the parametric study in Chapter 5). Various combinations of these altered parameters are trialled, and detailed in Table 26; the designations given in the table are suffixed to the *SV* and *AV* panel designations as required. In all cases, the specified material parameter is taken as half the nominal value given in Table 20, and the variations are performed on both symmetric and asymmetric panels.

Table 26: Material data variations [2]

Variation	σ_{TC}	$\tau_{L\ \&\ C}$	G_{ij}	$G_{C\ (skin)}$	$G_{C\ (bond)}$	$\sigma\ \&\ \tau_{\ (bond)}$
m1	√					
m2	√	√	√			
m3				√		
m4				√	√	√
m5	√	√	√	√	√	√

A final model (designated as *m6*) is trailed that halves all of the skin and bond material parameters, with exception of σ_{LC}, Poisson's ratio and the mode-mix ratio in the cohesive surface data. The rationale behind this final variation is to observe the effect of artificially generating a consistent data set based around the longitudinal compressive strength, which while standing out as anomalously low, does at least give a good estimate for the ultimate strength of the panel. Crucially, this test treats the rest of the experimentally-derived material data as suspect also. In all model variations, the material data for the core is left unchanged. Note that this exercise is intended to demonstrate the effect of changing the material data of the on the response of the panels, in an attempt to identify where the issue in the material data might lie, so as to explain the strange stress-strain response of the model. An effort to curve-fit the numerical model results to the experimental results will not be made, as that would defeat the whole purpose of using numerical modelling as an alternative to experimentation. It is more useful instead to understand precisely which items of data the structural response is sensitive to, and the effect of this sensitivity.

The results from this investigation are presented in Figure 104 and Figure 105 for the virgin symmetric and asymmetric panels respectively (the compressive longitudinal modulus is used in all cases, except *m6*, where the value given in Table 20 is halved). From these plots, it's clear that none of the applied data changes fundamentally alter the erroneous strain-strain response of the models, *m6* being a (partial) exception that will be discussed separately. For the symmetric panel, altering the transverse compressive strength, the skin fracture energies and the bond properties (*m1*, *m3* and *m4* respectively) all seem to produce approximately the same reduction in ultimate strength. These changes also give a marked reduction in the strain-to-failure, though it should be noted that, while this mitigates the unexpected load plateau, it also results in a considerable underestimate of the experimentally-observed strain-to-failure (also note that any reduction in the ultimate strength also represents an increasing underestimate of the experimental results when compared with the benchmark models). The effect is stronger for the *m3* and *m4* cases. The bilinear response before failure is unchanged.

The behaviour of the asymmetric panel is slightly different, only registering a change in strength when the skin energies and bond properties are changed, with no accompanying reduction in the strain-to-failure. In fact, there is a paradoxical increase in the strain-to-failure seen *AV-m4*. Conversely, changing the transverse compressive strength does reduce the strain-to-failure, but doesn't appear to influence the ultimate strength to any meaningful extent. For both panels, there is little difference between the strength results produced by *m3* and *m4*, suggesting that the bond properties have a negligible effect on the overall performance of the panel.

Reducing the shear modulus and strength has a noticeable effect on the response of both panels. Allowing for the influence of the altered transverse compressive strength in the *m2* variations, both the symmetric and asymmetric panels show a slightly less-stiff initial elastic response, slightly reduced ultimate strength and a considerable reduction in the strain-to-failure. The *m5* variations suggest that the cumulative effect of the above changes in the panel response are approximately additive.

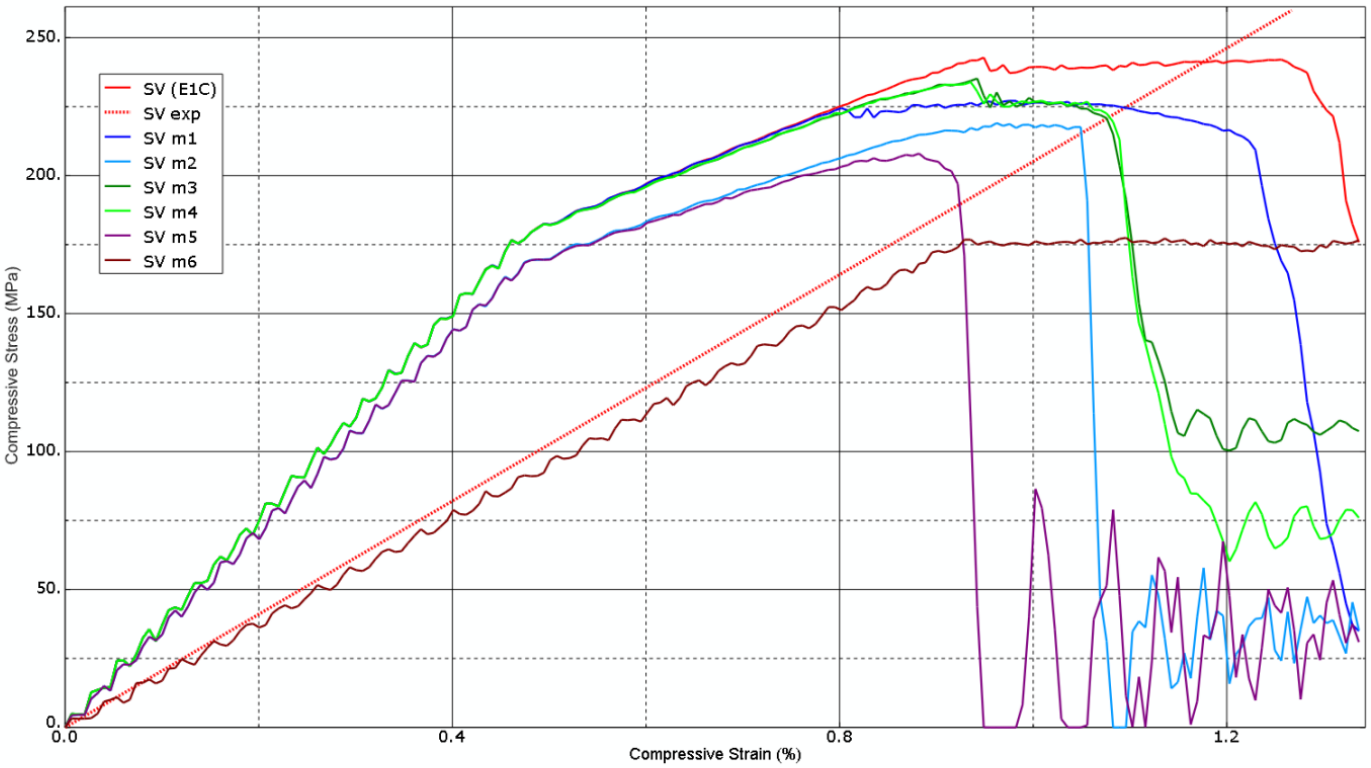

Figure 104: Undamaged symmetric panels with various changes to the material properties [2]

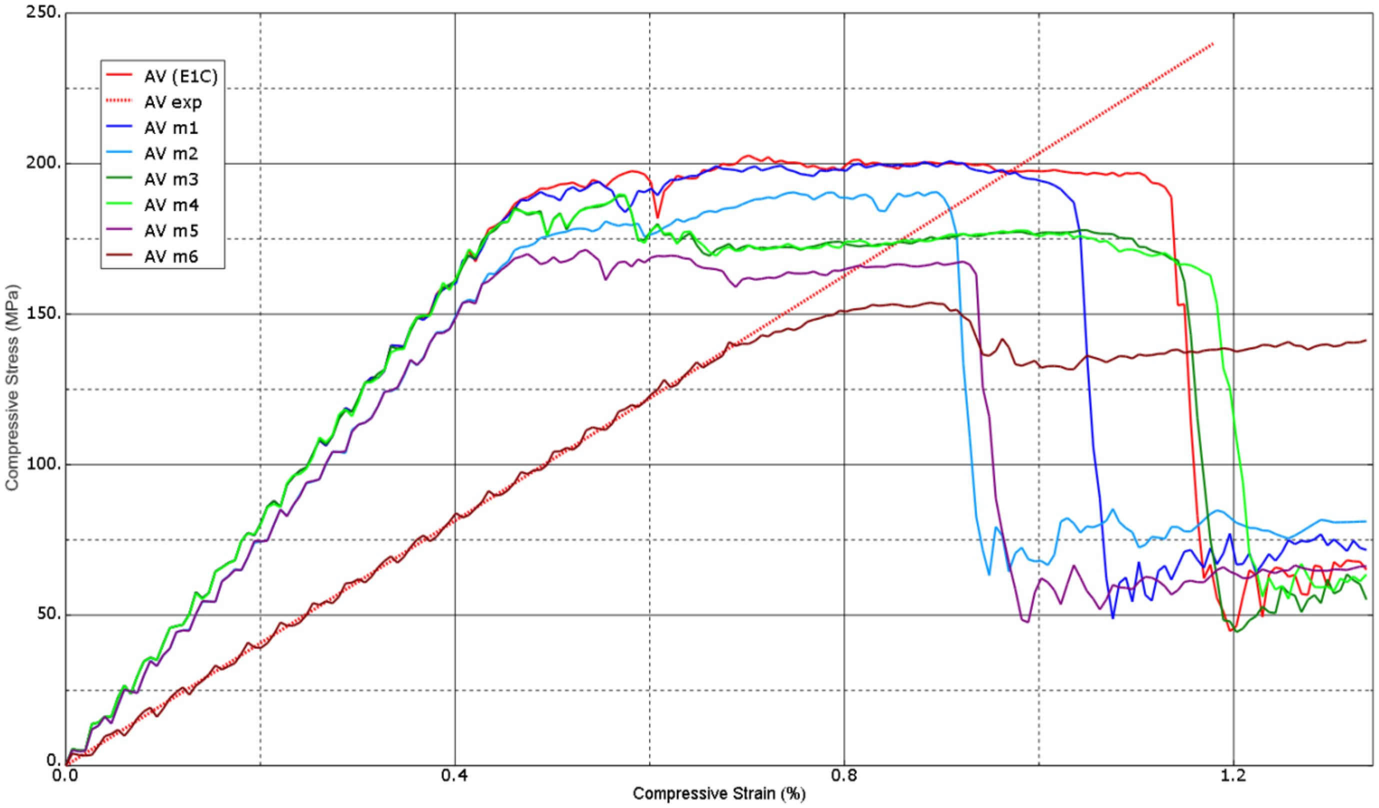

Figure 105: Undamaged asymmetric panels with various changes to the material properties [2]

The *m6* variations, as previously mentioned, are something as a special case as they treat the experimentally-derived material data as suspect, whereas the previous alterations only changed data gathered from literature sources, potentially for different material systems, and thus were already acknowledged as a potential source of error. The most striking result here is that the initial response of the model now agrees very well with the experiments. This suggests that the longitudinal and transverse ply stiffness found in the experiments is something of an overestimate, though recall that the overall panel stiffness calculated using the strain gauge data demonstrated fairly close agreement with the numerical model. However, even this change, which is cumulative with the previous model variations (the changes in *m6* are added to the changes in *m5*) does not eliminate the load plateau after maximum strength is reached, though it does at least eliminate kink in the symmetric panel response prior to ultimate strength. Furthermore, as the panel stiffness is dramatically reduced, the elastic stability of the panel is inevitably reduced in turn, resulting in a significant underestimate of the ultimate strength when compared with the experimental result as buckling resistance drops. This provides the further suggestion therefore that the ply stiffness found in the experiments is perhaps not as flawed as it appears at first glance. It is possible that the reduced longitudinal tensile strength is contributing to the reduced overall strength seen in *m6*, though this is unlikely, based on the results of the parametric study in Chapter 5 and given that the problem exclusively involves a uniaxial compression loading.

This investigation highlights the importance of gathering a complete and coherent set of material data for the material system under consideration. While it was to a greater or lesser extent unavoidable given the constraints of the project, a certain degree of inconsistency in the data used for this model has been revealed, and it cannot be easily corrected via small adjustments to the material parameters. This data inconsistency is the primary reason for the flawed response of the model in this investigation, rather than it being due to a fundamental failing of the model itself, which was shown to perform well when a self-consistent data set was available (refer to the simulation of the Czabaj et al experiments in Chapter 5).

It would not be reasonable to imply that certain pieces of data are unimportant, but it is fair to say that the longitudinal compressive modulus and strength are the critical parameters for achieving good results for the ultimate strength (which is this project’s primary objective), with the other material parameters refining the response. Based on these results, future studies must include the generation of a comprehensive material data set as an essential prerequisite to numerical modelling. Furthermore, it is clear that the model is fairly ineffective at simulating very severe levels of indentation causing fibre fracture in the skin, as the model does not allow any degree of penetration to occur. This might be addressed by the careful use of additional cohesive layers in the skin to provide a space in which fibre fracture is able to occur. It should be restated however that this model, despite its clear limitations and the requirement for further development, does achieve its main goal of accurately estimating the residual strength of the panels.

Chapter 7

Numerical Modelling of Combined Loadings in Sandwich Panels

7: Numerical Modelling of Combined Loadings in Sandwich Panels

In this chapter, the use of the model presented in Chapter 5 (*'Sandwich Model Development'*) is extended to address complex load cases in both damaged and undamaged panels. Additionally, the influence of geometric scaling is investigated, by increasing the planar dimensions of the panel (while holding the thickness constant). The investigation does not simulate a specific experimental investigation, and is instead intended to demonstrate the utility of the developed model in studying more realistic load cases.

7.1 Model Description

This investigation looks at square, flat sandwich panels, using the same material data as used for the developmental models using Czabaj's data (please refer to Table 10 in Chapter 5). The material thicknesses and lay-ups are the same also, that is to say, both skins use a quasi-isotropic $[45/0/-45/90]_S$ lay-up, with a ply thickness of 0.127mm, giving a skin thickness of 1.016mm. The 16.5mm core from the development work is used here. This material data is used since it produced good agreement with the experimental results for the ultimate stress of the sandwich panels, and also generated the expected elastic-brittle stress-strain response. By using this proven data, the intention is to avoid the problems of data inconsistency that dogged the numerical modelling of the experiments performed in Chapter 3 – these issues were discussed at length in Chapter 6. Three (planar) sizes of panel are used, with lengths of 150, 200 and 300mm. For square panels, this approximately doubles the planar area of the panel with each size increment. This variation is to study the influence of geometric scaling on the performance of the panel, which would be relevant to the use of the model in design studies. Both undamaged and damaged panels are studied here, with the damaged panels being subject to a quasi-static indentation with an applied displacement of 2.5mm, using ø16mm hemispherical indenter, as used in the experimental study in Chapter 3. The panel is rigidly supported during the indentation, thus eliminating global displacement, which would inevitably vary with the increasing width of the panels. By removing the global displacement, it is expected that the amount of damage produced would be independent of the panel size, and thus should be identical for all panels.

The numerical model most closely matches the *Q1-C2-sm-1* case from Chapter 5 (recall that this designation indicates that the single cohesive surface is placed closer to the free surface of the panel rather than the core, between the -45 and 90 plies). The model features two fundamental differences when compared with the models previously discussed, to investigate further improvements to the computational efficiency. Firstly, the model is built as a quarter-model rather than a half-model, making further use of the symmetry in the panel. This change halves the number of elements required in the model, but it also halves the displacement-to-failure, as it mimics a displacement being applied at both ends of the panel rather than just one. Consequently, this effectively doubles the loading rate as well. The second change, used sparingly in the Chapter 6 models, is the use of significant mass scaling. For this particular study, the solver aims for a target time increment of $1e^{-7}$s. This would result in a considerable improvement on the speed of the model, given that the stable time increment without mass scaling is in the region of 2 – 3e^{-8} s for this particular problem. Figure 106 shows the stress-strain response for the initial quarter-model and mass scaling tests, with the test models produced using the *SV* model from Chapter 6 as a convenient basis, and compared with the mass-scaled and non-mass-scaled versions of *SV* (red and crimson lines respectively). Displacing both ends of the benchmark panel at once provides a loading rate akin to the quarter-model, but is seen to have a negligible effect on the stress-strain response (purple line).

While the mass scaling does have a small influence on the post-failure response, the ultimate strength and the response prior to this point is not changed to any appreciable extent when compared with the benchmark half-model with no mass scaling. The model shown here uses an even larger target time increment of 5e^{-7}, which does introduce some noise into the response, hence the use of the smaller time increment stated before. Note that the displacement-to-failure is halved for the quarter model (blue line) as compared with the benchmark model, as expected, but as the gauge length of the quarter model is also halved, the stress-strain responses of the two models are seen to be very similar, though the quarter models lack the erroneous stress plateau of the original benchmark models. The upshot of these changes, of course, is a significantly reduced run time. The non-mass-scaled model runs in approximately 8 hours, whereas the highly mass-scaled quarter model (cyan) runs in 30 minutes (both using 12 processing cores). In the practice, the first model considered in this study, *75-0-0x*, which in terms of geometry and loading is very similar to the *SV* panel, runs slower than the fast quarter model, due to being a larger problem (in terms of element quantity) and reduced mass scaling. All the same, this model still runs in little over an hour using the same number of processors. Clearly, this updated model is far more efficient than earlier iterations, at the cost of a minor change in the structural response.

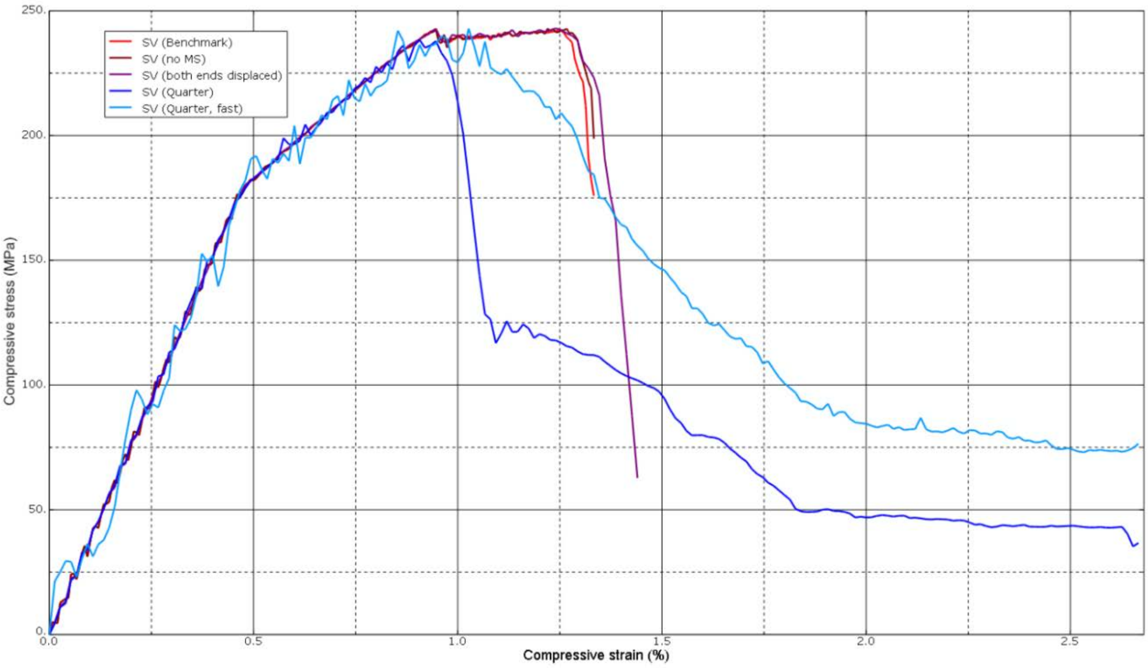

Figure 106: Comparison of quarter-models with benchmark half-models

As a final check, since this remains a quasi-static loading problem as before, the ratio of system kinetic energy to internal energy is compared. For the fast quarter model, this is 0.27%, which is far below the established 5% threshold for a valid quasi-static solution [147]. These two changes aside, the models are set up as before – please refer to Chapter 5 for the specifics.

Two different load cases are used, using either a longitudinal compressive load (as with the other simulations studied so far) or a combined longitudinal and transverse load, achieved by displacing the edges of the panel in the x- and y-directions simultaneously, at the same rate. Additionally, each of these loadings is applied to either pressurised or unpressurised panels. Pressure is applied to the distal (undamaged face of the panel) prior to the compressive loaded, and held at the required level for the duration of the compressive load. Two pressure levels are used, to simulate cabin pressurisation in an aircraft at altitude: 60.2 kPa (the ‘low’ pressure regime, simulating an airliner cruising at 12,000m with the cabin pressurised to an altitude of 2,000m [170]) and 94.8 kPa (the ‘high’ pressure regime, simulating an aircraft at 18,000m with the cabin at sea-level pressure – akin to the now-defunct *Concord*, but with even greater cabin pressurisation [171], for the sake of providing a more severe loading case for the model). These pressures are found using the difference in barometric pressure between the two altitudes, found using a simplified approximation assuming linear temperature change with altitude [172,173]:

$$P_h = P_0 \left(1 - \frac{L \cdot h}{T_0}\right)^{\frac{g}{R} \cdot \frac{M}{L}}$$

(32)

where:

P_h = the atmospheric pressure (Pa) at altitude h (m)

P_0 = standard atmospheric pressure at sea-level = 101.3 kPa [173,174]

L = temperature lapse rate for dry air = 0.0065 K/m [173,174]

T_0 = standard temperature at sea-level = 288.2 K [173,174]

g = acceleration due to gravity = 9.81 ms^{-2}

M = molar mass of dry air = 0.029 kg/mol

R = universal gas constant = 8.32 J/(mol K)

Solving this equation for the required altitudes gives the pressures stated above. Obviously, these pressures are very low, and should not cause much displacement in the panels, and certainly no damage. For the purposes of this study, the applied pressure is to a) show the response of the panel to the combined loading and b) see what effect, if any, this representative pressure would have on a loaded aerospace structure. During the pressure and compressive loadings, the boundary conditions around the external edges are set to constrain out-of-plane movement only, mimicking a simply-supported panel. The symmetry constraints along the internal edges of the quarter model also constrain the rigid body motion in the longitudinal and transverse directions. The model is shown schematically in Figure 107, showing the loads and the boundary conditions. Please refer to Figure 69 (Chapter 5) for the schematic describing the basic model construction. The models use a similar mesh density to the other sandwich models presented in this report, giving problem sizes (in approximate number of elements) of 20,000, 35,000 and 79,000 for the 150, 200 and 300mm panel models respectively. Compare this with the James experiment models (Chapter 6), which had approximately 52,000 elements each, and the closely-related *Q1-C2-…-1* Czabaj model (Chapter 5) which had around 94,000. In terms of problem size alone, the use of a quarter-model represents a considerable improvement in computational efficiency.

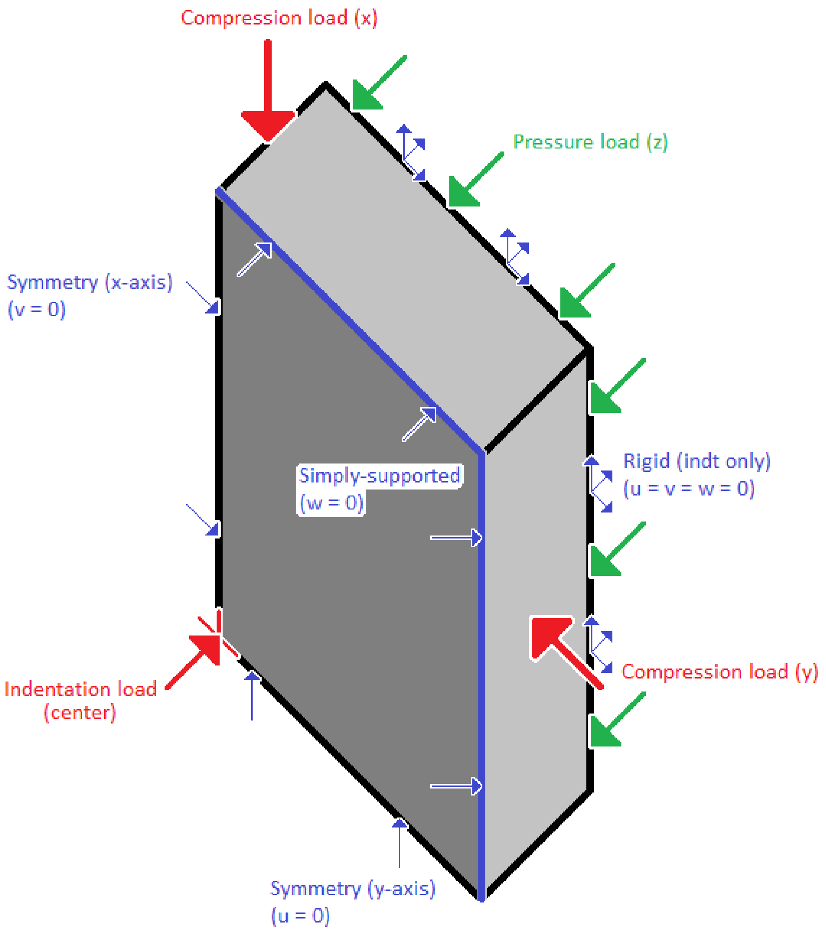

Figure 107: Schematic showing loads and boundary conditions for the combined loading study

Between the geometric scaling, damage, pressure and differing load cases, this study will consider a total of 36 unique models. The results will be designated thusly, for ease-of-understanding:

$$\boxed{L} \quad - \quad \boxed{\delta} \quad - \quad \boxed{Q} \quad \boxed{P}$$

where:

L = edge length of model (half the true length) = *75*, *100* or *150*
δ = applied displacement on the indenter = *0* or *2* (actually 2.5)
Q = high or low pressure case = *H* or *L*
P = compression load case = *xy* or *x*
(combined or longitudinal only)

Example: *100-0-Hxy*, denoting a quarter panel with a 100mm long edge (representing the 200mm size of panel), undamaged, with 94.8 kPa of pressure applied prior to a combined longitudinal and transverse pressure load.

7.2 Results

Before presenting the strength results from the model, it is appropriate to confirm the model is responding correctly to the complex applied loads. This is confirmed by considering the displacement of the panel at various stages of the analysis: indentation, pressurisation and compressive displacement prior to failure. The displacement profile at these three stages of the analysis are shown *150-2-Hxy* are shown in Figure 108 to Figure 110 (note the displacement due to pressurisation is scaled by a factor of 10, due to the low absolute value of the displacement). These displacement profiles are representative of all the panels featured in this investigation. From these images, it can be shown that the model is responding correctly to the applied loads. Note the direction of the displacements due to indentation and pressure – indentation acts in the negative z-direction, whereas pressure, which is applied to the distal face, displaces the panel in the positive z-direction. The triangular shape of the displacement contour for the compressive loading confirms that the longitudinal and transverse loads are being applied at the same rate, as required.

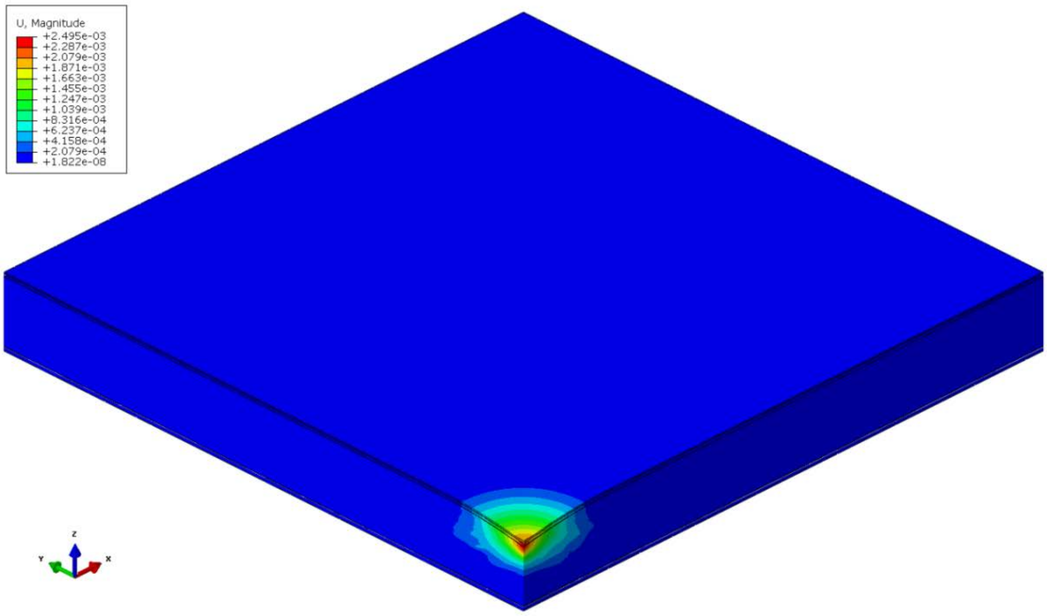

Figure 108: Displacement of 150-2-Hxy (indentation)

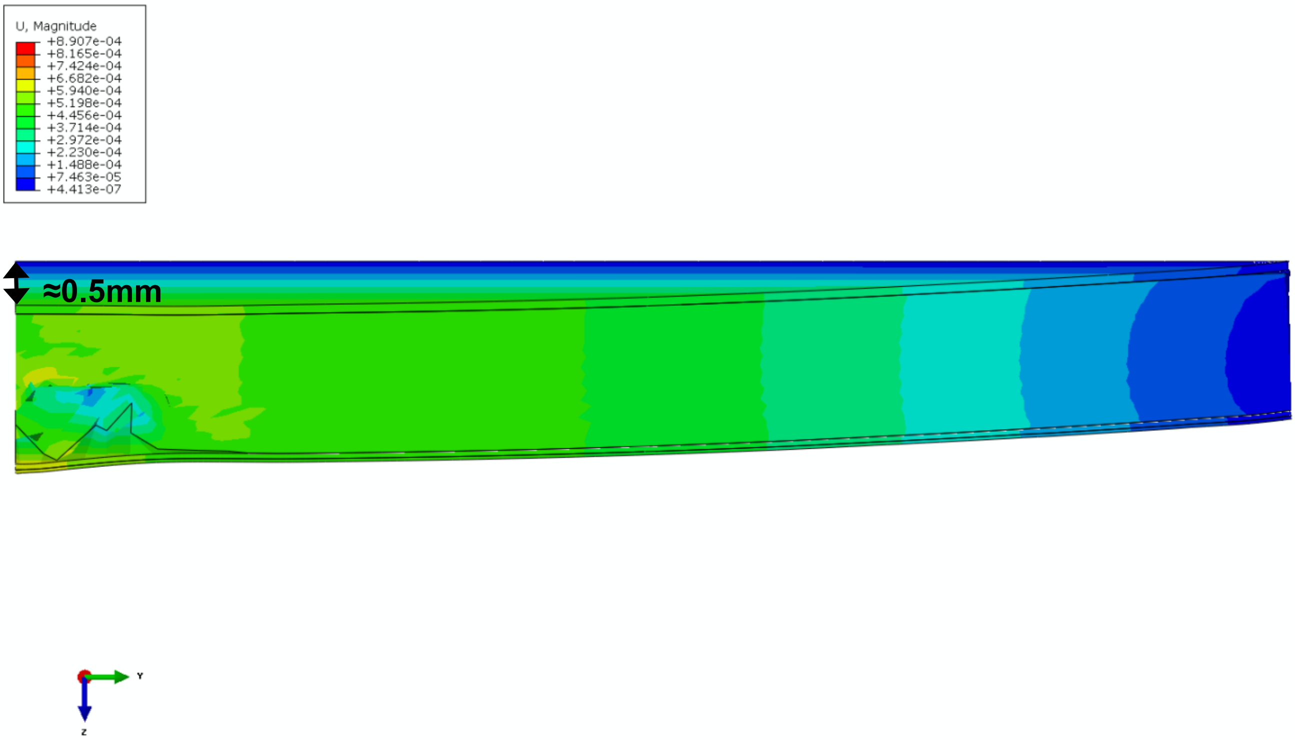

Figure 109: Displacement of 150-2-Hxy (pressurisation)

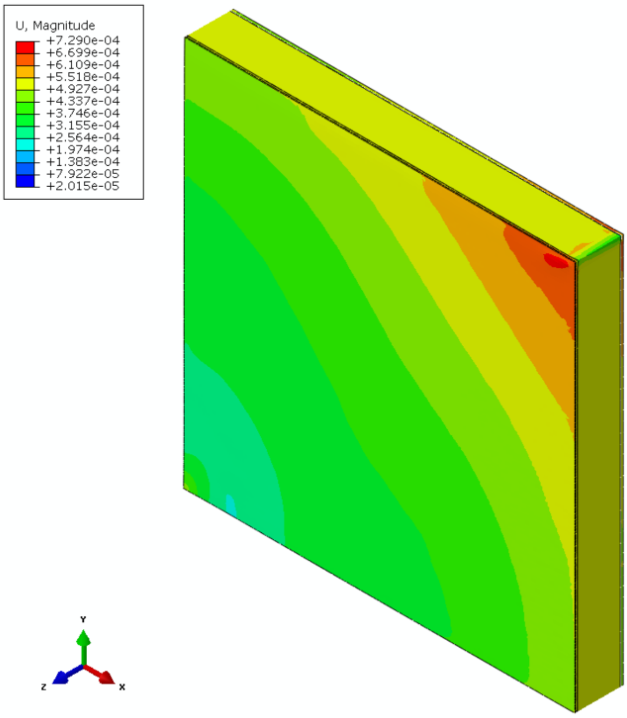

Figure 110: Displacement of 150-2-Hxy
(compression, prior to failure)

The complete results from this study are presented in Table 27. The dent size from the indentation is given for both its initial size and its resultant size after pressurisation. As with the Czabaj and James models presented earlier in this report, the dent diameter is measured for the region where the out-of-plane displacement exceeds 0.5mm, and is estimated from the average element size, which for these models is approximately 1.76 elements/mm. The dent depth is simply the peak local out-of-plane displacement. The global displacement of the panel due to the pressure loading is taken as the maximum displacement at the pressurised face (which is the distal face, taken relative to the damaged face). The stress and strain at failure is presented for both the longitudinal and transverse directions, as appropriate, with the % residual strength being given only in the longitudinal direction, as compared with the relevant model's undamaged counterpart. The stress-strain responses of the models are presented in Figure 111 to Figure 116. From the set-up of the analysis, it is expected that the initial dent sizes will be independent of the panel size and that global displacement and change in dent size due to the pressure loading will be independent of the subsequent compressive loadings. This was seen to be largely true, with minor variations in these parameters being observed, due to the dynamic and thus highly-variable nature of the numerical solution. Thus, average values for the damage size and global displacement are given in Table 27 where appropriate.

From these results, the following general trends can be observed. First of all, for all panel sizes, loading the panel in the longitudinal and transverse directions at the same time does not particularly harm the strength of the panel, and occasionally improves it. However, the strain to failure for the doubly-loaded panels is always much lower, due the larger magnitude displacement vector that results from loading in both directions at the same time. The strength in the transverse direction is higher than the longitudinal direction, despite the use of a quasi-isotropic lay-up. One possible explanation for this finding is that the 90º fibres, which are in the centre of the laminate, are the primary load-bearing fibres for the transverse loading. Since they have more layers on either side of them than the 0º fibres, which may be only a single ply away from the free faces, these plies may be slightly more stable than the 0º plies, improving their buckling resistance. This trend was also found by Hitchen & Kemp [34], where laminates having more 0º plies remote from the free surface of the composite plate tended to have greater compressive strength, either undamaged or damaged. Most studies on stacking sequence focus on the formation and consequences of delamination, so more work may be required to confirm this hypothesis.

Table 27: Results of combined loading study

Panel designation				Dent size (mm) (diameter x depth)		δ_{press} (mm)	Max stress (MPa)		Strain (at max stress) / %		% residual strength
				Initial	Pressurised		L	T	L	T	
75	0	0	x	-		-	343.0	-	0.63	-	-
			xy				335.8	364.2	0.41	0.45	
		L	x			0.052	362.0	-	0.68	-	
			xy				342.2	373.2	0.40	0.47	
		H	x			0.081	350.3	-	0.63	-	
			xy				344.2	362.6	0.39	0.43	
	2	0	x	14.8 x 2.51	-	-	380.2	-	0.69	-	110.8
			xy				347.5	379.0	0.40	0.49	103.5
		L	x		0 x 0.043	0.18	349.7	-	0.64	-	96.6
			xy				355.9	374.7	0.42	0.50	104.0
		H	x		0 x 0.028	0.19	362.4	-	0.66	-	103.5
			xy				355.7	376.6	0.42	0.48	103.3
100	0	0	x	-		-	350.6	-	0.64	-	-
			xy				309.5	343.3	0.36	0.42	
		L	x			0.11	343.6	-	0.61	-	
			xy				310.6	345.1	0.36	0.43	
		H	x			0.17	331.8	-	0.59	-	
			xy				315.9	335.8	0.36	0.41	
	2	0	x	15.6 x 2.45	-	-	323.3	-	0.59	-	92.2
			xy				330.1	356.9	0.38	0.44	106.6
		L	x		0 x -0.046	0.16	363.4	-	0.65	-	105.8
			xy				319.5	350.4	0.37	0.44	102.9
		H	x		0 x -0.019	0.23	349.4	-	0.63	-	105.3
			xy				325.1	348.5	0.36	0.42	102.9
150	0	0	x	-		-	314.0	-	0.56	-	-
			xy				291.3	324.9	0.34	0.37	
		L	x			0.34	322.2	-	0.58	-	
			xy				298.5	317.9	0.34	0.37	
		H	x			0.54	260.8	-	0.47	-	
			xy				248.4	292.3	0.30	0.35	
	2	0	x	15.9 x 2.50	-	-	323.0	-	0.58	-	102.9
			xy				302.9	329.3	0.35	0.38	104.0
		L	x		0 x -0.45	0.34	307.4	-	0.56	-	95.4
			xy				297.4	325.8	0.34	0.37	99.6
		H	x		14.5 x -0.63	0.50	282.8	-	0.51	-	108.4
			xy				299.4	320.5	0.34	0.36	120.5

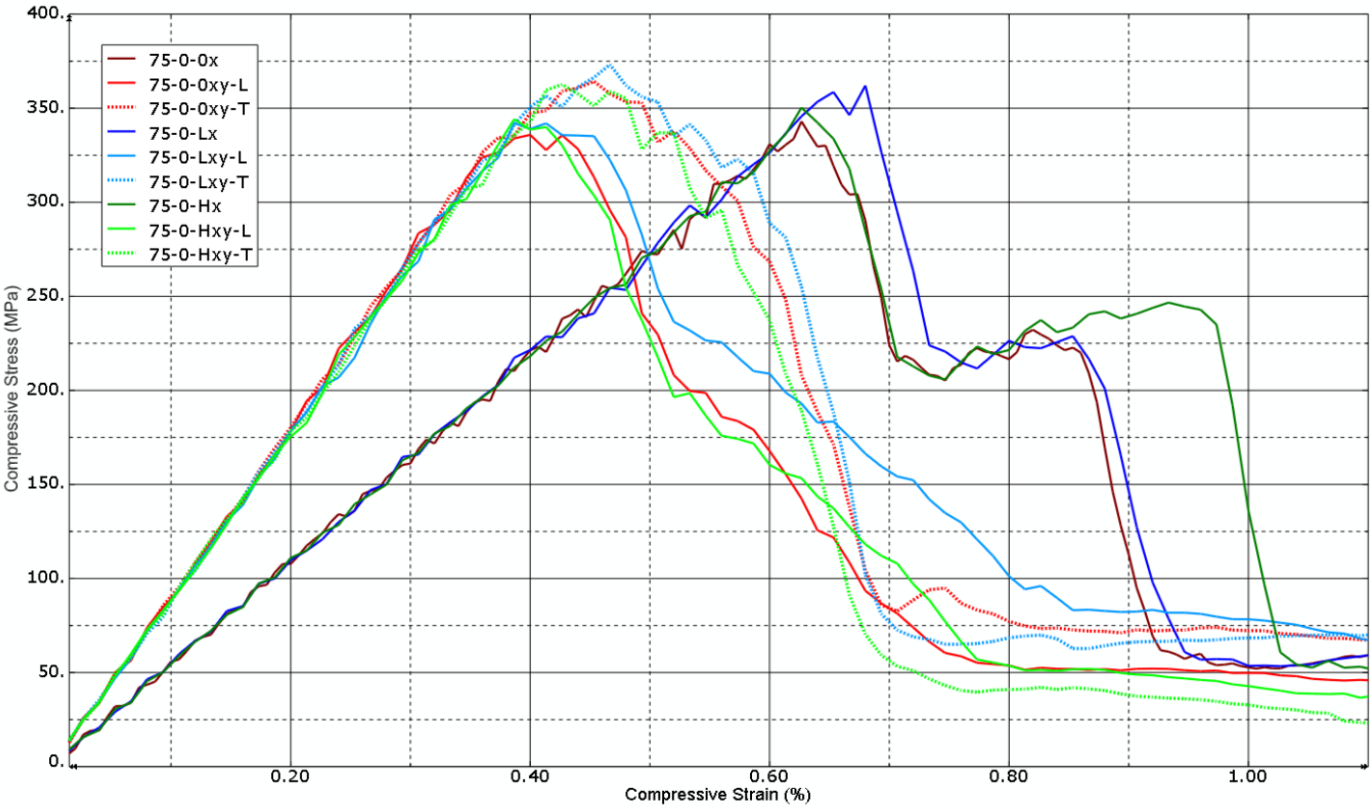

Figure 111: Stress-strain response for undamaged 150mm square panels with combined loading

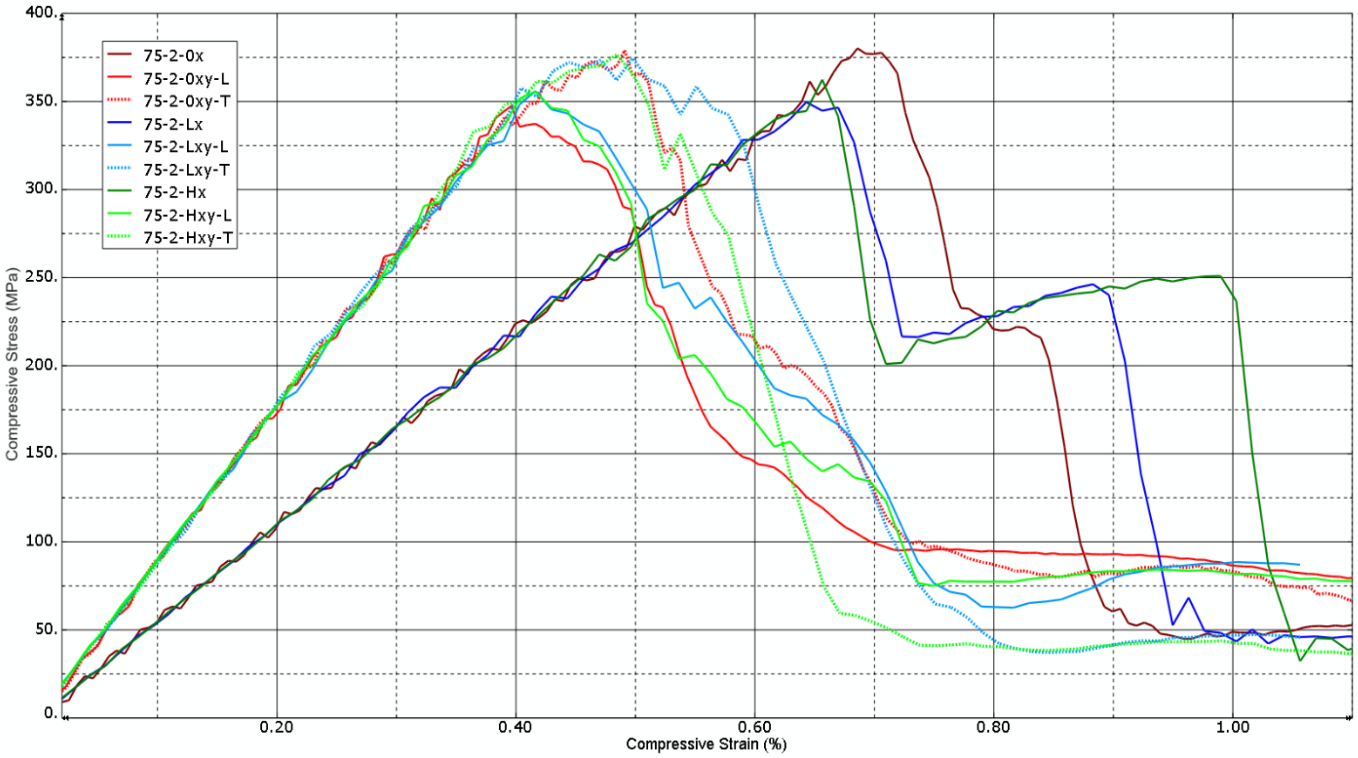

Figure 112: Stress-strain response for damaged 150mm square panels with combined loading

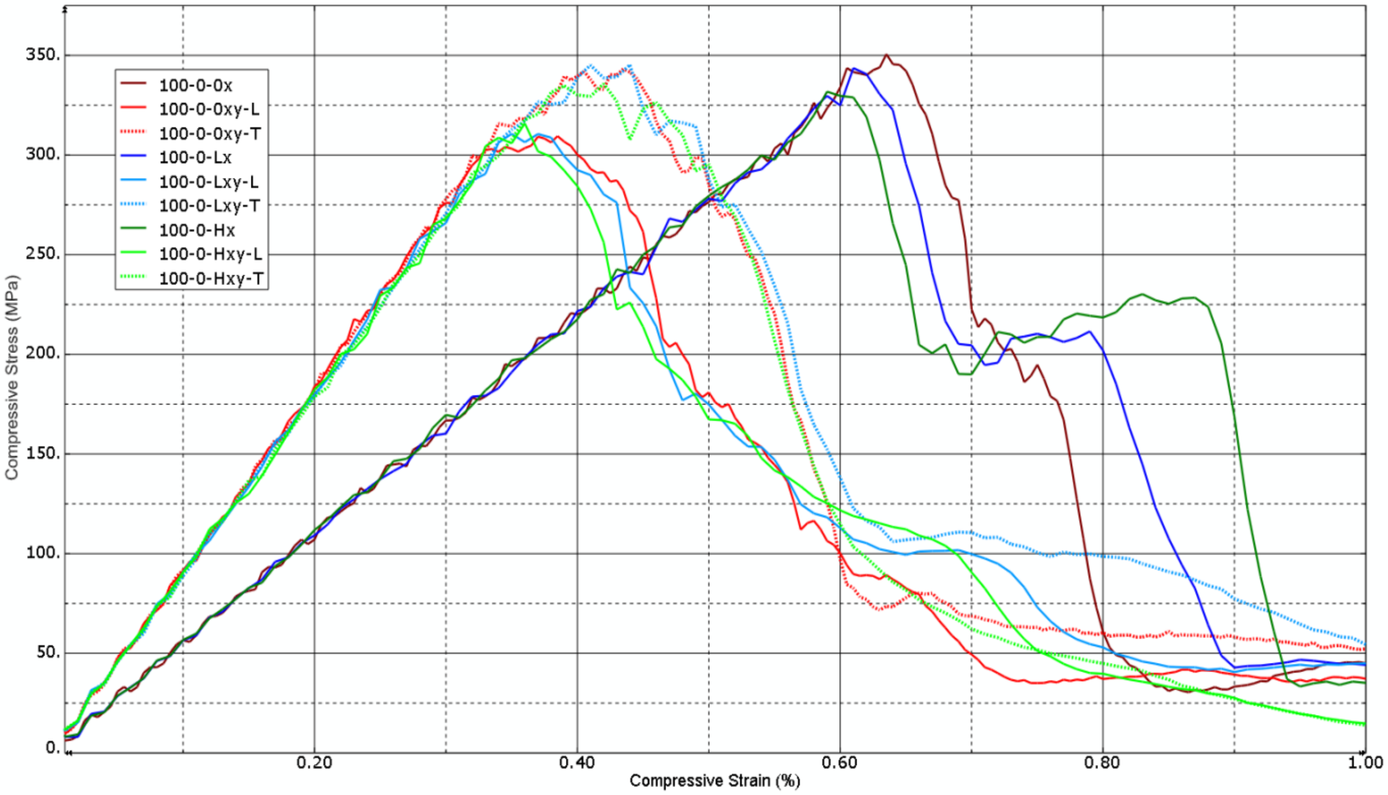

Figure 113: Stress-strain responses for undamaged 200mm square panels with combined loading

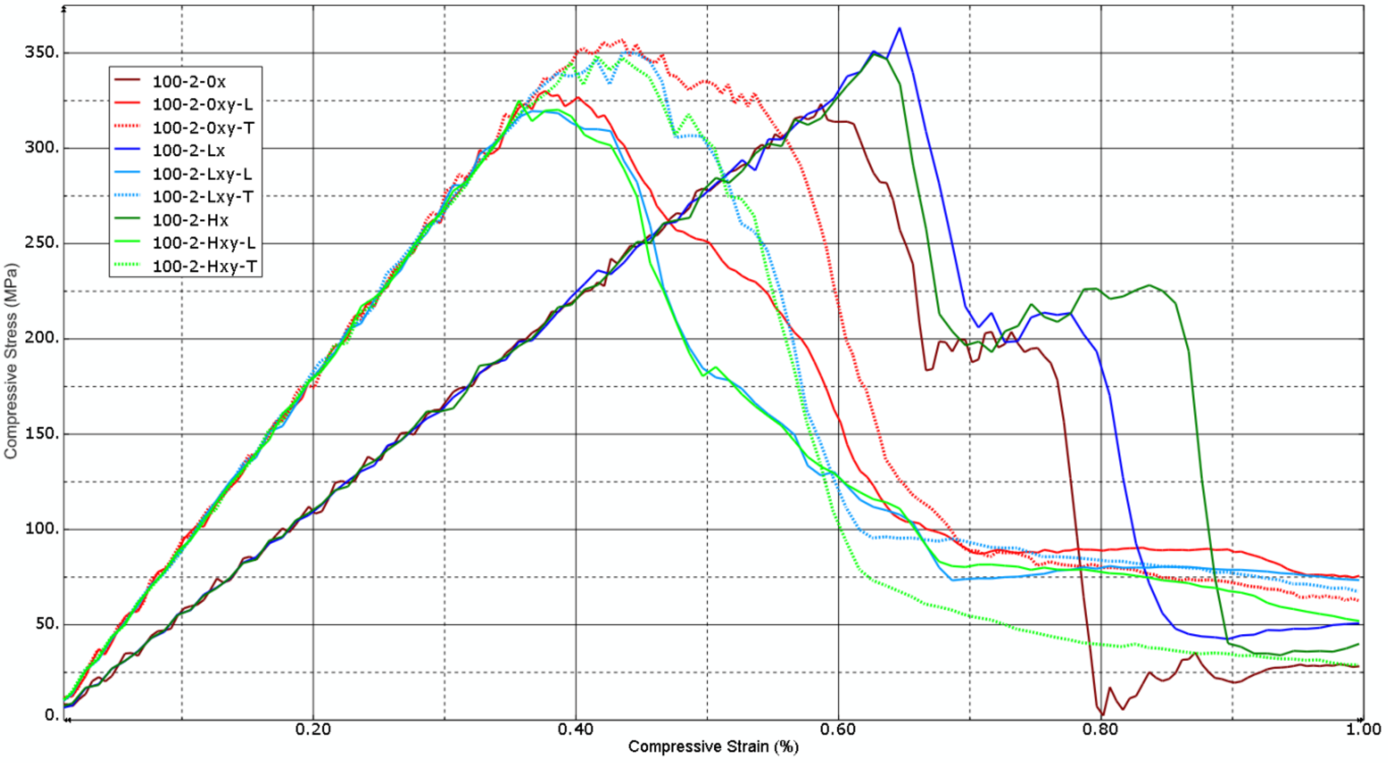

Figure 114: Stress-strain response for damaged 200mm square panels with combined loading

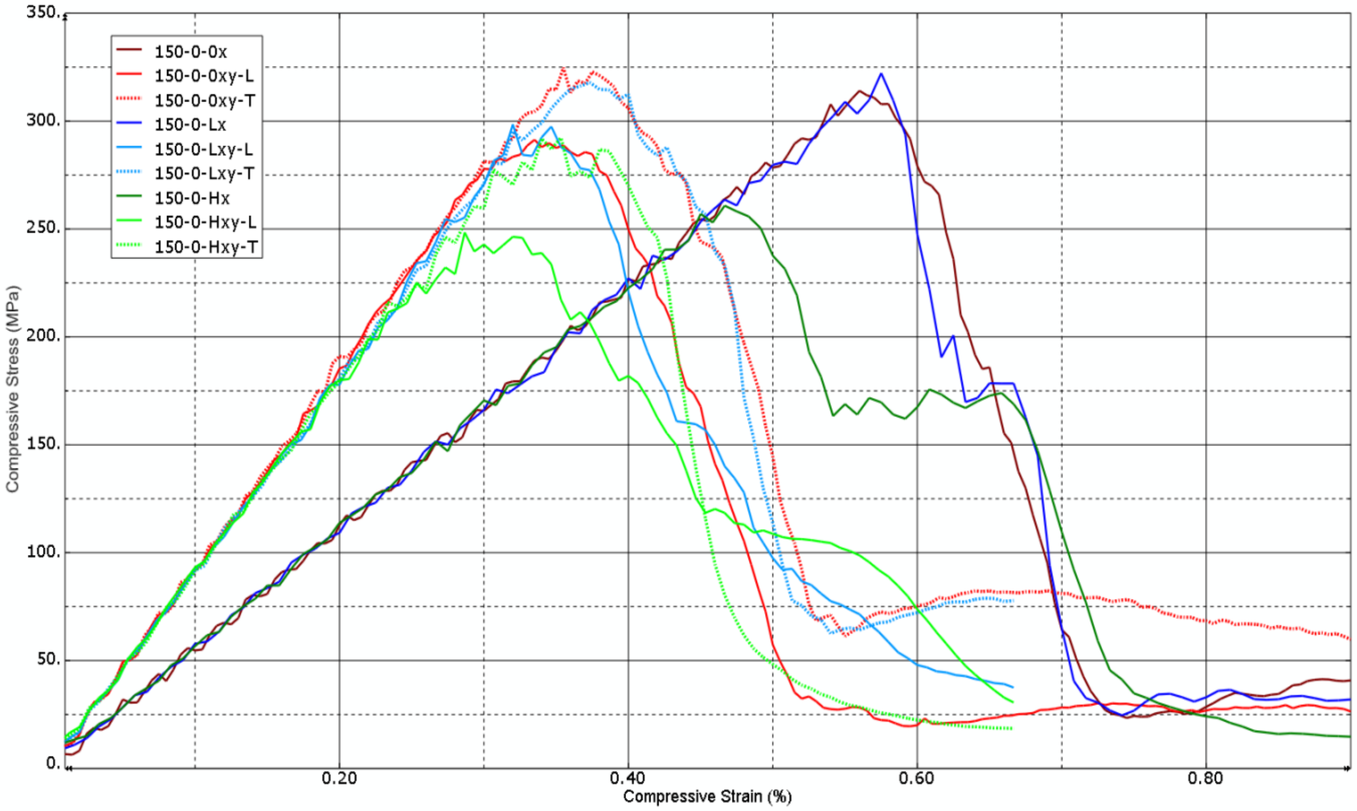

Figure 115: Stress-strain responses for undamaged 300mm square panels with combined loading

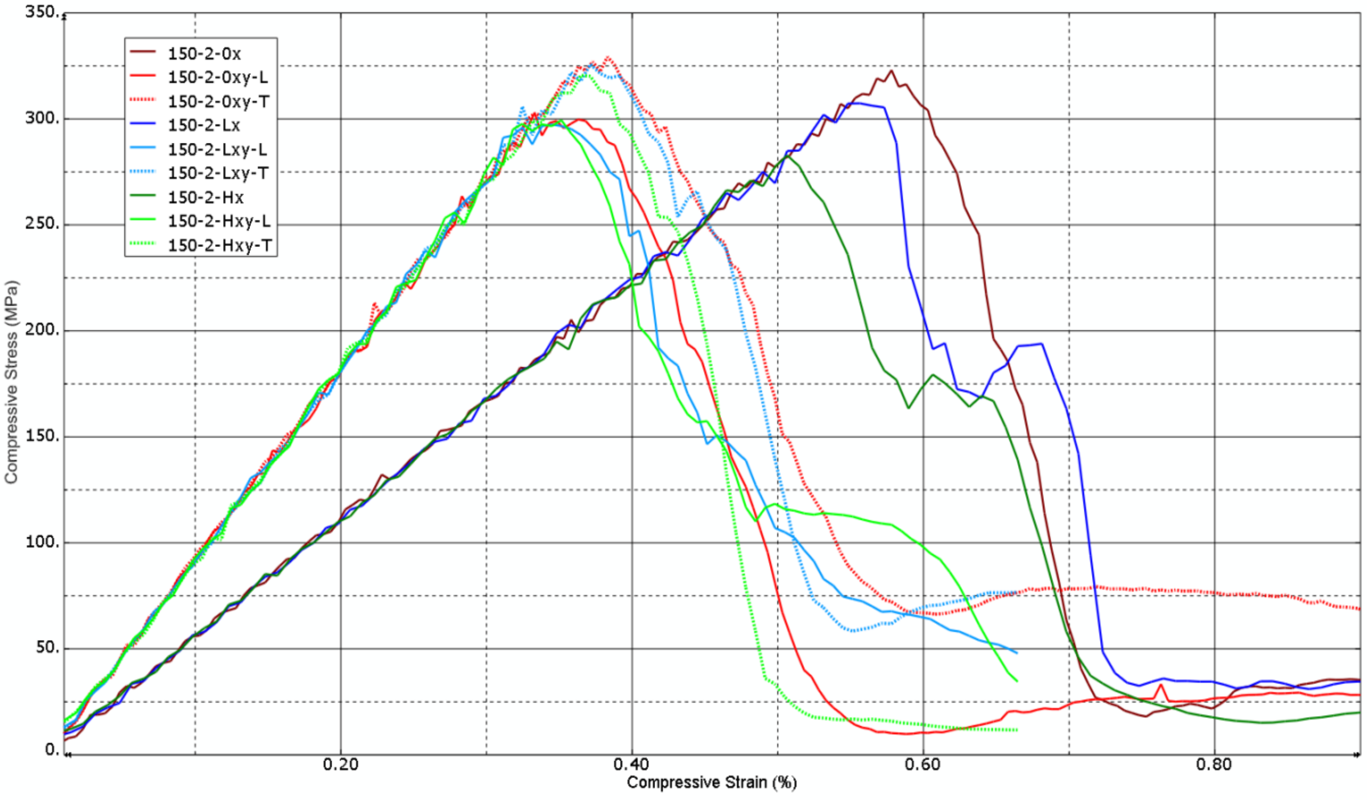

Figure 116: Stress-strain responses for damaged 300mm square panels with combined loading

Changing the size of the panel does not have a significant effect on the stress-strain response until it becomes quite large. Note how the ultimate strength of the 150mm and 200mm panels is quite similar for the longitudinal load only cases. The doubly loaded 200mm panels do show a noticeably reduced failure stress however, and the strength of the 300mm panels is significantly reduced across all cases as compared to the much smaller 150mm panels. The reason for this is that the elastic stability of the panels falls as the gauge length increases, increasing the tendency of these panels to buckle. The strain-to-failure does not change appreciably with increased size, which is expected, as the materials used in the panel construction are not changed.

For the undamaged panels, the application of pressure has only a small effect on the stress-strain response. In some cases, for example, with the 150mm panels, the pressure improves the strength of the panels, perhaps due to the application of a small beneficial preload, but this effect could just as easily be due to numerical variations – in lieu of comparative data, this question cannot be answered for certain. For the larger models, and especially the 300mm panel case, the use of the higher pressure harms the strength of the panel, as the large global displacement that the pressure load induces starts to act as an increasingly significant geometric imperfection, which when coupled with the large unsupported area of these panels, has a rather detrimental effect on the elastic stability of the panel.

On the other hand, applying a pressure load has a very interesting effect on the residual strength of the damaged panels, with the pressurised damaged panels usually (and the highly pressurised panels invariably) exhibiting increased strength over their undamaged or unpressurised counterparts. What appears to be happening when pressure is applied to the distal face of a damaged panel is that the dent is squeezed out, returning the damaged face to a nearly-flat condition, albeit with the presence of a delamination induced by the indentation (incidentally, intralaminar damage and core crushing due to a mild indentation appears to be very limited, as expected based on the experimental observations in Chapter 3). The elimination of the dent becomes more significant as the panel size increases, due to the increased global displacement generated by the pressure loading in these cases. Indeed, the dent actually develops into a convex bulge in the two larger panels, becoming especially prominent for the 300mm, highly pressurised panel. The mechanism by which this occurs is not immediately obvious, but one distinct possibility is that the panel bending under pressure induces tensile stresses in the damaged face which straighten out the deformed skin, removing the dent.

Unfortunately, the unpressurised panels have unexpectedly and entirely counterintuitively also tended to show improved strength with damage, though based on the previous panel models analysed in this report, the reduction in strength due to damage was not expected to be significant in any event. This error is perhaps due to the rather heavy mass scaling used in this model, but again, without comparative data, it can’t be conclusively stated one way or the other whether this effect invalidates the model. That being said, the results presented here do show some interesting trends which are worthy of further study, particularly with respect to using pressure loadings as a way to recover the strength of damaged sandwich panels.

The singly-loaded undamaged sandwich panels all fail via the propagation of delamination buckling across the full width of the panel at the loaded end, with the buckle tending to originate at the free edge of the panel. This is likely due to the stress concentration formed by contact with the rigid surface used for load application at this point (to avoid clashes between the two surfaces when the panel is doubly-loaded, the surface was made slightly narrower than the panel). Changing the panel size and the application of the pressure load does not affect the failure mode. The damaged panels also (usually) show the same failure mechanism.

While the indentation does induce a delamination at the centre of the panel, this delamination does not propagate to full-width before the delamination at the loaded end does so, and thus the inclusion of damage does not affect the failure mechanism. This might explain why the strength of the indented panels is not lower than the undamaged panels. Again, this is independent of size and pressure, though the initial delamination from the indentation is occasionally more prominent in the pressurised panels. The competition between these two delaminated regions can be seen in Figure 117. The only exception is the unpressurised 200mm panel, where the delamination due to damage does control the failure, reaching the full width of the panel before the loaded-end delamination can fully develop; this is shown in Figure 118. Additionally, the highly pressurised 300mm exhibits the formation of delamination at the unloaded edges at the point of failure. This effect is not observed in the other cases, but is not a significant feature of the ultimate failure.

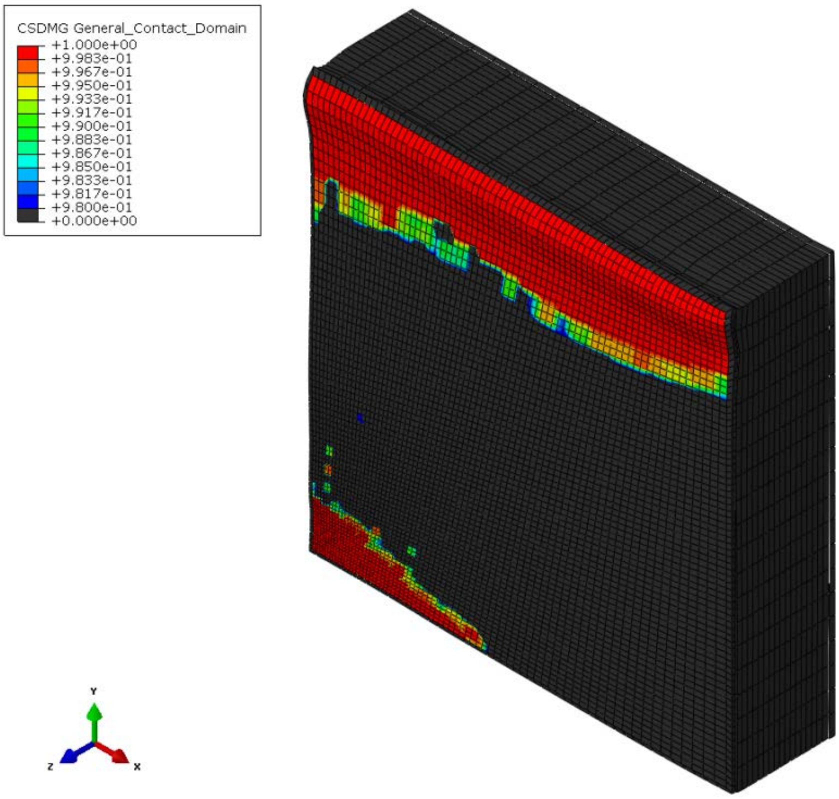

Figure 117: Failure of panel 75-2-Lx, showing competition between the two delaminated regions of the panel. The upper delamination, at the loaded end, controls the ultimate failure of this particular panel.

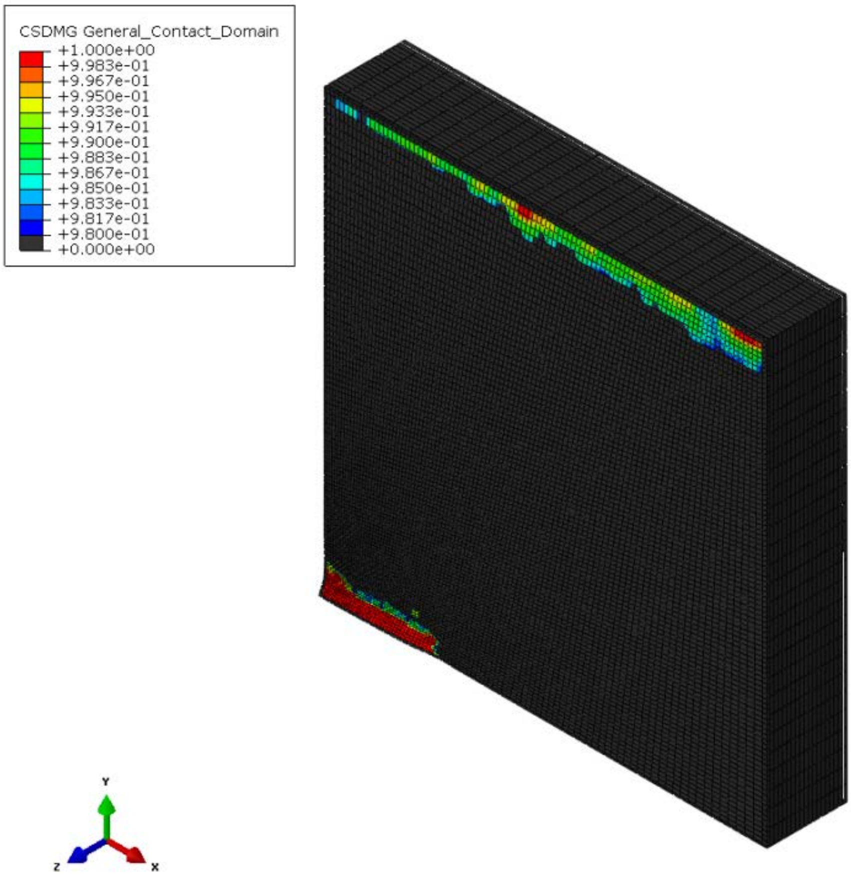

Figure 118: Failure of 100-2-0x. The delamination induced by the indentation in the centre (lower left) of the panel is propagating rapidly towards the free edge, before the top delamination can form. Ultimate strength has already been reached at this point.

The undamaged doubly-loaded panels, with both longitudinal and transverse compression loads, also fail via delamination propagation. As with the singly-loaded panels, the ‘upper’ edge, which is perpendicular to the longitudinal load, exhibits the full-length delamination first, with the other loaded edge, carrying the transverse load, following soon after. This explains the increased strength in the transverse direction, and supports the suggestion that the plies are slightly more stable in this direction. The delamination originates in the top corner of the panel, and propagates much quicker than the singly-loaded panels, with extensive delamination observed soon after the peak load. The failure mechanism is independent of pressure, as in the singly-loaded panels, though the transverse delamination develops more slowly than the longitudinal delamination with increasing panel size. This can be seen in Figure 119 for the undamaged, unpressurised 300mm panel. This panel also shows an unusual change in direction of the longitudinal delamination away from the free edge of the panel not seen in the other cases, but is otherwise representative of the failure of all of these panels. The doubly-loaded damaged panels also fail in the same manner, with the indentation-induced delamination having even less chance to propagate under loading than seen in the singly-loaded panels, though the 200mm unpressurised panel again proves something of an exception, with the longitudinal edge delamination and the central initial delamination seeming to grow at the same rate, making it unclear as to which one is controlling the ultimate failure of this particular panel.

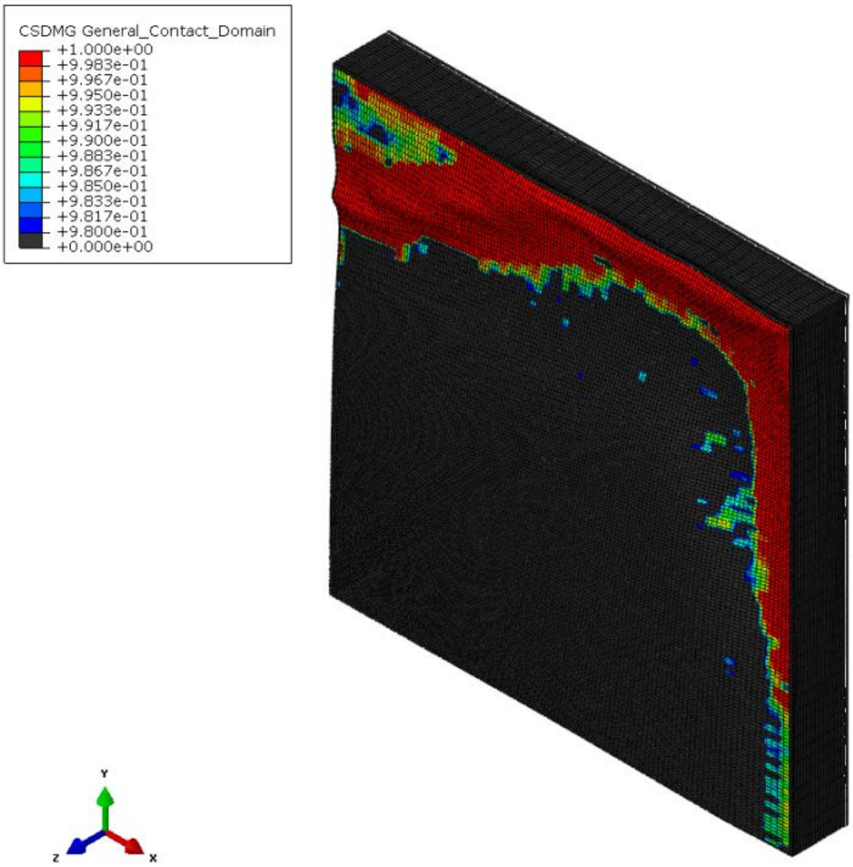

Figure 119: Failure of 150-0-0xy, showing delamination propagation in two directions.

The interaction of the various delaminations and loadings tend to result in complex buckling modes after ultimate strength has been reached. An example of this may be seen in Figure 120 for *150-2-Hxy*. The precise nature of the buckling mode is obviously highly dependent on the form of the delaminations under the surface, and can change with continued load application as this hidden damage propagates. It is also entirely possible that failure due to kink-band propagation could well result in different post-failure mode shapes, if these are seen at all. However, since this investigation is concerned only with ultimate strength and the causes of the final failure, post-buckling is only a curiosity for the current purposes.

The real utility of this exercise is in demonstrating the effectiveness of the sandwich model in a simulated design study, where an initial assessment of the suitability of a structure for a given application may be required. The use of mass-scaling and the reduction in problem size achieved by taking advantage of panel symmetry has provided a dramatic improvement in the computational efficiency of the model, which has allowed this example study to be completed very quickly. The analysis of all 36 models required less than 2,200 hours of processor time, which when divided over the 12 cores used for the analysis runs, equates to less than 8 days of real-time. This compares very favourably with earlier iterations of the sandwich model, which focussed more closely on achieving highly accurate results at the cost of increased computational effort. For example, the virgin Czabaj models (with a single cohesive surface) from Chapter 5 required an average of 167 hours of CPU time per analysis, increasing to 220 hours with the introduction of damage, even before considering the effect of simulating the larger panel sizes, which require a doubling of the number of elements used each time. Using this earlier model in this kind of design study would thus have required maybe 16,000 hours of processor time, resulting in nearly 2 months of continual computational effort if using 12 cores, for seven times the time taken to complete the study when the various efficiency improvements described here were applied.

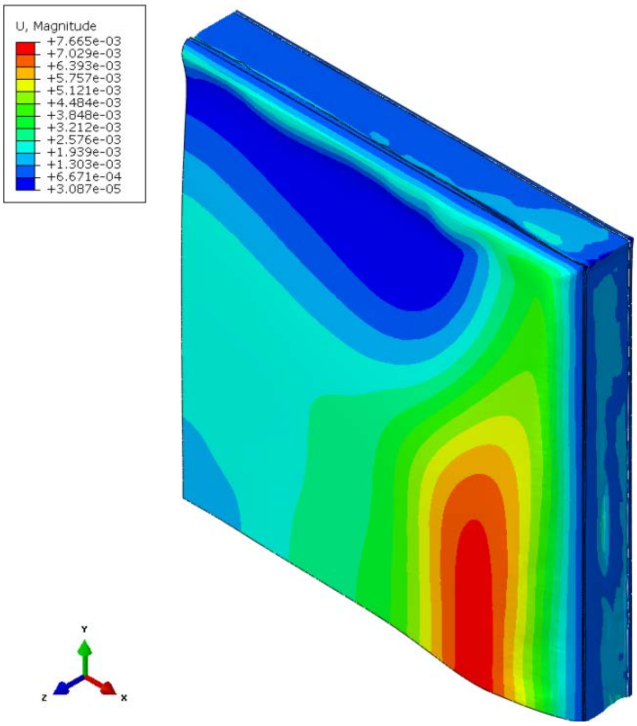

Figure 120: Post-failure buckling mode shape of 150-2-Hxy

The erroneous increase in strength of the unpressurised panels with damage obviously indicates some degree of inaccuracy in the model, but these errors can be eliminated by reducing some of the problem acceleration used here in the form of increased loading rate and mass scaling, and by increasing the mesh density. For instance, having made some initial conclusions about the suitability of a proposed design, the engineer may now reduce or eliminate these efficiency measures to increase confidence in the numerical results. It must be reiterated that despite the anticipated loss of accuracy, the model still captures the same fundamental composite damage and failure mechanisms that had been designed into the simulation from the very beginning. The retention of this considerable complexity in the solution is very encouraging, and despite the loss of accuracy, the model is still capable of producing valuable insights in the behaviour of the structure under these conditions. For example, the markedly reduced in-plane strength of the highly pressurised 300mm panel would be an observation that might be particularly valuable for a designer developing a large-scale aerospace structure. Another observation of note is the apparent recovery of strength with pressurisation on damaged panels.

Simulating this kind of complex loading problem is where the strength of finite element modelling truly lies, as it easily investigates loading states that might be difficult to perform experimentally. Crump et al [175] propose an experimental set-up for the pressurisation of sandwich panels at a low rate of loading, but most other experimental and numerical investigations focus on explosive blast loading of sandwich panels [176,177], rather than mild pressurisation as part of routine operation, such as in cabin pressurisation. Few of these also consider compressive loading as well, with a noteworthy exception being the work of Wang & Shukla [89]. Combined loads on composite and sandwich panels have received some consideration in the literature, including compression-and-shear loading [178], and biaxial compression akin to that considered in this chapter [179]. These two examples are concerned more with analytical solutions of buckling problems, however. Another work considers both shear and biaxial normal stress in the finite element environment for civil engineering applications [180]. However, experiments investigating this particular class of problems for these particular structures appear to be hard to come by, and certainly there is little evidence to suggest that the work presented in this chapter has been attempted either numerically or experimentally. The flexibility of numerical modelling allows for these structural investigations to be expanded further, for example by changing the loading rates, boundary conditions or panel geometry, such as introducing single and double curvature into the panel. Other new developments, such as through-the-thickness reinforcement of the skins, and perhaps even nanoscale reinforcement, might also be simulated in this environment. Additional studies of this nature are left to future research efforts, and are contingent on the satisfactory resolution of some of the model limitations that have been highlighted in this report.

Chapter 8

Summary and Conclusions

8: Summary and Conclusions

This report has presented a numerical model for the prediction of the compression-after-impact strength of composite sandwich panels, and an accompanying experimental study which provided data for model validation. The experimental study revealed that the use of a thinner distal (undamaged) skin could improve the strength of mildly damaged sandwich panels over undamaged sandwich panels using the same asymmetric configuration. It is believed that this effect is due to the movement of the neutral plane of the sandwich panel caused by the reduction in the stability of the damaged skin through stiffness reduction and geometric imperfections. This removes the eccentricity of the compressive loading that exists in the undamaged asymmetric panels, which has mismatched axial stiffness between the indented skin and the thinner distal skin, and thus a noticeably lower ultimate strength than the undamaged symmetric panels.

The numerical model generally agreed well with the ultimate stress found in the experiments for these different configurations, but is quite poor at estimating the magnitude of the damage induced by the indentation. When used to model the experimental study, the model gave generally good, conservative estimates for the residual compressive strength of both the symmetric and asymmetric panels. The tendency of the asymmetric panels to become stronger with mild damage was not captured by the model per se, with the numerical results instead showing an insensitivity to damage in the asymmetric panels, which was not shared by the symmetric panels. However, the numerical model did exhibit erroneous strain-stress responses for both panel configurations, particularly for the undamaged and mildly damaged cases. Investigations revealed that this erroneous behaviour was caused by inconsistency in the material data, which had been collected partially via experimentation and partly from literature sources.

Finally, the sandwich panel model is utilised in a simulated design study looking at the effect of combined longitudinal and transverse compressive loads and out-of-plane pressure loads on panels of varying size and with and without impact damage. This final exercise made extensive use of mass-scaling to significantly improve computational efficiency, as well as further use of panel symmetry to produce a quarter-model. Thanks to these improvements, the complete study of 36 models was completed with little over one week of computational effort. This supplementary investigation demonstrated the utility of the sandwich model developed by this project in studying different candidate designs for a given application, though there was a reduction in accuracy due to the considerable mass-scaling used. Of particular interest is the apparent recovery of compressive strength seen in damaged panels with a pressure loading, with the highly-pressurised damaged panels considered in this study invariably showing an improvement in strength over their damaged, but unpressurised counterparts. On closer inspection, it appears that the bending induced by the pressure load (applied to the distal face) causes the dent in the opposing face to get pulled out by the tensile forces induced on this side of the panel, mitigating the instability induced by this geometric imperfection. This finding certainly warrants further study.

This project achieved its primary goal of producing a numerical model for damaged sandwich panels that can reliably produce good estimates of the ultimate compressive strength for a number of different structural and loading configurations, while taking into account all of the major damage mechanisms for composite sandwich panels. However, there remains plenty of scope for improvement. It has already been stated that consistency of material data is crucial to give trustworthy numerical results – this must be gathered via dedicated and comprehensive experimental work for the material system/s in question. The experimental study itself could have been improved via more extensive use of strain gauging to give better estimates of the overall panel stiffness, and to confirm the hypothesis that mild damage in the asymmetric panel is providing a stabilising influence under compressive loading. The addition of an LVDT or similar instrument would allow experimental verification of the global displacement observed in the numerical model, and a future study would ideally use some form of non-destructive testing, such as ultrasonic measurement, to establish the size of the delamination induced by the indentation, thus establishing the quality of the cohesive surface response used in the numerical model. Another useful addition to the experimental effort would be to choose composite lay-ups such that both symmetric and asymmetric panels have the same overall cross-sectional thickness, so that any change in strength would be purely due to changes in the neutral axis rather than simple differences in thickness. As already mentioned, the effect of pressurisation on the compression-after-impact behaviour of damaged sandwich panels would also be a worthwhile investigation, if potentially difficult to perform in practice.

Particular weaknesses identified in the sandwich model are the skin damage model and the core model. The deficiency of the skin damage model, particularly the inability to capture extensive fibre breakage, has already been discussed. This may be solved by careful adjustment of the solution and meshing parameters, for example via element deletion (which carries its own difficulties in terms of the robustness of the numerical solution), but there are also a myriad of different composite damage theories that have been developed over the past decade which may be applied to this problem. These would require a great deal of care and expertise to implement these developments correctly, as they all require self-programmed subroutines within *Abaqus*. The use of the cohesive zone method may also be used for this purpose, via the addition of a width-wise cohesive layer through the centre of the damaged region. The core material and crushing response used in this project was very basic, and could be readily improved. A common approach is to explicitly create the geometry of a honeycomb, and apply basic isotropic material properties to the resultant structure. Other approaches capturing the response of the core in various directions are obviously more involved, again requiring extensive experimentation to gather the needed material data and implemented via the use of user-defined subroutines. The use of a quarter-model could have been attempted earlier in the project, and the benefits this approach offered in reducing the computational effort in solving these problems make it a very valuable technique, especially if using more complex material responses, more refined meshes, or explicit honeycomb geometries (though obviously, this approach has some limitations – for example, it would not be suitable for the investigation of shear loadings, due to the non-symmetrical shape this would produce).

Finally, there are other problems that this model could potentially be applied to. The combined loading study in Chapter 7 considered more realistic multiple loading cases, and another study could perhaps consider the behaviour of singly- and doubly-curve sandwich panels, representative of realistic aerospace structural geometries. A different study may involve the effect of shear loading on sandwich panels, or a further look at different materials (such as form cores common to the marine industry). A useful contribution might be a numerical investigation into the effect of through-the-thickness reinforcement of the skins on the compression-after-impact performance of a sandwich, which could be perhaps be implemented simply by altering the homogenous properties of the skin and the bond. The model might also be used for the investigation of high-energy impacts, provided that strain-rate dependency of the material was included. Preparing these continuation studies would be fairly straightforward as far as the numerical model is concerned (presuming the deficiencies mentioned previously were adequately addressed), but as with the other investigations presented here, experimental verification of this would be required, and potentially difficult and costly to implement. Ultimately, the entire purpose of numerical modelling is minimise, if not eliminate, the need for experimental work. Despite the promising advancements made by this project, there remain sufficient shortcomings in the models as they currently stand that experimental validation remains necessary, particularly for these more involved loading cases and more complex geometries.

Appendices and References

Appendix A: Results from Material Property Tests

		L (mm)	w (mm)	t (mm)	A (m2)	Pmax (N)	Stmax (MPa)	E (GPa)	v	Notes
T0	**1**	139	13.2	1.12	1.48E-05	24,386,36	1,649.58	112.07	-	No failure, no transverse gauge
	1i					29,900.68	2,022.50	113.75	-	Explosive failure, retest of 1
	2	138	14.88	1.07	1.59E-05	34,431.65	2,162.57	105.2	0.28	Explosive failure
	3	138	15.85	1.13	1.79E-05	32,933.51	1,838.78	104.83	0.22	
	4	138	15.81	1.1	1.74E-05	34,520.15	1,984.94	109.39	0.27	
	5	139	14.98	1.14	1.71E-05	33,737.18	1,975.57	98.16	0.38	
	6	139	14.26	1.08	1.54E-05	34,018.51	2,208.88	107.39	0.22	
						AV	***2032.209***	***106.453***	***0.27***	
						SD	***135.024***	***5.210***	***0.07***	
T90	**1**	124	25.4	2.24	5.69E-05	1802.68	31.684	6.471		Possible alignment error (ignore)
	2	124	24.96	2.25	5.62E-05	2543.05	45.282	5.744		
	3	125	25	2.2	5.50E-05	2408.08	43.796	5.984		
	4	123	25.1	2.21	5.55E-05	2493.19	44.946	6.094		
	5	125	24.82	2.22	5.51E-05	2645.49	48.012	5.849		
						AV	***45.509***	***5.918***		
						SD	***1.786***	***0.153***		
C0	**0**	19.5	9.76	1.4	1.37E-05	3555.55	260.213	51.67		Re-test after tab debond
	1	20.5	10.09	1.38	1.39E-05	5156.25	370.309	61.75		No fracture - buckled
	2	20.5	9.94	1.33	1.32E-05	5424.65	410.330	93.76		
	3	20	9.22	1.36	1.25E-05	6198.64	494.341	93.90		No fracture - buckled
	4	20	10.09	1.22	1.23E-05	5684.23	461.765	-		Faulty gauge
	5	20	10.19	1.07	1.09E-05	4873.45	446.970	90.63		
						AV	***439.688***	***92.76***		
						SD	***26.479***	***2.213***		

T0 = *longitudinal, tensile (for E_{1T} and σ_{LT} in models)*

T90 = *transverse, tensile (for T_{2T} and σ_{TT})*

C0 = *longitudinal, compressive (for E_{1C} and σ_{LC})*

Appendix B: Impact Jig Pendulum Setting

The initial kinetic energies selected for the impact tests were 4, 7 and 10J, as noted previously in Chapter 5. This appendix details how this was translated to a setting for the initial position of the pendulum, which was done via measuring the angle of the pendulum from its rest position.

Based on the principle of conservation of energy, kinetic energy equals the gravitational potential energy, therefore, for the energy levels given above:

$$E_{K,0} = mgh$$

(33)

where $E_{K,0}$ is the initial kinetic energy, g is acceleration due to gravity (taken as 9.81 for these calculations), m is the effective mass of the pendulum (discussed below) and h, the sole independent variable in this system, is the perpendicular height of the hammer above the target, taken from the centre of the hammer to the centre of the pendulum pivot.

The effective mass of the pendulum is found by considered the moment of inertia of its component parts about the pivot point:

$$I_i = m_i {r_i}^2$$

(34)

where I_i is the moment of inertia of component i, m_i is the mass of the component and r_i is the distance to the centre of the pivot from the centroid of the component. Where possible, the mass of the components of the pendulum were measured directly, but some estimates needed to be made, as the welded construction of the pendulum made complete disassembly impossible. The hammer and force transducer at the front of the pendulum, the two identical side weights and the single circular weight at the back of the pendulum where all weighed, giving masses of 36g, 1338g and 400g respectively (the 1338g quoted for the side weights is for both weights). The volumes of the weights were calculated based on their linear measurements, and this information used to estimate the precise density of the steel used in their construction, so as to have a representative value to use in the coming calculations. This was found to be approximately 8,103 kgm^{-3}.

The pendulum was dismantled as much as possible, and the resulting arm assembly, featuring an end block (onto which the weights and hammer head are fitted – they are not included in the following calculations), a long pendulum arm, a shaft forming the pivot, and a single bearing block were weighed as one unit. Two identical bearings are used to support the pendulum: one could be removed, and the other couldn't, due to a welded plate at one end of the shaft. The total mass of the entire assembly was measured as 3,677g. The mass of the bearing was measured at 662g. The mass of the shaft was estimated by calculating its volume from engineering drawings and direct measurement, and using the density of steel calculated above. The mass of the end block was calculated in the same way, taking into account the material removed for the two M6 through-holes used to fit the additional weights. From the calculations therefore, the masses of the end block and shaft were found to be 920g and 903g respectively. These masses, and the mass of the single irremovable bearing, are subtracted from the mass of the whole assembly to give the mass of the arm itself, at 1,992g.

The distance to the hammer from the pivot was measured at 357.5mm. This value was taken as the distance between pivot and centroid r_{end} for the end block and the side weights. The distance r_{arm} for the arm was measured as 176mm, and the distance r_{circ} for the circular weight and the hammer assembly was calculated to be approximately 362mm. Using these values, and *equation 34*, the moment of inertias of arm, end block (including side weights) and the combined circular weight and hammer were calculated to be 0.0368, 0.2888 and 0.0576 kgm^2, respectively. The sum of these inertias gives the total moment of inertia for the pendulum of 0.3832 kgm^2. Note the omission of the shaft and bearings from this calculation; as their centroids coincide with the pivot point, their masses do not contribute to the moment of inertia of the system. By rearrangement of *equation (34)*, the effective mass of the pendulum at the hammer was found to be approximately 3kg: this value can now be substituted for m in *equation (33).*

Rearranging *(33)* to find h, and solving for the energy levels required, gives the hammer heights required to produce 4, 7 and 10 J impact energies as 135.9, 238.0 and 339.8 mm respectively. Using elementary trigonometry, this gives the required pendulum angles from rest (the rest position being where the hammer is just touching the target, with the hammer square-on to the panel) for the three required impact energies as 51.7º, 70.5º and 87.2º respectively. These angles are measured with a digital inclinometer during testing. The limiting factor for maximising the impact energy is the range of the potentiometer. Beyond an angle of approximately 122.5º (from rest), the potentiometer would return an open-circuit signal. This corresponds to a height of approximately 550mm, for an impact energy of 16.2J. This theoretical maximum assumes the pendulum is a lossless system. This is obviously not true, but since the pendulum is properly supported on ball bearings, these losses are considered negligible. Working in reverse, using the measured rebound angle and basic trigonometry to find the rebound height, and then equation for gravitational potential energy, one can easily find the absorbed kinetic energy as well.

Appendix C: Instrument Calibration

Two measurement devices require calibration on this jig: a potentiometer fitted to the shaft, used to record the angle of the pendulum, and a force transducer, used to record the force at the hammer head. Calibrating the potentiometer was very straight-forward: the pendulum was rotated to various angles, the angle being measured with an inclinometer, and the output voltage at each angle was recorded with a voltmeter. This process was performed lifting the pendulum up from rest, and then repeated by gradually returning it to rest. The data was plotted for both actions, and shown in Figure 119. The potentiometer response was approximately linear, but a quadratic curve fit is used for improved accuracy. All voltages recorded from the potentiometer in testing were entered into the following equation, averaged from the ascending and descending curve fits, to give the instantaneous angle of the pendulum:

$$\theta = -1.1627v^2 - 70.6105v - 3.8598$$

(35)

The force transducer used was a Bruel & Kjaer Type 8200, coupled with a Bruel & Kjaer Type 2935 charge amplifier. To calibrate the force transducer, the device was stuck to a suspended 10kg mass using wax. The mass was then driven by an electrodynamic shaker. The inertance and coherence of the system were calculated and plotted on a computer monitor in real-time by signal-processing software: for this system, these quantities should equal 0.1 and 1 respectively. The force transducer was then calibrated by adjusting the charge sensitivity on the charge amplifier until the displayed inertance and coherence equal the values stated above. The test apparatus is shown in Figure 120. A detail view of the force transducer fitted to the suspended mass and shaker is shown in Figure 121. For this particular force transducer, the sensitivity was set to 376 pC/N. The charge amplifier outputs a voltage, multiplied by a user-specified factor to give the force. In this instance, the output was set to 1mv/unit (N for force).

No special setting and calibration procedure was required for the quasi-static indentation and compression-after-impact tests, as the force and displacement outputs are collected directly by the machine software. Where strain gauges are used, the strain output was also gathered directly by the LabWorks software, using the gauge factor provided by the manufacturer.

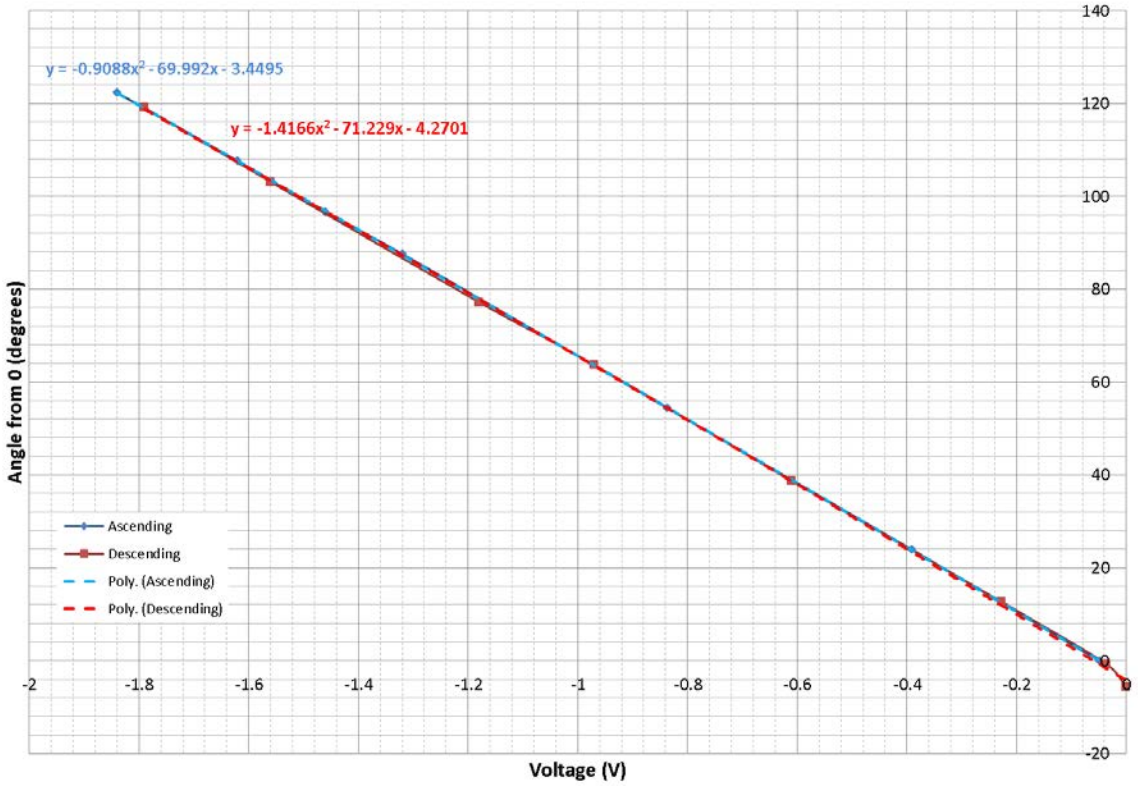

Figure 121: Angle-against-voltage plot for potentiometer calibration

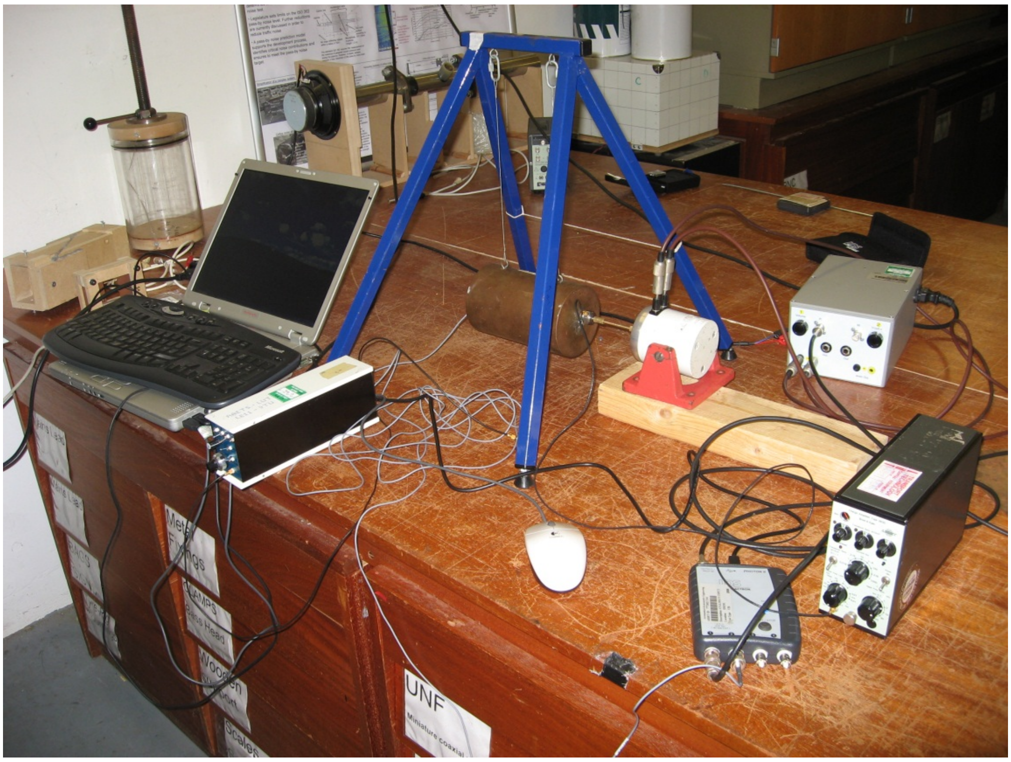

Figure 122: Apparatus for the calibration of force transducer

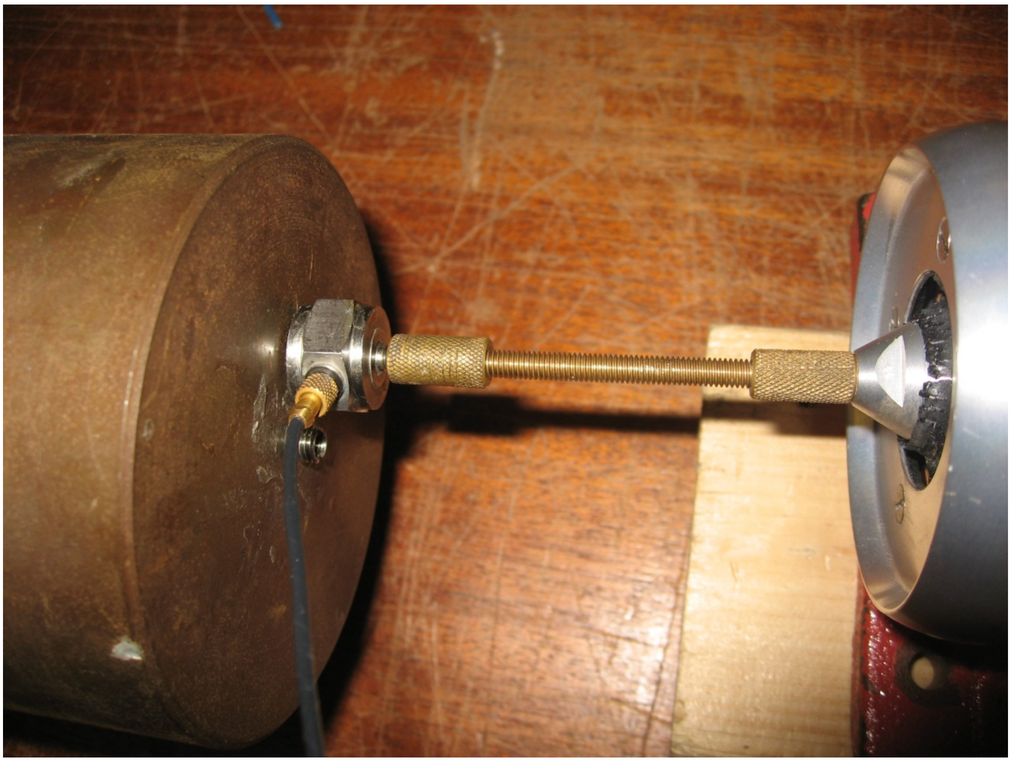

Figure 123: Close-up of force tranducer mounted to hanging mass (left) and electro-dynamic shaker right)

Appendix D: Raw Compression-after-Impact Data – Symmetric Panels [2]

Panel			L (mm)	W (mm)	T (mm) Panel	T (mm) Skins		P indt (N)	P (N)	sig (MPa)	strain at failure (%)	% residual strength	Failure mode/location	Notes
SCV	Phase 1	1	149.93	99.65	14.47	1.699		-	35,366.74	208.89	0.930	-	End	
		2	149.01	99.87	14.55	1.779			42,028.58	236.56	-		-	Strain gauged, no failure
		2-i							43,149.77	242.87	1.305		D/K, E	Re-test of '2'
		3	149.77	100.38	14.55	1.779			44,082.01	246.85	1.515		D, E	
	Phase 2	4	149.04	100.05	14.52	1.749		-	51,097.12	292.00	1.259	-	D/K, E	
		5	149.04	99.57	14.48	1.709			50,363.34	295.97	1.155		D, E	
		6	149.29	100.03	14.42	1.649			36,591.60	221.84	1.102		D, E	
							SV Av	-	***45,056.77***	***259.91***	***1.267***	-		
							SV S.D		***5,934.88***	***32.56***	***0.160***			
							SV Range		***14,505.52***	***74.13***	***0.413***			
SC2.5	Phase 1	1	150.44	98.87	14.56	1.789		2,269.48	34,961.56	197.66	1.372	76.05	D, E	
		2	150.49	100.38	14.49	1.719		2,250.19	39,231.42	227.36	1.221	87.48	D, E	Strain gauged
		3	150.17	98.98	14.49	1.719		2,273.37	49,252.82	289.47	1.179	111.38	D, E	
	Phase 2	4	148.37	99.25	14.53	1.759		2,202.89	52,553.95	301.03	1.281	115.82	D/B, E	
		5	148.82	98.99	14.42	1.649		2,183.46	34,506.19	211.39	0.928	81.33	D, E	
							S2.5 Av	***2,235.88***	***42,101.19***	***245.38***	***1.196***	***94.41***		
							S2.5 S.D	***40.54***	***8,326.16***	***46.90***	***0.167***	***18.05***		
							S2.5 Range	***89.91***	***18,047.76***	***103.37***	***0.444***	***39.77***		
SC5	Phase 1	1	150.48	99.65	14.6	1.829		3,047.72	38,204.87	209.62	1.295	80.65	K, C	Strain gauged
		2	149.98	100.13	14.49	1.719		2,947.23	38,831.70	225.60	0.961	86.80	K, C	
	Phase 2	3	149.69	99.86	14.46	1.689		2,896.40	38,900.71	230.64	0.932	88.74	K, C	
		4	149.69	99.81	14.46	1.689		2,733.02	35,297.27	209.38	0.901	80.56	K, C	
		5	150.18	99.93	14.5	1.729		2,985.77	38,679.16	223.86	1.009	86.13	K, C	
							S5 Av	***2,922.03***	***37,982.74***	***219.82***	***1.020***	***84.58***		
							S5 S.D	***119.25***	***1,525.57***	***9.75***	***0.159***	***3.75***		
							S5 Range	***314.7***	***3,603.44***	***21.26***	***0.394***	***8.18***		
SC7	Phase 1	1	149.93	99.55	14.45	1.679		2,769.44	33,760.12	201.98	1.035	77.71	K, C	
		2	149.88	99.71	14.58	1.809		2,571.72	31,363.05	173.88	1.454	66.90	End	Strain gauged
		3	150.05	99.45	14.56	1.789		2,924.45	34,381.06	193.24	1.141	74.35	K, C	
	Phase 2	4	149.74	99.85	14.49	1.719		2,657.40	35,702.68	208.01	0.855	80.03	K, C	
		5	148.9	99.81	14.44	1.669		3,059.49	33,843.34	203.16	0.952	78.17	K, C	Incomplete end pot - no influence on results
		6	148.19	99.58	14.5	1.729		2,811.81	37,077.00	215.35	0.893	82.86	K, C	
	Phase 3	7	149.5	99.5	14.48	1.709		-	34,726.05	204.22	0.977	78.57	K, C	Strain Gauged
	Sym Av		***149.59***	***99.69***	***14.53***	***1.729***	***S7 Av***	***2799.05***	***34,915.04***	***204.33***	***0.976***	***78.62***		
	Sym S.D		***0.65***	***0.40***	***0.05***	***0.05***	***S7 S.D***	***176.83***	***1,272.61***	***7.28***	***0.103***	***2.80***		
	Sym Range		***2.3***	***1.51***	***0.15***	***0.18***	***S7 Range***	***487.77***	***3,316.88***	***22.10***	***0.286***	***8.50***		

Failure codes: K = kink-band, D = delamination buckling, B = bending
E = near-end, C = centre

Appendix E: Raw Compression-after-Impact Data – Asymmetric Panels [2]

Panel			L (mm)	W (mm)	T (mm)			P indt (N)	P (N)	sig (MPa)	strain at failure (%)	% residual	Failure mode/location	Notes
					Panel	Skins								
ACV	Phase 1	1	150	100.05	14.28	1.509		-	25,460.22	168.64	1.258	-	K, E	
		2	150.59	99.83	14.3	1.529			41,964.75	274.93	1.415		K, E	Strain Gauged
		3	150.24	100.04	14.28	1.509			39,362.61	260.75	1.456		D, E	
	Phase 2	4	149.42	100.13	14.26	1.489		-	36,611.29	245.56	0.941	-	K, E	
		5	148.81	99.97	14.28	1.509			38,101.01	252.57	0.951		D/K, E	
	Phase 3	6	151	99.5	14.33	1.559		-	36,722.89	236.74	1.053	-	D, E	Strain Gauged
							AV Av	-	***36,370.46***	***239.86***	***1.179***	-		
							AV S.D		***5,700.16***	***37.26***	***0.229***			
							AV Range		***16,504.53***	***106.29***	***0.515***			
AC2.5	Phase 1	1	149.93	99.97	14.28	1.509		2,264.36	31,722.86	210.29	0.967	**87.67**	End	
		2	150.02	99.3	14.33	1.559		2,324.30	35,224.27	227.53	0.947	**94.86**	B, E	Strain gauged
		3	149.73	99.91	14.3	1.529		2,239.50	35,305.12	231.11	0.954	**96.35**	D, E	
	Phase 2	4	149.2	98.95	14.26	1.489		2,149.96	42,115.33	285.84	1.160	**119.17**	D/K, E	Significant instantaneous displacement at failure
		5	149.21	99.22	14.3	1.529		2,131.23	38,759.37	255.49	1.097	**106.51**	K, E	
		6	149.55	99.47	14.28	1.509		2,213.10	41,072.26	273.63	1.048	**114.08**	K, E	
							A2.5 Av	***2,220.41***	***38,495.27***	***254.72***	***1.041***	***106.19***		
							A2.5 S.D	***72.19***	***3,189.51***	***25.61***	***0.092***	***10.68***		
							A2.5 Range	***193.07***	***6,891.06***	***58.31***	***0.213***	***24.31***		
AC5	Phase 1	1	149.02	99.25	14.34	1.569		2,646.01	30,203.66	193.96	0.809	**80.86**	K, C	Strain gauged
		2	149.57	100.34	14.33	1.559		2,861.07	36,137.11	231.01	1.072	**96.31**	K, C	
	Phase 2	3	149.98	99.48	14.3	1.529		2,369.20	33,717.87	221.68	0.923	**92.42**	K, C & E	Two kink bands, unclear which controls failure
		4	149.19	99.82	14.28	1.509		2,828.06	32,573.55	216.25	0.906	**90.16**	D, E	Incomplete kink band forming at centre
		5	148.92	99.51	14.28	1.509		2,722.95	32,763.93	218.19	1.149	**90.97**	K, C	
							A5 Av	***2,685.46***	***33,079.22***	***216.22***	***0.972***	***90.14***		
							A5 S.D	***196.31***	***2,143.74***	***13.68***	***0.137***	***5.70***		
							A5 Range	***491.87***	***5,933.45***	***37.05***	***0.340***	***15.45***		
AC7	Phase 1	1	149.93	99.17	14.32	1.549		2,585.03	30,517.82	198.67	0.861	**82.82**	K, C	
		2	150.01	99.49	14.33	1.559		3,036.81	29,263.06	188.67	0.819	**78.66**	K, C	Strain gauged
		3	149.32	98.43	14.33	1.559		2,733.78	30,185.57	196.71	0.911	**82.01**	K, C	
	Phase 2	4	150.42	99.94	14.22	1.449		2,680.26	31,547.05	217.85	0.998	**90.82**	K, C	Overly deep end pot - no influence on results
		5	149.64	98.92	14.25	1.479		2,944.94	33,806.25	231.07	0.946	**96.33**	K, C	
	Asym Av		***149.71***	***99.58***	***14.31***	***1.523***	***A7 Av***	***2,796.16***	***31,063.95***	***206.59***	***0.907***	***86.13***		
	Asym S.D		***0.56***	***0.47***	***0.023***	***0.03***	***A7 S.D***	***188.38***	***1,736.85***	***17.38***	***0.070***	***7.24***		
	Asym Range		***1.78***	***1.91***	***0.06***	***0.12***	***A7 Range***	***451.78***	***4,543.19***	***42.40***	***0.179***	***17.68***		

Appendix F: Damage Magnitude Results from Development Sandwich Model [1]

Model			Dent depth (mm)			Dent ø (mm)			Delamination area (mm^2)				Core damage (mm)	
			Num	Exp	% error	Num	Exp	% error	Num 1	Num 2	Exp	% error	ø	Depth
Q1-C1	lg	1	1.05	1.04	***1***	62.6	58.2	***7.6***	517	-	-	-	62.5	8
		2	1.43		***37.5***	67.2		***15.5***	-	689			70	14
		3	1.32		***26.9***	64.4		***10.7***	-	689			65	15
	sm	1	0.44	0.58	***-24.1***	38.6	40.5	***-4.7***	592	-	215	***175***	30	3.5
		2	0.53		***-8.6***	68.1		***68.2***	-	1191		***454***	40	5
		3	1.37		***136***	63		***55.6***	506	1152		***436***	63.5	13
Q1-C2	lg	1	0.75	0.99	***-24.2***	58.9	54.9	***6.7***	517	-	-	-	57.5	4
		2	0.79		***-20.2***	59.8		***8.9***	-	644			57.5	5
		3	0.84		***-15.2***	59.8		***8.9***	-	681			57.5	5
	sm	1	0.49	0.47	***4.3***	43.2	34.6	***24.9***	588	-	400	***47***	35	6
		2	0.58		***23.4***	48.8		***41***	-	707		***76.8***	41.5	6.5
		3	0.59		***25.5***	52.9		***52.9***	443	1153		***188***	47.5	4.5
Q2-C1	lg	1	1.22	1.22	***0***	63.5	62.1	***2.3***	557	-	-	-	65	13
		2	1.31		***7.4***	65.8		***6***	-	728			73	13
		3	1.33		***9***	64.4		***3.7***	-	850			66	14
	sm	1	0.34	0.53	***-55.9***	24.8	38.7	***-35.9***	409	-	302	***35.4***	15	3
		2	0.41		***-35.3***	39.6		***2.3***	-	667		***121***	30	3.5
		3	1.26		***138***	61.4		***58.7***	491	1259		***317***	60	13

Appendix G: Complete Results from the Parametric Study

#	**Region**	**Parameter**		**Strength (MPa)**			**% difference (from 0)**		
				Vir	**Lg**	**Sm**	**Vir**	**Lg**	**Sm**
0	***Base model (Q1-C1-…-1)***			***467.80***	***328.70***	***376.70***	**-**		
1	Structure	0º fibres offset to…	1º	456.07	336.27	-	**-2.5**	**2.3**	-
2			9º	444.72	307.78		**-4.9**	**-6.4**	
3			18º	396.50	300.47		**-15.2**	**-8.6**	
4		+/- 45º fibres offset by…	1º	466.91	*321.02*		**-0.2**	**-2.3**	
5			9º	433.67	321.55		**-7.3**	**-2.2**	
6			18º	389.03	332.64		**-16.8**	**1.2**	
7			-45º $[0,0,90,90]_s$	532.27	314.57		**13.8**	**-4.3**	
8		Cross-ply lay-up $[0,90]_{2s}$		583.94	345.93		**24.8**	**5.2**	
9		90º fibres offset to 108º		440.09	300.12		**-5.9**	**-8.7**	
10		Core orientation offset by…	1º	472.45	316.51		**1.0**	**-3.7**	
11			18º	470.07	312.16		**0.5**	**-5.0**	
12			45º	471.30	313.58		**0.7**	**-4.6**	
13			90º	466.25	302.36		**-0.3**	**-8.0**	
14	Skin (strengths)	σ_{LT}	+20%	467.77	313.80	-	**0.0**	**-4.5**	-
15			-20%	467.71	315.42		**0.0**	**-4.0**	
16		σ_{LC}	+20%	494.52	315.03		**5.7**	**-4.2**	
17			-20%	415.79	314.90		**-11.1**	**-4.2**	
18			+10%	487.92	309.29		**4.3**	**-5.9**	
19			-10%	444.16	312.25		**-5.1**	**-5.0**	
20		$\sigma_{TT\ \&\ TC}$	+20%	466.67	344.51		**-0.2**	**4.8**	
21			-20%	483.87	314.07		**3.4**	**-4.5**	
22		$\tau_{L\ \&\ T}$	+20%	473.75	310.61		**1.3**	**-5.5**	
23			-20%	450.56	315.50		**-3.7**	**-4.0**	
24	Skin (energies)	G_{LT}	+20%	467.77	315.45	-	**0.0**	**-4.0**	-
25			-20%	467.77	311.16		**0.0**	**-5.3**	
26		G_{LC}	+20%	468.57	319.19		**0.2**	**-2.9**	
27			-20%	468.86	310.82		**0.2**	**-5.4**	
28		$G_{TT\ \&\ TC}$	+20%	474.97	314.82		**1.5**	**-4.2**	
29			-20%	469.13	310.11		**0.3**	**-5.7**	
30	Bond	σ_{m1}	+20%	469.01	316.94	-	**0.3**	**-3.6**	-
31			-20%	470.22	314.02		**0.5**	**-4.5**	
32		$\sigma_{m2\ \&\ m3}$	+20%	468.80	341.69		**0.2**	**4.0**	
33			-20%	469.49	316.24		**0.4**	**-3.8**	
34		G_{m1}	+20%	469.93	317.66		**0.5**	**-3.4**	
35			-20%	471.23	314.09		**0.7**	**-4.4**	
36		$G_{m2\ \&\ m3}$	+20%	467.77	319.13		**0.0**	**-2.9**	
37			-20%	466.84	312.97		**-0.2**	**-4.8**	
38		Mode-mix ratio	+20%	468.85	310.59		**0.2**	**-5.5**	
39			-20%	469.82	315.80		**0.4**	**-3.9**	
40	Core	σ_{ult}	+20%	477.67	355.89	347.98	**2.1**	**8.3**	**-7.6**
41			-20%	465.00	309.58	360.44	**-0.6**	**-5.8**	**-4.3**
42		σ_{crush}	+20%	474.66	333.98	408.84	**1.5**	**1.6**	**8.5**
43			-20%	449.31	312.02	379.19	**-4.0**	**-5.1**	**0.7**
44		E_3	+20%	471.62	311.62	376.25	**0.8**	**-5.2**	**-0.1**
45			-20%	468.71	311.78	399.90	**0.2**	**-5.1**	**6.2**

Appendix H: Damage Magnitude Results from the Parametric Study

#	DL area (mm^2)	% diff	Core ø (mm)				Core depth (mm)			
			lg	% diff	sm	% diff	lg	% diff	sm	% diff
30	569	10.1	-		-		-		-	
31	607	17.4								
32	474	-8.3								
33	649	25.5								
34	556	7.5								
35	544	5.2								
36	471	-8.9								
37	684	32.3								
38	524	1.4								
39	577	11.6								
40	-		61	**-2.4**	21	-30.0	6.3	-21.3	3	**-14.3**
41			71.3	**14.1**	45.5	**51.7**	14.6	**82.5**	6	**71.4**
42			68	**8.8**	33	**10.0**	17	**112.5**	4	**14.3**
43			64	**2.4**	28.5	**-5.0**	6.3	-21.3	4.5	**28.6**
44			71	**13.6**	30	**0.0**	13.6	**70.0**	4.2	**20.0**
45			70	**12.0**	33	**10.0**	13.7	**71.3**	3.5	**0.0**

References

1. James CT, Watson A, Cunningham PR. Numerical Modelling of the Compression-after-Impact Performance of a Composite Sandwich Panel. Journal of Sandwich Structures and Materials 2015;17(4):376-398.

2. James CT, Cunningham PR, Watson A. Experimental and Numerical Investigation of the Effect of Asymmetry on the Residual Strength of a Composite Sandwich Panel. Journal of Sandwich Structures and Materials 2015;17(4):417-445.

3. Hohe J, Librescu L. Advances in the Structural Modelling of Elastic Sandwich Panels. Mechanics of Advanced Materials and Structures 2004;11:395-424.

4. Hill MD. Damage Resistance and Tolerance Investigation of Carbon/Epoxy Skinned Honeycomb Sandwich Panels. , 2007.

5. Klaus M, Reimerdes HG, Gupta NK. Experimental and Numerical Investigations of Residual Strength after Impact of Sandwich Panels. International Journal of Impact Engineering 2012;44:50-58.

6. Zenkert D, Shipsha A, Bull P, Hayman B. Damage Tolerance Assessment of Composite Sandwich Panels with Localised Damage. Composites Science and Technology 2005;65:2597-2611.

7. Abrate S. Localized Impact of Sandwich Structures with Laminated Facings. Applied Mechanics Review 1997;50(2):69-82.

8. Tomblin J, Lacy T, Smith B, Hooper S, Vizzini A, Lee S. Review of Damage Tolerance for Composite Sandwich Airframe Structures. U S Department of Transportation 1999;DOT/FAA/AR-99-49.

9. Karger L, Baaran J, Tessmer J. Efficient Simulation of Low-Velocity Impacts on Composite Sandwich Panels. Computers and Structures 2008;86:988-996.

10. Tomblin JS, Raju KS, Liew J, Smith BL. Impact Damage Characterisation and Damage Tolerance of Composite Sandwich Airframe Structures, Final Report. Federal Aviation Administration 2001;DOT/FAA/AR-00-44.

11. Lacy TE, Hwang Y. Numerical Modelling of Impact-Damaged Sandwich Composites Subjected to Compression-after-Impact Loading. Composite Structures 2003;61:115-128.

12. Hwang Y, Lacy TE. Numerical Estimates of the Compressive Strength of Impact-Damaged Sandwich Composites. Journal of Composite Materials 2007;41:367-388.

13. Hayman B. Approaches to Damage Assessment and Damage Tolerance for FRP Sandwich Structures. Journal of Sandwich Structures and Materials 2007;9:571-596.

14. McQuigg TD. Compression After Impact Experiments and Analysis on Honeycomb Core Sandwich Panels with Thin Facesheets. NASA, Langley 2011;NASA/CR-2011-217157.

15. Zhou G, Hill M, Loughlan J, Hookham N. Damage Characteristics of Composite Honeycomb Sandwich Panels in Bending under Quasi-Static Loading. Journal of Sandwich Structures and Materials 2006;8:55-90.

16. Zhou G, Hill M, Hookham N. Investigation of Parameters Governing the Damage and Energy Absorption Characteristics of Honeycomb Sandwich Panels. Journal of Sandwich Structures and Materials 2007;9:309-342.

17. Zhou G, Hill MD. Impact Damge and Energy-Absorbing Characteristics and Residual In-Plane Compressive Strength of Honeycomb Sandwich Panels. Journal of Sandwich Structures and Materials 2009;11:329-356.

18. Reid SR, Zhou G. Impact Behaviour of Fibre-Reinforced Composite Materials. 2000.

19. Cartié DDR, Irving PE. Effect of Resin and Fibre Properties on Impact and Compression-after-Impact Performance of CFRP. Composites: Part A 2002;33:483-493.

20. Othman AR, Barton DC. Failure Initiation and Propagation Characteristics of Honeycomb Sandwich Composites. Composite Structures 2008;85:126-138.

21. Herup EJ, Palazotto AN. Low-Velocity Impact Damage Initiation in Graphite/Epoxy/Nomex-Honeycomb-Sandwich Panels. Composites Science and Technology 1997;57:1581-1598.

22. Zhou G, Nash P, Hill MD, Boston L. In-Plane Compressive Behaviour of Impact-Damaged Sandwich - I. Damage Characterisation. Composites Science and Technology Submitted.

23. Zhou G, Nash P, Hill MD. In-Plane Compressive Behaviour of Impact-Damaged Sandwich - II. Symmetrical Panels. Composites Science and Technology Submitted.

24. Zhou G, Nash P, Boston L, Coles N, Campbell L. In-Plane Compressive Behaviour of Impact-Damaged Sandwich - III. Unsymmetrical Panels. Composites Science and Technology Submitted.

25. Zhou G, Nash P, Boston L, Coles N, Campbell L. Experimental Study of In-Plane Compressive Behaviour of Unsymmetrical Sandwich Panels. 18th International Conference on Composite Materials, South Korea. p. 1-6.

26. Schultz MR. A Concept for Airfoil-like Active Bistable Twisting Structures. Journal of Intelligent Material Systems and Structures 2008;19:157-169.

27. Diaconu CG, Weaver PM, Mattioni F. Concepts for Morphing Airfoil Sections using Bi-Stable Laminated Composite Structures. Thin-Walled Structures 2008;46:689-701.

28. Schubel PM, Luo J, Daniel IM. Impact and Post-Impact Behaviour of Composite Sandwich Panels. Composites: Part A 2006;38:1051-1057.

29. Bailey NW, Battley MA, Zhou M. Experimental Method for Dynamic Residual Strength Characterisation of Aircraft Sandwich Structures. International Journal of Crashworthiness 2013;18(1):64-81.

30. Ratcliffe JC, Jackson WC. A Finite Element Analysis for Predicting the Residual Compressive Strength of Impact-Damaged Sandwich Panels. NASA 2008;NASA/TM-2008-215341.

31. Ratcliffe J, Jackson W, Schaff J. Predicting the Compression Strength of Impact-Damaged Sandwich Panels. ICCM 15th International Conference on Composite Materials, Durban, S.A.

32. McQuigg TD, Kapania RK, Scotti SJ, Walker SP. Compression after Impact on Honeycomb Core Sandwich Panels with Thin Facesheets, Part 1: Experiments. 53rd AIAA/ASME/ASCE/AHS/ASC Structures, Structual Dynamics and Materials Conference, Honolulu, Hawaii, 2012. p. 1-37.

33. Czabaj MW, Zehnder AT, Davidson BD, Singh AK, Eisenberg DP. Compression after Impact of Sandwich Composite Structures: Experiments and Modelling. 51st AIAA/ASME/ASCE/AHS/ASC Structures, Structural Dynamics and Materials Conference, Orlando, Florida.

34. Hitchen SA, Kemp RMJ. The Effect of Stacking Sequence on Impact Damage in a Carbon Fibre/Epoxy Composite. Composites 1995;26:207-214.

35. Gonzalez EV, Maimi P, Camanho PP, Lopes CS, Blanco N. Effects of Ply Clustering in Laminated Composite Plates under Low-Velocity Impact Loading. Composites Science and Technology 2011;71:805-817.

36. Hong S, Liu D. On the Relationship Between Impact Energy and Delamination Energy. Experimental Mechanics 1989;29(2):115-120.

37. Hwang S, Lie G. Buckling Behaviour of Composite Laminates with Multiple Delaminations under Uniaxial Compression. Composite Structures 2001;53:235-243.

38. Anon. Standard Test Method for Compressive Residual Strength Properties of Damaged Polymer Matrix Composite Plates. ASTM 2012;D7137 / D7137M-12:1-17.

39. Anon. Standard Test Method for Edgewise Compressive Strength of Sandwich Constructions. ASTM 2012;C364 / C364M-07:1-8.

40. Czabaj MW. Damage and Damage Tolerance of High Temperature Composites and Sandwich Composite Structures. , Cornell University, 2010.

41. Davies GAO, Zhang X, Zhou G, Watson S. Numerical Modelling of Impact Damage. Composites 1994;25:342-350.

42. Gonzalez EV, Maimi P, Camanho PP, Turon A, Mayugo JA. Simulation of Drop-Weight Impact and Compression after Impact Tests on Composite Laminates. Composite Structures 2012;94:3364-3378.

43. Aktay L, Johnson AF, Holzapfel M. Prediction of Impact Damage on Sandwich Composite Panels. Computational Materials Science 2005;32:252-260.

44. Guida M, Marulo F, Meo M, Riccio M. Analysis of Bird Impact on a Composite Tailplane Leading Edge. Applied Composite Materials 2008;15:241-257.

45. Meo M, Morris AJ, Vignjevic R, Marengo G. Numerical Simulations of Low-Velocity Impact on an Aircraft Sandwich Panel. Composite Structures 2003;62:353-360.

46. Hoo Fatt MS, Park KS. Dynamic Models for Low-Velocity Impact Damage of Composite Sandwich Panels - Part A: Deformation. Composite Structures 2001;52:335-351.

47. Hoo Fatt MS, Park KS. Dynamic Models for Low-Velocity Impact Damage of Composite Sandwich Panles - Part B: Damage Initiation. Composite Structures 2001;52:353-364.

48. Olsson R. Engineering Method for Prediction of Impact Response and Damage in Sandwich Panels. Journal of Sandwich Structures and Materials 2002;4:3-29.

49. Hufenbach W, Gruber B, Lepper M, Zhou B. Analytical Methods for the Stress Concentration Analysis of Multilayered Anisotropic Composites with Elastic Inclusions. 16th International Conference on Composite Materials, Kyoto, Japan.

50. Xiong Y, Poon C, Straznicky PV, Vietinghoff H. A Prediction Method for the Compressive Strength of Impact Damaged Composite Laminates. Composite Structures 1995;30:357-367.

51. Riks E, Rankin CC. Sandwich Modelling with an Application to the Residual Strength Analysis of a Damaged Compression Panel. International Journal of Non-Linear Mechanics 2002;37:897-908.

52. Foo CC, Chai GB, Seah LK. A Model to Predict Low-Velocity Impact Response and Damage in Sandwich Composites. Composites Science and Technology 2008;68:1348-1356.

53. Aminanda Y, Castanie B, Barrau J, Thevenet P. Experimental Analysis and Modelling of the Crushing of Honeycomb Cores. Applied Composite Materials 2005;12:213-227.

54. Hou JP, Petrinic N, Ruiz C, Hallett SR. Prediction of Impact Damage in Composite Plates. Composites Science and Technology 2000;60:273-281.

55. Chan S, Fawaz Z, Behdinan K, Amid R. Ballistic Limit Prediction using a Numerical Model with Progressive Damage Capability. Composite Structures 2007;77:466-474.

56. Tita V, de Carvalho J, Vandepitte D. Failure Analysis of Low Velocity Impact on Thin Composite Laminates: Experimental and Numerical Approaches. Composite Structures 2008;83:413-428.

57. Davies GAO, Hitchings D, Besant T, Clarke A, Morgan C. Compression after Impact Strength of Composite Sandwich Panels. Composite Structures 2004;63:1-9.

58. Besant T, Davies GAO, Hitchings D. Finite Element Modelling of Low-Velocity Impact of Composite Sandwich Panels. Composites: Part A 2001;32:1189-1196.

59. Prevorsek DC, Chin HB, Bhatnagar A. Damage Tolerance: Design for Structural Integrity and Penetration. Composite Structures 1993;23:137-148.

60. Xie Z, Vizzini A, Tang Q. On Residual Compressive Strength Prediction of Composite Sandwich Panels after Low-Velocity Impact Damage. Acta Mechanica Solida Sinica 2006;19:9-17.

61. Hawyes VJ, Curtis PT, Soutis C. Effect of Impact Damage on the Compressive Response of Composite Laminates. Composites: Part A 2001;32:1263-1270.

62. Soutis C, Fleck NA, Smith PA. Failure Prediction Technique for Compression Loaded Carbon Fibre-Epoxy Laminate with Open Holes. Journal of Composite Materials 1991;25:1476-1498.

63. Soutis C, Curtis PT. Prediction of the Post-Impact Compressive Strength of CFRP Laminated Composites. Composites Science and Technology 1996;56:677-684.

64. Maimi P, Camanho PP, Mayugo JA, Davila CG. A Thermodynamically Consistent Damage Model for Advanced Composites. NASA, Langley 2006;NASA/TM-2006-214282.

65. Maimi P, Camanho PP, Mayugo JA, Davila CG. A Continuum Damage Model for Composite Laminates: Part I - Constitutive Model. Mechanics of Materials 2007;39:897-908.

66. Maimi P, Camanho PP, Mayugo JA, Davila CG. A Continuum Damage Model for Composite Laminates: Part II - Computational Implementation and Validation. Mechanics of Materials 2007;39:909-919.

67. Gonzalez EV, Maimi P, Turon A, Camanho PP, Renart J. Simulation of Delamination by Means of Cohesive Elements using an Explicit Finite Element Code. CMC 2009;9(1):51-92.

68. Benzeggagh ML, Kenane M. Measurement of Mixed-Mode Delamination Fracture Toughness of Unidirectional Glass/Epoxy Composites with Mixed-Mode Bending Apparatus. Composites Science and Technology 1996;56:439-449.

69. Davila CG, Camanho PP, Rose CA. Failure Criteria for FRP Laminates. Journal of Composite Materials 2005;39(4):323-345.

70. Pinho ST, Davila CG, Camanho PP, Iannucci L, Robinson P. Failure Models and Criteria for FRP Under In-Plane of Three-Dimensional Stress States including Shear Non-Linearity. NASA, Langley 2005;NASA/TM-2005-213530.

71. Davila CG, Camanho PP. Failure Criteria for FRP Laminates in Plane Stress. NASA 2003;NASA/TM-2003-212663.

72. Rivallant S, Bouvet C, Hongkarnjanakul N. Failure Analysis of CFRP Laminates Subjected to Compression-after-Impact: FE Simulation using Discrete Interface Elements. Composites: Part A 2013;55:83-93.

73. Dang TD, Hallett SR. A Numerical Study on Impact and Compression-after-Impact Behaviour of Variable Angle Tow Laminates. Composite Structures 2013;96:194-206.

74. Lapczyk I, Hurtado JA. Progressive Damage Modelling in Fibre-Reinforced Materials. Composites: Part A 2007;38:2333-2341.

75. Camanho PP, Davila CG. Mixed-Mode Cohesion Finite Elements for the Simulation of Delamination in Composite Materials. NASA 2002;NASA/TM-2002-211737.

76. Bazant ZP, Oh BH. Crack Band Theory for Fracture of Concrete. Materials and Structures 1983;16:155-177.

77. Shipsha A, Hallstrom S, Zenkert D. Failure Mechanisms and Modelling of Impact Damage in Sandwich Beams - A 2D Approach: Part 1 - Experimental Investigation. Journal of Sandwich Structures and Materials 2003;5:7-31.

78. Shipsha A, Hallstrom D, Zenkert D. Failure Mechanisms and Modelling of Impact Damage in Sandwich Beams - A 2D Approach: Part 2 - Analysis and Modelling. Journal of Sandwich Structures and Materials 2003;5:33-51.

79. Shipsha A, Zenkert D. Compression-after-Impact Strength of Sandwich Panels with Core Crushing Damage. Applied Composite Materials 2005;12:149-164.

80. Castanie B, Aminanda Y, Bouvet C, Barrau J. Core Crush Criterion to Determine the Strength of Sandwich Composite Structures Subjected to Compression-after-Impact. Composite Structures 2008;86:243-250.

81. Minguet PJ. A Model for Predicting the Behaviour of Impact-Damaged Minimum Gage Sandwich Panels under Compression. AIAA/ASME/ASCE/AHS/ASC 32nd Structures, Structural Dynamics and Materials Conference, 1991.

82. Lee S, Ansari MZ, Wang N, Cho C. A Computational Study on Residual Strength of Sandwich Composite Panel. Advanced Materials Research 2012;393-395:521-525.

83. McQuigg TD, Kapania RK, Scotti SJ, Walker SP. Response of Honeycomb Core Sandwich Panel with Minimum Gage GFRP Face-sheets to Compression Loading after Impact. NASA, Langley 2011;NF1676L-11467.

84. McQuigg TD, Kapania RK, Scotti SJ, Walker SP. Compression after Impact on Honeycomb Core Sandwich Panels with Thin Facesheets, Part 2: Analysis. AIAA 2012;2012-1704, NF1676L-13332:1-51.

85. Mayes JS, Hansen AC. Composite Laminate Failure Analysis using Multicontinuum Theory. Composites Science and Technology 2004;64:379-394.

86. Klaus M, Reimerdes HG. Residual Strength Simulations of Sandwich Panels after Impact. ICCM 17th International Conference on Composite Materials, Edinburgh, UK.

87. Staal RA, Mallinson GD, Jayaraman K. Predicting Failure Loads of Impacted Damaged Honeycomb Sandwich Panels. Journal of Sandwich Structures and Materials 2009;11:213-232.

88. Ivanez I, Sanchez-Saez S. Numerical Modelling of the Low-Velocity Impact Response of Composite Sandwich Beams with Honeycomb Core. Composite Structures 2013;106:716-723.

89. Wang E, Shukla A. Blast Performance of Sandwich Composites with In-Plane Compressive Loading. Experimental Mechanics 2012;52:49-58.

90. Mouritz AP. Review of Z-pinned Composite Laminates. Composites: Part A 2007;38:2383-2397.

91. Aymerich F, Pani C, Priolo P. Effect of Stitching on the Low-Velocity Impact Response of [0(3)/90(3)]s Graphite/Epoxy Laminates. Composites: Part A 2007;38:1174-1182.

92. Yoshimura A, Nakao T, Yashiro S, Takeda N. Improvement on Out-of-Place Impact Resistance of CFRP Laminates due to Through-the-Thickness Stitching. Composites: Part A 2008;39:1370-1379.

93. Williams HR, Trask RS, Bond IP. Self-Healing Sandwich Panels: Restoration of Compressive Strength after Impact. Composites Science and Technology 2008;68:3171-3177.

94. Williams GJ, Bond IP, Trask RS. Compression after Impact Assessment of Self-Healing CFRP. Composites: Part A 2009;40:1399-1406.

95. Chou T, Gao L, Thostenson ET, Zhang Z, Byun J. Review: An Assessment of the Science and Technology of Carbon Nanotube-Based Fibres and Composites. Composites Science and Technology 2010;70:1-19.

96. Nettles AT, Lance DG. On the Enhancement of Impact Damage Tolerance of Composite Laminates. Composites Engineering 1993;3(5):383-394.

97. Hinton MJ, Soden PD. Predicting Failure in Composite Laminates: the Background to the Exercise. Composites Science and Technology 1998;58:1001-1010.

98. Soden PD, Hinton MJ, Kaddour AS. A Comparison of the Predictive Capabilities of Current Failure Theories for Composite Laminates. Composites Science and Technology 1998;58:1225-1254.

99. Kaddour AS, Hinton MJ, Soden PD. A Comparison of the Predictive Capabilities of Current Failure Theories for Composite Laminates: Additional Contributions. Composites Science and Technology 2004;64:449-476.

100. Hinton MJ, Kaddour AS, Soden PD. A Comparison of the Predictive Capabilities of Current Failure Theories for Composite Laminates, Judged Against Experimental Evidence. Composites Science and Technology 2002;62:1725-1798.

101. Hinton MJ, Kaddour AS, Soden PD. A Further Assessment of the Predictive Capabilites of Current Failure Theories for Composite Laminates: Comparison with Experimental Evidence. Composites Science and Technology 2004;64:549-588.

102. Soden PD, Kaddour AS, Hinton MJ. Recommendations for Designers and Researchers Resulting from the World Wide Failure Exercise. Composites Science and Technology 2004;64:589-604.

103. Hashin Z, Rotem A. A Fatigue Criterion for Fibre-Reinforced Materials. Journal of Composite Materials 1973;7:448-464.

104. Hashin Z. Failure Criteria for Unidirectional Fibre-Composites. Journal of Applied Mechanics 1980;47:329-334.

105. Puck A, Schurmann H. Failure Analysis of FRP Laminates by Means of Phenomenological Models. Composites Science and Technology 1998;58(7):1045-1067.

106. Puck A, Mannigel M. Physically Based Non-Linear Stress-Strain Relations for the Inter-Fibre Fracture Analysis of FRP Laminates. Composites Science and Technology 2007;67:1955-1964.

107. Garnich MR, Hansen AC. A Multicontinuum Theory for Thermal-Elastic Finite Element Analysis of Composite Materials. Journal of Composite Materials 1997;31:71-86.

108. Feng D, Cerioni A, Aymerich F. Simulation of Impact Damage in Laminated Composite by Progressive Damage Models. ECCM 15 - 15th European Conference on Composite Materials, Venice, Italy.

109. Chen C, Espinosa C, Michel L, Lachaud F. A Numerical Approach for Analyzing Post-Impact Behaviour of Composite Laminate Plate under In-Plane Compression. ECCM 15 - 15th European Conference on Composite Materials, Venice, Italy.

110. Yoshimura A, Nagakura K, Okabe T, Kusano H, Yamada M, Tanabe Y, Ogasawara T, Nakatani H, Ogihara S. 3D Simulation of High-Velocity Impact Damage Progress in the CFRP Laminates. ECCM 15 - 15th European Conference on Composite Materials, Venice, Italy.

111. Bouvet C, Honkarnjanakul N, Rivallant S. Discrete Ply-Modelling of Low-Velocity Impact and Compression after Impact in Unidirectional Laminated Composites. ECCM 15 - 15th European Conference on Composite Materials, Venice, Italy.

112. Ivancevic D, Smojver I. Multiscale Damage Analysis of Laminated Composite Structures using Generalized Method of Cells Theory and Abaqus. ECCM 15 - 15th European Conference on Composite Materials, Venice, Italy.

113. Soni G, Singh R, Mitra M, Falzon B. A Multifibre Multilayer Representative Volumn Element (M^2RVE) for Prediction of Matrix and Interfacial Damage in Composite Laminates. ECCM 15 - 15th European Conference on Composite Materials, Venice, Italy.

114. Pinho ST, Iannucci L, Robinson P. Physically-Based Failure Models and Criteria for Laminated Fibre-Reinforced Composites with Emphasis on Fibre Kinking: Part 1: Development. Composites: Part A 2006;37:63-73.

115. Pinho ST, Iannucci L, Robinson P. Physically-Based Failure Models and Criteria for Laminated Fibre-Reinforced Composites with Emphasis on Fibre Kinking: Part 2: FE Implementation. Composites: Part A 2006;37:766-777.

116. Paris F. A Study of Failure Criteria of Fibrous Composite Materials. NASA, Langley 2001;NASA/CR-2001-210661.

117. Matzenmiller A, Lubliner J, Taylor RL. A Constitutive Model for Anisotropic Damage in Fibre-Composites. Mechanics of Materials 1995;20:125-152.

118. Anon. Abaqus Analysis User's Manual (6.12): Dassault Systemes, 2012.

119. Anon. Standard Test Method for Mode 1 Interlaminar Fracture Toughness of Unidirection Fibre-Reinforced Polymer Matrix Composites. ASTM 2007;D5528-01:1-12.

120. Pinho ST, Robinson P, Iannucci L. Fracture Toughness of the Tensile and Compressive Fibre Failure Modes in Laminated Composites. Composites Science and Technology 2006;66:2069-2079.

121. Martin RH, Davidson BD. Mode II Fracture Toughness Evaluation using Four Point Bend, End Notched Flexure Test. Plastics, Rubber and Composites 1999;28(8):401-406.

122. Turon A, Davila CG, Camanho PP, Costa J. An Engineering Solution for Mesh Size Effects in the Simulation of Delamination using Cohesive Zone Models. Engineering Fracture Mechanics 2007;74:1665-1682.

123. Elices M, Guinea GV, Gomez J, Planas J. The Cohesive Zone Model: Advantages, Limitations and Challenges. Engineering Fracture Mechanics 2002;69:137-163.

124. Turon A, Camanho PP, Costa J, Davila CG. A Damage Model for the Simulation of Delamination in Advanced Composites under Variable-Mode Loading. Mechanics of Materials 2006;38:1072-1089.

125. Harper PW, Hallett SR. Cohesive Zone Length in Numerical Simulations of Composite Delamination. Engineering Fracture Mechanics 2008;75:4774-4792.

126. Yang Q, Cox B. Cohesive Models for Damage Evolution in Laminated Composites. International Journal of Fracture 2005;133:107-137.

127. Wisnom MR. Modelling Discrete Failures in Composites with Interface Elements. Composites: Part A 2010;41:795-805.

128. Chen J. Predicting Progressive Delamination of Stiffened Fibre-Composite Panel and Repaired Sandwich Panel by Decohesion Models. Journal of Thermoplastic Composite Materials 2002;15:429-442.

129. Han T, Ural A, Chen C, Zehnder AT, Ingraffea AR, Bullington SL. Delamination Buckling and Propagation Analysis of Honeycomb Panels using a Cohesive Element Approach. International Journal of Fracture 2002;115:101-123.

130. Gopalakrishnan K, Ramesh Kumar R, Anil Lal S. Cohesive Zone Modelling of Coupled Buckling - Debond Growth in Metallic Honeycomb Sandwich Structure. Journal of Sandwich Structures and Materials 2012;14(6):679-693.

131. Panigrahi SK, Pradhan B. Three Dimensional Failure Analysis and Damage Propagation Behaviour of Adhesively Bonded Single Lap Joints in Laminated FRP Composites. Journal of Reinforced Plastics and Composites 2007;26(2):183-201.

132. Irisarri F, Laurin F, Carrere N, Maire J. Progressive Damage and Failure of Mechanically Fastened Joints in CFRP Laminates - Part 1: Refined Finite Element Modelling of Single-Fasterner Joints. Composite Structures 2012;94:2269-2277.

133. Zubillaga L, Turon A, Maimi P, Costa J, Mahdi S, Linde P. An Energy Based Failure Criterion for Matrix Crack Induced Delamination in Laminated Composite Structures. ECCM 15 - 15th European Conference on Composite Materials, Venice, Italy.

134. Abisset E, Ladeveze P, Daghia F. On the Intra/Interlaminar Coupling of Laminated Composites. ECCM 15 - 15th European Conference on Composite Materials, Venice, Italy.

135. Bouhala L, Makradi A, Belouettar S. Debonding in Reinforced Composite by an XFEM Cohesive Model. ECCM 15 - 15th European Conference on Composite Materials, Venice, Italy.

136. Breitzman TD, Iarve EV, Mollenhauer DH, Swindeman MJ, Hoos KH, Hallett SR. Discrete Damage Modelling in Open Hole Polymer Matrix Composite Laminates. ECCM 15 - 15th European Conference on Composite Materials, Venice, Italy.

137. Turon A, Camanho PP, Costa J, Renart J. Accurate Simulation of Delamination Growth under Mixed-Mode Loading using Cohesive Elements: Definition of Interlaminar Strengths and Elastic Stiffness. Composite Structures 2010;92:1857-1864.

138. Grau DL, Qiu XS, Sankar BV. Relation Between Interfacil Fracture Toughness and Mode-Mixity in Honeycomb Core Sandwich Composites. Journal of Sandwich Structures and Materials 2006;8:187-203.

139. Foo CC, Chai GB, Seah LK. Mechanical Properties of Nomex Material and Nomex Honeycomb Structure. Composite Structures 2007;80:588-594.

140. Zhang J, Ashby MF. The Out-of-Plane Properties of Honeycombs. Internation Journal of Mechanical Sciences 1992;34(6):475-489.

141. Aktay L, Johnson AF, Kroplin B. Numerical Modelling of Honeycomb Core Crush Behaviour. Engineering Fracture Mechanics 2008;75:2616-2630.

142. Shi G, Tong P. The Derivation of Equivalent Constitutive Equations of Honeycomb Structures by a Two-Scale Method. Computational Mechanics 1995;15:395-407.

143. Chawla A, Mukherjee S, Kumar D, Nakatani T, Ueno M. Prediction of Crushing Behaviour of Honeycomb Structures. International Journal of Crashworthiness 2003;8(3):229-235.

144. Anon. Getting Started with Abaqus: Interactive Edition 6.12: Dassault Systemes, 2012.

145. Sun JS, Lee KH, Lee HP. Comparison of Implicit and Explicit Finite Element Methods for Dynamic Problems. Journal of Materials Processing Technology 2000;105:110-118.

146. Harewood FJ, McHugh PE. Comparison of the Implicit and Explicit Finite Element Methods using Crystal Plasticity. Computational Materials Science 2007;39:481-494.

147. Prior AM. Applications of Implicit and Explicit Finite Element Techniques to Metal Forming. J Mater Process Technol 1994;45:649-656.

148. Yu H, Burgess IW, Davison JB, Plank RJ. Numerical Simulation of Bolted Steel Connections in Fire Using Explicit Dynamic Analysis. Journal of Constructional Steel Research 2008;64:515-525.

149. Fan JP, Tsui CP, Tang CY. Modelling of the Mechanical Behaviour of HA/PEEK Biocomposite under Quasi-Static Tensile Load. Materials Science and Engineering A 2004;382:341-350.

150. Santosa SP, Wierzbicki T, Hanssen AG, Langseth M. Experimental and Numerical Studies of Foam-Filled Sections. International Journal of Impact Engineering 2000;24:509-534.

151. Siad L, Ouali MO, Benabbes A. Comparison of Explicit and Implicit Finite Element Simulations of Void Growth and Coalescence in Porous Ductile Materials. Materials and Design 2008;29:319-329.

152. Oliver J, Huespe AE, Cante JC. An Implicit/Explicit Integration Scheme to Increase Computability of Non-Linear Material and Contact/Friction Problems. Comput Methods Appl Mech Engrg 2008;197:1865-1889.

153. Mattiasson K, Bernspang L, Samuelsson A. Solution of Quasi-Static, Force-Driven Problems by Means of a Dynamic-Explicit Approach and an Adaptive Loading Procedure. Engineering Computations 1996;13(2/3/4):172-189.

154. Anon. Abaqus User Subroutines Reference Manual (6.12): Dassault Systemes, 2012.

155. Schwingshackl CW, Aglietti GS, Cunningham PR. Determination of Honeycomb Material Properties: Existing Theories and an Alternative Dynamic Approach. Journal of Aerospace Engineering 2006;19:177-183.

156. Anon. HexPly (R) M77 80-180 deg C Curing Epoxy Matrix Product Datasheet. HexCel 2011:1-3.

157. Anon. Redux (R) 609 Adhesive Film for Bonding Metallic and Composite Components Product Data. HexCel 2010:1-4.

158. Anon. Prime (TM) 20LV Epoxy Infusion System. Gurit:1-6.

159. Anon. Standard Test Method for Tensile Properties of Polymer Matrix Composite Materials. ASTM 2008;D3039/D3039M-08:1-13.

160. Anon. Standard Test Method for Compressive Properties of Polymer Matrix Composite Materials with Unsupported Gage Section by Shear Loading. ASTM 2008;D3410/D3410M-03:1-16.

161. Anon. Standard Test Method for Compressive Properties of Rigid Plastics. ASTM 2010;D695-10:1-7.

162. Anon. Standard Test Method for Measuring the Damage Resistance of a Fiber-Reinforced Polymer Matrix Composite to a Drop-Wieight Impact Event. ASTM 2012;D7136 / D7136M-12:1-16.

163. Lloyd JC. Impact Damage and Damage Tolerance of Fibre Reinforced Advanced Composite Laminate Structures. , 2002.

164. Anon. Standard Test Method for Measuring the Damage Resistance of a Fiber-Reinforced Polymer-Matrix Composite to a Contrated Quasi-Static Indentation Force. ASTM 2012;D6264 / D6264M-12:1-11.

165. Zhou G. Mechanics of Materials. Unpublished 2005;Departmental Publication Number 17.

166. Zhou G. Principles of Composite Materials and Structures. Unpublished 2007;Departmental Publication Number 20.

167. Anon. Abaqus/CAE User's Manual (6.12): Dassault Systemes, 2012.

168. Singh AK, Davidson BD, Eisenberg DP, Czabaj MW, Zehnder AT. Barely Visible Impact Damage Evaluation of Composite Sandwich Structures. 51st AIAA/ASME/ASCE/AHS/ASC Structures, Structural Dynamics, and Materials Conference, Orlando, Florida, 2010. p. 1-17.

169. Anon. Structural Design and Test Factors of Safety for Spaceflight Hardware. NASA Technical Standard 2008;NASA-STD-5001A.

170. Gubisch M. In Focus: Manufacturers Aim for More Comfortable Cabin Climate. Flight International 2012.

171. Hepburn AN. Human Factors in the Concord. Occupational Medicine 1967;17:47-51.

172. Berberan-Santos MN, Bodunov EN, Pogliani L. On the Barometric Formula. American Journal of Physics 1997;404:404-412.

173. Anon. A Quick Derivation Relating Altitude to Air Pressure. Portland State Aerospace Society 2004.

174. Anon. Standard Atmosphere. International Organization for Standardization 1975;ISO 2533:1975.

175. Crump DA, Dulieu-Barton JM, Savage J. Design and Commission of an Experimental Test Rig to Apply a Full-Scale Pressure Load on Composite Sandwich Panels Representative of an Aircraft Secondary Structure. Measurement Science and Technology 2010;21:1-16.

176. Karagiozova D, Nurick GN, Langdon GS. Behaviour of Sandwich Panels Subject to Intense Air Blasts - Part 2: Numerical Simulation. Composite Structures 2009;91(4):442-450.

177. Zhu F, Zhao L, Lu G, Gad E. A Numerical Simulation of the Blast Impact of Square Metallic Sandwich Panels. International Journal of Impact Engineering 2009;36(5):687-699.

178. Ko WL, Jackson RH. Combined Compressive and Shear Buckling Analysis of Hypersonic Aircraft Structural Sandwich Panels. NASA 1991;Technical Memorandum 4290.

179. Birman V, Bert CW. Wrinkling of Composite-Facing Sandwich Panels under Biaxial Loading. Journal of Sandwich Structures and Materials 2004;6:217-237.

180. Liang QQ, Uy B, Wright HD, Bradford MA. Local Buckling of Steel Plates in Double Skin Composite Panels under Biaxial Compression and Shear. Journal of Structural Engineering 2004;130(3):443-451.